“Analysis of Once-Through Boiler Concepts in Parabolic Troughs”

Von der Fakultät für Maschinenwesen der
Rheinisch-Westfälischen Technischen Hochschule Aachen
zur Erlangung des akademischen Grades eines
Doktors der Ingenieurwissenschaften
genehmigte Dissertation

vorgelegt von

Jan Fabian Feldhoff

Berichter: Univ.-Prof. Dr.-Ing. Robert Pitz-Paal
Univ.-Prof. Dr.-Ing. Dirk Abel

Tag der mündlichen Prüfung: 18. Dezember 2015

Diese Dissertation ist auf den Internetseiten der Universitätsbibliothek online verfügbar.

D 82 (Diss. RWTH Aachen University, 2015)

Acknowledgements

This thesis was conducted during my time at the Institute of Solar Research of the German Aerospace Center (DLR) in Stuttgart.

I would like to thank my supervisor Prof. Robert Pitz-Paal for his help and advice throughout the thesis. I also thank Prof. Dirk Abel for his co-supervision and his hints for 'tuning' of the control chapters as well as Prof. Singheiser for acting as the chair of the examination board.

My particular thanks go to my supervisors and mentors Markus Eck and Tobias Hirsch, who both had the trust in me to perform this work and who supported me whenever there were any questions or doubts.

I am also deeply grateful for my colleagues and friends at DLR, who supported me in all possible ways: Heiko Schenk, who shares the office and any suddenly arising idea with me and who still tries to teach me Swabian sentences; Michael Wittmann, who gave important inputs during the various coffee and whiteboard discussions and who always suprises me by his strict scientific thinking; and Maike Johnson, who slogged her way through the original version to decisively improve my English grammar.

Of course, I also thank Wolf-Dieter Steinmann, Stefan Zunft, Ralf Uhlig, Stefan Wilbert and Dirk Krüger for their fruitful discussions and modeling help throughout the work. There is no doubt that the experimental section of this work would not exist without my colleagues Martin Eickhoff, Mirko Meyer-Grünefeldt and Lothar Keller, who made everything work for me in Almería and, especially Mirko, who introduced and accompanied me to the best tapas bars around. It was also a great pleasure to work together with my colleagues of CIEMAT-PSA Loreto Valenzuela, Javier León and Eduardo Zarza. I also thank the operation and maintenance team of the DISS facility at PSA, especially Rafa and Juan.

Very valuable contributions to this work are owed to the students I had the pleasure to supervise during my time at DLR (in order of appearance): Camille Bachelier, showing the non-triviality of steady-state analysis, David Trebing, who enlightened my control understanding, Florent Morille, who enabled the fast simulations, Eva Faust, analyzing the vast experimental data, Gleb Savateev, now an expert in non-linear state estimation, and Aina Rosselló, who was a bonanza for thermo-mechanical analysis.

Last, but not least, such a thesis always requires the private support in the background. I thank my parents and friends for their help and motivation during the whole time. And my particular thanks go to Kadda, who was always supportive and patient during my long periods of writing and who makes me enjoy the time outside the office.

“Jetzt isch d’r Kiddel g’flickt!“

Heiko

Contents

Nomenclature

List of capital Latin symbols

Symbol	*Description*	*Unit*
A	Cross-sectional area	m²
A	State/system matrix for LTI state-space models	
B	Input matrix for LTI state-space models	
C	Output matrix for LTI state-space models	
$C(s)$	Controller transfer function	
D	Feedthrough matrix for LTI state-space models	
D	Damage or usage factor of material	-
$D'(s)$	Disturbance transfer function	
F_R	Frictional pressure loss correlation	bar/m
G_{pr}	Projected irradiance; DNI multiplied by cosine of incidence angle	W/m²
G_{eff}	Effective irradiance; DNI corrected by cosine of incidence angle and other optical collector losses	W/m²
$G_{x\text{-}y}$	Linear transfer function describing the change in variable y by a change in variable x	[y]/[x]
J	Objective function for optimization	
L	Length	m
N	Number of samples or cycles	#
$P(s)$	Process transfer function	
Pr	Prandtl number	-
Q	Thermal heat flux or power	W
R	Ratio	-
Re	Reynolds number	-
S_a	Stress amplitude	MPa
V	Volume	m³

List of small Latin symbols

Symbol	*Description*	*Unit*
c	Specific heat capacity of solid material	J/kg/K
c_p	Specific heat capacity of fluid	J/kg/K
c_1	Empirical heat loss coefficient	W/m/°C
c_4	Empirical heat loss coefficient	W/m/°C^4
d	Diameter	m
d	Disturbance input to LTI model	
e	Error; reference minus actual value	[y]
e_{sc}	Exponent for scaling of mass flow	e_{sc}
f	Dimensionless factor (further specified by index)	-
h	Specific enthalpy	J/kg
k	Transfer function gain (reference and unit according to index)	
l	Length	m
m	Mass	kg
$\dot{m}$	Mass flow	kg/s
p	Pressure	bar (= 10^5 Pa)
q	Thermal heat flux (without index: to fluid)	W/m²
s	Complex Laplace variable	1/s
t	(Continuous) time	s
u	Specific internal energy	J/kg
u	Control/input variable for LTI state-space models	
u'	Deviation/disturbance of input variable	
w	Fluid velocity	m/s
w_{ap}	Aperture width of a collector	m
w_x	Weighting factor	-
x	State or state vector for LTI state-space model	
$\dot{x}$	Derivative of state or state vector	
y	Controlled/output variable(s) for LTI state-space model	
z	Axial coordinate along the loop length	m

List of Greek symbols

Symbol	*Description*	*Unit*
α	Heat transfer coefficient	W/m²/K
δ	Damping of complex conjugate poles or zeros	
Δ	Indicating a finite difference of the subsequent variable	
$\epsilon(s)$	Sensitivity function	
$\gamma(s)$	Closed-loop transfer function of disturbance rejection	
γ_h	Derivative of density by enthalpy (constant pressure)	(kg/m³)/(J/kg)
γ_p	Derivative of density by pressure (constant enthalpy)	(kg/m³)/Pa
ζ	Pressure drop coefficient	-
η	Efficiency (further specified by index)	-
λ	Thermal conductivity	W/m/K
λ	Filter time constant	s
$\mu(s)$	Complementary sensitivity function	
φ_{dry}	Dry angle, indicating non-wetted surface of an inner cross-section [0° (wetted) to 180° (dry)]	°
ρ	Density	kg/m³
ρ_{track}	Track angle, indicating deviation of tracking position to collector-normal position [-90° to 90°; 0° at solar noon]	°
ϑ	Temperature (without index: fluid)	°C
θ_{inc}	Collector incidence angle	°
τ	Time constant	s

List of indices

Symbol	*Description*
*	Denoting optimal solution (superscript)
^	Denoting prediction/estimate of a variable (hat)
1ph	Single-phase flow
2ph	Two-phase flow
1	Loop inlet (of MBM)
13	Section between inlet and initial point of evaporation (of MBM)
15	Section between inlet and end point of evaporation (of MBM)
2	Preheating section (of MBM)
3	Initial point of evaporation (of MBM)
35	Section between initial point and end point of evaporation (of MBM)
4	Evaporation section (of MBM)
4I	Evaporation section before injection (of MBM)
4II	Evaporation section after injection (of MBM)
5	End of evaporation (of MBM)
6	Superheating section (of MBM)
6II	Superheating section before injection (of MBM)
6III	Superheating section after injection (of MBM)
7	Loop outlet (of MBM)
I	First sub-system of MBM, between inlet and evaporation injection
II	Second sub-system of MBM, between both injections
III	Third sub-system of MBM, between superheating injection and outlet
A	Location of evaporation injection (of MBM)
A5	Distance from evaporation injection to end of evaporation (of MBM)
a	Outer (tube wall)
a,i	Amplitude of case *i*
a,p	Amplitude of permanent stress strength
abs	Absorber
B	Location of superheating injection (of MBM)
bi	Steam property before (any) injection

Symbol	*Description*
befSHI	Steam temperature before superheating injection, equivalent to TbefInj
c	Control or controller, respectively
c,63%	Characteristic time constant referring to the time needed to reach 63 % of the final valued for the first time
c,imc	Characteristic time constant regarding internal model control
c,rp	Characteristic time constant regarding real parts
c,sl	Characteristic time constant regarding the slowest mode of all poles
clsky	Clear sky, also “cs”
coll	Collector
cs	Clear sky, also “clsky”
DNI	Regarding DNI or effective irradiation, respectively
d0	Initial start of disturbance
EVL	Evaporation loop (of recirculation mode)
eff	Effective; remaining after other (optical) losses
el	Electric
epc	Engineering, procurement and construction
F	Fluid
FF	Feedforward
foc	Focus position of collector
fract	Fractal length/dimension
GA	Gain acceleration/adaptation of controller gain
horizon	Time horizon for scaling
I	Integral time or reset time, respectively
i	Inner (tube wall)
i	Regarding case/amplitude *i*
in	Inlet
inj	Liquid water of injection
inj06	Regarding injection before DISS collector 6
Inj11	Regarding injection before DISS collector 11
inv,0	Initial investment
L	Indicating length-specific variable (unit [X]/m)
LS	Live steam temperature
LS,ref	Reference/nominal live steam temperature of turbine
loss	Heat loss
M	Regarding mass flow

Symbol	*Description*
meas	Measured value
mIn	Inlet mass flow of loop
mInj06	Injection mass flow before DISS collector 6
mInj11	Injection mass flow before DISS collector 11
mInj12	Injection mass flow before DISS collector 12
O&M	Operation and maintenance
opt	Optical
opt,0	Peak optical; defined for an incidence angle of 0°
out	Outlet
P	Process
PT1	First order delay element
PTn	n-th order delay element
p	Pole (of transfer function)
pre	Prediction/forecast horizon
ref	Reference value
rel	Relative value
res	Residence time
SF	Solar field
SHI	Superheating injection
SHL	Superheating loop (of recirculation mode)
sam	Sampling time
sc	Scaling
Tout	Outlet temperature
TbefInj	Steam temperature before superheating injection
TbefSHI	Steam temperature before superheating injection, equivalent to TbefInj
sfb	State feedback
th	Thermal
w	Wall of absorber tube
w,inj	Liquid water of injection
z	Zero of transfer function
λ	Regarding filter time constant; for tuning factor
ϑ	Temperature

List of abbreviations

Abbreviation	*Meaning*
-	
ABB	Company name (Asea Brown Boveri)
CSP	Concentrated solar (thermal) power, also called solar thermal electricity (STE)
DETOP	Former German research project regarding DSG
DFEM	Discretized, finite element model (for transient simulation)
DISS	Direct Solar Steam, European research project; name patron for the corresponding test facility at the PSA
DIVA	
DLR	Deutsches Zentrum für Luft- und Raumfahrt e.V. (German Aerospace Center)
DNI	Direct normal irradiance (unit W/m²)
DSG	Direct (solar) steam generation
DUKE	Research project, Durchlaufkonzept – Entwicklung und Erprobung (Development and demonstration of the once-through concept)
EBGS	Error-based gain scheduling (also denoted gain acceleration)
EPC	Engineering, procurement and construction
EPE	Position of end point of evaporation, i.e. the first location along the loop at which the water content is completely saturated/gaseous
EVI	Evaporation injection
EVL	Evaporation loop (only for recirculation mode)
FCR	Fixed charge rate (unit %/year)
FEM	Finite element method
FF	Feedforward
GA	gain acceleration (also denoted as error-based gain scheduling)
GUDE	Former German research project regarding DSG
HTC	Heat transfer coefficient (unit W/m²/K)
IAM	Incidence angle modifier (dimensionless)
IMF	Inlet mass flow of one collector loop
INDITEP	Former European research project regarding DSG
IPE	Position of initial point of evaporation, i.e. the location along the loop at which the water starts boiling
ITES	Former German research project regarding DSG
LCOE	Levelized cost of thermal energy
LHP	Left half plane (of pole-zero map)

Abbreviation	*Meaning*
LTI	Linear time-invariant model or transfer function
MBM	Moving boundary model
MPA	Materialprüfanstalt Stuttgart (Material Testing Institute of the University of Stuttgart)
MPC	Model predictive control
NMPC	Non-linear model predictive control
O&M	Operation and maintenance
OPC	Object Linking and Embedding for Process Control
OTM	Once-through mode (solar once-through boiler configuration)
PCM	Phase change material
PDE	Partial differential equations
PE-1/2	Puerto Errado 1 and 2, Fresnel-DSG plants in Spain
PI	Proportional integral controller
PRODISS	Preparational project for the DISS project
PSA	Plataforma Solar de Almería in Spain
RHP	Right half plane (of pole-zero map)
RM	Recirculation mode (solar steam generator configuration)
S-N	Curve of stress amplitude versus cycle number
SHI	Superheating injection
SHL	Superheating loop (only for recirculation mode)
TM	Trademark
TSE-1	Thai Solar Energy 1, Parabolic trough-DSG plant in Thailand

Abstract

Solar thermal power plants use collectors to concentrate the sunlight and heat up a fluid to high temperatures. This heat can be used to run a steam turbine and generate electricity. Such plants work similar to conventional steam power plants, with the only difference in replacing the fossil steam generator by a solar one. The steam can directly be generated within the solar field. This direct steam generation (DSG) process is analyzed in detail for parabolic trough collectors. As in conventional power plants, there exist two main concepts, one with forced circulation during the evaporation phase and one in a once-through configuration. This work covers the complete range of solar once-through steam generators for the first time. Design criteria are derived, transient models are validated and robust control strategies for large-scale commercial plants are developed. Those are validated by experiments at a commercial scale test facility at Plataforma Solar de Almería in Spain. Furthermore, a methodology for component life time estimation is proposed for such plants and the overall economic potential of the once-through configuration is compared to the state-of-the-art recirculation type. It is demonstrated for the first time that solar once-through steam generators are technically feasible and economically very promising.

Kurzfassung

Solarthermische Kraftwerke konzentrieren die direkte Solarstrahlung, um Wärme bei hohen Temperaturen zu erhalten. Diese Wärme kann zum Beispiel für einen Dampfturbinenprozess genutzt werden, um Strom zu erzeugen. Dies entspricht der Arbeitsweise eines fossilen oder nuklearen Kraftwerks, mit dem einzigen Unterschied, dass der konventionelle Dampferzeuger durch einen solaren ersetzt wird. Bei der direkten Dampferzeugung im Solarfeld ergeben sich zwei wesentliche, analoge Konzepte: zum einen das Umlaufprinzip für den Verdampferbereich; zum anderen das Zwangsdurchlaufprinzip, welches auch als Benson-Kessel bekannt ist.

Kommerzielle Kraftwerke mit solarer Direktverdampfung werden bereits in Spanien und Thailand erfolgreich im Umlaufkonzept betrieben. Die vorliegende Arbeit analysiert nun detailliert das Zwangsdurchlaufkonzept für solare Parabolrinnen-Kraftwerke. Eine besondere Herausforderung ist dabei die nicht regelbare Wärmezufuhr durch die Sonne, die durch eine angepasste Massenstromzufuhr ausgeglichen werden muss. Auslegungskriterien für solche Solarfelder werden herausgearbeitet, transiente Simulationsmodelle angepasst und robuste Regelstrategien für künftige kommerzielle Kraftwerke werden entwickelt. Alle Punkte werden anhand von Experimenten im kommerziellen Maßstab an einer Testanlage auf der Plataforma Solar de Almería in Spanien validiert.

Darüber hinaus wird eine Methodik zur Charakterisierung der Strahlungssituation vorgeschlagen, die eine einfache Lebensdauerabschätzung von potenziell kritischen Komponenten ermöglicht. Anhand letzterer kann beispielhaft die lange Lebensdauer eines bestrahlten Dampferzeuger-Rohres nachgewiesen werden. Die Vor- und Nachteile des solaren Benson-Kessels werden mit Hilfe eines detaillierten techno-ökonomischen Vergleichs mit dem Stand der Technik herausgestellt. Insgesamt kann so erstmalig der Nachweis der technischen Funktionsfähigkeit und des wirtschaftlichen Potenzials des solaren Durchlaufkonzepts erbracht werden.

1 Introduction

The availability of reliable and clean energy, especially electricity, will be one of the most important challenges in the future. Oil is still the most important energy carrier of our times, with consumption increasing rapidly [115] but price and availability a pawn in the hands of the exporting countries and their politics [219]. Energy diversity is therefore a key factor for long term energy supply systems. The demand for cleaner, sustainable energy supply at the same time paves the way for the development of renewable energy harnessing.

One of the vastly available energy resources is the sun. Countries in the world's Sun Belt such as Morocco, Egypt and USA as well as countries such as Chile or even China have a high potential due to high direct solar irradiation. This renewable energy carrier can be used to produce dispatchable electricity with the help of concentrated solar power (CSP). Countries that currently depend on the import of expensive energy carriers could even become energy exporters [249, 250].

CSP technology uses large mirrors to concentrate sunlight onto a small receiver (solar towers or solar parabolic dishes) or onto long receiver pipes (linear Fresnel collectors or parabolic troughs). The latter line focus collectors are the widest spread commercial CSP technology at the moment, but are still in its infancy compared to conventional fossil power plants. CSP technologies collect the sun's energy as heat, store the heat if needed, and finally transport it to a power block in which the heat is transformed to electricity by a steam turbine or a gas turbine. The main advantage of CSP is its dispatchability. This means that the heat of the solar field can be stored for hours or days before it is used to generate electricity, more cheaply than electricity storage such as batteries. In consequence, it is possible to generate solar electricity during the night, or whenever it is needed.

One option of CSP is to use water from the steam turbine and directly feed it to the solar field to generate steam at high temperatures of up to 550°C. The steam is fed back to the steam turbine and the cycle is repeated. This cycle is equivalent to a conventional coal power plant – but with the coal-fired steam generator being replaced by the solar field. This concept is called direct (solar) steam generation (DSG). Some commercial DSG plants already exist in Spain [168] and Thailand [141]. They apply the so-called recirculation mode with a steam drum in the solar field to separate the evaporation and superheating sections. Following the footsteps of fossil boilers, the current work aims at further developing the DSG technology to become more competitive. By the use of solar once-through boilers, the expensive steam drum, the header piping to and from the drum and the recirculation pump can be omitted. The investment of the so-

lar field can thus be reduced. Furthermore, the heat losses are reduced significantly and the solar field can be operated more efficiently. Another practical advantage is the easy scalability of one loop and its operational flexibility. Recirculation mode solar fields consist of two types of loops, one for evaporation and one for superheating. The collector area of evaporation and superheating sections must be balanced well for a certain design point and nominal temperature, which can be challenging depending on the total solar field size and the actual plant site. For once-through mode, each loop is identical, there is no fixed share of evaporation to superheating area and the outlet temperature can flexibly be defined by the mass flow provided to the loop.

Two drawbacks are usually associated with solar once-through boilers. One is the controllability, especially the stabilization of the solar field outlet temperature of the steam. The second one is the fluctuation of the end of the evaporation zone, which is supposed to cause high material stress in the absorber tubes and, thereby, to reduce the receivers' life time. Particular emphasis is thus put on those two aspects. The work suggests design criteria for solar once-through boilers in parabolic troughs, shows how to realistically control these plants under varying solar irradiation conditions and provides a methodology to estimate the life time and potential of the technology.

1.1 Objective and methodology of thesis

The overall objective of this work is the technical and economic evaluation of the solar once-through boiler concept in parabolic troughs. This concept is referred to here as once-through mode (OTM). The work is divided into five major parts. The first part (chapter 2) deals with general, mainly steady-state design criteria for the loop layout of a line focus once-through boiler. The main criteria are derived and exemplified by a reference loop for 500°C and 125 bar at the outlet. In addition, the criteria are applied to the DISS (Direct Solar Steam, see next sections for details) test facility and the basic layout for experiments is derived.

The second part (chapter 3) deals with the transient modeling of the once-through steam generation process. As the main energy source is not controllable, the transient simulation is the most important aspect in OTM design. A discretized model, a moving boundary model and linear time-invariant transfer functions are derived. The models are applied to the DISS test facility and validated by experiments. They are the basis for the remaining chapters.

The third part (chapter 4) of this work deals with controller design. The main task of control is to reject disturbances and keep the desired steam temperature setpoints. This is a challenging task due to quickly and uncontrollably changing solar irradiation, the lack of thermal buffer elements and long time delays in the manipulated mass flows. A new control strategy is developed,

which is based on adaptive PI controllers. This method especially aims at being robust, easy to understand and easy to implement. The strategy is demonstrated at the DISS test facility. As an outlook on advanced concepts, the potential of model predictive control is shown for the process. These concepts will be very useful, if a good forecasting/nowcasting of the irradiation is possible. This is a different but current field of research [109].

The fourth part (chapter 5) deals with the analysis of component life time. A methodology for predicting the life time of any CSP solar field component is suggested. Typical transient situations are identified and categorized for the superheater section and the endzone of evaporation. Thermo-mechanical stress analysis is performed for typical situations. These loads are then evaluated by means of pressure vessel design codes to predict the component life time.

The final part (chapter 6) assesses the overall comparison of the OTM with the state-of-the-art commercial recirculation mode for large power plants of 250 MW of nominal thermal power. The annual efficiency and yield performance is analyzed exemplarily for one year at the location of Tabernas, Spain. Solar field basic engineering is performed and the differences to recirculation mode are identified. The evaluation of both systems is summarized by a comparison of the levelized cost of thermal energy.

All of the parts are summarized in the last chapter and final conclusions are drawn. The work includes all relevant aspects such as controllability, reliability, efficiency, investment, system complexity and, to a small extend, the operation and maintenance. It focuses on parabolic trough solar fields. Nevertheless, all methodologies are transferable to other line focus systems such as linear Fresnel collectors. At some points, links to this technology are mentioned as well. Point focusing technologies such as tower or dish systems show only little correspondence in the main system characteristics and are not covered here.

1.2 A brief history of direct steam generation

Direct solar steam generation (DSG) was already used for solar-thermal process steam and power generation in the late 19th and at the beginning of the 20th century [82]. However, mainly because of cheap fossil fuel resources, it took the technology almost another 100 years to become applied at a large scale and commercially. Novatec Solar commissioned the first DSG Fresnel plants in Puerto Errado, Spain, in 2009 and 2012 [168]. These PE-1 and PE-2 plants provide a nominal electrical power of 5 and 30 MW, respectively. The solar field produces wet steam, which is then separated by a central steam drum. The liquid condensate is used again in the solar field, while the saturated steam is fed to a steam turbine for producing electricity. Current developments by Novatec Solar have also proven the ability to produce superheated steam at the PE-1 site [179].

The company Solarlite built the first commercial DSG parabolic trough plant with superheated steam. The TSE-1 plant is located in Thailand and was commissioned in 2011 [141]. The plant produces superheated steam in the solar field of about 30 bar and 330°C, which is fed to a steam turbine. A steam drum is used in the solar field to separate the evaporation and superheating section. Experience from this plant promotes the feasibility of the DSG technology and has proven a very robust operation even during strong transients [141].

The basis for these commercial plants was the development started in the 1990s. The projects GUDE and PRODISS analyzed fundamental principles of steam generation in horizontal tubes [97] before the DISS project was started in 1996 [275]. Although DISS is the official abbreviation for *Direct Solar Steam*, it seems a remarkable coincident that one of the researchers at those times hailed from the town Diss in Norfolk, England [273]. In the first phase of this project, the accordingly named DISS test facility was designed and built with 500 m of LS-3 type collectors. In the second phase, the DISS test facility was used to investigate the basic operation concepts of DSG, which are recirculation mode, once-through mode and injection mode [68]. A schematic diagram of these three classical concepts is shown in Figure 1.1. All concepts share that the water from the power block is preheated, evaporated and superheated in the solar field, and is then finally directly fed to the steam turbine or other steam consumers. In once-through mode, preheating, evaporation and superheating is done within the same loop. For injection mode, various injection lines are additionally foreseen in the loop to have a better controllability [65]. In recirculation mode, the solar field is divided into a steam generation part and a superheating section. The wet steam from the first section is separated by a steam drum into liquid condensate, which is fed back to the solar field inlet, and saturated steam, which is fed to the superheating section.

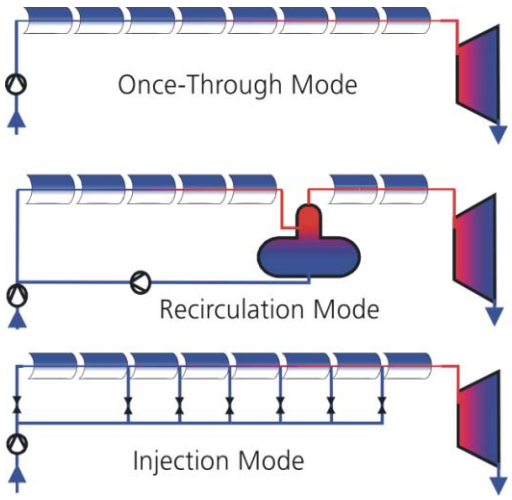

Figure 1.1: Classical DSG operation concepts as proposed in [68].

Experience of the DISS project supported the recirculation mode as the most promising option, because it showed a very robust operational behavior [276]. Injection mode was considered too expensive, while once-through mode was thought to be too challenging from a control point of view at that time. In consequence, a pre-commercial DSG plant for recirculation mode was designed in the project INDITEP [274]. In the same framework, two new Eurotrough collectors of 100 m length each were added at the inlet of the DISS test facility. A detailed system analysis of recirculation plants within the project DIVA then identified that higher steam parameters of 100 bar and up to 500°C offer further cost reduction and efficiency potential [72]. Component tests for such high parameters could successfully be demonstrated during the REAL-DISS project at a test facility in Carboneras, Spain [60]. At the same test facility, in the framework of the ITES project, a new thermal energy storage concept for DSG could be demonstrated by the world's largest prototype of a phase change material (PCM) storage system [145].

Research and commercial plants show reliable and robust operation of DSG solar fields with recirculation mode. However, the DETOP project revealed three missing development steps for the long-term success of DSG. These are (a) the development of a cheap commercial storage system, (b) the optimization of operation and maintenance procedures together with joint integration concepts of solar field, power block and storage system, as well as (c) the development of the once-through mode as a more cost-effective solar field option [81]. The latter research topic led to the initiation of the DUKE project, which aims at the demonstration of the once-through mode (OTM) on a commercial-scale test loop. In order to reach this goal, the DISS facility was extended by three new collectors to a total length of now 1000 m (as of 2013). More details on the performed changes and a history of the DISS facility can be found in [74]. The configuration of the facility relevant for the assessment of OTM is described in the next section. The DUKE project is expected to result in an evaluation of the OTM and a comparison with the recirculation mode.

The developments in solar-thermal steam generation remind one of the histories of classical fossil steam generators. The first power plants were operated in natural and forced circulation mode because of the simplicity of the approach. Then the trend to higher efficiencies, i.e. pressures, as well as the need for more flexibility led to the introduction of once-through boilers [53]. These were introduced as so-called Benson or Sulzer boilers [232] and are, obviously with variants, still the current commercial practice. The evolution of solar-thermal DSG is thus a consequent step. However, the boundary conditions are different for solar and fossil once-through boilers, e.g. simply by the fact that the energy source of solar boilers cannot be influenced. The current work has been performed in the framework of the DUKE project and aims at providing a

more scientific background on the most important aspects on solar once-through boilers.

The state of the art overview on particular topics such as modeling of steam generation in horizontal tubes or control of solar boilers is provided in the corresponding chapters.

1.3 Description of test facility

The DISS (Direct Solar Steam) test facility was the first large-scale experimental plant for research on the DSG process. It is located in the desert of Tabernas, close to Almería in Spain. The facility belongs to the test center for concentrating solar power called Plataforma Solar de Almería (PSA) and is owned and operated by the Spanish research center CIEMAT. The facility has seen many changes throughout the years of operation, each leading to another step forward in DSG research. All operating modes of DSG could and still can be tested at the facility. Detailed descriptions on the developments and background can be found in [74, 272, 275].

The facility is used in this work to study the once-through mode (OTM) characteristics in detail, to validate transient models and to demonstrate the newly developed control concepts. This section thus provides an overview on the whole facility and the most important features that are currently available. Figure 1.2 shows a schematic diagram of the plant in OTM configuration. Figure 1.3 shows two photos of the facility to get a real life impression. A feed water pump is included in the Balance of Plant (BOP) and provides water to the solar field inlet. The water enters collector 0A and is then forced through all other collectors in series. On its way, the water is preheated, evaporated and then superheated. After the last collector (12), the generated steam is directed back to the BOP. At the outlet of the solar field, the pressure level of the steam is controlled by a throttle valve (not shown). Normal operation of the facility is with a fixed pressure at the outlet. After the throttle valve, the steam passes through a heat exchanger. The steam is cooled down and its power is used to preheat the water that is going to the solar field inlet. This increases the solar field's inlet temperature to a level that is similar to the feed water temperature after the pre-heating section of a conventional power block. The de-superheated steam from the heat exchanger then passes a dry cooling system by which it is completely condensed. The condensate is collected in the feed water tank from which it is sucked by the feed water pump and again directed to the solar field. This completes the closed water circuit. Although a steam turbine is not installed in the facility, the solar field operation can be performed as if a turbine was present.

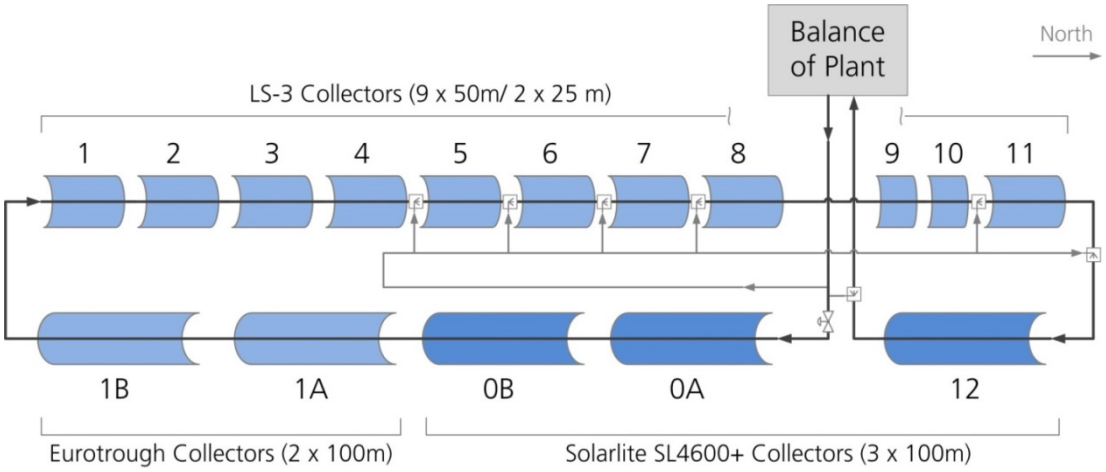

Figure 1.2: Diagram of the DISS test facility in once-through mode configuration.

Figure 1.3: Photos of collector 1A of the DISS test facility before extension in DUKE project (2007) and aerial view in north-eastern direction of complete new DISS facility (Jan. 2013). Source: DLR.

Typical operating parameters used in this work are an inlet temperature of 260°C, an outlet temperature of 400°C and an outlet pressure of 80 bar. However, during the DUKE project, the facility was equipped with new receivers and piping that allows operation with outlet steam conditions up to 500°C and 110 bar [76]. The receivers have a length of 4.06 m, an outer steel tube diameter of 70 mm and a wall thickness of 5.5 mm. They were produced by the company SCHOTT Solar in 2011. The length of all collectors in total is about 1000 m and the plant comprises 240 receivers. The collectors are connected with each other using ball joints of the company Advanced Thermal Systems Inc., which compensate the length variation of the receivers during the heating process and allow rotation of the collectors when tracking the sun, while still being connected by fixed steel piping.

The historical growth of the DISS facility led to a variety of collector types with different geometries and efficiencies. As these values are important for energetic analyses, Table 1.1 provides an overview of all the 16 collectors installed. Note that only the collector identifiers are used throughout this text,

thus, collector 0A indicates the first collector in the loop and collector 1 indicates the fifth collector of the loop. This corresponds to Figure 1.2. In total, there is an aperture area of 5195.9 m² available, with a mean optical efficiency of 69.8 %. In consequence, during summer irradiation conditions, the loop can provide a thermal power of up to 3 MW. This corresponds to a commercial-scale size and allows for testing close to power plant conditions. The optical efficiencies were determined by cold water experiments with a transient evaluation. The uncertainties are higher than ±4.5 % due to the measurement equipment available at the plant [75].

Table 1.1: Collectors' geometries and nominal optical efficiencies at DISS facility.

Name	*Number*	*Type*	*Aperture width [m]*	*Length (Nominal module length) [m]*	*Nominal aperture area [m²]*	*Nominal optical efficiency [%]*
0A	1	SL4600+	4.60	100 (96)	441.6	76.3
0B	2	SL4600+	4.60	100 (96)	441.6	75.4
1A	3	ET-100	5.76	100 (96)	553.0	65.1
1B	4	ET-100	5.76	100 (96)	553.0	70.1
1	5	LS-3	5.76	50 (48)	276.5	69.4
2	6	LS-3	5.76	50 (48)	276.5	71.4
3	7	LS-3	5.76	50 (48)	276.5	64.1
4	8	LS-3	5.76	50 (48)	276.5	66.4
5	9	LS-3	5.76	50 (48)	276.5	70.9
6	10	LS-3	5.76	50 (48)	276.5	70.2
7	11	LS-3	5.76	50 (48)	276.5	72.7
8	12	LS-3	5.76	50 (48)	276.5	68.1
9	13	LS-3	5.76	25 (24)	138.3	55.6
10	14	LS-3	5.76	25 (24)	138.3	65.9
11	15	LS-3	5.76	50 (48)	276.5	66.6
12	16	SL4600+	4.60	100 (96)	441.6	73.7
Total				1000 (960)	5195.9	69.8

To allow the injection of water during the evaporation and superheating process, various injectors are installed along the loop between some collectors (see Figure 1.2). Feed water can directly be injected into the steam flow by them. An additional injection is located after the last collector. It is used to guarantee a steam temperature below 450°C when entering the BOP because of design limitations. During this work, only the injectors before collector 6 and collector 11 are used.

After each collector, Pt100 temperature sensors are installed to measure the fluid temperature. Fluid temperature, pressure and mass flow are measured at the loop inlet. Pressure is also measured after collector 8, after collector 12 and after the BOP throttle valve, the latter serving for pressure level control. The steam mass flow is measured after collector 11 and after collector 12. All injection mass flows are measured as well. Furthermore, differential pressures are measured over each collector, over collectors 1 to 8 as total, over collectors 9 to 11 as total and over the complete loop.

Two additional features are foreseen for a more detailed study of the OTM behavior. First, there are 57 thermocouples installed between the receivers of collectors 6 to 9. In this area, the change between evaporation and superheating is expected for nominal operating conditions. The sensors are located between each or every second receiver, i.e. every four or eight meters, and measure the fluid temperature. At some locations, two sensors are installed, with one sensor tip slightly above and the other slightly below the middle of the fluid cross section. While evaporation takes place at constant temperatures, the superheating shows rising fluid temperatures. Thus, the thermocouples can be applied to detect and visualize the end of evaporation by measuring the fluid temperature.

The second feature is the special receivers designed to measure the steel wall temperature around the circumference of one cross-section. There are six thermocouples welded to the steel surface and distributed around the circumference as shown in Figure 1.4. Each thermocouple is shielded by a thin metal sheet to be protected against the incoming concentrated solar radiation, which would influence the temperature measurement [272]. The thermocouples are of type K, class 1, but measurement uncertainties are higher than standard values due to the complex set-up. The thermocouples have been installed during receiver production and work within the receiver's vacuum. The heat losses of these cross-section receivers are the same as for the normal ones. This configuration permits an analysis close to real receiver wall conditions. Figure 1.5 shows the locations of the cross-section receivers as installed at the DISS facility. In total, there are 23 of these receivers in the loop. 16 of them are installed close to the outlet of almost each collector. The remaining 7 receivers are located at potentially critical points close to the end of evaporation, where a dryout might appear, as well as at the locations with the highest steam temperatures in the superheating section. The wall temperature measurements are used to detect the temperature gradient around the wall during operation, which provides valuable insight into the heat transfer conditions of the fluid. Low temperature gradients indicate high heat transfer coefficients. It is also possible to detect flow regimes in the evaporation section to a certain degree [94, 103]. For example, a very high gradient can suggest stratified flow with liquid, i.e. with

high heat transfer coefficients, at the bottom and steam, i.e. with low heat transfer coefficients, on the top of the receiver. Such insights are decisive for the overall evaluation of the life time of a receiver tube.

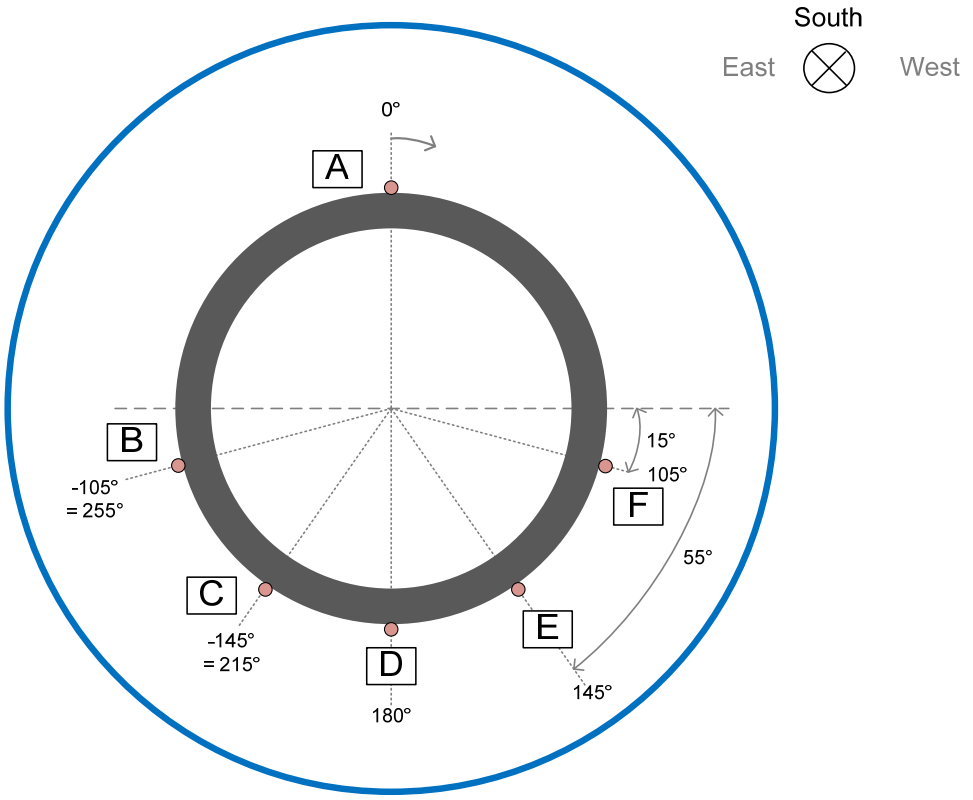

Figure 1.4: Diagram of a receiver's cross-section with thermocouples A to F distributed around the outer circumference; B to F face the mirrors, while A always faces the sun.

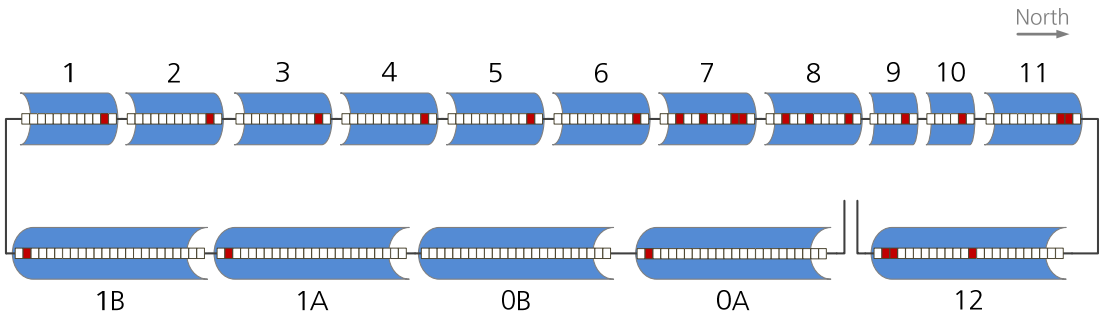

Figure 1.5: Locations of the receivers with cross-sectional measurements; white boxes indicate normal receivers, marked boxes indicate cross-section receivers with thermocouples.

2 Design of once-through collector loops

The design of a once-through collector loop is important to allow for a wide range of safe operating conditions and for enabling the efficient conversion of solar power. Design criteria are developed and summarized in the following sections. Examples are provided for an exemplary loop with 500°C/110 bar at the outlet and a length of 1500 m. Some results are also presented for the 400°C/80 bar configuration of the DISS test facility.

2.1 General layout of one loop

The serial connection of collectors is called a loop and one loop comprises various collectors. The main influencing factors to decide how many collectors form a loop are the inlet and outlet temperature as well as the geometry of the collector. If not stated elsewise, a Eurotrough collector with 150 m length and an aperture width of 5.76 m is used here as standard collector type. Considering the design criteria, which follow in the next sections, a desired outlet temperature of 500°C would result in a loop of ten collectors in series.

The classical layout of a once-through loop [68] foresaw that all of the water enters at the inlet and the steam leaves the loop at the outlet. It is shown later that this concept is deemed to fail because of controllability and reliability constraints. Thus, the additional injection of water at another location in the loop must be foreseen. Figure 2.1 shows four possible loop layouts with injections. It can best be interpreted together with Figure 2.2. The latter shows the temperature profile and steam quality profile along the loop. Note that by scaling the loop length to 1 an almost general profile is achieved, which would be valid for the same radiation and the same inlet/outlet temperature constraints, but with different total length and collectors. Looking at the temperature profile, one can see the three important sections of a once-through loop: liquid water is preheated at first until the saturation temperature is reached (at a position of about 235 m or 16 % of the loop length). Then, the water is completely evaporated, which is indicated by a steam quality of 1 (at positions 950 m to 1030 m depending on the variant, about 2/3 of the loop length). This process takes place at a constant temperature or at a slightly decreasing temperature due to the pressure losses along the loop, respectively. In the next section, the saturated steam is superheated to the desired temperature at the loop outlet. These are the preheating, evaporation and superheating sections. Two important locations are considered throughout this work. The initial point of evaporation (IPE) is the first location at which steam is produced. It is indicated by an initial steam quality of greater than 0. The end point of evaporation (EPE) is the loca-

tion at which no water is in the liquid phase anymore, indicated by the first location at which steam quality is equal to one.

Variant A is considered the most robust variant with one injection in the evaporation section (EVI) and one injection in the superheating section (SHI). The EVI can be seen as a drop in the steam quality profile, while the SHI is seen in the temperature profile.

Each injection line must be installed and maintained, such that certain costs are associated with it. The power plant owner or project engineers must decide whether one or two injections shall be foreseen and at which locations. Variant B only has the EVI, while variant C assumes only having the SHI. Variant D is a compromise, which only applies the EVI in each loop, but for which one central injection before the steam turbine is foreseen for safety. If this variant D is to be designed for the same live steam temperature of the turbine, the solar field must provide a higher outlet temperature to give the central injection a certain working range. This can be seen in the temperature profile of variant D with an exemplary outlet temperature of 525°C.

Neither the steam quality nor the enthalpy can be measured. In single-phase flow, the steam temperature and pressure are the only measurable properties indicating the state of the fluid. In the evaporation section, the saturation temperature is directly linked to the pressure. Both are constant for all steam qualities. This causes the saturation temperature to decrease slightly along the evaporation section due to the pressure loss. However, no fluid state is measureable. This non-observability causes problems for control, as will be explained in chapter 4.

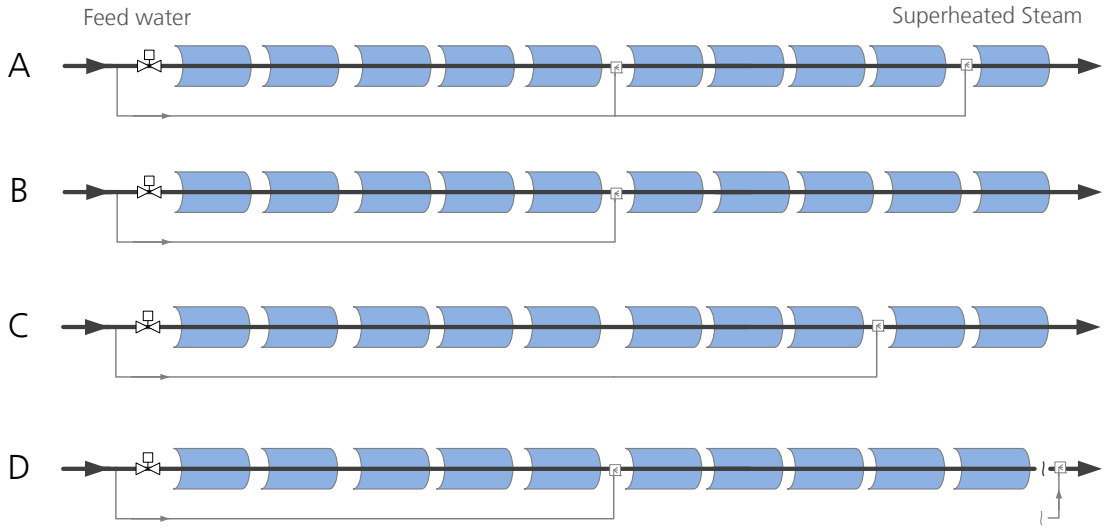

Figure 2.1: Overview on variants for general loop layout with different number and locations of the injectors.

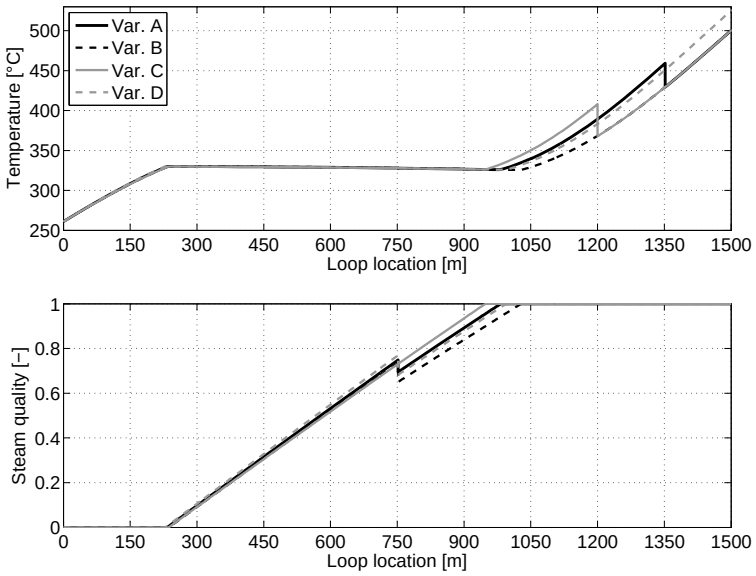

Figure 2.2: Temperature and steam quality profile along the loop for different loop layouts.

The pressure is an important variable of the loop. It is assumed in this work that the outlet pressure of the solar field is fixed during normal operation. This corresponds to a fixed pressure operation of the steam turbine, which is recommended for once-through mode [136, 150]. The main reason is that the load-dominating irradiation can change quickly because of passing cloud. Sliding pressure operation would result in fast changes of the loop's mass content and in high temperature and EPE variations. The transient behavior of fixed pressure mode, especially during short cloud events, can be handled much easier by keeping the temperature profile along the loop close to nominal conditions. Pressure sliding should therefore only take place very slowly under controlled conditions.

The pressure drop along the loop is shown in the upper graph of Figure 2.3 for an outlet pressure of 110 bar. The pressure drop is the highest in the superheating section due to the high velocity of the steam. The liquid water does not show significant pressure loss. In both single-phase flow sections, the length-specific pressure drop increases with mass flow and with a reduction of outlet pressure level. The pressure loss in the evaporation section additionally depends on the steam quality. Special correlations exist for this dependency in literature. The ones by Friedel [92] (also in section Lbb of [257]), Thom [244] and by Müller-Steinhagen and Heck [181] have shown good agreement with data from DSG facilities [69, 107, 206]. The Friedel correlation is used here. Uncertainty of pressure drop correlations is rather high, in the range of about ±30 % [233], a more detailed overview is provided in [107]. The pressure drop in the bends of the piping between the collectors (steps in Figure 2.3) is calculated by the correlation of Chisholm [39]. The uncertainty of all two-phase flow correlations must be taken into account when determining the design pressure level of

the solar field and of the components. Detailed analyses on large-scale DSG plants have not been published yet, but offer a potential for cost reduction by better designed components.

The profile of the average heat transfer coefficient between fluid and the inner tube wall is shown in the lower graph of Figure 2.3. The heat transfer coefficient in the single-phase region can be calculated e.g. by correlations of Gnielinski [95], as used here, Dittus-Boelter [263] or Petukhov [191]. The liquid phase shows a higher heat transfer than the gas phase. The heat transfer in the two-phase region is much higher due to boiling. Suggestions for the calculation of two-phase flow correlations are published e.g. by Odeh [186], Gunger and Winterton [99], as used here, or Chen [37]. For parabolic trough plants with DSG at pressures of 30 to 70 bar, Goebel [96] developed specific correlations from experimental data, but with limited validity for other pressure levels. The lowest heat transfer is always found at the loop outlet and varies between about 3200 and 1200 W/m²/K in the example of the 1500 m/500°C loop. Note that for these diagrams a scaling of the loop length to one is not useful, as the absolute loop length alters the mass flows and the resulting heat transfer and pressure loss. Only the qualitative shape would remain the same for a scaled diagram. Also note the small fluctuations at the transitions between single-phase and two-phase, e.g. at 185 m of the 300 W/m² curve in Figure 2.3 (bottom). They are caused by different saturated heat transfer coefficients from the correlations used in both regions. A linear interpolation results in a smoother transition, but does not imply a better estimate due to the high uncertainty, which must be considered anyway.

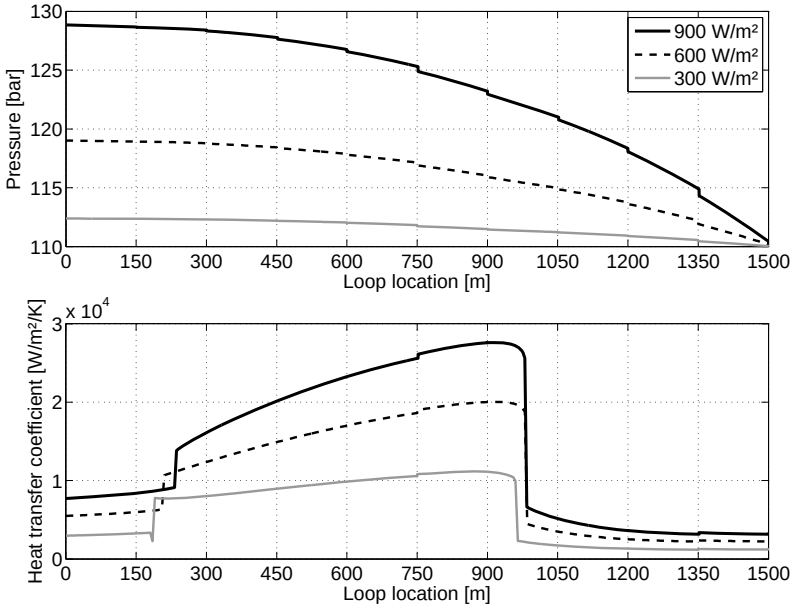

Figure 2.3: Pressure and heat transfer profile along the 1500 m/500°C loop of variant A for different steady-state load conditions.

The inlet and outlet temperatures of the loop are usually fixed. The outlet temperature is determined by the design parameters of the steam turbine. The inlet temperature is determined by the cooling and preheating conditions of the power block. The latter conditions may result in a significant part load variation of the inlet temperature, especially if the turbine is operated in sliding pressure mode. With the inlet and outlet temperature fixed, the heat input or direct normal irradiance (DNI) determines the overall mass flow that can be superheated. For each irradiation condition, the ideal mass flow can be calculated by steady-state heat balances. The irradiation level also dominates the temperature profile at the end of the loop. Variants with the same outlet temperature always also have the same temperature profile directly before the outlet if irradiation conditions are the same. This can be seen for variants A to C in Figure 2.2 in the last collector. It is an important aspect for design. If no SHI is installed, the steady-state end of evaporation is solely determined by irradiation. The share of mass flow injected by the EVI only influences the share of mass flow at the inlet, but not the position of the EPE. If an SHI is installed, the EPE is shifted upstream. The irradiation level and the share of SHI mass flow determine the EPE.

The share of the SHI mass flow of the overall mass flow also determines the difference between temperatures before and after the injection. The temperature difference by the SHI is used as a more intuitive measure in Figure 2.4. If it is increased, the injection share is obviously increased as well (upper left graph). For high loads, equivalent to high DNI levels, there is no significant difference for variants A (SHI at 1350 m) and C (SHI at 1200 m). With low loads, the same temperature difference is equivalent to an increase in mass flow share. This increase is slightly smaller for variant C.

The loop efficiency is another important aspect of the design. The EVI does not have any measurable influence on the efficiency. Although the IPE is shifted upstream with an increase of the EVI mass flow share, the heat loss in this preheating zone is very low. Furthermore, the heat transfer coefficient in the evaporation section is very high, such that small changes by the mass flow are negligible for efficiency. Dependencies on the temperature difference by the SHI are shown in the lower left graph of Figure 2.4. A temperature difference of zero is equivalent to the efficiency of variant B, which is set to 100 % in the graph. Its absolute value is 71.45 % at 900 W/m² and 65.16 % at 300 W/m² in the example. A temperature difference by the SHI of 50 K is assumed now for variants A and C. The loop efficiencies at 900 W/m² are 71.27 % for variant C (SHI at 1200 m) and 71.11 % for variant A (SHI at 1350 m). This is an overall efficiency reduction of 0.25 % (variant C) or 0.5 % (variant A) compared to variant B. At a very low load of 300 W/m², these reductions are 0.8 % for variant C and 1.7 % for variant A.

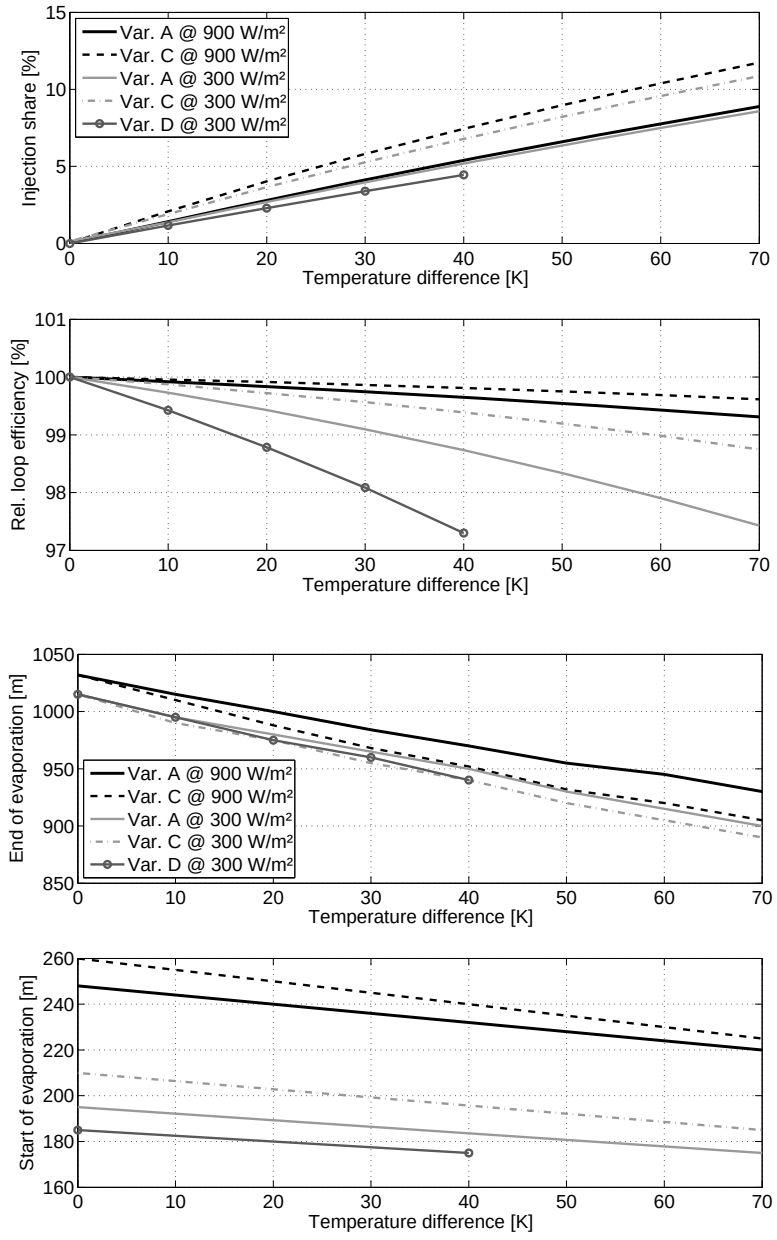

Figure 2.4: Influence of steady-state temperature difference by SHI on (from top to bottom) injection share, total loop efficiency, EPE and IPE for variants A (SHI 1350 m) and C (SHI 1200 m) for two different irradiation levels and variant D (central) for low irradiation level.

Those efficiency differences are an important result for overall system analysis as well. One might have assumed that a temperature difference of 50 K is achieved by a certain collector length and that this length is comparable to the loss of the injection. The temperature increase of 50 K along the loop requires about 110 m of collector length (compare Figure 2.2). The wrong assumption would have suggested an efficiency loss by the injection of 110/1500 or 7.3 % of collector surface, respectively. This is by far not the case. The efficiency loss is only caused by the difference in heat loss, which is 1.7 % at maximum for variant A. In fact, the annual average is much lower, since the loop is mainly

operated at high and medium loads throughout the year. It will be shown in chapter 4.6 on control that a high temperature difference by the SHI increases the controllability significantly. From an efficiency point of view, this must be compared to using the equivalent collector area for control, a maximum of 1.7 % in this case. This corresponds to a length of about 25 m or 17 % of one collector.

Variant D is a special case. The superheating injection is centrally in the power block and the temperature difference by the SHI is achieved by the same increase of loop outlet temperature. A temperature difference of 40 K therefore corresponds to an outlet temperature of 540°C. As the heat loss increases significantly with high temperatures, the efficiency of variant D is very low. The corresponding curve for 900 W/m² is not shown in Figure 2.4 for readability. Its efficiency is almost the same as the 300 W/m² curve of variant C. This does not include the additional losses of the header piping. Thus, from an efficiency point of view, variant D does not make sense. Variants A and C are also superior for control, as they offer a higher injection share at the same temperature difference or at the same efficiency level, respectively. Another problem of variant D is that the design temperature of the solar field must be increased. This can significantly increase the investment cost. The outlet temperature is thus limited in the graphs to 540°C. In consequence, variant D is only relevant, if the installation of a superheating injection in each loop is extremely expensive.

Figure 2.4 depicts the change in EPE and IPE on the right hand side. It can be expected that the EPE varies by about 17 m in steady-state conditions for all relevant loads. It varies by about 25 m for variant A and by only 12 m for variant C with 50 K temperature difference by the SHI. The EPE is well within the seventh collector of the loop for all these variants, between 900 m and 1050 m. As there might occur reduced life times of receivers close to the EPE, as studies in [230] suggest, it might be beneficial to demand this bordering for simpler maintenance. More details are provided in chapter 5, which puts this demand into perspective.

In this respect, it is a useful objective of control to keep the EPE in a narrow bandwidth during transient operation. This is the main motivation for the EVI, as will be discussed in chapter 4. It is best discussed looking at Figure 2.5, which shows the temperature profiles of variant A for various steady-state cases. The problem of EPE control is that the EPE cannot be measured directly. One option is to use the temperature measurements between the collectors limiting the EPE, at locations 750 m, 900 m, 1050 m and 1200 m in this case. The temperature gradient between 750 m and 900 m can be extrapolated. The temperature gradient between 1050 m and 1200 m can be extrapolated back, i.e. upstream. The intersection of the gradients can be used as a measure for the location of the EPE. This is sufficient for limiting the EPE during transients,

even if it is clear from the temperature profile that the gradient measure does not provide the correct location of the EPE.

Another option is to control the temperature before the superheating injection. The nominal case of Figure 2.5 has an inlet temperature of 260°C and a temperature difference by the SHI of 30 K. The resulting temperature before the SHI is almost constant for high and medium loads, 460°C in the example. At lower loads, the superheating efficiency is reduced. Keeping the desired temperature difference, the temperature before the SHI is 467°C. Keeping the temperature before the SHI at 460°C, the working range of the SHI is reduced to 23 K. By following the latter approach, the control of the temperature before the SHI keeps the EPE within 10 meters during all loads. So far, it has not been considered that the inlet temperature usually varies with load for large-scale power plants. Figure 2.5 exemplifies this at a low load with an inlet temperature of 180°C. Note that this case fulfills both a temperature drop of 30 K and a temperature before the SHI of 460°C. However, the EPE is shifted downstream by about 45 m. To keep the EPE at the nominal location, a temperature before the SHI of 486°C would be needed.

Control variants for the EPE by the EVI are patented by Feldhoff and Eck [73]. An example for shifting the setpoints of the temperature before the injection is elaborated in [248]. It is assumed in this work that a small fluctuation of the EPE is acceptable. If it can be kept within one collector, it is even beneficial to let it vary slightly in order to distribute the thermo-mechanical loads associated with the EPE along the whole collector. More details are derived in chapter 5. Other items for the steady-state design of an OTM loop are derived in the upcoming sections.

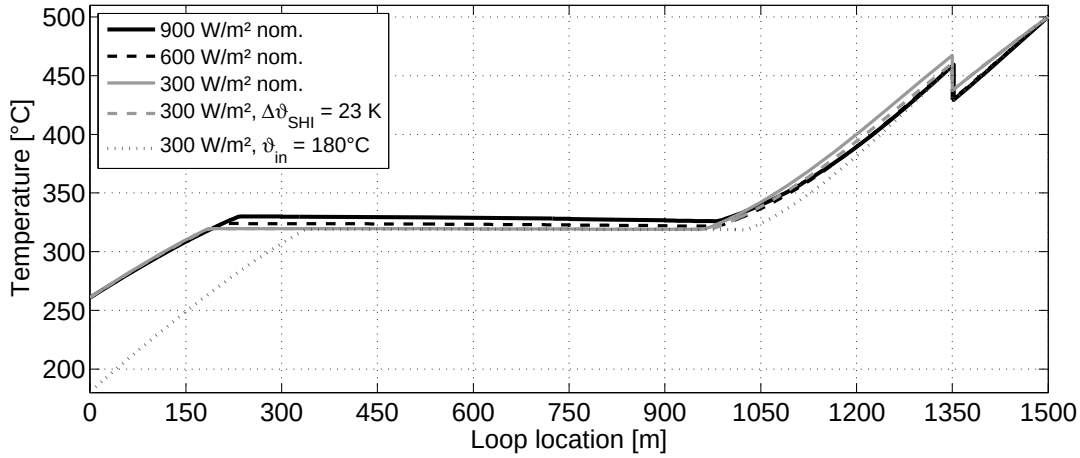

Figure 2.5: Part load temperature profiles for loop variant A with 1500 m/500°C; variation for irradiation level, temperature drop by the SHI and inlet temperature; nominal case with 30 K by SHI and 260°C inlet temperature.

2.2 Considering thermo-mechanical loads

The receivers and other components of the solar field must be designed for safe operation of the plant. The high pressure of the fluid causes mechanical stress within the components' wall. The wall thickness is thus chosen such that the component can permanently resist this stress level. In solar boilers, there is additional stress caused by the high temperature, its variation over time and the irradiation incident on the receiver tubes. These thermal stress loads must be analyzed and considered in detail to guarantee safe operation. Good overviews for the design of DSG systems are published by Steinmann [230] and Eck [66, 69]. The corresponding ideas are used here to briefly exemplify the procedure for steady-state design of the receivers. First, single-phase flow is considered, then, the situation in the evaporation section is examined. A methodology for transient stress analysis is suggested separately in chapter 5.

2.2.1 Single-phase flow

During steady-state operation, the single-phase heat transfer coefficient (HTC) between fluid and inner wall can be assumed constant around the tube's circumference. A schematic diagram of an irradiated receiver cross-section is shown in Figure 2.6, left. The intensity of irradiation varies along the circumference of the tube and depends on the collector type. The graph on the right illustrates an irradiance profile of a Eurotrough collector with data based on [221]. An incidence angle of 0° is assumed and one can imagine the sun from the top and mirrors located at the bottom. The circles represent constant irradiation intensity with high values corresponding to large diameters. The diameter steps shown correspond to 20 % steps in intensity. Intensity peaks are found at about 40° from the mirror center to both sides. The lower intensity in the middle can be explained by the shadowing effect of the receiver itself and the gap in the mirrors. The shape of the profile can vary significantly in reality depending on the quality of the mirrors, collector structure, aperture width, receiver diameter and other influences. It stays nearly the same for parabolic troughs as long as the collector tracks the sun. Only the orientation of the profile changes, while the axes remain. This is different for Fresnel collectors, which undergo significant changes in the shape of the profile during the day.

The location of the maximum circumferential stress depends on the value of the HTC [230], which is illustrated by Figure 2.7 for a Eurotrough irradiance profile as of Figure 2.6 (right). The radial temperature gradient dominates the stress, if the HTC is high. The resulting maximum stress is then found at the location of the highest incident heat flux, usually on the side of location B in Figure 2.6 (left), with deviations according to the actual inhomogeneous irradiation profile. For low values of the HTC, the heat conductivity within the cross-section has more impact and the location of the highest stress is shifted to loca-

tion A [230]. The temperature profile within the tube wall can be determined by steady-state energy balances, when the flow conditions, the material properties and the irradiation profile are known.

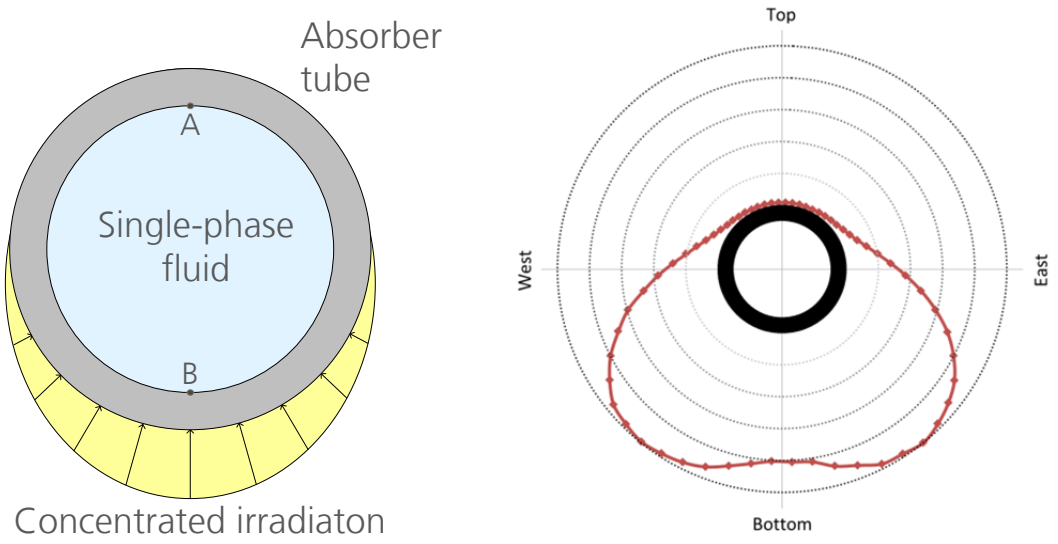

Figure 2.6: Schematic diagram of an irradiated cross-section of an absorber tube with single-phase flow (left) and normalized distribution of incident heat flux on the absorber tube of a Eurotrough collector at an incidence angle of 0° (right).

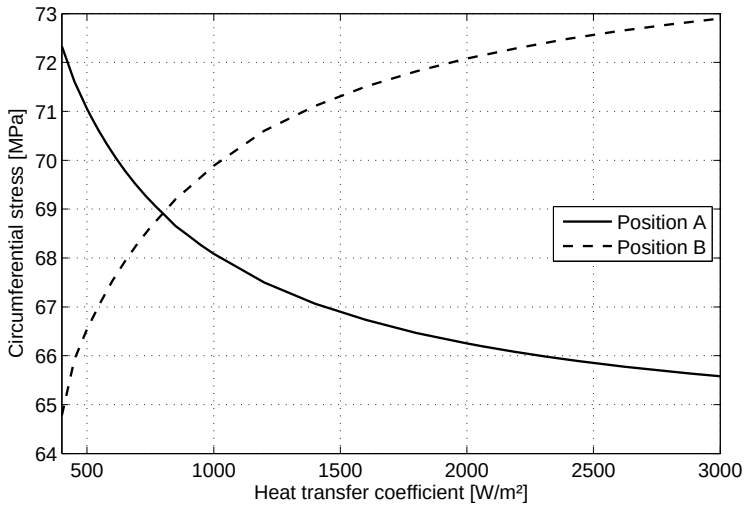

Figure 2.7: Circumferential stress depending on heat transfer coefficient for DISS facility with steam of 400°C/80 bar; position A at inner wall of unirradiated side, position B inner wall of irradiated side; based on [211, 230].

The finite element method (FEM) tool ANSYS with a receiver model developed by Uhlig [19, 62, 251] is used in this work to carry out such calculations. A receiver of 4 m is considered for each simulation. A diagram of the maximum temperature gradient around the cross-section versus the steam mass flow provides a good overview on the design. Such a diagram is shown in Figure 2.8 for

the new DISS facility and steam parameters of 400°C and 80 bar. The characteristic lines are given for constant irradiation levels between 900 W/m² and 300 W/m². A Eurotrough collector is assumed, which is similar to an LS-3 collector, e.g. collector 11 of the DISS facility. The irradiation intensity is smaller for a Solarlite collector due to its smaller aperture width. It is thus sufficient for design to consider only the Eurotrough curve. The design steam mass flow is calculated from steady-state heat balances. It is used to derive the corresponding HTC with the help of the fluid properties. Temperature and HTC are then used as boundary conditions for the receiver simulation. The resulting design curve is shown as dashed line in Figure 2.8. This diagram is derived for steady-state conditions, but DISS experiments and simulation studies [211] show that it can be applied for normal transient conditions in the superheater as well.

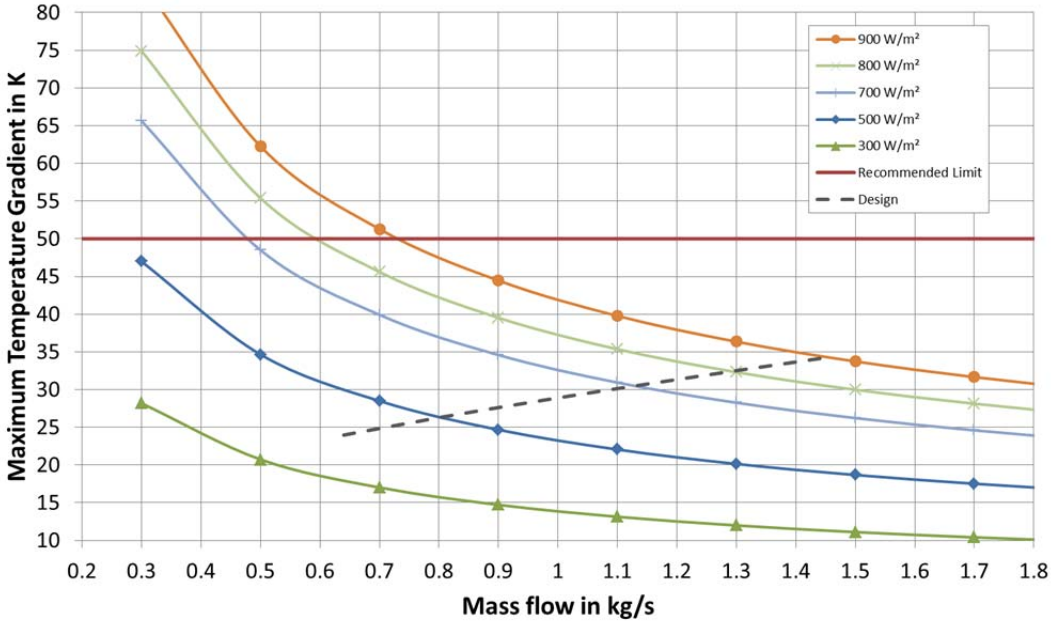

Figure 2.8: Maximum temperature gradients in the superheater section of the DISS test facility at 400°C and 80 bar depending on mass flow and effective irradiation; simulations for Eurotrough collector and new DUKE receivers.

The irradiation to be considered in the diagram is the effective irradiation, which is the DNI corrected by the cosine of the incidence angle and other optical effects (for details see definition in equation (3.15) on page 39). A temperature gradient of about 35 K is derived for an effective irradiation of 900 W/m² at nominal conditions. This is well below the recommended limit of 50 K [66]. Note that the limit is usually provided by the receiver manufacturer. The 50 K limit is a rather general suggestion for steam generators, which must be analyzed in more detail and altered according to stress analyses, e.g. with the ANSYS receiver model. The value of 50 K is kept here for simplicity and already offers some safety margin for the DISS case. The applied receiver model was validated

against the model in [69] and data from the new DISS facility. Both results suggest an accuracy of about ±3 K for the maximum temperature gradient. Nevertheless, it is recommended to choose a buffer of at least 10 K to the maximum allowable gradient for safety and as a buffer for peak deviations of the irradiation profile. The buffer for the DISS facility is at least 15 K for steady-state conditions when operating at an outlet temperature of 400°C.

During normal operation, the irradiation level can quickly vary and the inlet mass flow is adapted accordingly. There might be situations in which the irradiation increases quickly, e.g. after a long field of passing clouds. The low inlet mass flow is then combined with a high irradiation level. To avoid critical temperature gradients in those situations as well, the minimum mass flow should be chosen accordingly. It is suggested here to limit it according to the maximum effective irradiation at clear sky level. This is exemplified in the following. During a winter day, clouds can cover the solar field and show an effective irradiation of 500 W/m². The minimum mass flow to the loop should then not be chosen lower than 0.4 kg/s, i.e. with 40 K temperature difference in Figure 2.8. However, the maximum clear sky irradiation might be as high as 700 W/m² when clouds suddenly disappear. As a safety measure, one should thus look at the temperature gradient at this irradiation level. The same temperature gradient of 40 K results in a minimum mass flow of 0.7 kg/s. The plant can be operated safely, because the nominal mass flow at 500 W/m² (0.8 kg/s) is higher than the minimum mass flow (0.7 kg/s). This situation changes for a lower irradiation level of 300 W/m² of the same winter day. The steady-state design mass flow (about 0.5 kg/s) is below the most conservative minimum mass flow (0.7 kg/s). The desired outlet temperature cannot be reached under the conservative mass flow and a trade-off is needed to continue operation. It must then be checked, whether a short term load with a higher maximum temperature gradient might be allowable. If the plant is operated at 0.5 kg/s, the maximum temperature gradient at suddenly disappearing clouds can be almost 50 K at 700 W/m². This is usually acceptable, but must be checked in advance. If the same situation is assumed for a summer day with a maximum irradiation of 900 W/m², the temperature gradients at 0.5 kg/s may reach more than 60 K. If the stress load from such an event is still acceptable, operation can be continued. Otherwise, a lower outlet temperature must be accepted or collectors must be quickly defocused for a short time when clouds suddenly disappear. Note that this is a worst case estimate. If reflectivity of the collectors is low on that day or the cloud field will not disappear, the plant can be operated safely. On the other hand, the example shows that a simple global minimum mass flow can lead to critical situations in summer. Thus, the suggested method of an adaptive limitation leads to a better range in winter and a much safer operation in summer time. Note that a strict interpretation of Figure 2.8 does

not limit the inlet mass flow to the loop, but the mass flow in the superheating section.

The two critical locations to be checked in the superheating section of an OTM loop are the outlet of the loop and the collector outlet before the SHI. As mentioned above, the outlet collector of the DISS facility has a lower heat flux and thus is less critical than shown. The situation before the SHI is conservatively estimated by reducing the mass flow in the graph by 10 %, which is a kind of maximum injection share for DISS operation. The resulting temperature gradient can then be read from the corresponding irradiation curve at a reduced mass flow. For the DISS design, this still guarantees a buffer of more than 12 K during all situations.

Another location with single-phase flow to be analyzed is at the loop inlet, as the inlet mass flow can be significantly lower than the superheating mass flow.

2.2.2 Two-phase flow

A similar analysis must be performed for the evaporation section. The maximum temperature gradient around the circumference shall be small. Certain flow regimes exist that guarantee a homogeneous heat transfer around the circumference and, by that, limit the temperature gradient. It must thus be shown that such flow regimes are maintained during all operating conditions. This replaces the calculation of temperature gradients as a function of mass flow, as used for the superheating section. The design can therefore be limited to verifying the desired flow patterns along the evaporation path.

The determination of the flow patterns is a complex task because of the various types of flow that can occur in the evaporation section. Figure 2.9 provides an overview of such flow patterns. The actual pattern depends on the vapor void fraction, mass flow, geometries and other conditions. Not all types of flow are present in a forced convection boiler. In fact, the ideal transformation from liquid to pure gas is via bubble and annular flow only. Both flow patterns guarantee a homogeneous and high heat transfer coefficient at the inner pipe wall. A good introduction to this topic is found in [67]. The main question for heat transfer, and thus stress analysis, is the actual flow pattern in the receiver.

Baker [12] was one of the first to publish a flow pattern map for oil/gas flows in horizontal pipes, which is still used. Taitel and Dukler [237] developed a common flow pattern map to distinguish analytically between the flow regimes. It was slightly adapted by Steiner [228] and can also be found in section Hbb of [257]. Thome and colleagues [129-131] developed another map, which is more accurate for refrigeration systems, but rather complicated to apply. It was extended to diabatic flow in [266, 267, 280]. A simplified version [246] is achieved by applying void fraction calculations of [212]. An overview can be found in [245]. Nakamura [184] analyzed the particular transition from wavy to

dispersed flow for horizontal pipes. Matuszkiewicz [164] investigated the bubble to slug flow transition and explained it by instabilities of void fraction waves. The latter approach was used to model a wide range of flows in [7].

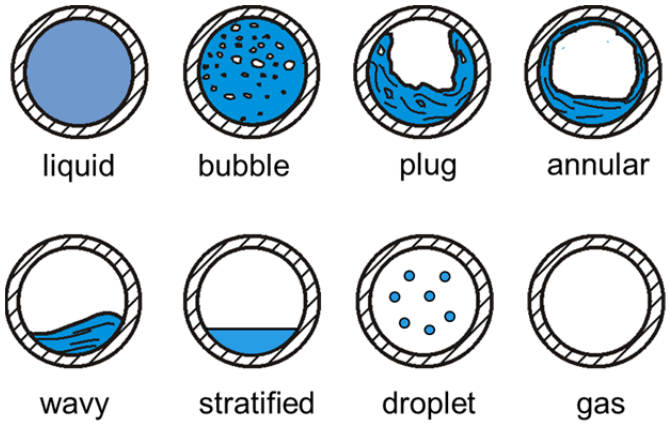

Figure 2.9: Flow patterns in horizontal two-phase flow [257].

Note that most of the flow pattern maps have been developed for oil/gas, water/air or refrigeration systems. Only Müller [182], Odeh [185] and Hermann [103] especially analyzed the case of solar boilers in parabolic troughs. Goebel [96] analyzed the heat transfer in some regimes for the DSG case in detail.

The flow pattern map of Taitel/Dukler is shown in Figure 2.10. Their approach is based on dimensionless numbers that are derived from the physical parameters of gas and liquid phase and the mass flows of the two phases [107]. The Martinelli parameter X defines a ratio of liquid to gas phase pressure drop when considered separately. A modified Froude number Fr* is used to distinguish between annular and wavy flow. The variable K separates stratified and wavy flow. Eventually, the dimensionless number T indicates the ratio of turbulent to gravity forces acting on the gas phase. It is used as a measure to distinguish between plug and bubble/dispersed flow. Besides the limits of the flow map, there are two design curves (above and almost parallel to the Fr* line of the map) characterizing the loop and the flow path of a once-through steam generator at high (solid line) and low (dashed line) irradiation conditions. The spike of the lines is caused by the evaporation injection, which shifts the curve to higher mass flows. The lines must be compared with the Fr* boundary between wavy and annular flow. All conditions are within annular and plug flow according to the Taitel/Dukler map. It can be seen that the design of the DISS facility at 400°C (Figure 2.10, right) is similar and slightly less conservative than the 1500 m/500°C loop (Figure 2.10, left). Experiments at the DISS facility show that the chosen design is sufficient to guarantee a good heat transfer in

the evaporation section. It can thus be expected that the high temperature loop is also in the annular flow region.

One must be aware that all maps only indicate an approximate transition border. The design should be done such that the evaporation path along the loop is conservatively in the annular flow region. For a given collector geometry, this is achieved by increasing the mass flux or the length of the loop, respectively. The resulting pressure drop of the loop increases and a compromise must be found during the design stage. During low part load and with OTM, the evaporation path is shifted closer to the wavy flow region. Even a fast annular flow might lead to a short dry-out region, when not enough water for wetting of the whole wall is left. This happens close to the end of evaporation and cannot be avoided in practice. Especially this transition from annular to pure gas flow and the corresponding heat transfer coefficient is hardly predictable [107].

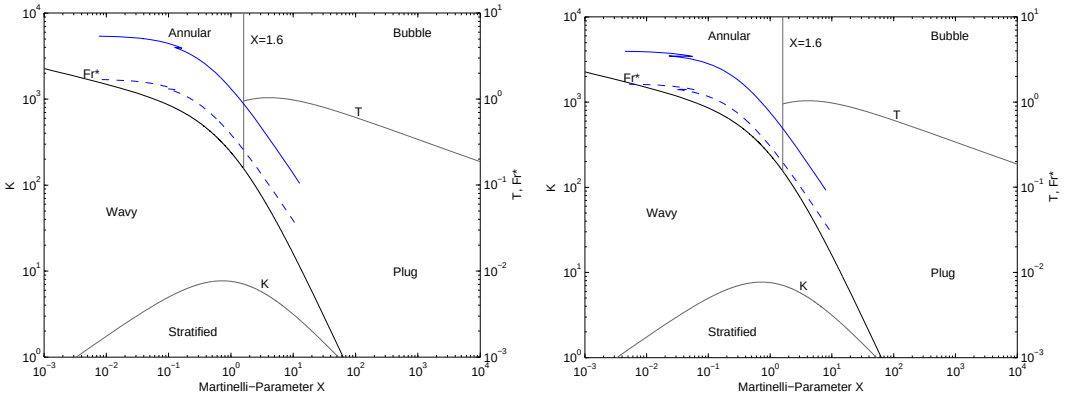

Figure 2.10: Transition between wavy and annular flow by Fr* shown in Taitel/Dukler flow regime map for 1500 m/500°C loop (left) and DISS facility/400°C/80 bar (right); each at 900 W/m² (-) and 300 W/m² (--); each with Schott PTR-70-DSG receivers of DISS facility.

Herrmann [103] analyzed the particularly important transition between wavy and annular flow for irradiated absorber tubes. A simplified corresponding map is shown in Figure 2.11, which has also been used in [205]. It is based on the superficial velocities of the separate phases. The existence of a water film on top of the inner tube is explained by the local heat flux. If the local heat flux is lower than the energy needed for the evaporation of the water in the wetting film, the annular flow can be maintained. If the heat flux is higher, the film will not be closed at the top. The resulting temperature gradient around the cross-section is increased. Characteristic curves of a constant temperature gradient show the same shape as the transition curve. A deterministic model to predict the characteristic lines was developed. It can be applied for choosing good mass flow conditions for a once-through loop. Nevertheless, uncertainty must be taken into account for this specialized model as well. It must be mentioned that the transition line is now dependent on the effective irradiation. The situation of

a once-through loop is represented by a straight line connecting the two velocities of completely saturated liquid and steam in the absorbers, since the superficial velocities are calculated as if each phase would be alone within the cross-section. The 1500 m/500°C loop is described by the combination of 1.3 m/s liquid and 12.2 m/s gas velocities for high loads and 0.38/ 4.2 m/s for low loads. For the DISS facility at 400°C/80 bar, the combination is 0.7/ 12 m/s for high loads and 0.3/ 5.0 m/s for low loads. The model of [103] can be applied for detailed designs providing a good estimation of wetted surface and temperature differences. Nevertheless, results from the DISS facility show that the simple map of Taitel/Dukler [237] provides an already sufficient result when the part load design considers a certain distance to the critical transition line of Fr*. The latter approach was chosen here, as shown in Figure 2.10.

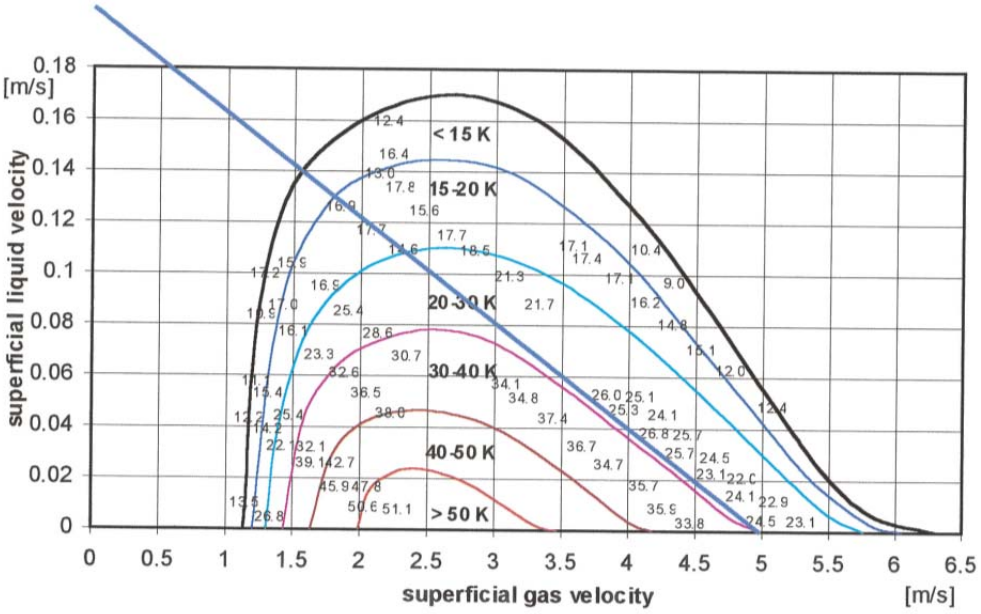

Figure 2.11: Simplified flow pattern map for the transition between stratified and annular flow; 60 bar, 4° tilted collector; straight line representing once-through loop conditions along the evaporation path; numbers indicate cross-section temperature difference; taken from [103, 205].

An interesting phenomenon gets apparent in the flow maps of Herrmann [103]. The transition curve is shifted to the left and has a higher peak when the pressure level is increased. This means that the mass flux must be increased with pressure to achieve the same maximum temperature gradient. Recall that the pressure drop increases with mass flow and decreases with pressure level. Thus, the absolute pressure drop of two loops at different, fixed outlet pressure levels will differ less than one might expect, if the loop is designed for the same maximum nominal temperature gradient. Nevertheless, it is usually more beneficial to choose the higher pressure level.

Also note that the collector and the absorber tube are tracked with the sun. At solar noon, the irradiation comes from the bottom and does not intercept with the top of the absorber. This is positive for maintaining annular flow. During the morning and evening, the irradiation comes further from the side and wavy flow is more likely. However, the heat flux density is usually also reduced due to the lower DNI level. In consequence, the nominal temperature gradients are close to the ones at low loads in the afternoon. Design and results from the new DISS facility suggest that annular flow is achieved during all loads, establishing a maximum temperature difference of about 10-15 K. Only a small increase very close to the EPE is observed, which is hardly predictable. It is below or close to the superheater values and, therefore, not critical at steady-state.

For additional safety of the design, it is highly recommended to check the resulting temperature gradients within a cross-section for the case of a loss of wetted surface near the end of evaporation. A design example and illustrating experimental results are presented in chapter 5.3.

Daily start-up and shut-down of the solar field causes high thermal stress to the receivers. This is probably the main challenge for the stability of the receiver tubes, if the temperature gradients are designed to be low by the methods explained above. A similar problem is known from modern fossil plants with fast load changes and start-up demand [29, 102]. This fatigue must already be taken into account in the design phase. The design should consider that there might be days with long cloud periods, which require the solar field to be started-up twice a day.

For Fresnel collector fields, it is a viable option to build the collectors on a tilted ground. One example is Novatec Solar's PE-1 plant. It is then beneficial to locate the initial evaporation on a lower level than the end of evaporation, since this increases the flow regime of annular flow in the evaporation section [67, 103]. The irradiation profile of Fresnel collectors around the absorber tube is very different from parabolic troughs. This difference must be considered for the analysis of temperature gradients.

2.3 Considering thermo-hydraulic instabilities

There are three types of thermo-hydraulic instabilities to be considered for OTM loops. A stationary analysis is performed to identify so-called Ledinegg instabilities. In addition, various types of dynamic instabilities exist. For large solar fields, the parallel flow instabilities might arise as well. The good news is that there are two simple counter-measures for these instabilities: the pressure at the loop inlet must be increased and the inlet mass flow must be controlled. For completeness, the following short paragraphs provide more details.

Ledinegg [148] derived a reason for flow instabilities from the characteristic of pressure loss versus mass flow of a steam generator. A typical diagram of

such a characteristic is given in Figure 2.12 for the DISS test facility at 80 bar and 900 W/m². Instabilities arise when one system pressure drop can be established by two or more different mass flows. Let us consider the curve of 120°C inlet temperature. The pressure drop of 6.6 bar of the loop could in principle be the result of three different mass flows, namely about 1, 2 and 3 kg/s. If the system is at 2 kg/s and a small irradiation or pressure disturbance happens, the mass flow might immediately change to 1 kg/s. A reduction to half the mass flow may have severe impact on the loop, e.g. very high temperature gradients within the receivers. Such damages in fossil plants were the motivation for the analysis by Ledinegg. Note that this is not deterministic but a rather stochastic event. A very good description is given by Dolezal [51-53]. Mathematically, it can be postulated that the pressure drop must always increase with mass flow to achieve "Ledinegg stability", i.e. $dp/d\dot{m} > 0$. This is usually achieved with low subcooling or a high temperature at the loop inlet, respectively. For power plants with a high preheating of the feed water, the temperature at the solar field inlet is usually high enough. Nevertheless, Ledinegg stability must be guaranteed during all operating conditions, especially during the start-up procedure when feed water preheating in the power block is started after solar field operation. If the characteristic is not monotonically increasing, a throttle valve or orifice at the loop inlet can be installed. The throttling must be increased until the sum of the pressure losses has a monotonically increasing characteristic. This must be checked for all relevant irradiation conditions.

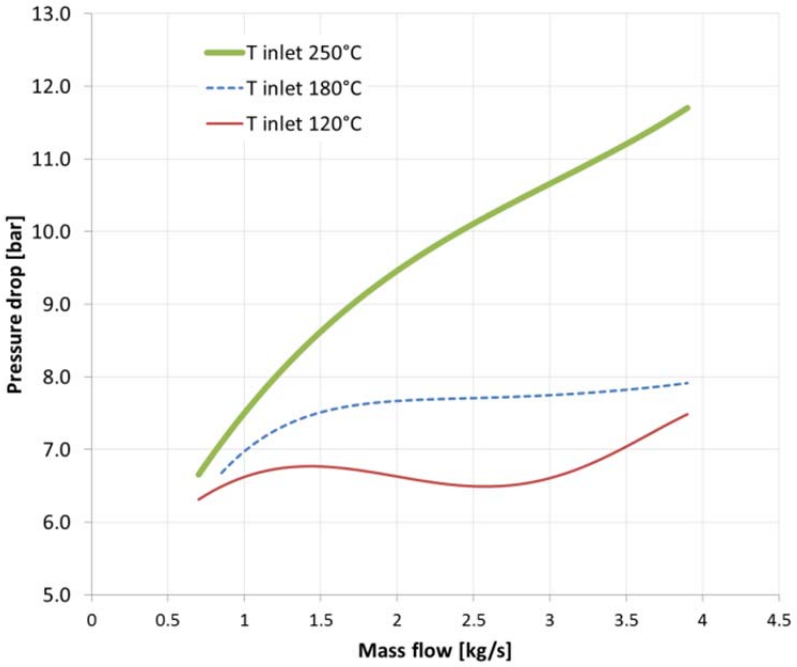

Figure 2.12: Pressure drop vs. mass flow rate; characteristic Ledinegg diagram for OTM parabolic trough loop with 1000 m at 80 bar outlet pressure and 900 W/m² DNI.

Such an analysis can be extended in a transient manner as well, as demonstrated by Taitel [236]. There is a vast field of dynamic instabilities that have been observed in two-phase flow systems, such as density wave oscillations (DWO), pulsating burnout, pressure drop oscillations and thermal oscillations. Good overviews are provided in [28, 49, 124]. Most of these instabilities can be traced back to the Ledinegg characteristic and can thus be avoided by adapting it by inlet throttling [214]. DWO are the most commonly described dynamic instability, as it can induce burnout, component vibration or control problems [14, 18, 231]. Therefore, various approaches to model these instabilities have been performed, e.g. in [210, 240]. Steinmann [229] simulated DWO for a DSG loop. He showed that DWO do not occur, if the inlet mass flow is controlled. This is also beneficial for temperature control.

Parallel flow distribution is commonly considered a topic of concern. If the DNI to parallel evaporator loops is not the same, an imbalance in mass flow can occur. It originates from an imbalance in pressure drop. The loop with the highest irradiation shows a higher steam fraction at the outlet. This causes a higher pressure drop in the loop. As the loops are connected at the outlet to the same header line, the pressure drop of all loops tends to be the same. Thus, the mass flow of the irradiated loop is decreased to reduce the pressure drop. This causes an even higher steam fraction or superheating at the outlet [217]. Eventually, it can result in the dryout of the irradiated tube section. In order to avoid this, Taitel and Minzer [172, 173, 235, 238] developed a control strategy for evaporators and Koch [139] studied the control of parallel superheating sections for the recirculation concept. Their works can be used for design of a suitable control. The controllability of parallel flow is also proven by commercial DSG plants in the evaporation section [168]. Thus, one must take care about this control, but it is no major problem. The control for once-through boilers is similar or even simpler. There is a high overall loop pressure loss due to the long superheating section of the once-through loop, while the superheating section is separate for recirculation mode. For safe operation, each once-through loop requires its own inlet control valve. By foreseeing a pressure drop reserve at these valves, no particular problem should arise from parallel loops in once-through boilers.

It can thus be concluded that the active control of the inlet mass flow with a certain offset pressure drop over the control valve is sufficient to avoid all kinds of hydraulic instabilities in the solar field.

2.4 Considering further design aspects

There are other design criteria that may depend on the particular boundary conditions of a project or an adjacent process. These could be site conditions, water quality, feed water conditions, material limitations, storage requirements and other items. Some aspects are covered in the following paragraphs.

The live steam, which is fed to the steam turbine, must not only be provided at a certain temperature and pressure level, but must also fulfill high chemical composition requirements. The water entering the solar field must already comply with this water quality. Potable water cannot be used and must be demineralized in advance to avoid corrosion and other degradation effects in the pipes. Salt in the water can lead to the blockage of steam attemperator orifices. For steel with high shares of chrome, chloride usually is the main driver for corrosion and its formation must be avoided. Conditioning of the water may only be done using volatile matters in order to avoid their deposit in the absorber tubes or solar field piping. If certain substances cannot be omitted, other measures must be taken to avoid deposit on the superheating tubes. This may be the installation of condensate traps, which can offer the possibility to remove water during the night and to thereby reduce the concentration of those substances. Although this seems trivial, various tube cracks in nuclear power plants have reportedly been associated to insufficient water quality due to accelerated corrosion [47, 201]. Thus, corresponding water quality standards exist for conventional boilers and it is highly recommended to comply with those for solar boilers as well. These are e.g. the VGB guideline VGB-S-010-T-00 and the DIN EN 12952-12.

The final loop shape must be taken into account for the design of the loop length. If a U-turn of the loop is desired, i.e. the header for inlet and outlet are close to each other, the number of collectors per loop is even. The loop length can only be varied in steps of two collectors. The decision for an adequate loop length is then usually unambiguous. If the loop does not have a U-turn, i.e. the inlet header is far away from the power block and the outlet header close to it, the loop length can be chosen more flexibly.

A thermal energy storage system for DSG plants ideally consists of a latent phase change material (PCM) storage in combination with a sensible molten salt two-tank or three-tank storage system [81, 143]. Such a storage system has not been built commercially yet, but various research activities aim at its development [195, 277]. Sodium nitrate (NaNO3) is a promising PCM option and a prototype with this material has already been tested successfully [144]. It has a melting temperature of 306°C [17] and is used for evaporation and condensation, respectively. For charging, the condensing steam must have a temperature difference of about 10 K above the PCM. This corresponds to saturated steam at about 316°C or 110 bar, respectively. For discharging, the wa-

ter/steam temperature must be below the PCM temperature, which results in evaporation at about 296°C or 80 bar. A once-through loop must thus be designed for a constant pressure level of about 110 bar at the outlet. In part load, the pressure can be reduced to about 80 bar to allow for a combined operation from the solar field and the storage system. A variety of inlet and outlet conditions can occur in the solar field by these operating conditions. They must already be taken into account during the design stage.

The final loop design should be checked for its robustness against deviations from the design conditions. Especially the start-up conditions in combination with a power block or thermal energy storage system should be evaluated in detail. The influence of a reduced optical or thermal efficiency should be evaluated as well. These variations may impose fairly different conditions onto the loop compared to the nominal design conditions.

2.5 Derived design criteria and reference loops

The methodology to design a once-through loop is straightforward. In fact, only a few variables are free to choose, namely the collector geometry, the loop length and the shares and positions of the evaporation injection (EVI) and the superheating injection (SHI). The difficulty is to model and to jointly consider all relevant aspects, which are partly contradictory. The recirculation mode offers more design freedom, since the evaporation and the superheating loops can be designed almost independently and the mass flows are considerably different [69]. This freedom is exchanged by a simple scalability of the OTM loop.

In practice, the collector geometry, the feed water temperature and the desired outlet steam parameters are already fixed at the beginning. A simple procedure is proposed for a loop with two injections (variant A) in the following. The design of the other variants can be derived accordingly.

Define a desired temperature drop by the superheating injection (SHI), e.g. 40 K or half of the temperature increase of one collector. For a defined effective irradiation, the mass flow is then given by the steady-state heat balance. It is sufficient to consider the inlet mass flow and the mass flow behind the SHI. The EVI can be ignored at first. The loop length is then chosen such that a good compromise of the following aspects is achieved:

- Low steady-state temperature gradients in the receiver walls of the superheating section (end of loop and before SHI; mind the reduced mass flow before the SHI)
- Evaporation path conservatively in the annular flow regime for nominal and part load
- Low pressure drop along the loop
- EPE within one collector for all/most of the loads.

The loop shape (U-turn or straight) and collector geometry defines how flexibly the loop length can be varied. After this first design result, the nominal operating range of the evaporation injection (EVI) is chosen, e.g. a constant mass flow or share of the inlet mass flow. A value in the range of about 5 to 10 % of the inlet mass flow seems reasonable. The EVI is then located at a position that allows an injection around a steam quality of 80 to 85 %. The flow regime is checked with the split evaporation mass flow and the EVI position and share are adapted iteratively. If no acceptable compromise can be found, the SHI mass flow can be varied slightly while keeping the loop length constant. If still no compromise can be found, the position and nominal mass flow of the SHI must be adapted, and the procedure to find a new loop length must be started again.

The same methodology has been used to design the 1500 m/500°C loop and the experimental set-up for the DISS facility at 400°C. For the latter loop, the SHI is chosen to be before collector 11 and the EVI before collector 6. The EVI reduces the steam quality from 93 % to about 85 %. It would be positioned more conservatively before collector 5 for a commercial plant. However, the very high steam quality before the EVI is used for experiments in order to test an extreme case. The same injection was also used for experiments at lower outlet temperatures at the beginning of the test campaign and in winter time. The EVI should be located further upstream with increasing outlet temperature. It should be before collector 3 for temperatures of 500°C. However, the design criteria are hardly fulfilled for such high temperatures in the 1000 m DISS loop, since the ideal length is around 1500 m. Experiments for testing the limits are recommended for the future to validate the models at these high temperatures.

Figure 2.13 shows the design mass flow as a function of the effective irradiation for the 400°C DISS loop with two injections. The mass flow before the SHI defines the temperature before the SHI, which is 350°C in the example. The EVI mass flow was chosen to be 5 % of the inlet mass flow. The underlying design is used especially in chapter 3.4 for the derivation of transfer functions of the DISS facility. Figure 2.14 shows the design of the 1500 m/500°C once-through loop.

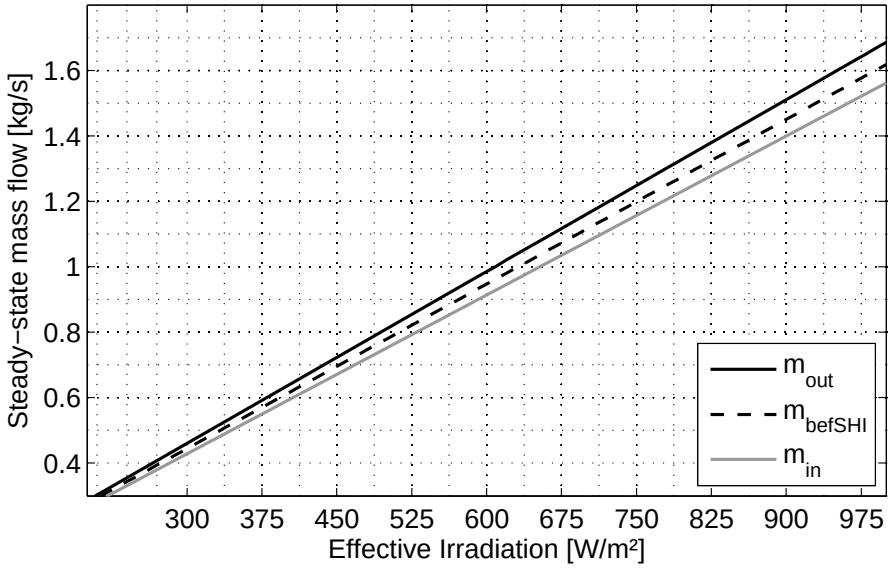

Figure 2.13: Stationary mass flow as a function of effective irradiation for DISS test facility with inlet temperature 260°C, outlet temperature 400°C, temperature before SHI 350°C and outlet pressure 80 bar.

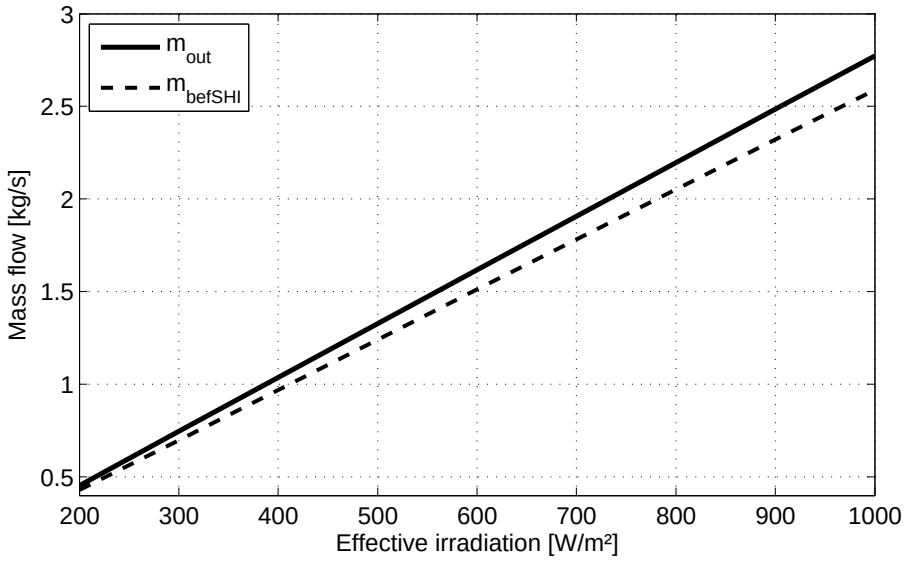

Figure 2.14: Stationary mass flow as a function of effective irradiation for 1500 m/500°C loop with inlet temperature 260°C, temperature before SHI 480°C and outlet pressure 110 bar.

3 Transient process models for once-through mode

The transient behavior of temperature, mass flow and pressure is of major importance for the analysis of once-through mode (OTM) solar fields. In conventional Benson boilers, the amount of fuel can be adapted to the current needs in order to avoid large deviations from the desired operating point. This degree of freedom does not exist in solar-thermal power plants. The sun cannot be influenced directly. In consequence, the deviations from the nominal operating point will be pervasive – or in other words: a real steady-state will not occur.

Once the loop has been designed, the geometric boundary conditions for a transient analysis are fixed. In order to analyze the transient behavior, one can run real experiments and/or use transient simulation models. As real large-scale experiments for the plants considered here would be too expensive and time-consuming, this option should usually be avoided. Transient simulation models offer the possibility for assessing various situations and boundary conditions to find an optimal solar field configuration, operating instructions and control strategies. Such models already exist for conventional steam generators. However, the boundary conditions are different e.g. in absorber tube length and diameters, heat input and order of local distribution. Therefore, new suitable models had to be derived.

Depending on the desired result and the allowable effort, different process models shall be used. A detailed model of the process should be available for understanding the main dynamics and system characteristics. The detailed model can serve as good approximation of the real plant. For extensive parameter studies or for use in real-time control applications, it is desirable to have a model that has a short simulation time, while still catching the main dynamics. Furthermore, for control system design, the most practical forms of transient models are linear transfer functions or state-space representations.

All three types of models are presented in this chapter. The detailed model is a spacially discretized model with partial differential and algebraic equations. It is implemented in Modelica/Dymola and was mainly developed by Hirsch [105]. A simplified lumped, moving boundary model is developed based on [203] and combined with a partly distributed approach. This model catches the main dynamics by 26 differential and additional algebraic equations. For the design of controllers, linear transfer functions of some sections are available based on Eck [57], while transfer functions for the complete loop must be identified. All models are described and validated in this chapter. They are then used in the following chapters for concept analysis.

3.1 Detailed model with axial discretization

There are many applications that require two-phase or multi-phase flow modeling, e.g. in chemical and process industry, and specialized journals have existed for many decades. One example is Minami [171], who studied transient two-phase flow phenomena of kerosene-air mixtures experimentally in horizontal pipelines (420 m length, 78 mm in diameter) of comparable dimensions as those in parabolic troughs. Taitel and Minzer [239] suggested simplified transient models for such pipeline flows. However, these models neither include heated pipes nor the complete process from preheating, evaporation to superheated conditions.

The following section gives an insight into modeling approaches by extending the work in [78]. While modeling of single-phase fluid behavior in parabolic troughs is rather simple [35, 278], the case of direct steam generation (DSG) is more complex. This is due to a long section of two-phase flow and a large density difference in the fluid between the inlet and outlet of a loop. In fact, the fluid density at the inlet is about 20 to 40 times higher than at the outlet for a typical once-through loop. For single-phase loops with synthetic oil or molten salt it is only in the range of 1.1 to 1.2. Various modeling approaches for the DSG process – or steam generation in general – exist. They can predominantly be distinguished by the way the two-phase flow is considered in the derivation of the main equations. The model must consider that at the inlet, a first part of the collector will preheat the water, such that a liquid single-phase flow with a low dependency on pressure exists. This section is followed by two-phase flow in the evaporation part before a single-phase flow again exists in the superheating part. The latter sections with steam both significantly depend on pressure.

Complex models developed for the nuclear industry consider the flow by a 6-equation model: mass, momentum and energy balance equations are stated for each phase separately. The equations are then closed mainly by empirical interaction laws [15]. Simulation tools such as CATHARE [22], ATHLET [227], APROS [146] or RELAP5 [48] use such models for steam generation. ATHLET is currently also adapted for the simulation of the solar DSG process in parabolic troughs [113]. The drawback of these models is that the empirical interaction laws are not known and require a considerable effort to be derived, if at all possible.

Therefore, many model approaches assume that the two-phase flow can be considered as a homogeneous fluid, i.e. liquid and steam are in thermodynamic equilibrium, have the same velocity and are distributed equally within a cross-section. Lippke [150] uses such a model with mass and energy balances for the homogeneous fluid. As described in [189], the pressure, i.e. the impulse balance, is updated separately from the mass and energy equations based on static pressure loss correlations.

Steinmann [229] developed a model based on transient mass, energy and momentum balances. The finite differences model uses the method of characteristics for solving the boundary conditions at the discretization bounds. Even very fast dynamics can be caught well with this model because of the non-steady impulse balance.

Hirsch [105] derived the mass and energy balances as explicit functions of enthalpy and pressure to simulate the DSG process. The programming language Modelica and its Dymola interface are used. The momentum balance is incorporated by an inverse pressure loss correlation. The outlet pressure, inlet mass flow and inlet enthalpy are the main boundary conditions. This model is used here and is described in the next section.

A model based on similar equations has been implemented in commercial computational fluid dynamics software by Lobón [154]. This tool allows for the combined modelling of fluid dynamics and thermo-mechanical analysis. However, computing times are very large and take about 10 to 100 times longer than a comparable simulation with the Dymola model [153]. Therefore, such a model is not useful for the purpose of system characterization as desired here.

3.1.1 Transient model description

The main model used in this work has been developed by Hirsch [105] and is also described in [105]. Thus, only the most important aspects are compiled here. A discretized approach is used to solve the set of partial differential equations. The term discretized finite element model (DFEM) or simply Dymola model is used in the following to refer to this model, although the category of a finite difference model may be more suitable.

The mass, energy and momentum balance for a unidirectional fluid flow can be written as [57, 78, 105]:

$$\frac{\partial \rho}{\partial t} + \frac{\partial (\rho w)}{\partial z} = 0 \tag{3.1}$$

$$\rho \frac{\partial h}{\partial t} + \rho w \frac{\partial h}{\partial z} - \frac{\partial p}{\partial t} = \frac{Q}{V} \tag{3.2}$$

$$\frac{\partial (\rho w)}{\partial t} + \frac{\partial (\rho w^2)}{\partial z} + \frac{\partial p}{\partial z} + \zeta \frac{\rho w^2}{2d} = 0 \tag{3.3}$$

These equations include density ρ, fluid velocity w, enthalpy h, pressure p, pressure drop coefficient ζ, inner diameter d and convective heat transfer Q to the fluid per volume V. The equations form a set of partial differential equations (PDE) with derivatives of time t and location z. The latter non-steady impulse

balance can be approximated by a stationary frictional pressure loss correlation [105]:

$$\frac{\partial p}{\partial z} = F_{\mathrm{R}} \tag{3.4}$$

These equations are valid for single-phase flow as well as for the homogeneous equilibrium two-phase flow assumption. For two-phase flow, the average properties calculated by steam quality or enthalpy are used.

As the thermal inertia of the piping plays a dominant role in line focus systems, the wall temperature must be considered as well. A simple approach is applied, which neglects axial heat conduction and temperature gradients within a cross-section. The transient heat balance for the tube wall is then given by

$$\frac{\partial \vartheta_{\mathrm{w}}}{\partial t} = \frac{1}{\rho_{\mathrm{w}} A_{\mathrm{w}} c_{\mathrm{w}}} \left(q_{\mathrm{abs,L}} - q_{\mathrm{loss,L}} - q_{\mathrm{L}} \right) \tag{3.5}$$

This includes mean wall temperature ϑ_{w}, wall density ρ_{w}, wall cross-section A_{w}, wall heat capacity c_{w} as well as the length-specific absorbed heat from solar input $q_{\mathrm{abs,L}}$, heat loss $q_{\mathrm{loss,L}}$ and thermal power to the fluid q_{L}.

The mass and energy balances for the fluid (3.1) and (3.2) are reformulated in explicit form of enthalpy and pressure. This step is simplified by neglecting the time derivative of pressure in (3.2). The resulting formulation has the important advantage that the spatially discretized system results in a set of decoupled equations, which is much easier to solve numerically [105]:

$$\frac{\partial h}{\partial t} = \frac{1}{\gamma_p} \left(\frac{\gamma_p h}{\rho A} \frac{\partial \dot{m}}{\partial z} - \frac{\gamma_p}{\rho A} \frac{\partial (h\dot{m})}{\partial z} - \frac{\gamma_p}{\rho V} Q \right) \tag{3.6}$$

$$\frac{\partial p}{\partial t} = \frac{1}{\gamma_p} \left(- \frac{\gamma_h h + \rho}{\rho A} \frac{\partial \dot{m}}{\partial z} - \frac{\gamma_h}{\rho A} \frac{\partial (h\dot{m})}{\partial z} - \frac{\gamma_h}{\rho V} Q \right) \tag{3.7}$$

with mass flow $\dot{m}$ and

$$\rho = \rho(p,h); \quad \gamma_p = \left. \frac{\partial \rho}{\partial p} \right|_h ; \quad \gamma_h = \left. \frac{\partial \rho}{\partial h} \right|_p \tag{3.8}$$

Note that γ_p is only introduced to equation (3.6) to show the same structure as in (3.7). In order to replace the partial, directional derivative of the mass flow $\partial \dot{m}/\partial z$, the pressure loss correlation by Müller-Steinhagen and Heck [181] is used in inverse form, which results in the following relation:

$$\dot{m} = \dot{m}(h, p, \Delta p) \tag{3.9}$$

The partial derivatives in space are replaced by an upwind discretization such that the equations can be written for each element as

$$\frac{\partial h^i}{\partial t} = \frac{\gamma_p^i}{V\gamma_p^i\rho^i}\left(\dot{m}^{i-1}\left(h^{i-1} - h^i\right) + Q^i\right) \tag{3.10}$$

$$\frac{\partial p^i}{\partial t} = \frac{1}{V\gamma_p^i\rho^i}\left(\rho^i\left(\dot{m}^{i-1} - \dot{m}^i\right) - \gamma_h^i\left(\dot{m}^{i-1}\left(h^{i-1} - h^i\right) + Q^i\right)\right) \tag{3.11}$$

The pressure p^i is constant in each element i. The energy balance for the wall temperature is

$$\frac{\partial \vartheta_\mathrm{w}^i}{\partial t} = \frac{1}{m_w c_w}\left(Q_\mathrm{abs}^i - Q_\mathrm{loss}^i - Q^i\right) \tag{3.12}$$

Thus, each element has the three states h^i, p^i and ϑ_w^i. Local boundary conditions are h^{i-1}, $\dot{m}^{i-1}$, p^{i+1}, DNI^i, ϑ_amb and the sun's incidence angle θ_inc. A schematic diagram of the discretization is shown in Figure 3.1. Due to the used discretization, the terminal constraints are the mass flow and enthalpy at the collector inlet and the pressure at the collector outlet.

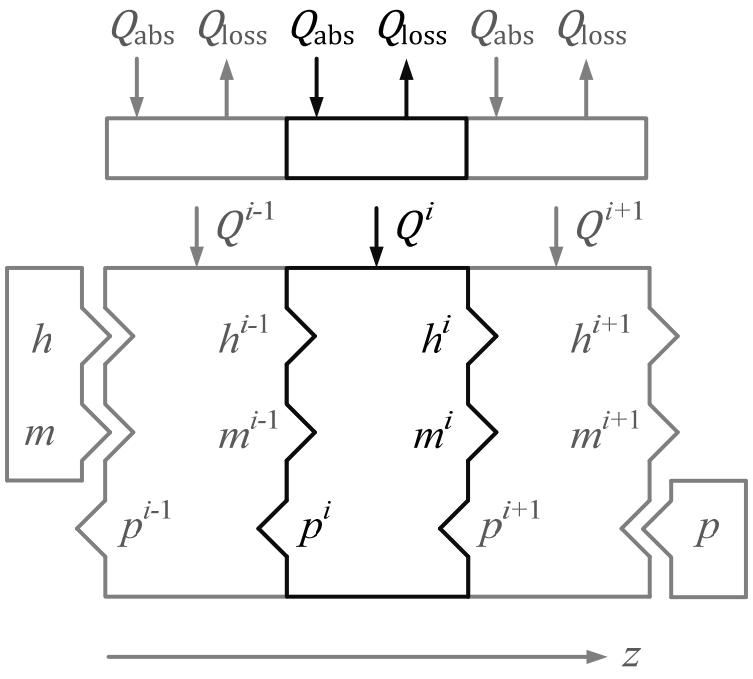

Figure 3.1: Discretization scheme for the Dymola model based on Hirsch [105].

3.1.2 Modeling of heat input and heat loss

The absorbed heat by the receiver element with length Δz is the direct normal irradiance DNI to the collector corrected by various optical factors:

$$Q_{\mathrm{abs}} = w_{\mathrm{ap}} \Delta z \; DNI \cos(\theta_{\mathrm{inc}}) \, \eta_{\mathrm{opt,0}} \; IAM \; \eta_{\mathrm{clean}} \eta_{\mathrm{endloss}} \eta_{\mathrm{shading}} \tag{3.13}$$

The term w_{ap} describes the aperture width of the concentrator or the collector, respectively. The term DNI times the cosine of the incidence angle θ_{inc} is called projected irradiation G_{pr}. The nominal optical efficiency $\eta_{\mathrm{opt,0}}$ is valid at perpendicular irradiation (θ_{inc} = 0°). This value already includes reflectivity of the mirrors, transmissivity of the receiver's glass envelope and absorptivity of the absorber tube wall. For other incidence angles, it must be corrected by the collector type-specific incidence angle modifier (IAM). Further corrections should be done depending on the cleanliness of the mirrors and glass envelopes (η_{clean}), the share of irradiated receiver length as a function of the incidence angle and solar field alignment (η_{endloss}), as well as the shading by other collectors in the morning or evening (η_{shading}). A more concise introduction to optical characteristics of line focus systems is given e.g. in [56, 156, 157, 216]. All these factors must be considered for a good approximation of the absorbed heat. All of them can be calculated in advance from known correlations except the cleanliness, which depends on the current soiling and dirt level of the mirrors. For the sake of brevity, the following short notation will be used:

$$Q_{\mathrm{abs}} = w_{\mathrm{ap}} \Delta z \; G_{\mathrm{pr}} \eta_{\mathrm{opt}} \; ; \qquad \eta_{\mathrm{opt}} = \eta_{\mathrm{opt}}(t, \theta_{\mathrm{inc}}) \tag{3.14}$$

Note that the current overall optical efficiency η_{opt} is a function of time and incidence angle. At this stage, it is also convenient to introduce the effective irradiation, which will play a key role in later chapters. It is defined as:

$$G_{\mathrm{eff}} = \frac{f_{\mathrm{foc}} G_{\mathrm{pr}} \eta_{\mathrm{opt}}}{\eta_{\mathrm{opt,0}}} \tag{3.15}$$

It is the irradiance effectively incident on the receiver after all other current optical losses are considered, especially including the cosine losses and IAM. The factor f_{foc} is between 0 and 1 and indicates whether (or to which extent) the collector is focused or not. If not stated otherwise, the factor f_{foc} is equal to one during normal operation. The effective irradiation is applied in order to show the cosine and incidence angle effects compared to the DNI. It is then simplified to G_{pr} multiplied with the IAM.

The receiver heat loss Q_{loss} can be modeled in various ways. It can be implicitly derived by empirical thermal efficiencies [55, 157], by a simple radiation loss term [57] or empirical correlations from heat loss measurements [54]. It is assumed that the empirical correlation for the heat loss is known, since it is a standard for commercial state-of-the-art receivers. Examples for the determina-

tion of such correlations are given in [31, 32, 54, 76]. As shown in [265], it is convenient for high temperature receivers to model the length-specific heat loss $q_{\mathrm{loss,L}}$ depending on two coefficients (c_1, c_4) as a function of the tube wall temperature:

$$q_{\mathrm{loss,L}} = c_1 \vartheta_{\mathrm{w}} + c_4 \vartheta_{\mathrm{w}}^4 \tag{3.16}$$

The values used here were determined in [76] for the latest DSG receiver tubes by SCHOTT Solar and correspond to the ones used in the upgraded DISS test facility. The values are c_1 = 0.16155 W/m/°C and c_4 = 6.4407e-9 W/m/°C⁴. Note that the wall temperature must be inserted in Celsius and not in Kelvin.

The effective heat Q transferred from the inner tube wall to the fluid is calculated assuming a mean wall temperature [105]:

$$Q = \pi \Delta z \frac{1}{\frac{1}{d_{\mathrm{i}} \alpha} + \frac{1}{2\lambda_{\mathrm{w}}} \ln\left(\frac{d_{\mathrm{i}} + d_{\mathrm{a}}}{2 d_{\mathrm{i}}}\right)} (\vartheta_{\mathrm{w}} - \vartheta) \tag{3.17}$$

In this equation, d_{i} and d_{a} are the inner and outer absorber tube diameters, respectively. The thermal conductivity of the tube wall is denoted λ_{w}, the heat transfer coefficient between inner tube wall and fluid is denoted α. For single-phase flow, the heat transfer coefficient can be calculated using the correlation by Gnielinski [257] or by Dittus and Boelter [263]. The latter is also used in [105] and many others. It is formulated by the fluid's Reynolds number Re, Prandtl number Pr and thermal conductivity λ_{F}:

$$\alpha_{\mathrm{1ph}} = 0.0235 \frac{\lambda_F}{d_{\mathrm{i}}} Re^{0.8} Pr^{0.4} \tag{3.18}$$

The heat transfer coefficient for the two-phase flow was determined empirically for horizontal absorber tubes and pressures up to 70 bar by Goebel [96]. Further options are presented in [257] and compared in [70]. However, the heat transfer coefficient is high and thus the influence on the dominating time constant for heat transfer is low [105]. Therefore, the heat transfer coefficient in two-phase flow can be assumed constant for our purposes without loss of accuracy. A typical value is in the range of 10'000 W/m²/K [105]. Note that this is a good approximation for all operating points analyzed here, because high mass flow densities and corresponding flow regimes must be assured during operation anyway, as derived in chapter 2.2. The application of heat transfer correlations for stratified flow or similar flow regimes is thus of no practical importance for this analysis.

The model equations are implemented and simulations are performed with the software package Dymola. The integrator DASSL is used for solving the numerically stiff system. As a trade-off between accuracy and computation time, the relative tolerance is defined as 10^{-6} or 10^{-5}.

3.2 Extended moving boundary model

The detailed model with axial discretization implemented in Dymola/Modelica works very accurately. However, the simulation time is rather long. In order to be able to simulate the transient system behavior in a wide range with a low computational effort, another model shall be developed. This shall serve for larger simulation studies as well as for application in a model predictive control scheme.

The partial differential equations of the distributed system depend on time and space (as shown in equations (3.1) to (3.5)). In order to achieve a significant simplification of the system description, the distributed character is now ignored, that is any derivatives in space are avoided and only the ordinary differential equations in time are kept. Such models are called lumped or concentrated parameter models. The boiler/loop is divided into three sections, namely the preheating, evaporation and superheating sections. Only the main mass and energy balances are considered for these sections separately. The state of the system can then predominantly be characterized by the lengths of the sections or their control volume boundaries, respectively. These boundaries can vary in a transient model and led to the name *moving boundary model* (MBM) theory. Such an approach is usually a good compromise between accuracy and computational speed in many applications.

One of the first papers using this MBM approach for steam generators was by Adams [1]. It was extended to nuclear once-through boilers by Ray [204] who divided the boiler into its three sections. The two boundaries of phase change (liquid to two-phase and two-phase to gas) between these sections can move with time, i.e. the length of each section can vary. Later, Ray [203] already suggested a similar model for a solar boiler system.

A slightly different MBM formulation has been used by Jensen and Tummescheit [118, 119] for refrigeration systems. While Ray uses the thermodynamic approach of internal energy in the two-phase flow region, Jensen follows the approach of mean void fraction, which can also consider slip, i.e. the velocity ratio of gas and liquid flow within a cross-section [78]. The latter approach has lately been used by Zapata [271] for the simulation of a parabolic dish steam engine and by Bonilla [27] for the classical once-through mode (without injections) in parabolic troughs. Bonilla validates his MBM against experimental data from the old DISS test facility of 500 m length. An extension of [119] for momentum conservation has been presented for solar tower and trough systems [268], since for long boiler tubes the pressure drop might not be negligible.

Due to the rather empirical character of the mean void fraction, the MBM developed in this work is based on the articles of Ray [203]. However, the model must still be extended to meet the particular requirements here. Originally, it is

not foreseen to have injections within the loop, but for the system considered here, they are important to have. Furthermore, information at least at those locations of injections is desired for control purposes. Thus, a mixed approach of lumped and distributed modeling is used. The main ideas and necessary adaptations are described in the following. First, a base model is formulated for normal operation, for which there is one EPE between the evaporation and the superheating injection. Then, two disturbance models are added. The alpha model considers the EPE being shifted downstream the superheating injection, while the beta model considers it being shifted upstream the evaporation injection.

3.2.1 Base model description

The original model of Ray [203, 204] is used as basis for the newly derived equations. A schematic diagram of the sub-volumes applied to a once-through parabolic trough loop is given in Figure 3.2. The boundaries and volumes are enumerated consecutively. 1 denotes the inlet of the boiler, 2 is the preheating section, 3 is the boundary between the liquid and 2-phase flow (or the initial location of boiling, respectively), 4 is the evaporation section, 5 denotes the boundary between the 2-phase and pure steam flow, 6 is the superheater section, and 7 represents the outlet of the boiler. The boundary 5 is also denoted as end point of evaporation (EPE) in the following. The advantage of this model is the explicit modeling of the EPE as defined as length l_{15} [203], which is not present in the DFEM:

$$\frac{dl_{15}}{dt} = \frac{\dot{m}_3(h_3 - u_4) - \dot{m}_5(h_5 - u_4) + q_{\mathrm{L},4} l_{35} - l_{35} A \rho_4 \frac{du_4}{dt} + \rho_3 A (h_3 - u_4) \frac{dl_{13}}{dt}}{\rho_5 A (u_4 - h_5)} \tag{3.19}$$

The change in EPE location depends on the energy balance of the adjacent volumes, characterized by specific internal energies u, and the change of the adjacent boundaries, characterized by the specific enthalpies h. The mass flow at the initial point of boiling is indicated by $\dot{m}_3$, densities are denoted by ρ, length-specific heat flow to the fluid by q_L and the inner tube cross-section by A.

For the simulation of the outlet conditions, this approach would already be sufficient for most types of loop layouts. Injection mass flows can often be treated as additional inlet mass flows, which do not change the results significantly. However, the model should also be applied for control purposes and thus must be able to predict other states along the loop, the most important one being the temperature before the superheater injection (see control strategy chapter for reasons) and the end point of evaporation. This means that the model may not completely be lumped, as spacial information is needed. The resulting scheme is shown in Figure 3.3. The injection A in the evaporation sec-

tion divides the original system into the two sub-systems I and II. A third sub-system is introduced for the additional superheating section after the superheating injector (B). This model is able to predict the dynamic behavior at the outlet as well as at locations before and after the injections.

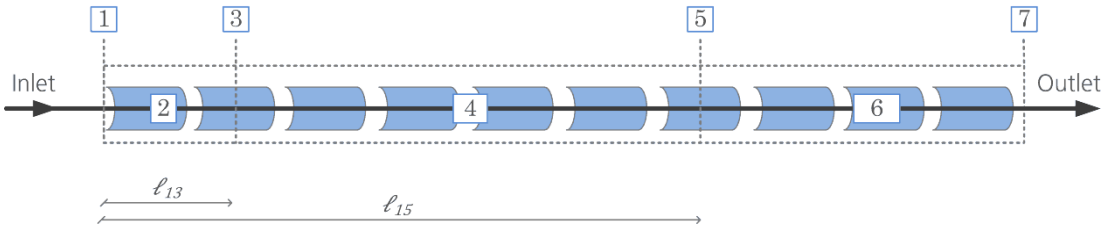

Figure 3.2: Sub-volumes based on original approach by Ray [204] (Ray model).

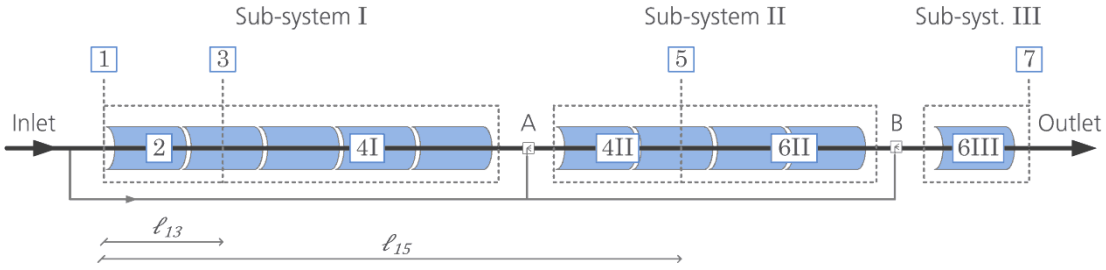

Figure 3.3: Sub-systems and volumes for a loop with two injectors (base model).

The model equations for this base model have been derived using mass and energy conservation and have been applied to the new DISS test facility by Morille [178]. There are 13 system state variables that represent the volumes or boundaries of the model. These are the wall temperatures and specific internal energies of each of the five volumes (2, 4I, 4II, 6II, 6III), the start and end of boiling (l_{13} and l_{15}) as well as the density of the saturated steam (ρ_5). In addition, the pressure p_A at injection A is added as intermediate state for simplifying the calculation procedure and to consider the pressure drop along the loop. This is another difference to [118]. The pressure is updated for each iteration step by a frictional pressure loss correlation.

If only these states were accounted for in the model, changes in the input would immediately take effect on the outlet conditions, bearing in mind that it is a lumped and not a distributed representation of the loop. For example, a change in inlet mass flow would result in an immediate drop in outlet temperature. However, the real system has significant delay that must be considered in the model as well. Thus, 12 intermediate state variables for delaying the input are added. Such states are defined for the input mass flows and enthalpies (inlet, injection A, injection B) and the solar heat input for each volume. These de-

lays can be interpreted as simple first order prefilters. In accordance with [203], the prefilter of the inlet mass flow is chosen to be a second order filter, i.e. two states are added. However, Ray [203] only uses a prefilter for the inlet mass flow, but not the other ones suggested here, which can be seen by the abrupt step responses in his graphs (not shown here). Without prefilters, the system response shows a first strong deviation in the wrong direction directly after an input step, before it meets the final characteristic trajectory. This introduction of initial counter-reactions or non-minimum phase zeros, respectively, is typical for plain lumped parameter models. This is well described in [118] for some cases. In the MBM of this work, it is present for a change in injection mass flow. Although it can be avoided by introducing a second order enthalpy filter element, which is further interconnected with other states, the computational effort increases significantly. As the effect is negligible for small input changes and the model shall be fast, the version with the simple first order prefilter is chosen here for the injections.

As a result, a system of 26 non-linear, but ordinary differential equations is achieved. These are constrained by 96 algebraic equations, such that a differential algebraic equation (DAE) system of index one is stated [215]. The system states are given in Table A.1 on page 247.

The derivative of boundary 5, the EPE, is now formulated by the new base model as follows:

$$\frac{dl_{15}}{dt} = \frac{\dot{m}_{\mathrm{II,in}}\left(h_{\mathrm{II,in}} - u_{4\mathrm{II}}\right) - \dot{m}_5\left(h_5 - u_{4\mathrm{II}}\right) + q_{\mathrm{L,4II}} l_{\mathrm{A5}} - l_{\mathrm{A5}} A \rho_{4\mathrm{II}} \frac{du_{4\mathrm{II}}}{dt}}{\rho_5 A\left(u_{4\mathrm{II}} - h_5\right)} \tag{3.20}$$

The change in l_{13} influences the system states $u_{4\mathrm{I}}$ and $u_{4\mathrm{II}}$, such that its derivate is not directly present in the time derivative of the EPE anymore. Further details can be found in Annex A and [78].

The outlet variables of each subsystem are extrapolated from the internal energy of the volume before. In this way, the temperature at the loop outlet is extrapolated from the conditions after injection B via the internal energy of volume 6III. The same is done for the temperature before injection B. Both temperatures are no original states of the system and cannot be exchanged with others (as they would be meaningless for some two-phase conditions). Nevertheless, a numerical trick is applied and they are added as additional states by using a first order delay with a short time constant. This can be interpreted as measuring the states. By that, both temperatures are available at each iteration step, which is important for control purposes later on. This trick is also different to the other MBMs, but very helpful to get an insight into various transient conditions of the system, which usually are not visible in a lumped parameter model. Numerically, they only add minor computational effort, as they are not interconnected with other system states.

3.2.2 Alpha model description

A model for control prediction must be numerically robust and valid in a wide operating range. The base model as described above is limited to the situation in which the EPE is between injectors A and B. If strong disturbances occur or the system is not controlled, the EPE might be shifted to a different position. If irradiation is too low or the mass flow is too high, respectively, the EPE is shifted downstream of injection B (Figure 3.4) and might even move out of the system. The latter case is equivalent to having two-phase flow at the loop outlet. The corresponding model is denoted as alpha model here.

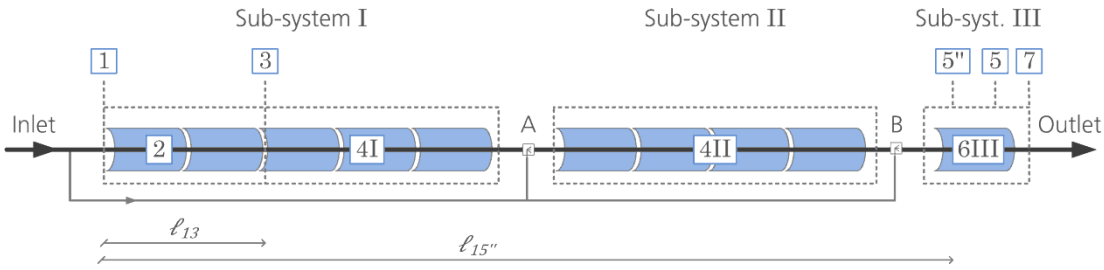

Figure 3.4: Sub-systems and volumes for a loop with two injectors, EPE located after injection B (alpha model).

If the length l_{15} of the base model approaches injection B, two changes in modeling occur. First, sub-volume 6II shrinks until it does not exist anymore as a volume, such that volume 4II represents the complete sub-system II in the new alpha model. Second, there may exist two locations with saturated conditions or two EPEs, respectively. If the length l_{15} from the base model is directly before injection B and a certain mass flow is injected, there will be a second EPE after injection B as well. If the length l_{15} from the base model exceeds the location of injection B (indicated as boundary 5" in Figure 3.4), there is a jump of the EPE to this second location (indicated as boundary 5). One possibility for handling this problem is the switching between two models as suggested in [118, 178]. If the base model is not valid anymore, the complete simulation is repeated with the alpha model and a "simulation master" selects the corresponding results afterwards. This procedure causes problems for control, since a shifting back and forth in the same simulation is not feasible or would require cross-initialization of one another. Such initializations and state transformations can become numerically unstable and cause most of the computational effort in practice. Therefore, a different approach with smooth state transition is chosen here. This is another important difference compared to the other MBM approaches such as [27, 118, 178, 203]. In this work, the same number of states as in the base model is kept and only very few equations are adapted to calculate them.

The alpha model uses the internal energy $u_{4\mathrm{II}}$ and the length l_{15} in their base definitions, which consider mass flows at the inlet and injection A. This definition predicts the EPE without considering the mass flow of injection B. It thus serves as virtual EPE. To distinguish the virtual length from the real EPE, the virtual length is denoted as $l_{15"}$ here:

$$\frac{dl_{15''}}{dt} = \frac{\dot{m}_{\mathrm{II,in}}\left(h_{\mathrm{II,in}} - u_{4\mathrm{II}}\right) - \dot{m}_5\left(h_5 - u_{4\mathrm{II}}\right) + \dot{q}'_{4\mathrm{II}} l_{\mathrm{A5}} - l_{\mathrm{A5}} A \rho_{4\mathrm{II}} \frac{du_{4\mathrm{II}}}{dt}}{\rho_5 A \left(u_{4\mathrm{II}} - h_5\right)} \tag{3.21}$$

Note that properties of boundary 5 are calculated assuming the properties of the virtual point 5". The saturation pressure 5" is interpolated between pressures p_{B} and p_7 for a consistent transition to and from the base model; a minimum of p_7 is used, if $l_{15"}$ exceeds the loop length.

The outlet condition of sub-system II is interpolated by the virtual length $l_{\mathrm{A5"}}$, exceeding injection B, and the fixed length L_{AB} between the injectors. By that, the local information at injection B can be estimated. Sub-system III would include a sub-volume 4III with evaporation in a strict definition. However, volume 6III is used as an average for the complete sub-system III. As in the base model, the outlet conditions are extrapolated from the conditions after injection B and the internal energy $u_{6\mathrm{III}}$. In that manner, the alpha model can be simulated without introducing new states. Furthermore, the model can also handle situations easily when the length l_{15} exceeds the collector length and a two-phase mixture leaves the loop. The coupling of the length $l_{15"}$ with the mass flows at the inlet and injection A is kept, such that there is no switch in dependencies.

3.2.3 Beta model description

A shift of the EPE upstream injection A is assumed in this paragraph, which is illustrated in Figure 3.5. It can be caused by a strong increase in irradiance at the inlet of the loop, while the mass flow remains too small. From a modeling point of view, sub-system I is now equivalent to the original Ray model with a short length $L_{1\mathrm{A}}$. Sub-systems II and III can be treated the same way as sub-system III of the base model. This has been implemented in [178]. However, such a situation should be avoided for safety reasons. In a real system, the collectors before injection A should at least partly be defocused during such a disturbance. Therefore, it is not considered anymore in detail in the following.

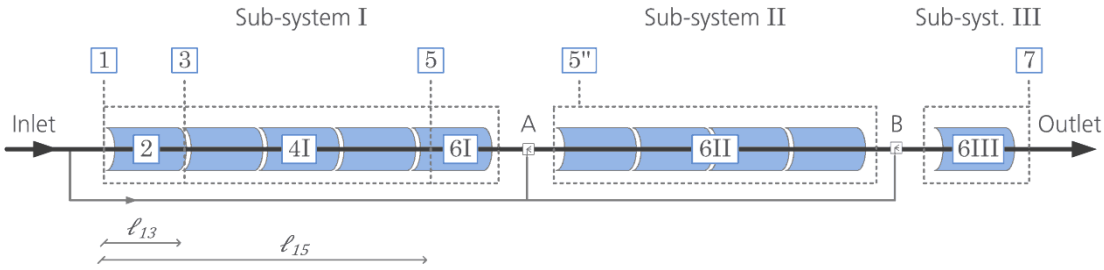

Figure 3.5: Sub-systems and volumes for a loop with two injectors, EPE located before injection A (beta model).

3.2.4 Main differences to axially discretized model

During start-up of the system, the boundary 3 or the initial point of evaporation, respectively, is virtually located behind the loop outlet at first, such that there is liquid water at the outlet. In consequence, there is no boundary and the system reduces to a simple first (or low) order approximation. Then, shortly after focusing the collectors, boundary 3 is quickly shifted to the loop inlet. These steps are not included in the MBM here, as the main application is foreseen for nominal conditions so far. Note that the case when boundary 3 is behind injection A is very unlikely in practice during nominal conditions. Usually, only about the first 10 % of the loop are used for preheating and injection A is located in the second half of the loop. In fact, boundary 3 barely moves, even during strong transients. This can be explained by the high density difference between the sections/volumes. Numerically, this leads to a very stiff system, which must be treated with corresponding integration algorithms. Nevertheless, the MBM can be extended by the same state transition technique as the alpha model to meet the start-up boundary conditions. The prefilters of the MBM would then probably have to be adapted accordingly. On the other hand, these start-up conditions can easily be handled by the DFEM. The accuracy of the DFEM will be significantly higher compared to the MBM, because it remains its high order independent from the flow conditions. Since a pure single-phase flow is numerically easy to handle, the DFEM will simulate significantly faster than for normal operating conditions.

The extended MBM is implemented in Matlab® software environment. It represents the main system dynamics by using only 26 states. For comparison, the DFEM needs about 200 discretized elements with 3 states each, so that an overall of about 600 states must be calculated. In consequence, the computation time of the MBM is only about 1/1000 of the DFEM for normal operating conditions. Thus, the goal of deriving a fast model for simulation studies and online control has been achieved. A comparison of the simulation results is presented in the following validation section.

3.3 Experimental validation of the models

Some aspects of model validation have already been published in [78]. This section recalls them and gives a more detailed insight. The validation is performed with experiments at the new DISS test facility in once-through mode. The schematic diagram of the facility is depicted in Figure 1.2 on page 7. Compared to a commercial loop configuration, there are three long/crossover piping sections between collectors 1B and 1, 8 and 9, as well as between 11 and 12. A commercial configuration would have only one crossover piping or even none for a straight loop. Therefore, the models include the additional piping as well. During all presented experiments, the pressure was kept constant at the outlet of the loop at a level of 80 bar and DNI did not vary significantly, if not stated otherwise. A validation experiment is performed with constant inputs, i.e. all mass flows, the inlet temperature and the focus signals of collectors are not varied in the plant. In consequence, only the DNI is a varying (uncontrollable) input. One of the controllable inputs is then changed to perform a step response test in order to compare the transient behavior of the simulation against the plant data. Completely stable outlet conditions can rarely be established before and after a response test. Nevertheless, this is taken into account as the measured input data is used as simulation input. Sometimes, two or more inputs are changed at once to cross-validate their influence. Overall, more than 50 useful step response tests were performed in 2013 for the most important process variables. Table 3.1 provides an overview on the selected tests that are explained in more detail in the following.

Table 3.1: Overview on the experiments at DISS test facility presented in this work.

Test No.	*Outlet phase*	*Purpose of test*
A	Water	Single-phase validation of whole loop
B	Steam	Step response collector 12 (superheating)
C	Steam	Step response inlet mass flow
D	Steam	Step response injection mass flow bef. coll. 11
E	Steam	Step response inlet temperature
F	Steam	Step response collector 5 (evaporation)

Test A: Single-phase validation of whole loop

The DFEM is very flexible and can be applied for the complete range of DSG solar fields; that is for single collectors and whole loops, as well as for water, steam and two-phase flow. The configuration of the new DISS facility is validated by an experiment with single-phase liquid water flow. The resulting comparison of temperature between data and simulation is shown in Figure 3.6. The measured data of loop inlet mass flow, loop inlet temperature, DNI and focus

signals f_{foc} (0 or 1) of each collector is used as input for the simulation. The dynamic behavior and test is complex due to various focus and defocus periods of several collectors. Nevertheless, the DFEM can handle these transients with a very high accuracy. Not only the outlet temperature $\vartheta_{out,12}$ is well met, but also temperatures along the loop at the outlet of collectors 0A and 1. Only a very small phase deviation between temperature data and simulation is present, which promotes the good representation of the piping system of the complete 1000 m loop. Also note that the first collector of the loop (0A) is focused at around 13.58 h (i.e. 13:35 h) and defocused at around 14.15 h. Its outlet temperature is very well reproduced by the DFEM even for this extreme transient. This illustrates that the model is also well suited for single-phase flow systems such as synthetic oil or molten salt. It could reliably be used for transient analyses such as optical efficiency/IAM determination or performance tests. The DFEM configuration with the same lengths, same number of elements and all other parameters being kept constant is used for the validation.

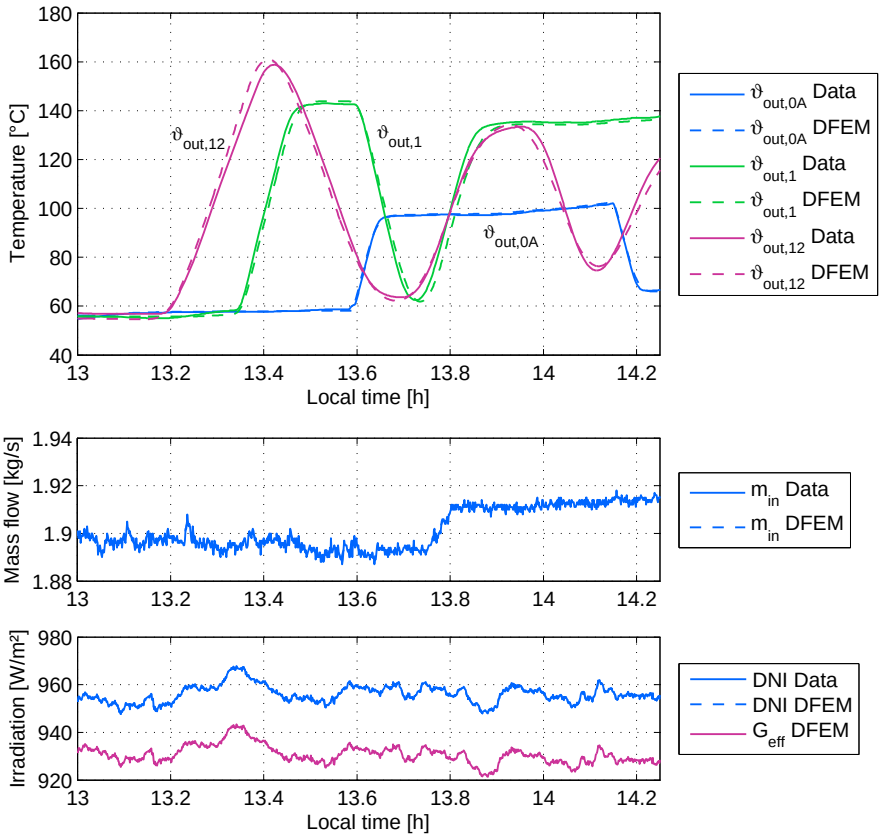

Figure 3.6: Test A: Validation of water flow through complete loop with DFEM compared to DISS data of June 18, 2013; collector outlet temperatures (top) denoted by T, inlet mass flow (middle), irradiation (bottom); collectors in focus: #2 to #7 at 13.0h-13.25h, coll. #1A to #1B at 13.3h-13.55h, coll. #0A to #0B at 13.58h-14.15h.

Test B: Step response collector 12 (superheating section)

Figure 3.7 shows a test in once-through mode with superheated steam on July 17, 2013. At 13.43 h, the last collector of the loop (collector 12) is defocused. At 13.66 h it is refocused again. The top graph illustrates this focus signal over time. The second graph shows the outlet temperature (left) and the temperature before injection (right). In this case, the latter is the temperature after collector 11. The outlet temperature behavior is well met by both models. The lower graph shows the absolute temperature deviation between simulation and data. The maximum deviation during the test is 8.3 K for the MBM and 11.4 K for the DFEM. Both deviations occur because of a slightly different reaction time. While the DFEM reacts faster, the MBM reacts slower than the real plant. Considering that 10 % of the total heat input is suddenly dumped by defocusing, the transient is represented very well by the model. The temperature before injection (Figure 3.7, right) varies strongly in the real plant, while it is rather smooth in the simulation. This is due to unmeasured tracking disturbances at the inlet, which are not present in the simulation input. The underlying tracking problem was solved in 2013 such that disturbances are not present in experiments of 2014 and later. The deviation to simulations can be up to 12 K during the experiment (Figure 3.7). Note, however, that the MBM and DFEM behave very similarly, such that they are consistent with each other for this high temperature and steam conditions as well.

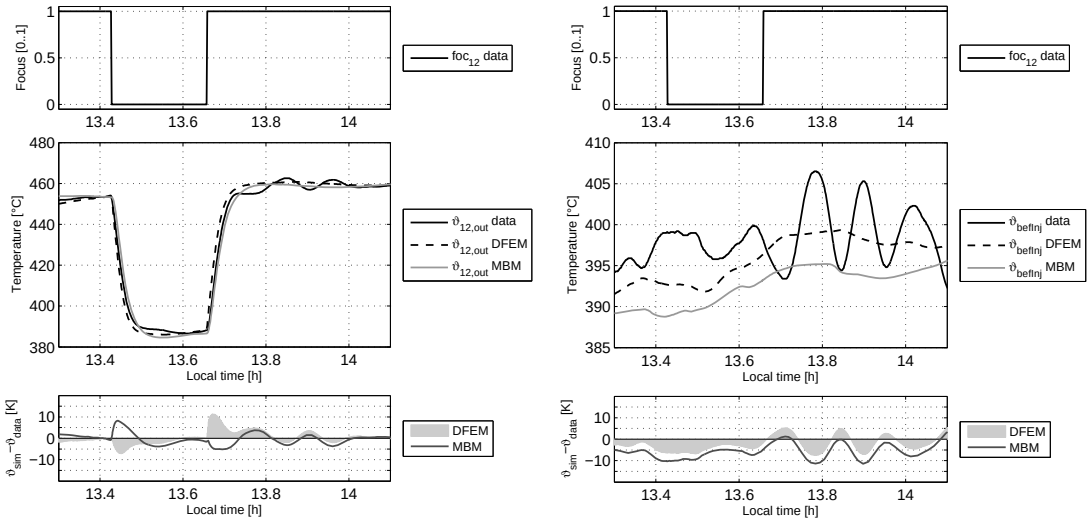

Figure 3.7: Test B: Validation of defocus and refocus of superheating collector 12 with DFEM and MBM compared to DISS data of July 17, 2013; collector outlet temperatures (left) and temperatures before superheater injection or before collector 12, respectively (right); average inlet mass flow 1.32 kg/s, DNI 870 W/m², G_{eff} 810 W/m² (focused), ϑ_{in} 270°C.

The variation of the end of evaporation is not shown explicitly here, but its dynamic behavior is well approximated as a mirrored behavior of the tempera-

ture, e.g. an increase in superheating temperature corresponds to a decrease/upstream-shift of the end of evaporation in the loop.

In general, the change in optical loop efficiency by 1 % results in an outlet temperature change of about 6 to 8 K. At the same time, the uncertainty in determination of optical efficiency and IAM correlations from the plant is at least 3 %. Furthermore, unmodeled disturbances are often present during the experiments and increase the uncertainty of the validation. Thus, the validation is focused on the comparison of dynamic characteristics rather than trying to exactly meet the same temperatures.

Test C: Step response inlet mass flow

Figure 3.8 shows an experiment with small step variations of the inlet mass flow of July 25, 2013. The DFEM meets this transient very well. Only a maximum deviation of 6 K occurs during the steep 90 K-increase of temperature. This is caused again by a slightly earlier reaction of the DFEM compared to the real plant. The DFEM is about 90 seconds faster for a reaction of overall 1800 seconds (about 5 %). The MBM reacts even earlier (17 K deviation) and shows a flat peak in temperature (7 K deviation at 16.0 h). This is due to the second order delay chosen for the MBM's inlet mass flow. A higher order would improve the response, but again increase the computational effort. Note, however, that the peak at 16.0 h is usually met by the MBM as well and that the selected response in Figure 3.8 represents a rather low accuracy compared to most experiments. It is explicitly shown here to provide an impression on the uncertainty in the MBM's behavior.

Test D: Step response injection mass flow before collector 11

Figure 3.9 depicts the response experiment of the injection mass flow before collector 11. This injection is used in the next chapter for control purposes. The DFEM again shows a slightly faster reaction of the model of about 36 s to 70 s compared to the real plant. The temperature gain of the response is smaller by about 5 % to 10 %. The thermal inertia of the piping system therefore seems to be overestimated by the DFEM. The MBM shows slightly higher gains than the real plant when large changes are performed, while it also damps too much for small changes. At 15 h and 15.25 h, the initial counter-reaction typical for MBMs is visible as mentioned in the modeling section. The sudden decrease in injection mass flow provokes a fast counter-reaction – that is a decrease – of the temperature. This is due to the interpolation of variables within the MBM, which immediately take effect. These variables and the response can be smoothed by adding another model order in the MBM, but at the price of significantly higher computational effort. As control action itself should be smooth, the effect is negligible and the simpler model is used here.

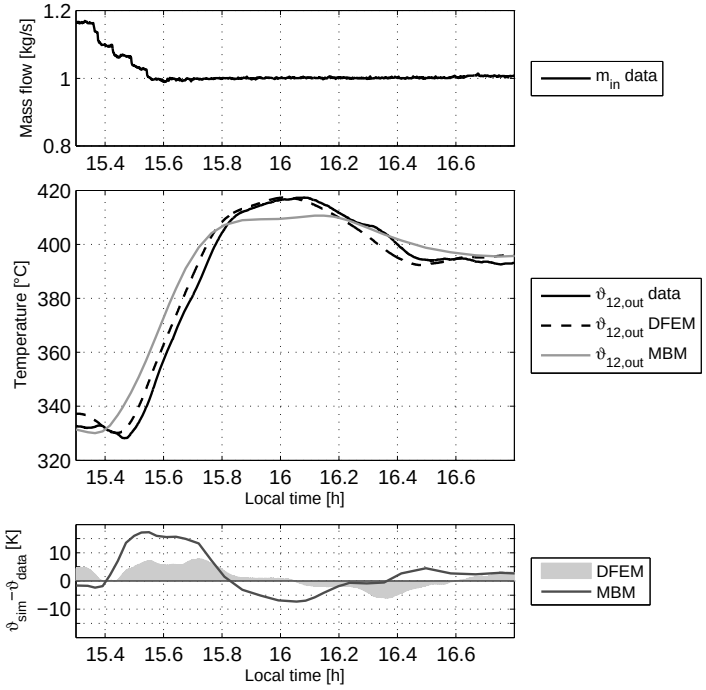

Figure 3.8: Test C: Validation of inlet mass flow step with DFEM and MBM compared to DISS data of July 25, 2013; inlet mass flow (top), outlet temperature (middle) and temperature deviation between simulation and data (bottom); average DNI 740 W/m², G_{eff} 700 W/m², ϑ_{in} 265°C.

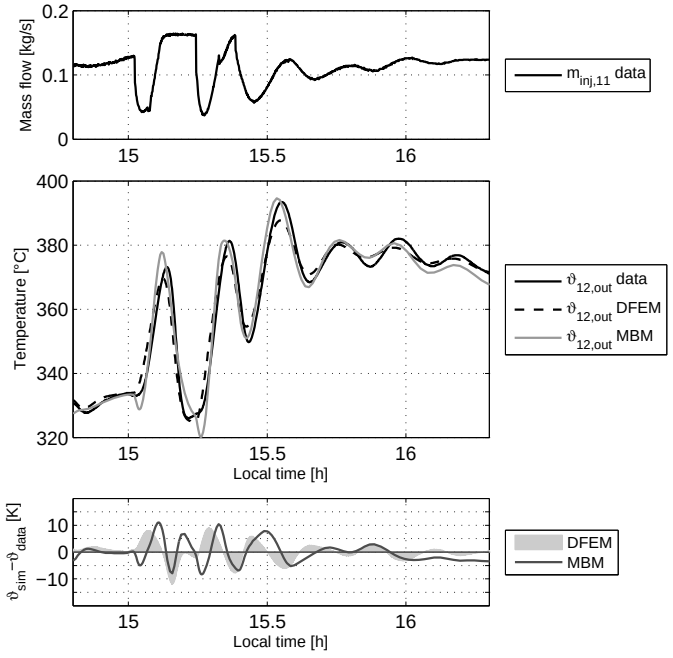

Figure 3.9: Validation of injection mass flow changes step before collector 11 with DFEM and MBM compared to DISS data of November 6, 2013; injection mass flow (top), outlet temperature (middle) and temperature deviation between simulation and data (bottom); average inlet mass flow 0.77 kg/s, DNI 880 W/m², G_{eff} 570 W/m², ϑ_{in} 240°C, $\vartheta_{\text{inj11,water}}$ 200°C.

Test E: Step response inlet temperature

A particular characteristic of steam generators is shown in Figure 3.10 for August 9, 2013. When the inlet temperature is decreased (at 14.7 h local time), the typical non-minimum phase behavior of the outlet temperature is seen. That means that, at first, the outlet temperature will increase and reach a maximum (at about 15.25 h) before it decreases to its final lower value (after 15.5 h). This is due to the density increase of the reduced temperature at the inlet – an increase of only 2.2 % in the experiment. This density increase is intensified downstream through the preheating section. When reaching the beginning of the evaporation section (after about 12 min), it causes a lower velocity and thus a lower mass flow of the steam in the system. In consequence, more heat can be transferred to the steam at the outlet, which results in a higher temperature. Note that the pressure drop effect described in [154] is a result of this density or mass flow disturbance. After the residence time of the fluid between loop inlet and outlet, the temperature starts decreasing (15.25 h) and reaches its lower value. This density effect is reproduced by the DFEM, but with an earlier and higher local maximum. The DFEM reacts about 3 min earlier during the overall disturbance of 61 min, which was considered acceptable. The MBM has an even smaller phase shift and underestimates the local peak. During the whole experiment, its deviation is less than 8 K. The vice versa reaction is visible after 15.75 h for an increase in inlet temperature.

Test F: Step response collector 5 (evaporation section)

Figure 3.11 gives an example of an energy disturbance in the evaporation section on July 26, 2013. Collector 5 is defocused at 14.1 h local time. The same density effect as described above is again visible. The sudden loss in energy input results in a higher density, which again causes a slightly lower mass flow at the outlet and, in consequence, a higher outlet temperature. This effect is very small and short, as the residence time of the steam from collector 6 to the outlet is also short, in the range of one to three minutes. After that, the temperature decreases rapidly to its final lower value. The same can be seen for the focusing of collector 5 at 14.70 h, with a local minimum at about 14.78 h before the final value is approached.

The DFEM represents this behavior with a smaller peak reaction. The peaks of the MBM response are barely visible. This is due to the lumped character of the model. Collector 5 is only a small part of the first evaporation section 4I (see section 3.2.1 for details) and the model reacts for an average change in that section with a rather long time delay for reaching the final value. This illustrates the price to be paid for the simplifications. Note that it might in principle be possible to tune this response by adding collector-specific time delays and

superposing corresponding inlet temperature disturbances in order to better meet the distributed character. However, this would be an extreme tuning effort and significantly complicate the MBM, since it would leave the path of analytical equations with simple first order prefilters. Therefore, such tuning is not performed here. This ignorance must especially be considered when applying the MBM within a model predictive controller and combining it with locally distributed DNI values. The minutes directly after such an evaporation disturbance can be misleading, while the main response will fit well to the overall plant behavior. The deviation does not appear when considering homogeneously distributed DNI along the loop.

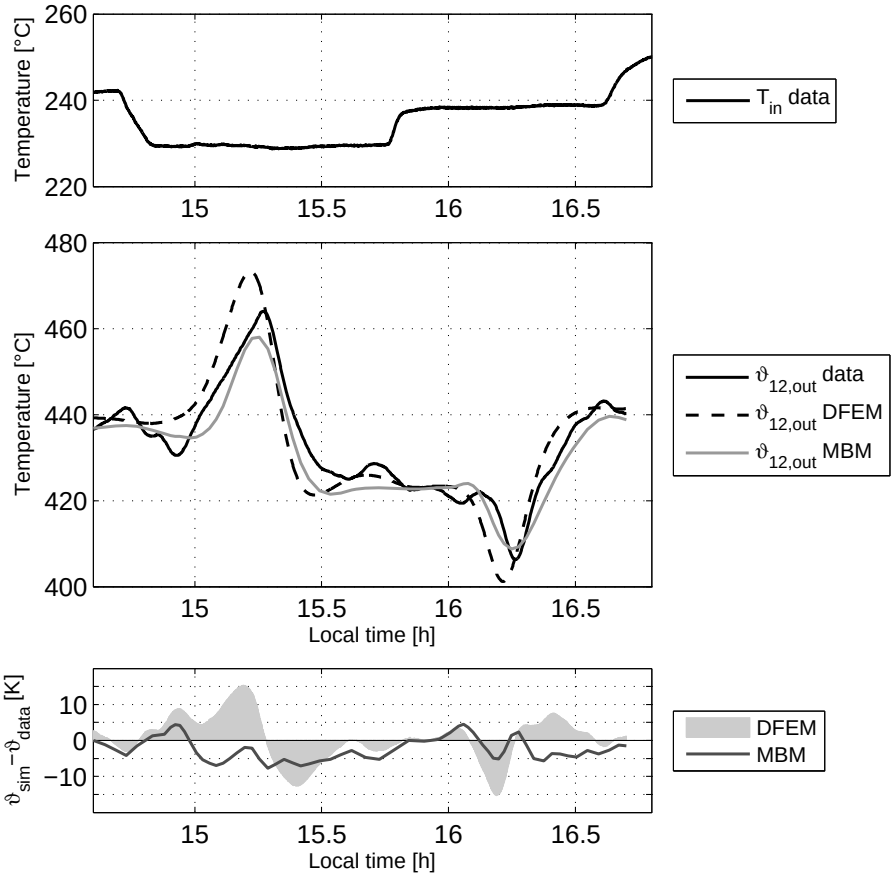

Figure 3.10: Test E: Validation of inlet temperature steps with DFEM and MBM compared to DISS data of August 9, 2013; inlet temperature (top), outlet temperature (middle) and outlet temperature deviation between simulation and data (bottom); average inlet mass flow 1.0 kg/s, DNI 945 W/m², G_{eff} 870 W/m², collectors 0A and 0B defocused.

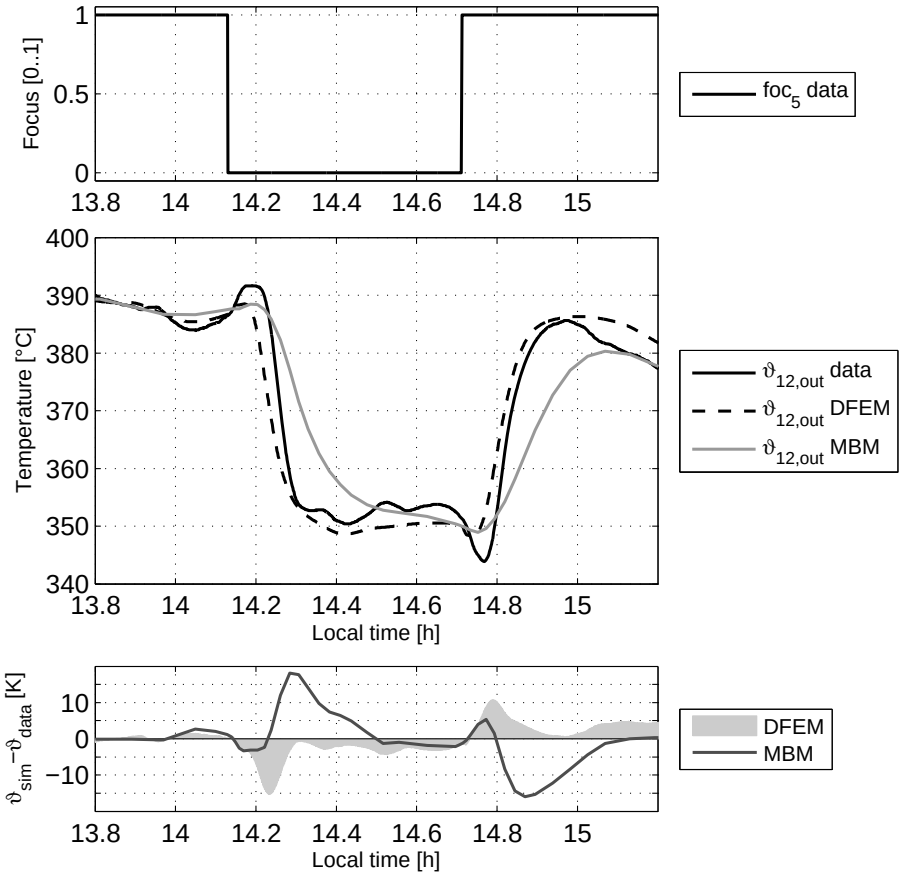

Figure 3.11: Test F: Validation of de-/re-focus steps of collector 5 with DFEM and MBM compared to DISS data of July 26, 2013; focus signal (top), outlet temperature (middle) and temperature deviation between simulation and data (bottom); average inlet mass flow 1.1 kg/s, DNI 820 W/m², G_{eff} 750 W/m², ϑ_{in} 270°C, collectors 0A and 0B defocused.

Conclusions of experiments

Various other experiments have been performed at the DISS facility, but for brevity only the most important ones are presented here. Concluding the experimental results, both the DFEM and the MBM meet the main dynamics of the system very well. Nevertheless, both models show deviations from the data to a certain extent as expected. Especially, the MBM output differs from the real plant output, when the distributed character has a strong influence on the transient behavior. Those aspects must be considered during the interpretation of the model outputs. For controller design, they must be considered in the uncertainty of the underlying models.

3.4 Linear time-invariant transfer functions for control

Linear time-invariant (LTI) transfer functions are used in control design to describe the linearized system deviations from a pre-defined operating point. Significant simplifications are used to derive these models. LTI models show very good agreement with the real system behavior if single-phase flow and small deviations are analyzed. As the steam generating system is non-linear and has large deviations in operating points (e.g. caused by fluctuations of DNI), one LTI model is not sufficient. Instead, a complete set of LTI models is needed, each of which being valid for a small range of operating conditions. The following paragraphs illustrate an analytical model for the superheating section, while the following subsections derive suitable LTI transfer functions for the design of controllers in chapter 4.3. The latter LTI models are identified from simulations, but do not contain physical parameters.

Background to analytical LTI approaches

LTI models for single-phase flow collectors exist based on first principles [57, 63, 138, 139]. They are numerically stable both in the time and frequency domain. These models work very well in a small range around the operating point. Their model order can become very high for commercial scale plants and their simple gain approximation can lead to significant deviations from the real behavior. Furthermore, all collectors are characterized by the same PT_n approximation with the order n being the only parameter to vary. This is practical on the one hand, but can lead to misinterpretations during controller design on the other hand. The model is presented in detail in Annex B and a comparison with oil systems is performed. Only the main general relations are shown here to get an impression of the structure. A superheating collector is considered in the following. The transfer function from a change in inlet temperature to the resulting change in outlet temperature is approximated by [57]:

$$G_\vartheta(\mathrm{s}) = \frac{\Delta\vartheta_{\mathrm{out}}(\mathrm{s})}{\Delta\vartheta_{\mathrm{in}}(\mathrm{s})} = k_\vartheta G_t(\mathrm{s}) = k_\vartheta k_1 \frac{1}{(1+s\tau_1)^{n_1}} e^{-s\tau_{\mathrm{res}}} \tag{3.22}$$

The complex argument s denotes the Laplace variable for frequency domain. The order n_1 of the PT_n element mainly depends on the collector length and process design, while the time constant τ_1 is predominantly influenced by the residence time or mass flow, respectively. For small collector lengths, the order of the system can well be kept constant, while the time constant must be adapted to the current operating point. τ_{res} is the throughput time or the residence time of the fluid in the collector, respectively. It can be calculated from the equation

$$\tau_{\mathrm{res}} = \frac{\rho_{\mathrm{F}} A_{\mathrm{F}} L_{\mathrm{coll}}}{\dot{m}} \tag{3.23}$$

This includes fluid density ρ_{F}, inner cross-section A_{F}, collector length L_{coll} and mass flow $\dot{m}$. With the temperature transfer function, one can also formulate the transfer functions for mass flow and irradiance. The change in irradiation/DNI to outlet temperature can be expressed by [57]:

$$G_{\mathrm{DNI}}(\mathrm{s}) = \frac{\Delta\vartheta_{\mathrm{out}}(\mathrm{s})}{\Delta G_{\mathrm{eff}}(\mathrm{s})} = k_{\mathrm{DNI}} \frac{1}{s\left(1+s\tau_{\mathrm{p}}\right)}\left(1 - G_{\vartheta}(\mathrm{s})\right) \tag{3.24}$$

This transfer function has an integral term $(1/\mathrm{s})$, which is at first dominant and is then smoothed by a first order delay $(1+s\tau_{\mathrm{p}})$ with time constant τ_{p}, depending on fluid residence time and heat transfer relations. Note that the temperature transfer function G_{ϑ} is included in the DNI transfer function.

The transfer function from a change in inlet mass flow to outlet temperature is nearly identical [139]:

$$G_{M}(\mathrm{s}) = \frac{\Delta\vartheta_{\mathrm{out}}(\mathrm{s})}{\Delta\dot{m}_{\mathrm{in}}(\mathrm{s})} = -k_{M} \frac{1+s\tau_{Mz}}{s\left(1+s\tau_{\mathrm{p}}\right)}\left(1 - G_{\vartheta}(\mathrm{s})\right) \tag{3.25}$$

Only an additional, slightly faster zero element $(1+s\tau_{Mz})$ and the gain k_{M} are different. The models are based on [278] for synthetic oil and [57, 139] for steam. Annex B describes the models in more detail and joins the two approaches to a common framework. The negative sign indicates that an increase in mass flow results in a decrease of temperature.

Analytical LTI models for the evaporation section of line focus collector fields exist as well. They are derived and explained in [57] in detail. Their drawback is that they lead to very complex models and are not stable in the time domain. The same is true, if the frequency domain equations in [57] are re-transformed and further simplified [77]. The system is stiff and has a bad conditioning [215] due to the different speed of dynamics involved. Thus, neither a simple scaling nor a transformation of the equations is possible. Other models for conventional steam generation exist analytically, e.g. in [10, 137, 198]. Their simplified forms are only based on the main energetic assumptions, but neglect the influences of inlet temperature and density effects. In consequence, no sufficient model for the evaporation section is available for the desired purposes.

Furthermore, a common analytical approach for transfer functions of the complete once-through loop does not exist at the moment. One way to derive an LTI model of the complete loop is the numerical or analytical linearization of the MBM. This linearization again is not stable in the time domain due to the same reasons as above [215]. Nevertheless, such models are needed in the time domain for two reasons. First, controller design supported by simulations in the time domain is usually more intuitive to interpret and to validate. Second, the application within a model predictive control scheme requires time domain simulations for prediction of the system behavior.

Introduction to model identification

As a consequence of the missing analytical model descriptions, simplified LTI model structures are identified in this work by simulations with the discretized model for the complete loop in the sequel. A similar way has been chosen by Valenzuela [253] based on experimental data, for which a first order element with deadtime was chosen. The difference in the approach taken here is that the usage of the discretized model allows for assessing a wider range of operating points, that all relevant disturbances can be considered dynamically and that the model structures are of higher order without deadtime. This enables a much better representation of the system behavior.

The main controlled variable is the outlet temperature of the loop, which shall be kept within a small range during nominal operation. Thus, deviations of all other variables are linked to deviations of the outlet temperature here. The temperature before the superheater injection is also an important variable for control and is therefore modeled as well. Structurally, the transfer functions for both temperatures look very similar.

Main manipulated variables are the inlet mass flow, the injection mass flow in the evaporator and the injection mass flow in the superheater. Disturbances occur from inlet temperature, irradiation and injection water temperatures. Furthermore, the location of irradiation disturbances has significant influence on the outlet temperature. Models for such energy disturbances are identified collector-wise. Other disturbances such as ambient temperature, wind speed or wind direction are negligible compared to the mentioned variables. No transfer functions are derived for those minor influences.

The identification process is performed as follows:

1. Various step responses are simulated with the detailed DFEM in Dymola for various operating points.
2. A suitable transfer function structure of low order is identified for each relation, e.g. a third order model is chosen for the relation between injection mass flow to outlet temperature.
3. All step responses of one relation are fitted to this structure via the Matlab® System Identification Toolbox.
4. One step variation magnitude is selected as typical LTI model of the set and the other magnitudes' results are provided as uncertainty of this typical LTI model.

The main transfer functions of interest for controller design are identified and provided in this manner. Note that this approach must be repeated for every plant. The DFEM is based on first principle parameters and can be adapted easily. The LTI model parameters are pure numerical representations and only the LTI model structures can be kept the same for other plants. Table 3.2 provides an overview on all the identified relations and in which section of this

chapter they are described. Section 3.4.1 is very detailed and also serves as introduction to LTI models in general and to the characteristic numbers used in this work. The main characteristics of the system relations are explained in all corresponding sections, which are valuable for controller design later on.

Table 3.2: Overview on considered LTI model relations and the corresponding section in this chapter.

Relation to / *Steps by*	*Outlet temperature*	*Temperature before superheater injection*
SHI mass flow	3.4.1	-
EVI mass flow	3.4.3	3.4.2
Inlet mass flow	3.4.5	3.4.4
DNI (on complete loop)	3.4.6	3.4.6
Local DNI or collector-wise focusing, respectively	3.4.8	3.4.8
Inlet temperature	3.4.7	3.4.7
SHI water temperature	3.4.9	-
EVI water temperature	3.4.9	3.4.9

Table 3.3: Variation of DFEM simulation inputs for identification of LTI model parameters; all simulations started from steady-state value for all DNI variants.

Input	*Number of variations*	*Variation range*
DNI steady-state values	9	375 to 975 W/m² in 75 W/m² steps
Inlet mass flow	90	±1, 2, 4, 6 and 10 %
Mass flow injection 11	126	±1, 2, 4, 6, 10, 20 and 50 %
Mass flow injection 6	117	±2, 4, 6, 10, 20 and 50 %
DNI (on whole loop)	90	±1, 2, 4, 6 and 10 %
Inlet temperature	36	±1, 2, 5 and 10 K
Inj. 11 water temperature	90	±1, 2, 5, 10 and 20 K
Inj. 6 water temperature	90	±1, 2, 5, 10 and 20 K
Collectors 0A to 9	936	±1, 2, 4 and 6 %
Collectors 10 to 12	324	±1, 2, 4, 6 %, -10, -20, -50 and -98 %

All DFEM simulations are started from the steady-state as designed in chapter 2.5. Thus, every value for DNI is linked to steady-state mass flows at the inlet and the injectors. Nine different steady-state operating points are defined by

DNI with a resolution of 75 W/m² between 375 and 975 W/m². Step responses of all other input variables are then generated for each of those conditions. Note that the name DNI is used as synonym for effective irradiation G_{eff} in this chapter, because all simulations assume ideal incidence angles of 0°. Simulations are performed for the DISS test facility for an outlet temperature of 400°C at 80 bar and an inlet temperature of 260°C. An overview on the performed simulations for identification is provided in Table 3.3. The suitable model structures are provided in Table 3.5 at the end of this subchapter. The identified numerical LTI model parameters can be found in Annex C for selected models of mass flows and DNI.

3.4.1 Superheater injection to outlet temperature

The influence of the injection mass flow in the superheating section is now analyzed regarding the loop outlet temperature. Analytical relations between injection mass flow and outlet temperature are provided in Annex C as mentioned before. For long superheating sections or special system configurations, the analytical models result in high order transfer functions or do not hold anymore due to invalidity of assumptions. One special case arises for the DISS facility. If the injection before collector 11 is used, an LTI model for a 50 m LS-3 collector in series with a long crossover pipe and another 100 m SL4600+ collector should be found. A common method is to multiply the three corresponding transfer functions. The analytical approach by [139] suggests a structure with n_1+3 poles including a pure integrator and n_1+2 zeros for each superheater section. If a simple Padé approximation is assumed for the crossover pipe, this leads to a model order of (1+3)+1+(3+3) = 11 and nine process zeros. Furthermore, the resulting transfer function implies many simplifications, which no longer necessarily hold. Thus, a system identification approach is used to reduce the model order and better meet the real system behavior.

Model structure

Figure 3.12 shows the step responses from the mass flow of injection before collector 11 to outlet temperature for the DISS facility. At steady-state conditions with high effective irradiation, the mass flows are high and the response is relatively fast. At lower irradiation levels or loads, respectively, the response time is more than doubled. The efficiency of the superheating section decreases for a fixed outlet pressure. Thus, the temperature increase is lower and, in consequence, the same share of injection mass flow results in a lower temperature deviation as well. At low DNI levels, e.g. 375 W/m² in Figure 3.12 (left), a slow response is seen at first (until time 250 s), followed by a steeper response. At high DNI levels, those two parts are less distinguishable. A slight overshoot of

the response before reaching the new steady-state appears, but is rather negligible. In Figure 3.12 (right) it can be seen that response times and gains vary slightly with the relative share of the injection mass flow variation. Thus, one response cannot be scaled to the other, even at the same operating point.

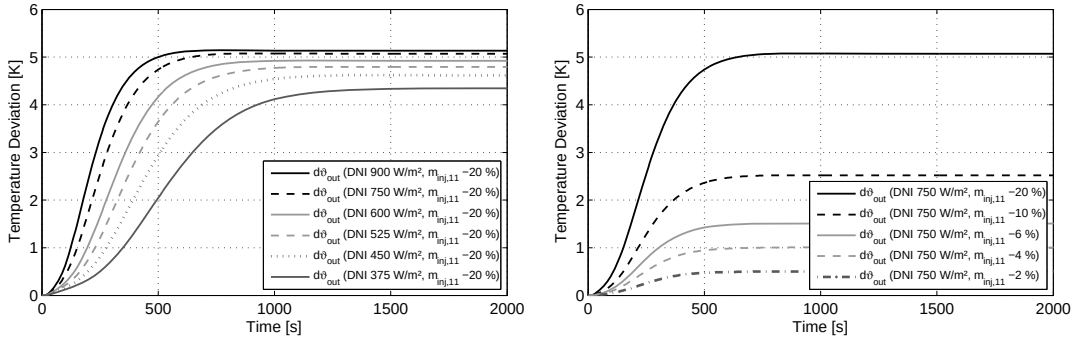

Figure 3.12: Step responses of outlet temperature to a reduction in injection mass flow simulated with the discretized model of DISS facility for different load situations (left) and injection variations (right).

To meet the described behavior, a model structure with three poles and two zeros is chosen:

$$G_{\mathrm{mInj11-\vartheta out}} = k_{\mathrm{P}} \frac{(\tau_{z1}^2 s + 2\delta_{z1}\tau_{z1} s + 1)}{(\tau_1^2 s + 2\delta_1\tau_1 s + 1)(s\tau_2 + 1)} \tag{3.26}$$

In accordance with Table 3.3, 126 different step response simulations are performed with the DFEM. Using the Matlab® System Identification Toolbox, one can identify all responses to an accuracy of more than 98.5 % for the chosen structure. The parameters of the identified models are listed in Annex C.

Pole-zero maps

Neglecting four outliers, Figure 3.13 (left) shows the resulting pole-zero maps for all models. These maps are a common means to analyze the system characteristics. Roots of the denominator of the transfer function are called poles. Roots of the numerator are called zeros. The easiest way to check stability of a dynamic system is to calculate the real part of the poles. If all real parts are negative, i.e. all poles are in the left half plane (LHP) of the pole-zero map, the system behavior is stable. A stable steady-state value is reached after an excitation of the system. The places of poles define the main dynamic behavior. Poles close to the imaginary axis are slow – and dominate the dynamic response -, while poles with high negative real parts are fast and do not significantly influence the dynamics. Complex conjugate poles with imaginary parts unequal to zero indicate oscillating systems. The oscillation is more significant the greater the imaginary part is compared to the real part [175]. The interpretation of zeros is more complex, especially if they have positive real parts. Such a sys-

tem is called non-minimum phase. The step response of a system with an odd number of non-minimum phase zeros usually shows a characteristic undershoot. A very nice introduction is found in [111], some examples are given later on.

All poles of the system, as shown in Figure 3.13 (left), are in the left half plane. Thus, as expected, all transfer functions are stable. It can be concluded that the pole structure is twofold. On the one hand, there are models with one fast pole and two slower complex conjugate poles (which corresponds to high DNI, as will be seen later). On the other hand, there are models with all three poles in the same range (low DNI). The complex conjugate zeros are scattered around the imaginary axis, some in the left and most in the right half plane (RHP). This already suggests that the system is somehow non-minimum phase. The identified poles and zeros for one example are illustrated in Figure 3.13 (right) for the 150 m section.

Note that the analytical approach by Eck (p. 41 in [57]) already has five poles for a 50 m collector, of which two are quasi integrators, i.e. they are very close to the imaginary axis. The analytical approach also gives five non-minimum zeros and an additional five in the left half plane. As a result, the analytical model can become instable because of the integrators, though the plant would not [248]. In the real system response and the identified LTI models, the integrative part is smoothed by the heat transfer behavior and can thus be well approximated by stable poles. A simpler and more suitable LTI model can be achieved.

Definition of characteristic time constants

A characteristic time constant $\tau_{c,rp}$ is defined as follows:

$$\tau_{c,rp} = \tau_2 + \frac{\tau_1}{\delta_1} \tag{3.27}$$

This definition can be understood better when looking at the pole zero map in Figure 3.13 right. A pole with τ_2 can be found on the negative x-axis at frequency $-1/\tau_2$. The real part (thus "rp") of the complex conjugate pole pair with τ_1 and δ_1 can be found on the x-axis at frequency $-\delta_1/\tau_2$. Thus, the characteristic time $\tau_{c,rp}$ is defined as the sum of both reciprocal real parts.

The identified poles are analyzed in the following. Figure 3.14 shows the pole parameters of equation (3.26) and the characteristic time constant $\tau_{c,rp}$ of equation (3.27). A broad variation is apparent. First, the identified time constants increase by a factor of up to four with decreasing DNI. Thus, the responses are significantly slowed down at lower loads. Second, there is a large variation of time constants ($\tau_{c,rp}$ and τ_2) and damping δ_1 at the same DNI level. This is caused by the different share of injection, which is varied. There is no smooth transition of the damping with load, not even for the same injection

variation (see e.g. -2 % injection changes in Figure 3.14). This is a result from numerical regression when searching for parameters, as no restrictions were imposed on the identification process. Nevertheless, there is a trend that the damping is significantly reduced in most cases when the share of variation is small and when the load is low. This is illustrated for the case of -2 % injection changes in Figure 3.14. Or vice versa, a smoother and faster response is achieved for higher injection mass flow variations, e.g. -10 %. This is an interesting result from model identification. The step response is oscillating more at lower loads and by smaller injection shares.

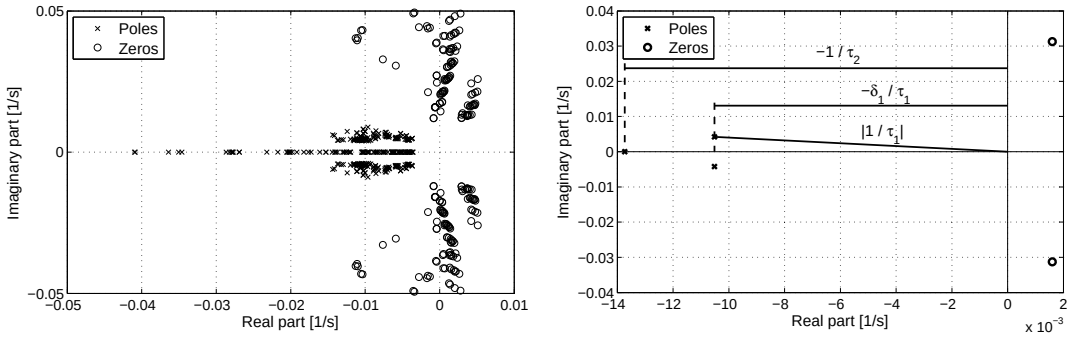

Figure 3.13: Pole-zero map of identified models from step responses of superheating injection mass flow to outlet temperature at DISS facility for different load situations; all models (left) and one for -10 % at 750 W/m² (right).

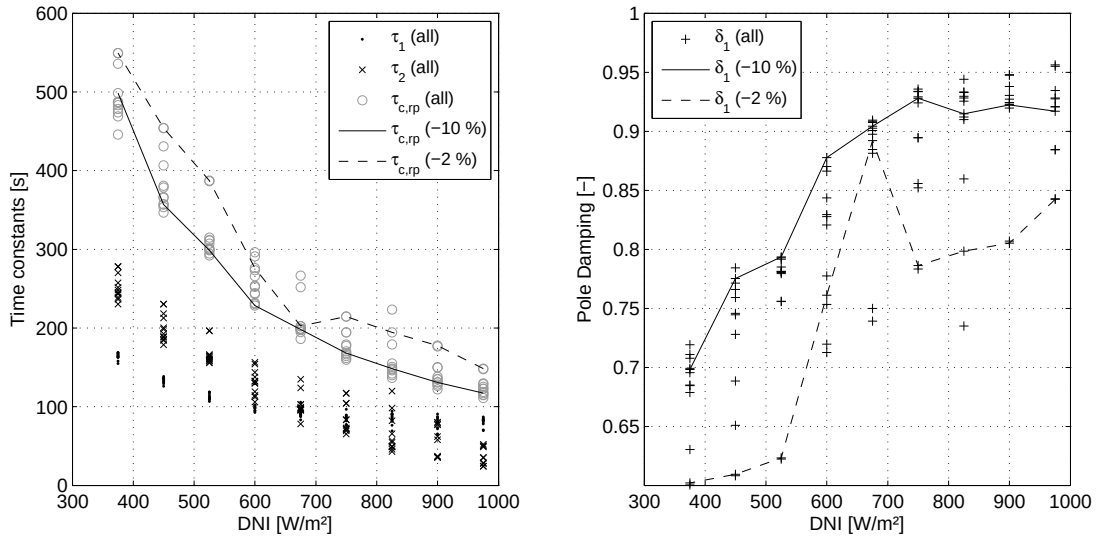

Figure 3.14: Time constants (left) and damping (right) of the identified LTI models for injection mass flow to outlet temperature.

An additional common characteristic measure of control is introduced at this stage. The most important one is the characteristic time constant derived from Internal Model Control (IMC) principles as suggested by Morari [175]. First

order elements are characterized by their time constants (τ_2) and second order elements by two times the damping multiplied with the time constant ($2\delta_1\tau_1$). All times are summed up, which gives the following definition:

$$\tau_{\mathrm{c,imc}} = 2\delta_1\tau_1 + \tau_2 \tag{3.28}$$

This time constant plays a key role in optimal controller design and will be the basis for controllers developed in the next chapter.

In order to get a feeling of the speed and development of the response in an unambiguous way, the characteristic time $\tau_{\mathrm{c,63\%}}$ is defined as the time after which 63 % of the final (temperature) deviation, or of the new steady-state, respectively, are reached:

$$\Delta\vartheta\left(\tau_{\mathrm{c,63\%}}\right) = 0.63\,\Delta\vartheta(t \to \infty) \tag{3.29}$$

Note that for a simple first order element $\tau_{\mathrm{c,imc}} = \tau_{\mathrm{c,63\%}}$.

The third characteristic time constant $\tau_{\mathrm{c,sl}}$ corresponds to the slowest mode of the transfer function. It is the reciprocal value of the real part with the smallest absolute value (which was already used for $\tau_{\mathrm{c,rp}}$):

$$\tau_{\mathrm{c,sl}} = \max\left(\tau_2; \frac{\tau_1}{\delta_1}\right) \tag{3.30}$$

This number is helpful when pursuing pole placement strategies for controller design. Figure 3.15 gives a better feeling for the characteristic times. Time constants are plotted versus the final (new steady-state) total mass flow after the injection. Clustering of the mass flows corresponds to DNI levels as in the figures above, e.g. 1.25 kg/s at 750 W/m². Within these load clusters, there are strong variations for $\tau_{\mathrm{c,sl}}$ and $\tau_{\mathrm{c,rp}}$ (see Figure 3.14). Those two time constants are characteristic for the approximation of the single transfer function. Together, they show what the slowest mode is and how dominant it is compared to the other modes. (One could also express this domination by the factor of $\tau_{\mathrm{c,rp}}/\tau_{\mathrm{c,sl}}$, being around one for domination and increasing with the influence of additional modes.)

On the other hand, one can see a good clustering or a small deviation, respectively, for times $\tau_{\mathrm{c,imc}}$ and $\tau_{\mathrm{c,63\%}}$. This is because both numbers characterize the overall system behavior instead of the single composition. Note that the 63 % value is significantly higher than the IMC value. In fact, in the current example for the superheater, the IMC time constant almost exactly corresponds to a 45 % value, that is $\Delta\vartheta\left(\tau_{c,imc}\right) \approx 0.45\,\Delta\vartheta(t \to \infty)$. For further discussions, it is important to note that the total mass flow after the injection, i.e. at the inlet of the superheating collectors, is a good measure to cluster the system parameters. In fact, a small variation of optical collector efficiency would only shift the corresponding clusters along the curve, but would not shift the complete curve.

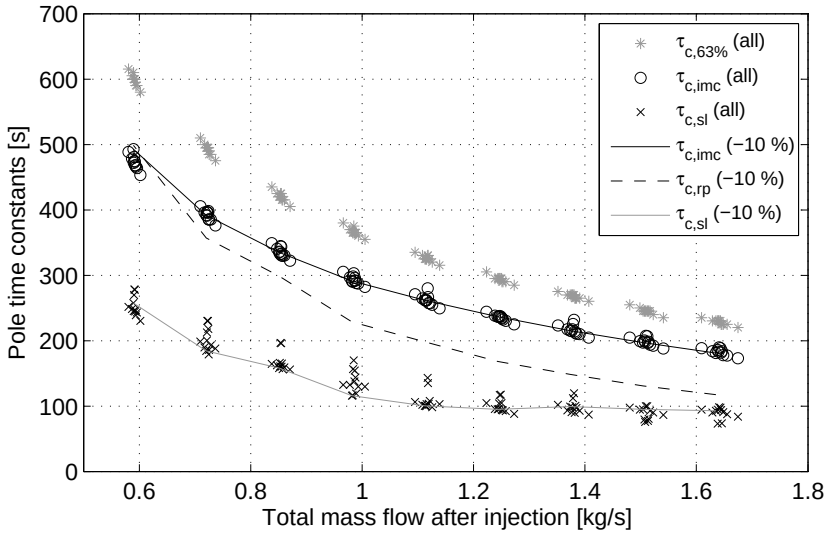

Figure 3.15: Characteristic time constants of the identified LTI models for superheater injection mass flow to outlet temperature.

The analysis is continued for the zeros of the models. Figure 3.16 shows the identified time constant τ_{z1} (left) and damping δ_{z1} (right) for the same LTI models as above, but for the numerator polynomial of equation (3.26). Again, the parameters are scattered and, due to the numerical regression, for one share of variation there is no unambiguous trend visible. The zero damping gets negative for all loads with only some exceptions with small variation share (e.g. -2 %). Thus, most of the systems are non-minimum phase, although this characteristic is not very dominant. Their values are close to zero, which indicates that the zeros are close to the imaginary axis and might lead to oscillations. This has to be considered during the controller design and results in a reduction of performance.

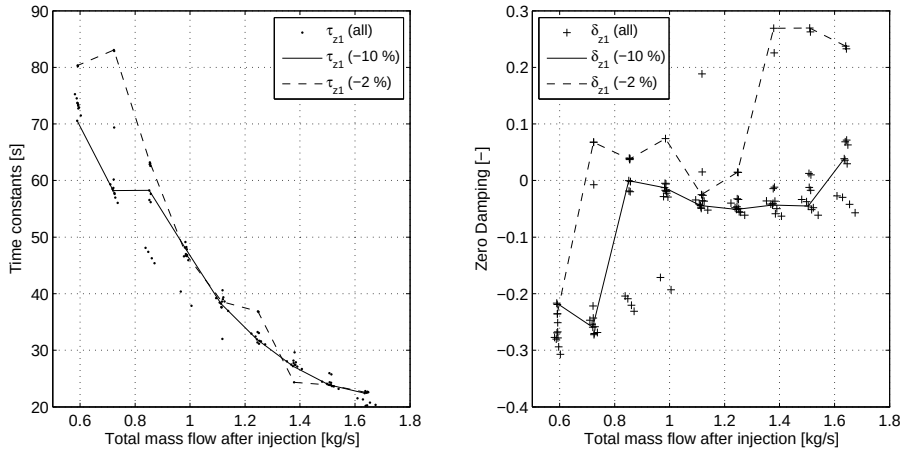

Figure 3.16: Zero time constants (left) and zero damping (right) of the identified LTI models for injection mass flow to outlet temperature.

Process gain

Another important parameter is the process gain k_p of the system. Figure 3.17 (left) shows the gain dependent on the injection mass flow variation. The gain changes almost linearly around the operating point. Normal LTI models, however, would lead to constant gains at the same operating point. Thus, another non-linearity of the system is thereby shown. At a variation of 50 % of the injection mass flow, the gain varies about ±4 %. Again, a very good characteristic is achieved, if the gain is plotted over the total mass flow after injection (Figure 3.17 right).

Conclusions

A step response of the discretized simulation and the LTI model is depicted in Figure 3.18. The model fitted to the detailed simulation has an almost identical response. The LTI model for a different load case, simulated with the same absolute deviation as the other model, is similar in the first reaction, but reaches a different final value. This behavior was expected from the former analysis due to the non-linear gain characteristic. Note that the analytical models assume a linear behavior, which is only valid in a very small range.

The LTI models can be characterized by the relative shape of the step response and by the scaling of this response to a defined final value. The latter scaling is done by the process gain. In consequence, the gain characteristic versus mass flow (Figure 3.17, right) can in principle be used for a correction of the characteristic shape of one operating point. Such models with a non-linear (steady-state) pre-scaling of a transient LTI response are called Hammerstein models [101]. The controller design presented here does not explicitly use this kind of models, but they can be helpful for the implementation of model predictive controllers for non-linear systems [260].

Drawing a conclusion, the superheating injection system is non-linear and non-minimum phase, but the gain can be approximated well as a function of overall mass flow. The main characteristic time constants such as $\tau_{c,imc}$ also show a good clustering around their approximation dependent on the overall mass flow or operating point, respectively. However, the numerically identified model parameters are not suited for simple approximation by a function of the mass flow.

The same analyses are performed for the other desired transfer functions in the following sections.

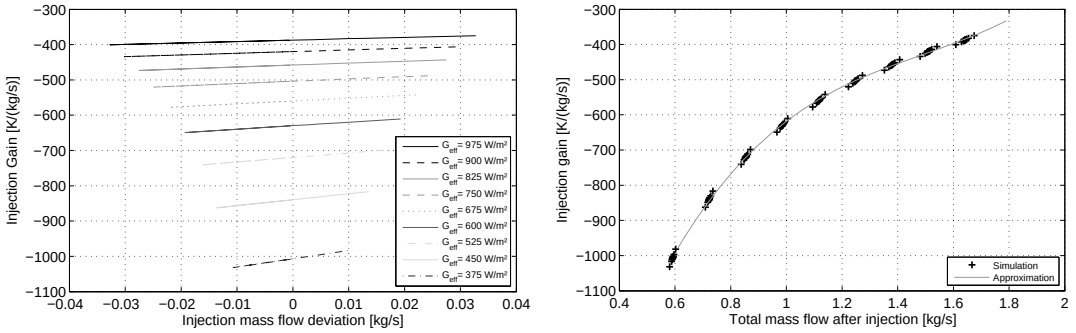

Figure 3.17: Process gain of the identified LTI models for injection mass flow to outlet temperature; left: versus injection mass flow variation; right: vs. total mass flow after injection.

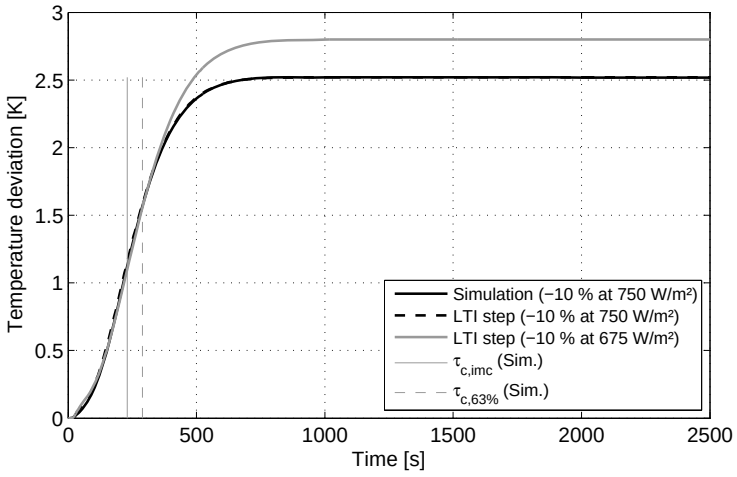

Figure 3.18: Step responses of outlet temperature by change in superheating injection mass flow simulated with the discretized model and two different LTI models for the same absolute variation (in kg/s).

3.4.2 Evaporation injection mass flow to temperature before injection

For the basic control scheme, a transfer function from the evaporation injection before collector 6 to the temperature before the superheating injection (after collector 10) is needed. This temperature is denoted the "temperature before injection" $\vartheta_{\mathrm{befInj}}$, or the temperature before the SHI. From a control point of view, the temperature before the evaporation injection does not provide any information, because it usually remains constant at saturation temperature. This temperature is thus ignored and it is concentrated on the one before the superheating injection. Figure 3.19 provides an overview on the responses in the time domain.

Two LTI model structures are well suited for this transfer function. Both have four poles, but differ in the number of zeros, which is either one or three. The structure with four poles and three zeros is chosen here to be equivalent to

the outlet temperature in the next section as well. It has the following transfer function:

$$G_{\mathrm{mInj06-\vartheta befInj}} = k_{\mathrm{P}} \frac{(\tau_{z1}^2 s + 2\delta_{z1}\tau_{z1} s + 1)(\tau_{z2} s + 1)}{(\tau_1^2 s + 2\delta_1 \tau_1 s + 1)(\tau_2^2 s + 2\delta_2 \tau_2 s + 1)} \tag{3.31}$$

The models have been identified from 117 different step responses for the chosen structure.

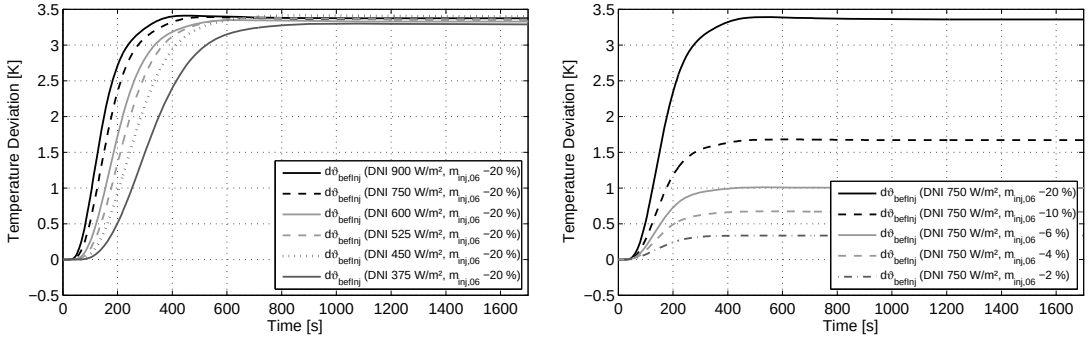

Figure 3.19: Step responses for evaporation injection mass flow to temperature before superheating injection simulated with the discretized model for different load situations (left) and injection variations (right).

The relation of gain and total mass flow after the evaporation injection is shown in Figure 3.20. The approximating linear regression has a standard deviation of 4.2 K/(kg/s). The reference mass flow is the total mass flow after the evaporation injection. The absolute values of the curve are about 20 % smaller compared to the ones of the superheating injection (compare Figure 3.17).

The typical pole-zero maps of the LTI models are shown in Figure 3.21. The two complex conjugate pole pairs are close to each other and nearly have the same damping. All the three zeros are in the RHP. The zero pair is close to the imaginary axis, while the real zero is far on the right. With reduced load, the zeros are put further to the right and the zero pair has a greater imaginary part.

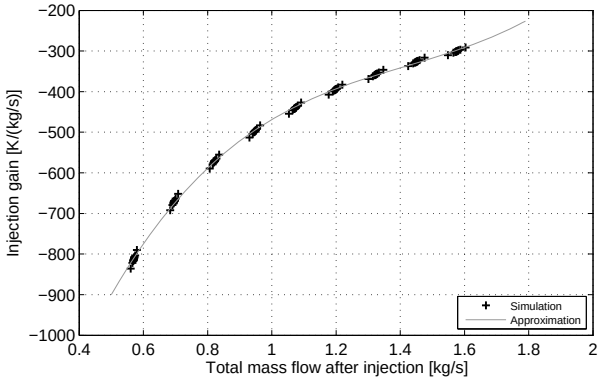

Figure 3.20: Process gain of the identified LTI models for evaporation injection mass flow to temperature before superheating injection.

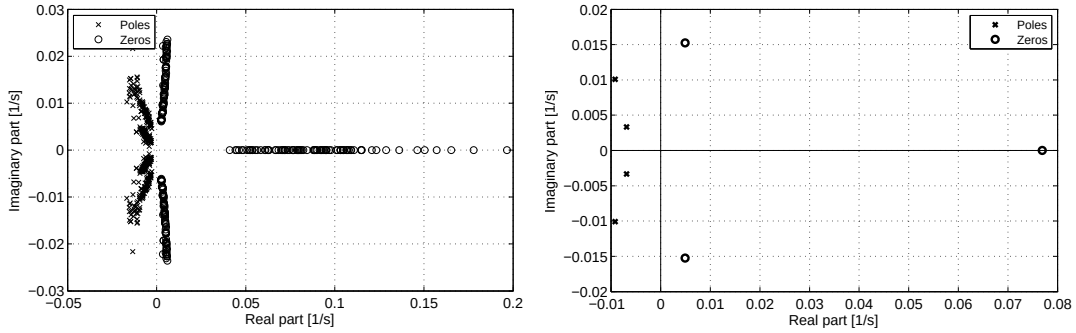

Figure 3.21: Pole-zero map of identified models from step responses of evaporation injection mass flow to temperature before injection at DISS facility; all models (left) and one for -20 % at 750 W/m² (right).

The poles can be analyzed again with the help of the characteristic time constants. With two complex conjugate poles one finds

$$\tau_{\mathrm{c,imc}} = 2\delta_1\tau_1 + 2\delta_2\tau_2$$

$$\tau_{\mathrm{c,rp}} = \frac{\tau_1}{\delta_1} + \frac{\tau_2}{\delta_2} \tag{3.32}$$

$$\tau_{\mathrm{c,sl}} = \max\left(\frac{\tau_1}{\delta_1}; \frac{\tau_2}{\delta_2}\right)$$

Figure 3.22 shows the resulting plot for both proposed model structures with one zero (left) or three zeros (right). The time constant $\tau_{\mathrm{c,63\%}}$ is clustered quite well around its linear regression curve. This number is directly derived from simulations with the discretized model. On the other hand, the approximation of $\tau_{\mathrm{c,imc}}$ has a different shape and clustering is broad. This is caused by a strong variation and uncertainty in LTI parameter identification. The model with three zeros shows a slightly smoother curve than the one-zero model. Other simple LTI structures lead to a similar or usually worse result. In consequence, these models must be treated with care during controller design and application. Also note that the IMC time constant is slower than the 63 % value for high loads and faster for low loads in the current case. This makes sense from a control point of view. The response at high loads can roughly be interpreted as a deadtime followed by a step. If the controller is too fast, the system will react harshly and oscillate. In consequence, a large IMC time constant needs to be chosen. When the response is smoothened, at lower loads in this case, it can be chosen more aggressively. This can be perfectly studied in Figure 3.22.

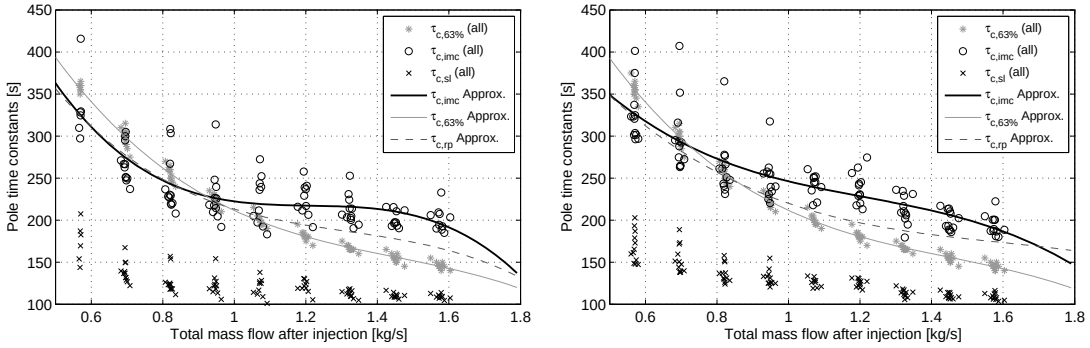

Figure 3.22: Characteristic time constants of the identified LTI models for evaporator injection mass flow to temperature before injection; LTI models with 4 poles and 1 (left) or 3 (right) zeros.

3.4.3 Evaporator injection mass flow to outlet temperature

Another option for control is to use only one injection in the evaporation section to control the loop outlet temperature. This concept will also be investigated in the control chapter. Thus, it is important to analyze its transfer behavior.

There is an additional delay caused by the distance from the superheating injection to the loop outlet compared to the transfer function analyzed in the former section (evaporator injection to temperature before SHI). This suggests introducing another zero to the transfer function. In fact, the least order for suitable model structures is four poles and two zeros. A slightly better approximation is achieved with four poles and three zeros. Therefore, the latter structure is chosen this time:

$$G_{\mathrm{mInj06-\vartheta out}} = k_{\mathrm{P}} \frac{(\tau_{z1}^2 s + 2\delta_{z1}\tau_{z1} s + 1)(\tau_{z2} s + 1)}{(\tau_1^2 s + 2\delta_1 \tau_1 s + 1)(\tau_2^2 s + 2\delta_2 \tau_2 s + 1)} \tag{3.33}$$

Again, the models have been identified from the 117 different step responses for the chosen structure. Figure 3.23 shows the typical shape of the step responses. These are very similar to the ones of the superheating injection to outlet temperature (compare Figure 3.12 on page 61). The response is now obviously slower or stretched in time, respectively. Note that the same variation at DNI levels 675 to 450 W/m² results in an almost identical temperature gain in Figure 3.23, left. This is due to the fact that the absolute nominal evaporation injection mass flow is constant for all loads in the shown simulations. The superheating injection mass flow varies with load (although it is held constant for step responses of the evaporation injector). Despite the non-linear gain character, the injection gain can be well approximated as a function of mass flow after the injection as shown in Figure 3.24.

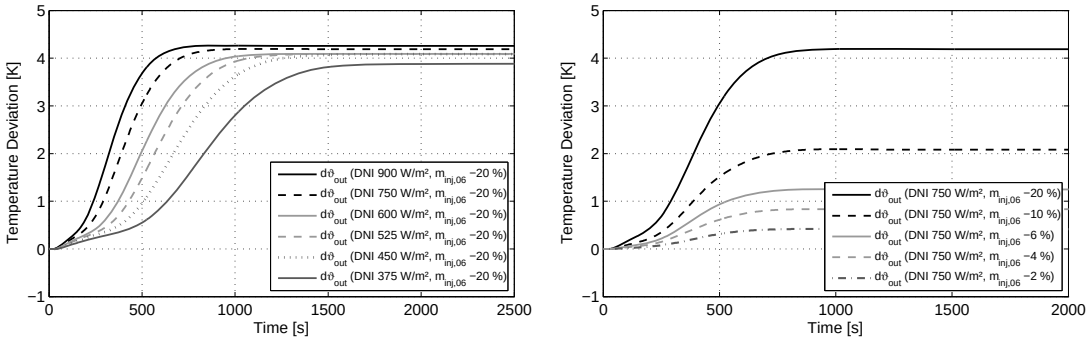

Figure 3.23: Step responses for evaporation injection mass flow to outlet temperature simulated with the discretized model for different load situations (left) and injection variations (right).

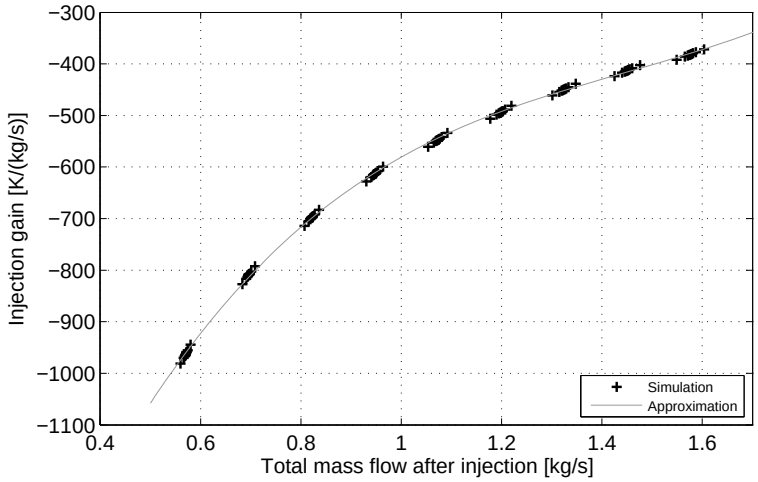

Figure 3.24: Process gain of the identified LTI models for evaporation injection mass flow to outlet temperature.

The pole-zero maps of the LTI models are illustrated in Figure 3.25. There are two complex conjugate poles close to each other with different damping. They are in the RHP very close to the imaginary axis and the single zero is also in the RHP. Thus, it is a very similar non-minimum phase situation to the one of the superheating injection to outlet temperature. This can also be seen on the characteristic time constant plot in Figure 3.26. The definitions are the same as for the transfer function with four poles in the above section. The increase in temperature response is rather slow due to the dominating thermal inertia effect. Thus, the IMC time constant is now continuously increasing and always smaller than the 63 % value. The IMC time constant rather corresponds to 35 % values and varies between 250 s and 670 s. The IMC time constants of the superheating injection to outlet temperature are in the range of 180 s to 500 s, which is about 25 % faster. Thus, a significant reduction in control performance can be expected, if only the injection in the evaporation section is applied.

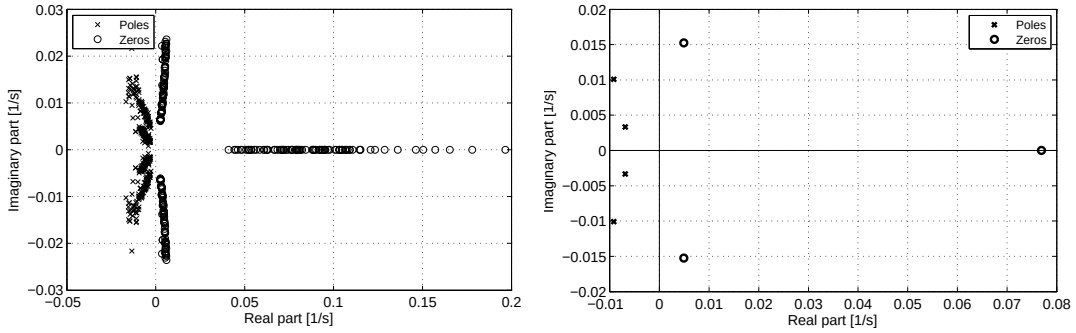

Figure 3.25: Pole-zero map of identified models from step responses of evaporation injection mass flow to outlet temperature at DISS facility; all models (left) and one for -20 % at 750 W/m² (right).

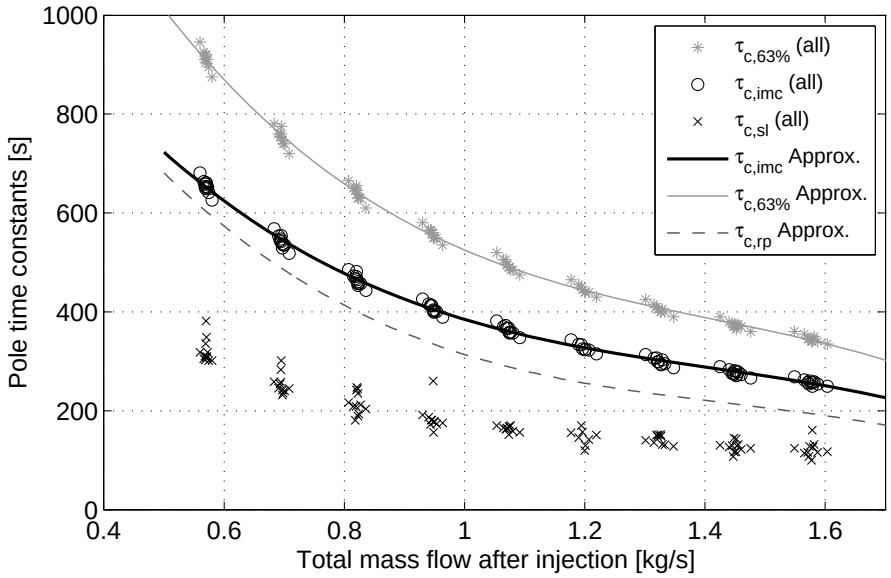

Figure 3.26: Characteristic time constants of the identified LTI models for evaporator injection mass flow to outlet temperature.

3.4.4 Inlet mass flow to temperature before injection

State-of-the-art control concepts foresee the control of the temperature before superheating injection (or outlet temperature) by the inlet mass flow. An LTI model for this path needs at least five poles. Models using two or four zeros are suitable. The structure with two zeros and a transfer function of the following form is selected:

$$G_{\mathrm{mIn-\vartheta befInj}} = k_{\mathrm{P}} \frac{(\tau_{z1}^2 s + 2\delta_{z1}\tau_{z1} s + 1)}{(\tau_1^2 s + 2\delta_1\tau_1 s + 1)(\tau_2^2 s + 2\delta_2\tau_2 s + 1)(\tau_3 s + 1)} \tag{3.34}$$

The models have been identified from 90 different step responses for the chosen structure. Figure 3.27 shows the typical shape of the step responses.

This transient path is significantly slower than the ones before. At 900 W/m², the final value is not reached before about 1000 s or about 20 min, respectively. At 375 W/m², the response takes about three times as long. One can also see the sensitivity of the temperature to a variation in inlet mass flow in Figure 3.27 right. 1 % influences the temperature by about 5 K. The absolute value of the gain is depicted in Figure 3.28 and is similar to those of the injectors. However, the approximation of the gain now has a very high standard deviation. Good agreement is only achieved for low shares of variation, while at high shares, the system cannot be considered to be working at the same operating conditions anymore. At the same mass flow, one finds deviations of 15 % or 75 K, respectively. This situation might be unacceptable, especially if the model is used for predictive controllers instead of only being used for controller design. A theoretical analysis of the gains reveals that the gain mainly depends on DNI linearly and on the square of the mass flow. As mass flow dependencies have already been considered here, it seems reasonable to scale the gain with the square root of the DNI or, more precisely, with the square root of the effective irradiation G_{eff}.

$$k_{\mathrm{P}}^{*} = \frac{k_{\mathrm{P}}}{\sqrt{G_{\mathrm{eff}}}} = k_{\mathrm{P}}^{*}(\dot{m}_{\mathrm{in}}) \tag{3.35}$$

This simple scaling provides a very convenient correlation as shown in Figure 3.29, left. When being rescaled, the operating characteristics for the inlet mass flow and effective irradiation as shown in Figure 3.29 right are achieved. Note that the latter data is the same as in Figure 3.28, but the suggested scaled approximation gives a variation of less than 1 % or 5 K, respectively, instead of 15 %.

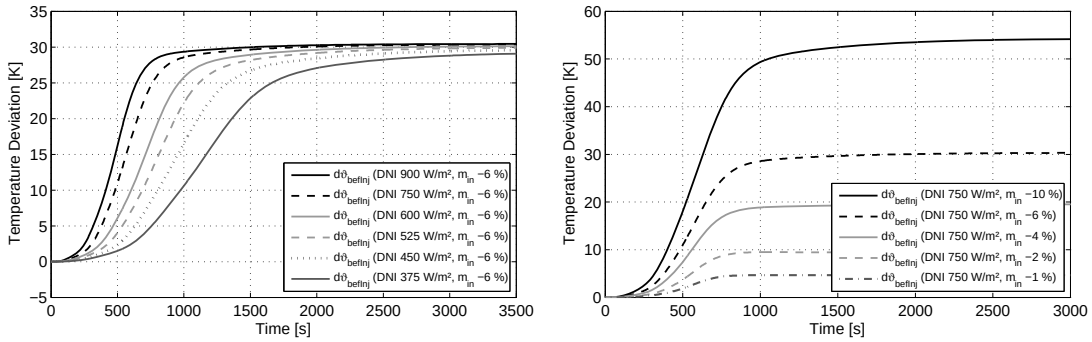

Figure 3.27: Step responses for inlet mass flow to temperature before injection simulated with the discretized model for different load situations (left) and variations (right).

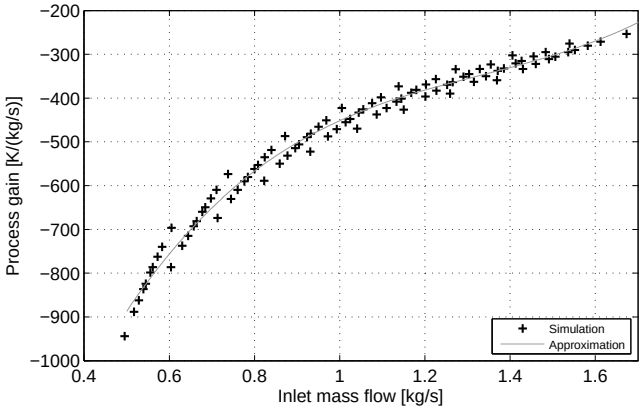

Figure 3.28: Process gain of the identified LTI models for inlet mass flow to temperature before injection.

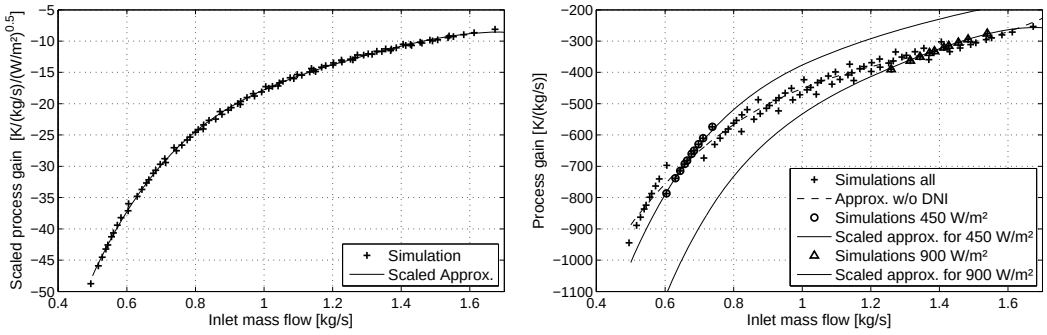

Figure 3.29: Process gain of the identified LTI models for inlet mass flow to temperature before injection; gain scaled by square root of DNI (left) and re-scaled correlation for different levels of DNI (right).

The pole-zero maps of the LTI models are depicted in Figure 3.30. Two pairs of complex conjugate poles are found together with a single, slightly faster pole. The complex conjugate zeros are in the RHP with some distance to the imaginary axis. Thus, again, it is a non-minimum phase system. Note that the slowest poles also have the least damping. This combination results in a small oscillation of the step responses around the final value, which is not that distinct in the responses simulated with the DFEM. They thus introduce a small identification error, which is negligible for the purposes of controller design here.

The time constant graph is shown in Figure 3.31. Due to the strong deviations from operating points, a broad clustering of the IMC time constants appears. The lack of accuracy is accepted and considered as additional uncertainty or robustness later. Otherwise, a scaling with DNI, as performed for the process gain, might lead to a better approximation. The IMC time constants are between the slowest mode and the 63 % times, close to the 35 % times. A typical step response is shown in Figure 3.32. With the LTI model being out of operating range, a rather large gain deviation between the two simplified step responses exists. This underlines the need for the scaled gain correction.

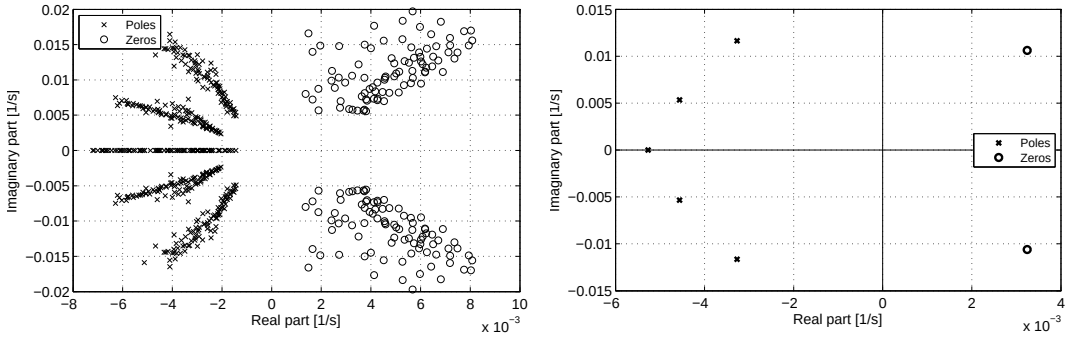

Figure 3.30: Pole-zero map of identified models from step responses of inlet mass flow to temperature before injection at DISS facility; all models (left) and one for +2 % at 750 W/m² (right).

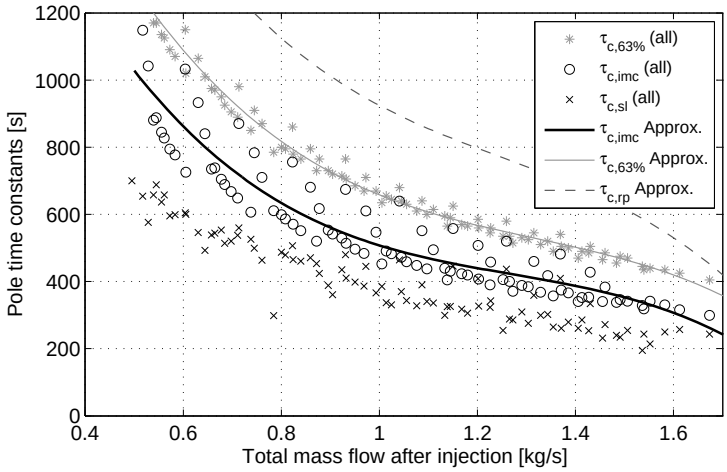

Figure 3.31: Characteristic time constants of the identified LTI models for inlet mass flow to temperature before injection.

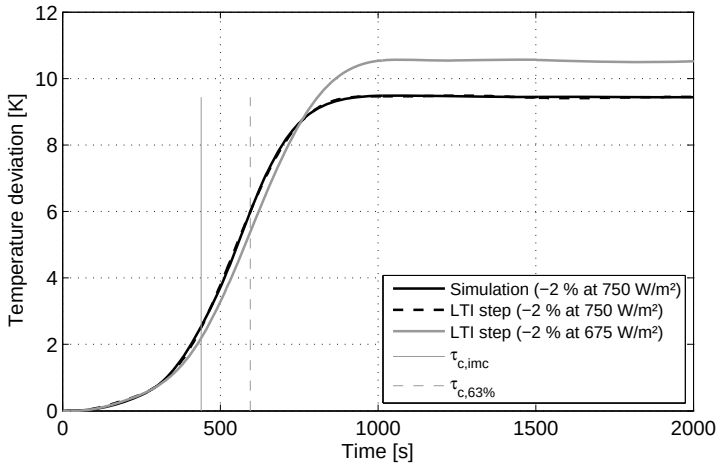

Figure 3.32: Step responses of temperature before injection by change in inlet mass flow simulated with the discretized model and two different LTI models for the same absolute variation (in kg/s; without scaled gain correction).

3.4.5 Inlet mass flow to outlet temperature

The original once-through concept envisaged the control of outlet temperature only by means of the inlet mass flow. This transfer path is now analyzed and it is shown why that concept is deemed to fail.

In fact, the characteristics are very similar to the one of the inlet mass flow to the temperature before the superheating injection. The transfer function is chosen to have the same LTI structure with five poles and two zeros:

$$\mathrm{G_{mIn-\vartheta out}} = k_\mathrm{P} \frac{(\tau_{z1}^2 s + 2\delta_{z1}\tau_{z1} s + 1)}{(\tau_1^2 s + 2\delta_1\tau_1 s + 1)(\tau_2^2 s + 2\delta_2\tau_2 s + 1)(\tau_3 s + 1)} \tag{3.36}$$

The same 90 response simulations as before are used for identification. Typical load and variation dependencies are shown in Figure 3.33. Final values are not reached before 10 min to 35 min. The IMC time constants are depicted in Figure 3.34. Again, the dependency on DNI level is not corrected, but taken as uncertainty. The time constants range from 400 s at high load to 1500 s at low load. In consequence, the reaction of the corresponding controller would be very slow. This is unacceptable for disturbance rejection. The IMC constants for controlling the earlier temperature before injection are in the range of 250 s to 1000 s. This is at least 35 % to 50 % faster and thus favorable. The IMC time constants for the evaporation injection to temperature before injection are much lower, in the range of 180 s to 360 s.

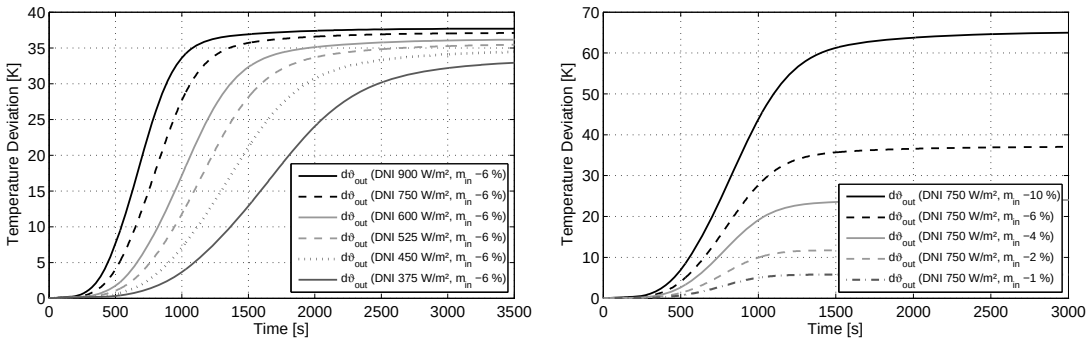

Figure 3.33: Step responses for inlet mass flow to outlet temperature simulated with the discretized model for different load situations (left) and mass flow variations (right).

The gain again significantly depends on the DNI level. This is considered by scaling it with the square root of the effective irradiation as formulated in equation (3.35). The results are given in Figure 3.35. Note that a better scaling for lower loads is achieved, when the irradiation is scaled by the exponent 0.4 instead of 0.5. For simplicity, and because the result is sufficient for the needs of this work, the exponent of 0.5 is maintained here. A typical step response and a deviation from operating point are provided in Figure 3.36.

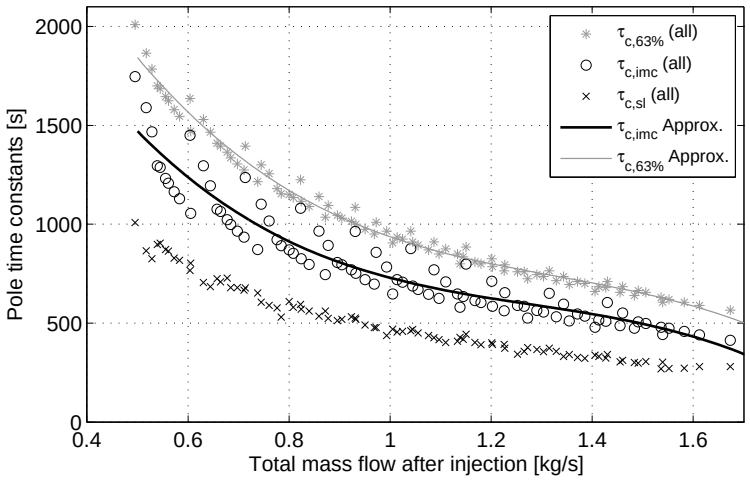

Figure 3.34: Characteristic time constants of the identified LTI models for inlet mass flow to outlet temperature.

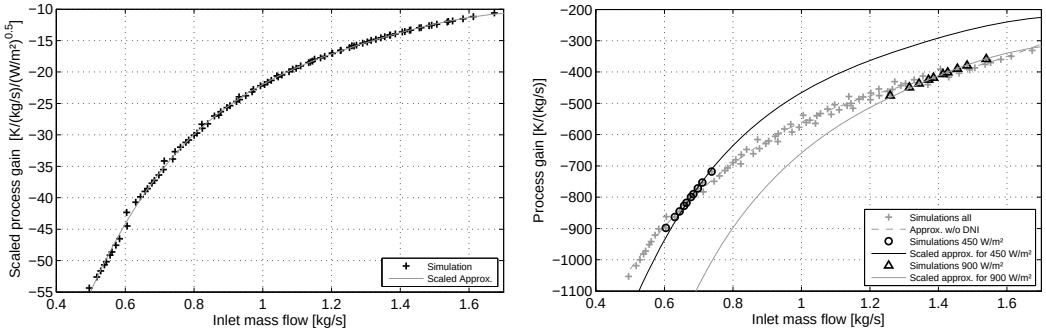

Figure 3.35: Process gain of the identified LTI models for inlet mass flow to outlet temperature; gain scaled by square root of DNI (left) and re-scaled correlation for different levels of DNI (right).

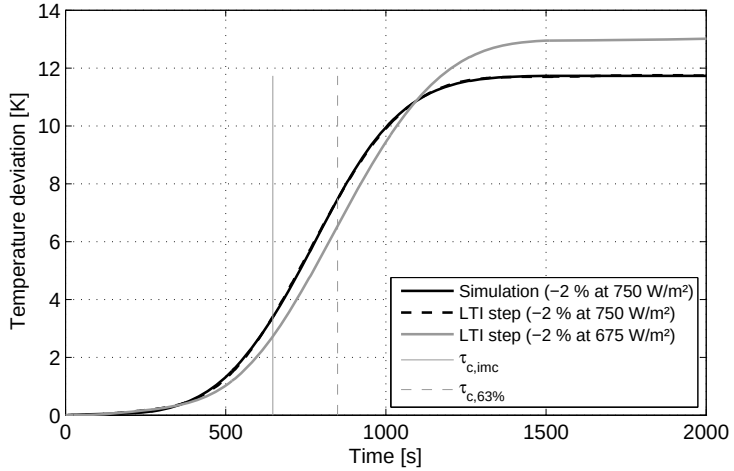

Figure 3.36: Step responses of outlet temperature by change in inlet mass flow simulated with the discretized model and two different LTI models for the same absolute variation (in kg/s; without DNI-scaled gain correction).

3.4.6 DNI to superheating temperatures

The previous sections analyze the control path transfer functions. The following sections focus on the transient disturbance behavior. As the effective irradiation is the main energy resource of a solar thermal power plant, it suggests itself to begin with a disturbance of DNI. Note again that DNI is used in this chapter as a synonym for effective irradiation. All DNI disturbances are assumed to be the same along the complete loop. For the sake of brevity, the main temperatures of interest are covered together, namely the outlet temperature and the temperature before the SHI. 90 different step responses are simulated. The responses for -10 % are not used for identification of the temperature before the SHI, because it falls to saturation level at such uncontrolled disturbances. The model structure chosen for both temperatures is five poles and four zeros:

$$G_{\mathrm{DNI-\vartheta out}} = k_{\mathrm{P}} \frac{(\tau_{z1}^2 s + 2\delta_{z1}\tau_{z1} s + 1)(\tau_{z2}^2 s + 2\delta_{z2}\tau_{z2} s + 1)}{(\tau_1^2 s + 2\delta_1\tau_1 s + 1)(\tau_2^2 s + 2\delta_2\tau_2 s + 1)(\tau_3 s + 1)} \tag{3.37}$$

Figure 3.37 shows step responses of both temperatures. The temperature before injection decreases about 20 % faster than the outlet temperature. The superheating section provides a small buffer because of the thermal inertia of the crossover piping. The temperature before injection has less inertia and thus decreases much faster.

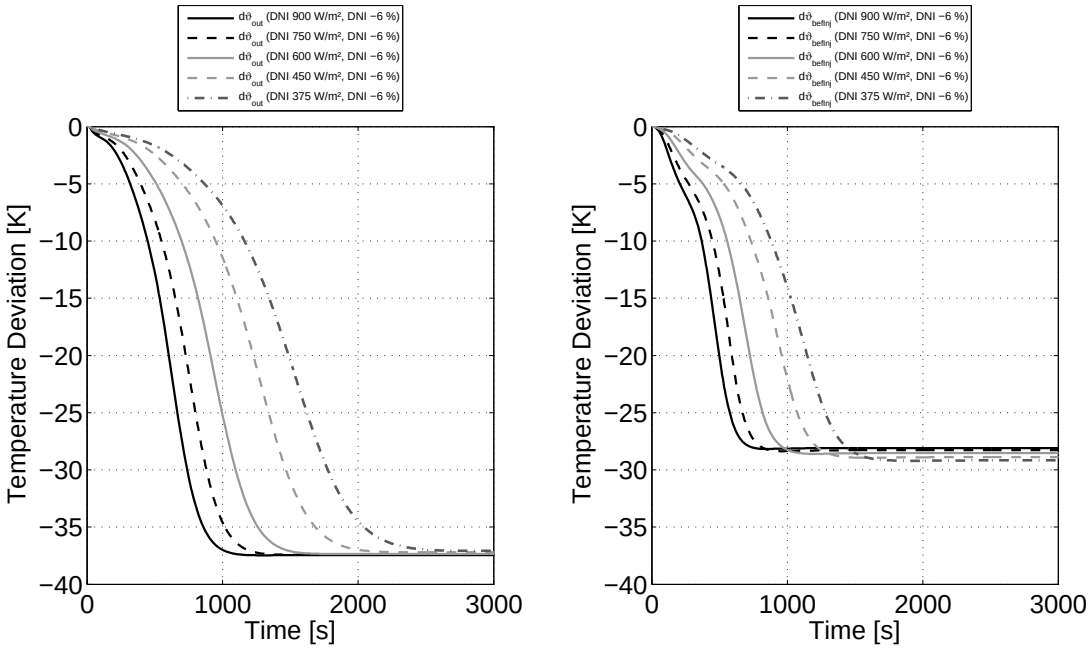

Figure 3.37: Step responses by change in effective irradiation simulated with the discretized model for different load situations; to outlet temperature (left) and to temperature before injection (right).

Figure 3.38 illustrates the resulting pole-zero maps of the identified LTI models for the outlet temperature. The structural appearance is the same as for other temperatures. Poles and zeros are nearly mirrored by the imaginary axis, being pushed closer together for lower DNI levels and further away for higher DNI levels.

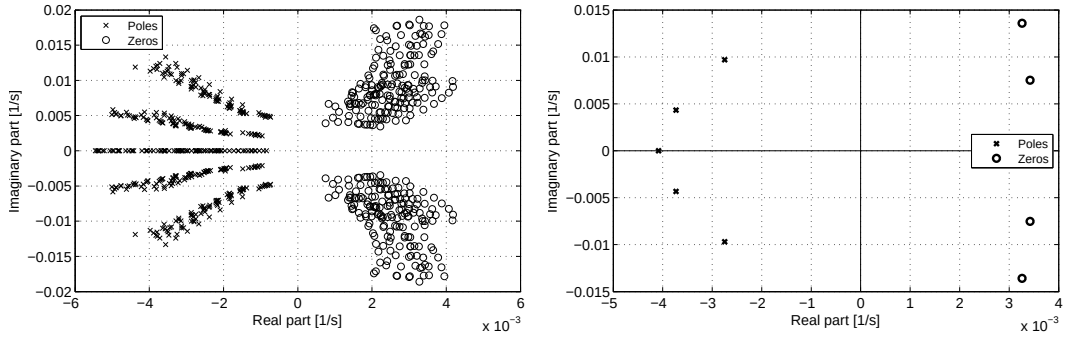

Figure 3.38: Pole-zero map of identified models from step responses of effective irradiation to outlet temperature at the DISS facility; all models (left) and one for -6 % at 750 W/m² (right).

Figure 3.39 left depicts the process gain as a function of DNI level. As the mass flow is kept constant during the step responses, there are characteristic lines in the graph. A pure approximation of the gain by DNI corresponds to the design curve, but can lead to significantly misleading results during transient situations. It is thus recommended to calculate the characteristic field of the gain in advance by detailed steady-state energy balances. For the assumption of constant inlet conditions, the energy balances can be reformulated to give the characteristic lines:

$$k_{\mathrm{P,DNI-\vartheta out}} = \frac{\vartheta_{\mathrm{out},1} - \vartheta_{\mathrm{out},0}}{G_{\mathrm{eff},1} - G_{\mathrm{eff},0}}$$
$$\text{with } \frac{\dot{m}_{\mathrm{out}}\left(c_{p,\mathrm{out},1}\vartheta_{\mathrm{out},1} - c_{p,\mathrm{out},0}\vartheta_{\mathrm{out},0}\right)}{\eta_{\mathrm{th},1}G_{\mathrm{eff},1} - \eta_{\mathrm{th},0}G_{\mathrm{eff},0}} = 1 \tag{3.38}$$

Indices 0 and 1 indicate different steady-state conditions. The gain is very sensitive to heat capacity c_p and overall thermal loop efficiency η_{th}, that will be different for each operating point. Thus, care must be taken when a simple theoretical approximation shall be used to identify operating points off the design curve. It may lead to a significant deviation of up to about 30 %, a problem from which the analytical models suffer as well. Thus, it is suggested to solve the steady-state energy balances, determine the gain for some points in a small range and then find a scaling factor that meets the shape of Figure 3.39 (right). The gain itself is not scaled, but the variable of the gain function with the following dependency:

$$k_{\mathrm{P,DNI-\vartheta out}} = k_{\mathrm{P}} \left(\frac{G_{\mathrm{eff}}}{\dot{m}_{\mathrm{out}}^{e_{\mathrm{sc}}}} \right) \tag{3.39}$$

The scaling exponent e_{sc} that fits the loop is 2.6 for the outlet temperature in this case. The scaling exponent is particular for each plant and temperature location because of different shares of superheating/evaporation lengths, temperatures and pressures. The scaling exponent for the temperature before injection is determined to be 2.2 and the mass flow is the one before the superheating injection. The high loads are found in the lower left corner of Figure 3.39 (right) and uncertainties increase with lower loads. This is obvious as the temperature profile and heat transfer along the loop change significantly for low loads. If the equation is rescaled to the original chart, as shown in Figure 3.40, the approximation is able to meet the gains dependent on DNI and mass flow very well. Deviations in a real plant will occur, if the mass flows are balanced differently than foreseen in the design. Nevertheless, it will remain a good guess, much better than a misleading linear scaling. Note that the characteristic mass flow line is limited on the left by saturation. If DNI decreases further at some point, the water will not be superheated anymore and the definition of temperature gain will become meaningless. If such a high variation is to be considered, the enthalpy gain must be chosen accordingly. The gains of outlet temperature are greater than the ones for the temperature before injection, because it is directly correlated to the total aperture width of the system.

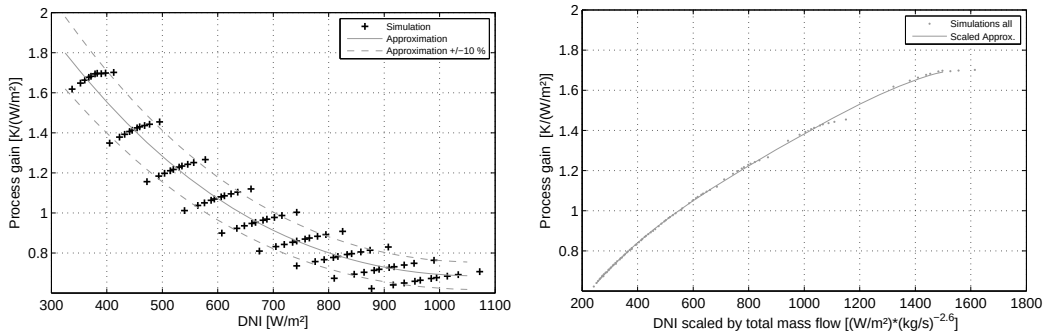

Figure 3.39: Process gain of the identified LTI models for effective irradiation to outlet temperature; gain dependency on DNI (left) and scaled variable (right).

Figure 3.41 depicts the characteristic time constant plots. Again there is a dependency not only on DNI, but also on mass flow. A similar scaling as for the gain is possible, but not performed here. The characteristic response time is slightly longer when irradiation increases than when irradiation decreases. However, when looking at Figure 3.42, LTI models for DNI increase and decrease are almost identical for the first 600 s. Requirements for effective disturbance rejection are therefore very similar for both cases. If the controller

shall be designed for irradiation step rejections, one can conclude that considering irradiation decreases is sufficient to also handle irradiation step increases.

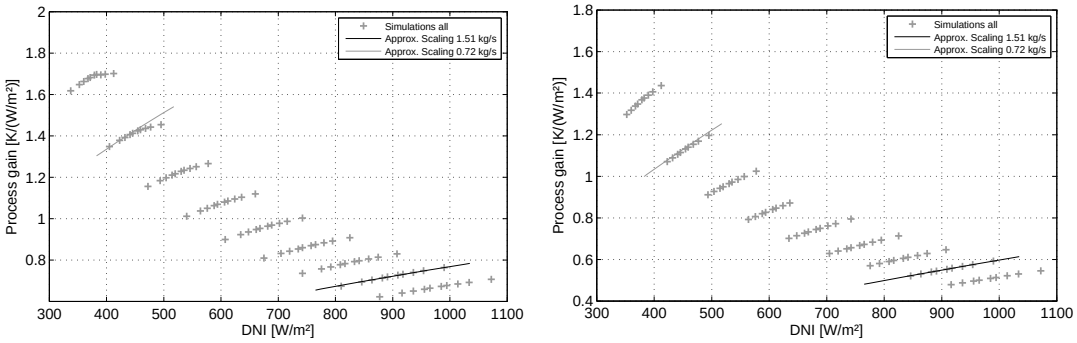

Figure 3.40: Process gain of the identified LTI models for effective irradiation with characteristic lines of scaling approximation for outlet temperature (left) and temperature before injection (right).

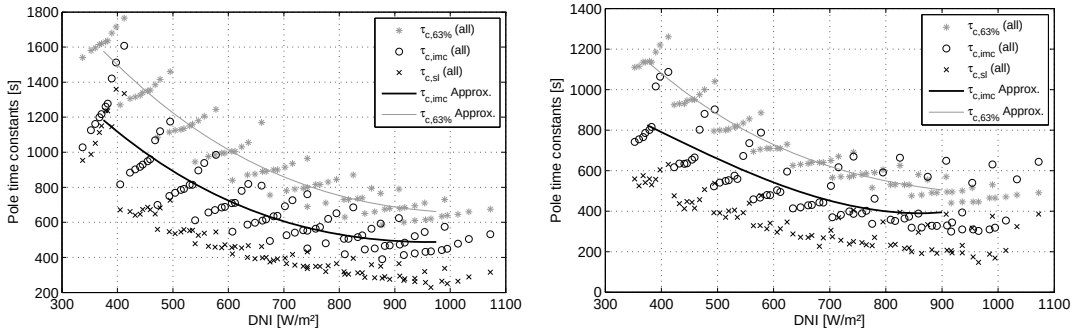

Figure 3.41: Characteristic time constants of the identified LTI models for effective irradiation to outlet temperature (left) and temperature before injection (right).

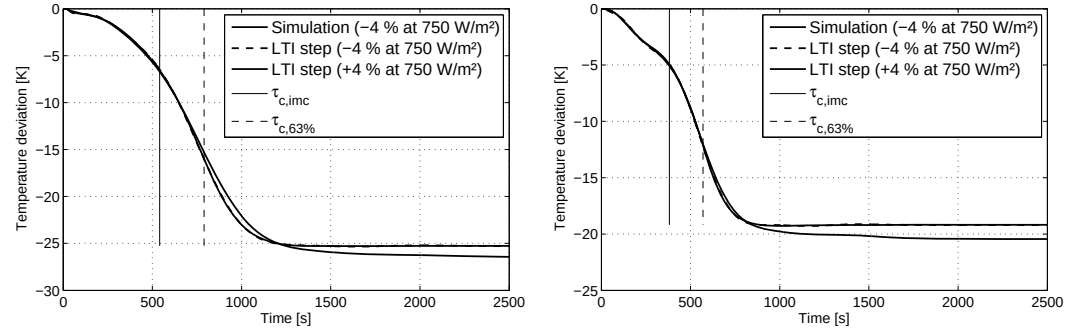

Figure 3.42: Step responses of outlet temperature (left) and temperature before injection (right) by change in effective irradiation simulated with the discretized model and two different LTI models for the same absolute variation (in W/m²; without scaled gain correction).

3.4.7 Inlet temperature to superheating temperatures

The inlet temperature can cause severe disturbances in once-through mode. As shown in the experimental validation section above, this is caused by the twofold dynamics of the system. A first short-term density disturbance is followed by an enthalpy response at the velocity of throughput time. A decrease of temperature thus leads at first to an increase in outlet temperature and, only after that, to a drop in temperature to its new lower steady-state value. This behavior is shown for an inlet temperature reduction of 10 K at different loads in Figure 3.43. The initial inlet temperature is always 260°C. The graph on the right shows the behavior of the temperature before the injection. There is a higher peak with lower loads, while the final values are nearly the same. The graph on the left shows the outlet temperature, which reacts more slowly because of the additional damping of the pipes. The latter is also the reason why no significant change with load is visible. The non-minimum phase peak has a temperature variation of 30 K to 40 K, while the disturbance is only 10 K at the inlet. There is a leverage factor of 3 to 4 for this disturbance. This leverage factor reduces with higher disturbances, but is even higher for lower disturbances. For a disturbance of 5 K at the inlet, the leverage factor can reach up to 5, i.e. about 25 K peak increase in temperature before injection. A moderate example for 900 W/m² is illustrated in Figure 3.44. The peak has only a very small phase shift at constant load, which is favorable for the LTI models and their scaling.

The model structure chosen to meet the transient behavior is seven poles and six zeros for the outlet temperature. For the temperature before injection, a structure of 8 poles and seven zeros is identified, which is not significantly better for the outlet temperature. Note that the DFEM simulations for identification purposes can be considered as worst case estimations, since the experimental validation has shown that the DFEM reacts slightly faster and with a slightly higher gain than the real plant. The resulting LTI models are not directly used for controller design, but are meant as disturbance models. Less detail is therefore provided here.

However, the pole-zero maps in Figure 3.45 reveal a dominating single zero far on the right of the right half plane. This zero causes the strong counterreaction at the beginning of the disturbance. All the zeros and poles are shifted further to the imaginary axis with lower loads. The same holds for lower gradients of the inlet temperature change.

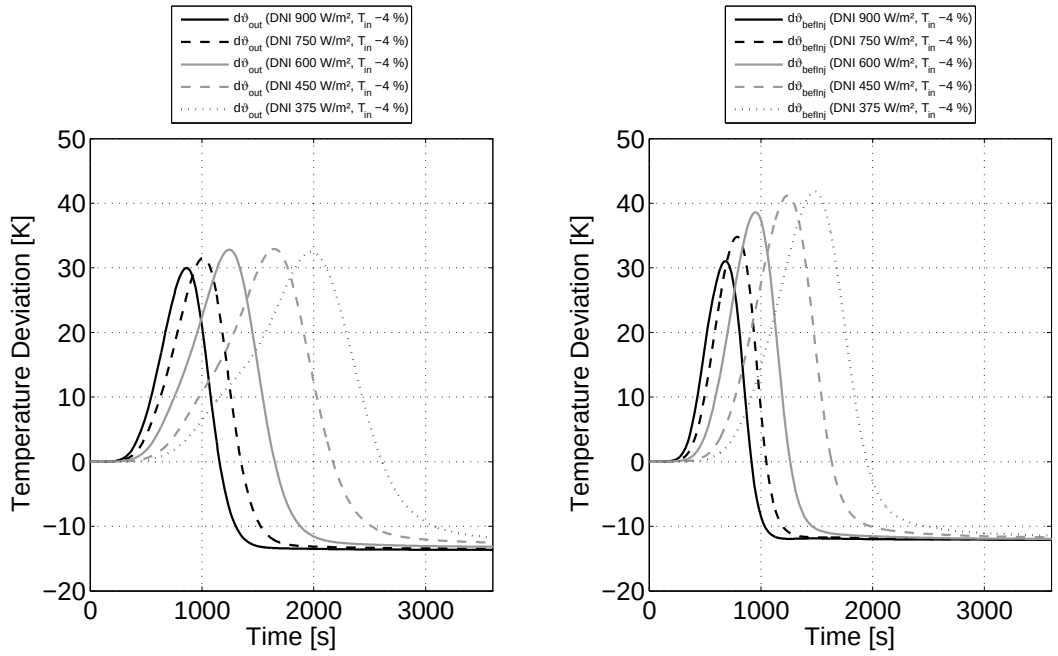

Figure 3.43: Step responses by change in inlet temperature by 10 K simulated with the discretized model for different load situations; to outlet temperature (left) and to temperature before injection (right).

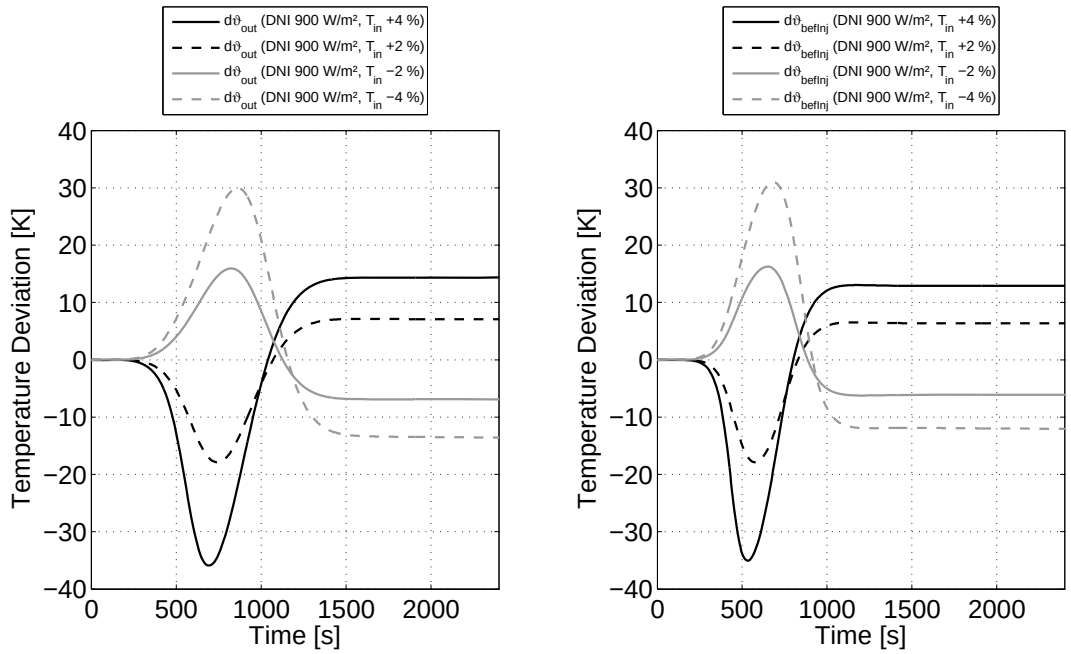

Figure 3.44: Step responses by change in inlet temperature by 5 K and 10 K simulated with the discretized model; to outlet temperature (left) and to temperature before injection (right); initial inlet temperature of 260°C.

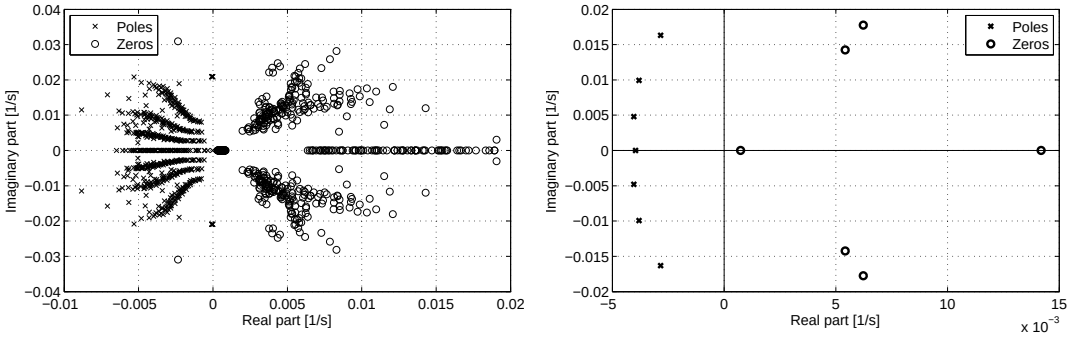

Figure 3.45: Pole-zero map of identified models from step responses of inlet temperature to outlet temperature at DISS facility for different load situations; all models (left) and one for -5 K at 900 W/m² (right).

3.4.8 Collector-wise focusing to superheating temperatures

The heat input to the solar field can be variable in location. For example, most collectors of a loop are in focus, while one collector is defocused. A similar situation occurs if only a small part of the collector field is shadowed, while the rest is under clear sky conditions. The transient behavior during and after these disturbances is particularly interesting for a once-through solar boiler. These disturbances are summarized by the terms local energy disturbance, focus disturbance or local irradiation disturbance, respectively. Local energy disturbances near the inlet of the loop cause density disturbances similar to those of the inlet temperature (see LTI models above and experimental validation section). If the disturbance is further downstream, i.e. it happens in a part of the loop closer to the outlet, the density and non-minimum phase effect is smaller. In the superheating section, it is no longer dominating. Figure 3.46 illustrates this separately for the 100 m and 50 m evaporation collectors of the DISS facility. Note that according to experimental data, the peak of the first counter-reaction might be underestimated by the simulation for some collectors in the middle of the loop.

The transient behavior not only varies with location, but also with load and intensity of variation. The load dependency is shown in Figure 3.47. The left graph shows the outlet temperature, which is significantly influenced by the long crossover piping. Thus, in a commercial plant, the transient response would rather be similar to the reaction of the temperature before injection (right graph).

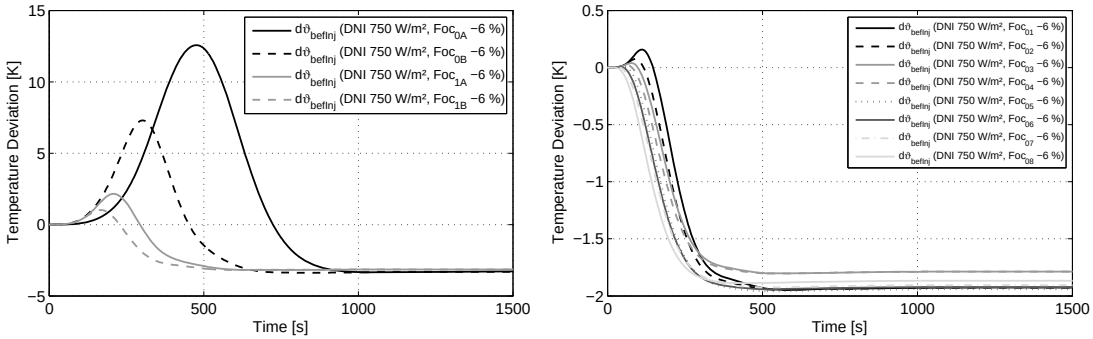

Figure 3.46: Step responses by change in collectors' focus/energy input to temperature before injection simulated with the discretized model for the DISS facility; first 100 m collectors (left) and following 50 m collectors (right).

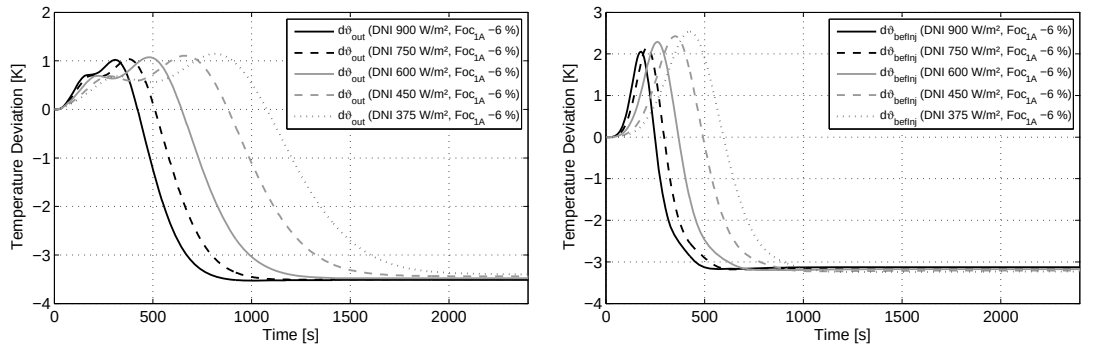

Figure 3.47: Step responses by change in collectors' focus/energy input simulated with the discretized model for collector 1A at different loads; to outlet temperature (left) and to temperature before injection (right).

Figure 3.48 depicts the reaction to an energy loss in the last 100 meters of collector of the DISS facility (collector 12). There is no counter-reaction and the final value is rapidly approached. The graph on the right illustrates that the gain is almost constant for small and large deviations, which is a good approximation for all (constant) loads.

The described transient behavior is transferred into LTI models, for which an overall of 1260 step responses are analyzed. Models of -6 % are used as LTI reference models. Their structures depend on collector location and temperature and are listed in Table 3.4. As they are not directly needed for controller design, further details are omitted here. A joint defocusing of all collectors results in a transient behavior very similar to the one of a DNI disturbance on the complete loop (as described in detail above).

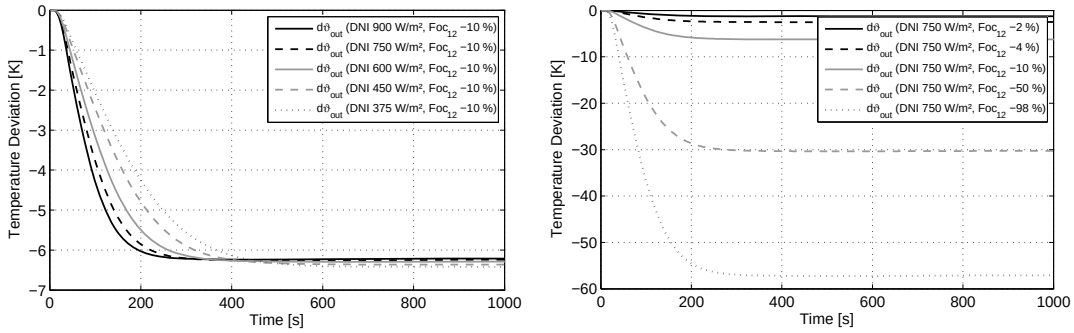

Figure 3.48: Step responses by change in collectors' focus/energy input simulated with the discretized model for collector 12 at different loads (left) and for various change variations (right).

Table 3.4: LTI model structures for collector-wise focusing and de-focusing or energy input disturbances, respectively.

Collector	*Outlet temperature: poles/zeros*	*Temperature before injection: poles/zeros*
0A	7/3	7/3
0B	7/3	7/3
1A	6/3	6/3
1B	5/3	5/3
1	4/3	4/3
2	4/3	4/3
3	4/3	4/3
4	4/3	4/3
5	4/3	4/3
6	4/3	4/3
7	4/3	4/3
8	4/3	4/3
9	4/2	3/2
10	4/2	3/2
11	4/2	-
12	3/2	-

3.4.9 Injection water temperature to superheating temperatures

Another disturbance to the loop is the change in injection water temperature. This change is usually caused by a change in inlet temperature or, more precisely, by a change in the temperature after the feed water pump. All water

mass flows are fed by the same line and the water temperatures at the loop entry only differ because of other insulation and piping characteristics.

Figure 3.49 shows the influence of the water temperature at the injection before collector 6. For brevity, it is denoted injection 6. The gain of its transfer function is about 0.05, i.e. 20 K change in water temperature result in a 1 K change in superheating temperature. Strictly speaking, the gain depends on the relation between enthalpy flows of the fluid in the main line and the injected water as well as on the heat capacity of the steam at the outlet. The speed of the transfer function depends again on the load as shown in Figure 3.50.

It is interesting to compare the transfer functions of the temperature before the SHI for changes of injection water temperature (Figure 3.50 right) and for changes of the injection mass flow (Figure 3.19 left on page 68). The shape of the transfer function is nearly identical. If no other way for identification is available, the same parameters can be chosen and only the gain needs to be adapted. The gain can be calculated from steady-state energy balances.

The same holds for injection 11. Figure 3.51 illustrates the dependency on load and variation share to outlet temperature.

The LTI model structures are chosen as follows: four poles and three zeros are used for the injection water temperature to outlet temperature for both injections. Four poles and two zeros are chosen for the transfer function from the evaporation injection to the temperature before the superheating injection. They are considered for disturbance estimation.

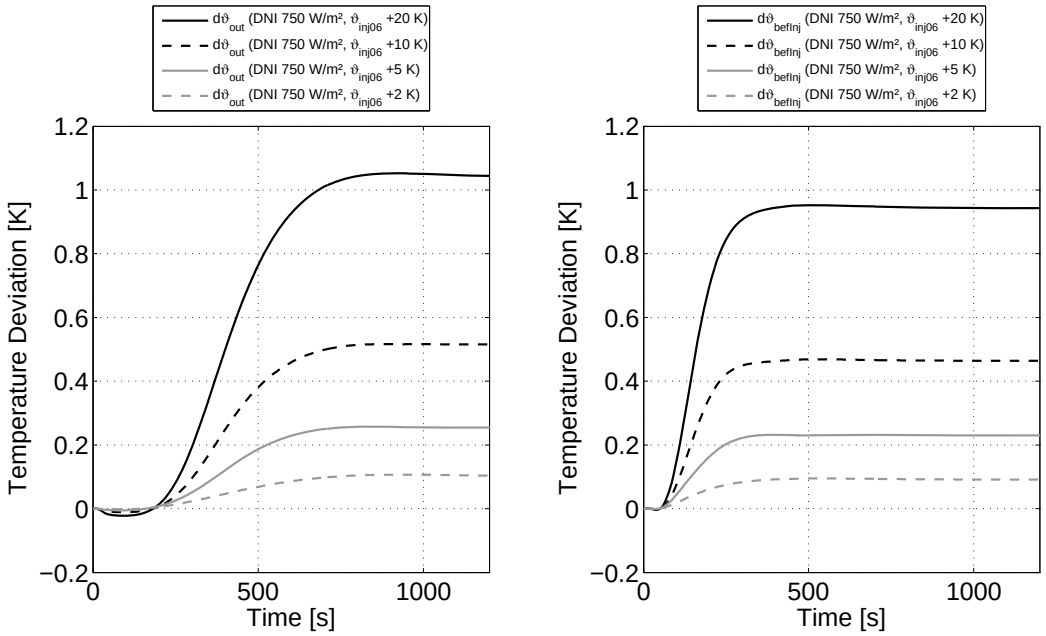

Figure 3.49: Step responses by change in water temperature at injection before collector 6 simulated with the discretized model for different variations; to outlet temperature (left) and to temperature before superheating injection (right).

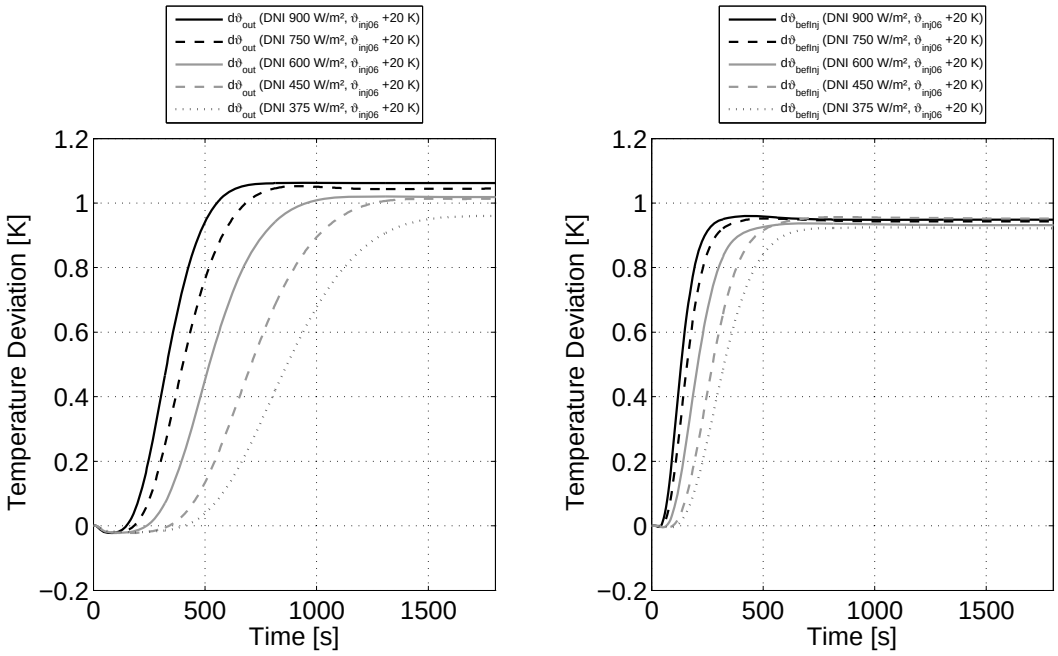

Figure 3.50: Step responses by change in water temperature at injection before collector 6 simulated with the discretized model for different loads; to outlet temperature (left) and to temperature before superheating injection (right).

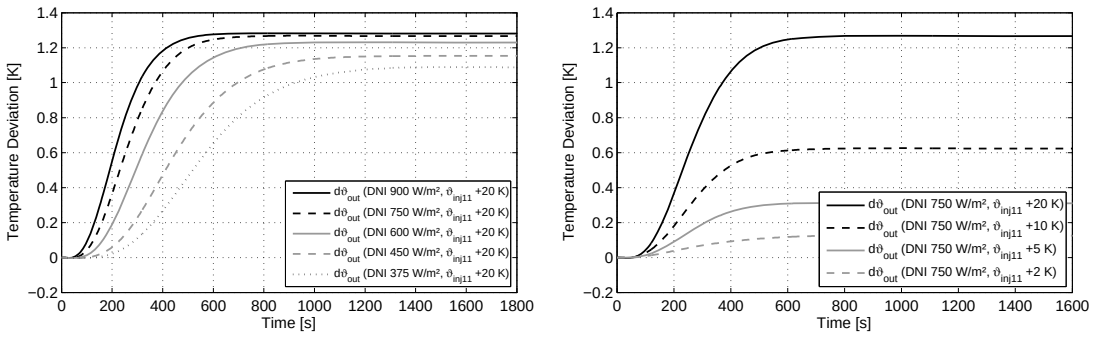

Figure 3.51: Step responses by change in water temperature at injection before collector 11 simulated with the discretized model at different loads (left) and for change variations (right).

3.4.10 Summary of LTI models

The prior sections describe the typical shapes and characteristics of the most important transfer functions of a once-through solar field. Those transfer functions are used for controller design in the next chapter. They are also needed in the time domain for the application in a model predictive control (MPC) scheme. For design and MPC, it is advantageous to have a good estimation of the transient shape without using deadtime elements. Thus, the earlier approach in [253, 254] with first or second order models including deadtime is not recommended. Such simplified approaches are too rough for an accurate

controller design. The LTI models identified in the previous sections therefore use higher order transfer functions without deadtime.

The identification of the transfer functions is based on simulations by the DFEM and not on analytical approaches. This is because current analytical models do not cover the complete range of preheating, evaporation and superheating. Analytical models for superheaters are of very high orders to cope with commercial scale loops. Analytical models for the evaporation section are not (numerically) stable in the time domain because of the stiffness of the system.

Each identified transfer function is described by a fixed model structure. These structures are summarized in Table 3.5. The parameters strongly depend on the load, as the system gets slower with lower mass flows. Due to the nonlinearity of the system, the variation share or intensity, respectively, also changes the parameters and the gain of the transfer function. For a first guess, a typical model of the various variation shares is also given in the table. These typical representatives are used for controller design and predictive control implementations. The other models are considered as uncertainty and for stability analysis. The validation of the models is omitted here as they fit very well with the DFEM, which in turn has already been validated with experimental data. The goal of deriving stable, low order time domain transfer functions for the complete loop is achieved for all necessary dependencies.

Table 3.5: Identified LTI model structures for the DISS test facility; values in brackets indicate the particular LTI model identified as typical/representative for all LTI models of the same relation.

Input	*Outlet temperature: poles/zeros (variation of typical model)*	*Temperature before superheater injection: poles/zeros (variation of typical model)*
Inlet mass flow	5/2 (+2 %)	5/2 (+2 %)
Injection 11 mass flow	3/2 (-10 %)	-
Injection 6 mass flow	4/3 (-20 %)	4/1 (-20 %)
DNI (on complete loop)	5/4 (-6 %)	5/4 (-4 %)
Inlet temperature	7/6 (+5 K)	8/7 (+5 K)
Inj. 11 water temperature	4/3 (+10 K)	-
Inj. 6 water temperature	4/3 (+10 K)	4/2 (+10 K)

3.5 Comparison of modeling approaches

The current chapter describes various model approaches for once-through line focus solar fields. A good model is the foundation for optimal control and a meaningful system characterization. It is also a trade-off between accuracy and computational as well as modeling effort. Each model described above has its justification and application area in this sense.

The discretized finite element model (DFEM) as developed in [105] allows a very deep insight into the system behavior. It is also able to analyze the distributed character of the system. This is especially true for irradiation/focus disturbances that occur only on a small part of the loop. Clouds seldom appear as a closed front over the complete loop, but are very often scattered throughout the collector field area. This can change the transient behavior significantly, as shown in sections 3.3 and 3.4.8. If the local energy disturbance is given as an input to the DFEM, it can reliably reproduce the transients with only small deviations. It is thus very well suited for system characterization as well as for plant representation during verification of control strategies.

The moving boundary model (MBM) approach, as extended for injections in this work, is also a very good system representation. Disturbances over the complete loop are reproduced very well with only minor deviations. The MBM is limited by the location of the boundaries of the end and beginning of evaporation. If there is two-phase flow at the outlet, additional MBM structures or state transition techniques must be applied, as has been demonstrated here. Care must be taken when interpreting the simulation for two cases. First, as typical for MBM approaches in general, the initial response to a fast input step can lead to non-physical counter-reactions (see Figure 3.9 on page 52). This non-minimum phase behavior is usually, however not always, due to modeling simplifications. Second, also as a matter of modeling, the lumped MBM cannot represent the distributed character of the system well. By the new implementation with two injections, this is somehow improved, because there are now five different sections instead of only three. Nevertheless, a collector-wise local resolution is not possible. This must be taken into account when applying the MBM in MPC schemes. Note however, that it might be possible to transform local disturbances (e.g. on collector 1) to inlet disturbances (e.g. to a certain sequence of inlet temperature trajectories) or to superpose the MBM with LTI models. Those are complex tasks and extremely increase the modeling effort. Furthermore, the locally resolved energy input is usually not available online (as of yet) during operation and only very rough estimations can be made. Therefore, such mixed modeling is not considered in this work, but is left for future improvements. Another important aspect of the MBM is its tuning. There are prefilters that must be parameterized to meet the delayed characteristics of the plant. An intuitive one is the deadtime of inlet enthalpy. If the measured inlet temperature

(from which enthalpy is calculated) is delayed by the throughput time of the preheating section before being used as input to the MBM, the inlet temperature disturbances are met very well. Other delays are closely related to typical time constants of the corresponding sections. Those are not known well without either another model in advance or experimental data. Therefore, the modeling itself is based on analytical equations, while its fine-tuning must be supported by additional information.

Purely analytical and linear time-invariant (LTI) transfer functions can be modeled based on [57, 139]. They reduce the model to a characteristic time constant and a certain model order. This works well for short superheating sections of up to 150 m, but accumulates errors for large commercial-scale ones. Nevertheless, it is a good and fast estimation if no other model is available or if the influence of geometries or other parameters is to be studied.

The analytical LTI transfer functions for the evaporation section are also based on [57]. They can be used for frequency domain controller design only, as the models are not numerically stable in the time domain. They also have the same limitation in length of the section as the superheater models. They are very helpful, if no other means for injection control design is available.

The newly identified, low order LTI transfer functions are stable in the time domain and cover the full range of once-through system relations throughout all sections (preheating, evaporation and superheating). Although the structures are identical or very similar for other plants, their parameters are not available analytically. Only most of the gains can be calculated analytically by steady-state heat balances in advance. The values of the poles and zeros typical for the transient behavior must be identified for each particular plant. As shown above based on [57] for the superheating section, the order of the LTI transfer function mainly depends on the collector dimensions, whereas the parameters (time constant and gain) highly depend on the operating point. A step response or similar data should therefore be available from a DFEM or experimental data for various operating points. If LTI identification is possible, it is recommended for control purposes as demonstrated here.

More than 1800 step responses are analyzed in this work. Since the general behavior is now understood and typical variations are selected, a future ideal identification process may only require one DFEM simulation per operating point and input variable. A loop with ten collectors has to consider 15 input variables for full characterization of each operating point, when neglecting the injection water temperatures with their small influence. The pure injection controller design, as outlined in the next chapter, only needs two typical DFEM simulations or LTI models per operating point, respectively. A reduction of 99 % in simulation effort could be achieved. Nevertheless, reliable LTI models should

always be validated by various DFEM simulations to have a high confidence in their accuracy.

Table 3.6 summarizes the main items of the models' strengths and weaknesses. In the next chapter, the MBM is used as a plant model for control concept verification, when DNI is assumed the same all over the loop. This is the case for the design of classical controllers as well as for model predictive control (MPC) schemes. It is also used as an internal controller plant model in a nonlinear model predictive control (NMPC) scheme. The DFEM could be used for this as well, if a faster implementation was available. The identified LTI models are used for controller design. They are also applied in the linear MPC scheme as internal controller models for a fast and numerically reliable prediction. The analytical LTI models for the superheater can be used within an MPC scheme for the superheater injection control, as well, as shown in [248]. As the identified models are available, there is no need to do so in this work.

Table 3.6: Overview on model characteristics and application (*computational effort for 1000 s simulation in the time domain with Dymola (DFEM) or Matlab® (all others); SHL for superheating sections only; EVL for evaporation section only.

Item	*DFEM*	*MBM*	*Analytical LTI SHL*	*Analytical LTI EVL*	*Identified LTIs*
Good gain estimation	Yes	Yes	Partly	Partly	Yes, with corrections/ scaling
Good transient behavior	Yes	Main dynamics, but initial deviation	Rough	Only frequency domain	Yes
Local resolution	Yes	Very limited	No	No	Roughly, by superposition
Relative computational effort*	1	10^{-3}	10^{-4}	10^{-4}	10^{-4}
Modeling effort	High	Medium	Low	Low	Low
Parameterization effort	Low	Medium to high	Low	Low	Medium to high
Numerical stability in time domain	Medium	Low to medium	High	Not at all	High
Application in linear controller design	Indirect by simulation tests	Indirect by simulation tests	Rough, only SHL	Only frequency domain, only EVL	Yes
Application as internal model in MPC	If fast implementation available and numerical stability guaranteed (usually not the case)	If numerical stability is guaranteed	Yes, but only for SHI	No	Yes

4 Control strategies for collector loop

The control of steam generators is a complex task and a lot of sub-controllers are needed. Control loops of conventional power plants are well explained in [85, 136, 137, 149]. The particular control loops of DSG solar fields are described in [253, 255]. Most of the control loops can remain unchanged for solar once-through boilers, e.g. control of the solar field outlet pressure, the feed water pump, the condensate system or the de-aerator. Thus, this work focuses on the main challenge of solar once-through boilers. This is to keep the live steam temperature before the turbine constant during operation. This objective is achieved best, if the outlet temperature of each collector loop is maintained in a stable and safe bandwidth during normal operation and disturbances. As the main energy resource, the sun, cannot be influenced, the mass flow of the loop must be adapted according to the irradiation level. It is shown in [152, 242, 254] that this is not a trivial task and, so far, good results have been demonstrated only for almost clear sky conditions with slow changes in irradiation. State-of-the-art control concepts are not yet sufficient to be applied for large power plants.

The objective of this chapter is to prove the feasibility of temperature control. A first robust and easy-to-apply concept is developed for the direct application in commercial plants. It is based on proportional-integral (PI) controllers, and must be extended by feedforward and non-linear concepts to work reliably. The resulting control strategy is demonstrated at the DISS facility. The number of sensors needed is also reduced as much as possible to decrease the investment and maintenance costs.

Subsequently, a look into the future is dared by analyzing model predictive control (MPC) concepts. They are theoretically promising, since the once-through system is a multivariable problem and has long time delays as well as input and output constraints. Concepts are suggested and their potential is roughly estimated.

Note that this chapter is different to former works on solar field control mainly because of two aspects. A more realistic approach is considered on how reliable local irradiation is measureable in large-scale commercial power plants – that is not at all locally, at the moment, and only as average for the whole field. Furthermore, a strictly practical approach for the first robust concept is taken. Control theory is used to simplify the control as much as possible in order to be applied. This approach is chosen from experience with solar plants using oil as heat transfer fluid. Although a lot of theoretical, advanced control concepts exist, almost none of them seem to have found their way to commercial parabolic trough plants so far.

This chapter is limited to the most challenging part of keeping the loop outlet temperature constant. Neither start-up nor parallel loop control are analyzed. Both of the latter can be solved independently. Start-up requires a reliable feedforward control and parallel loop operation is achieved by the same measures as in evaporation loops of commercial DSG plants with recirculation. The optimization of those controllers is not part of this work. Furthermore, operation at constant outlet pressure is assumed. The turbine is operated in fixed pressure mode, which is preferred for once-through boilers [136, 150] and for the charging of an integrated thermal storage system with phase change material [23].

4.1 System characterization

The system characterization and its interpretation from a control point of view are best understood with the background of section 3.4. A lot of interpretation has already been provided there. Thus, the important issues are summarized briefly. The main characteristics of the control problem are:

- The system is open loop stable.
- The loop outlet temperature is the controlled variable and shall be kept constant.
- The mass flows at the loop inlet and at certain injection locations are the manipulated variables.
- Collectors can be defocused (heat input can be reduced) and used as manipulated variable as well, if needed. This is applied only in particular situations and not for nominal control to keep efficiency high.
- The system is highly distributed and disturbance location plays a major role for the system response.
- The main energy source of the process, irradiation, acts as disturbance, which cannot be controlled.
- Irradiation disturbances can only be measured at very few locations. Thus, it cannot be measured distributed, while it can usually be well averaged in the time frame of the inlet mass flow response.
- The delay and shape of the system response depends on the manipulated variable(s), mainly the inlet mass flow.
- The system is unobservable in the evaporation section, which is the major part of the loop. In consequence, estimation of distributed irradiation disturbance is not possible.
- Energy/density disturbances close to the loop inlet result in a non-minimum phase reaction with very strong undershoots.
- The plant is non-linear; linear scaling is possible on gain and behavior only in a very small range around an operating point. Non-linearity becomes more distinct with lower loads.

- The system has slowly varying time variant parameters (such as optical efficiency of each collector).
- The transient behavior is very complex and even detailed models have a high uncertainty. Because of the distributed character, many additional disturbances (component damage, wind conditions, irradiation conditions, soiling etc.) cannot be detected and further increase uncertainty.
- Regarding modeling, the system is very stiff, such that analytical or numerical linearization is only possible in the superheating section, but not for the whole loop or the evaporation section, respectively.
- Regarding physics, density between inlet and outlet changes by a factor of 20 to 40. In consequence, the fluid residence time and time delays depend highly on location (Figure 4.1).

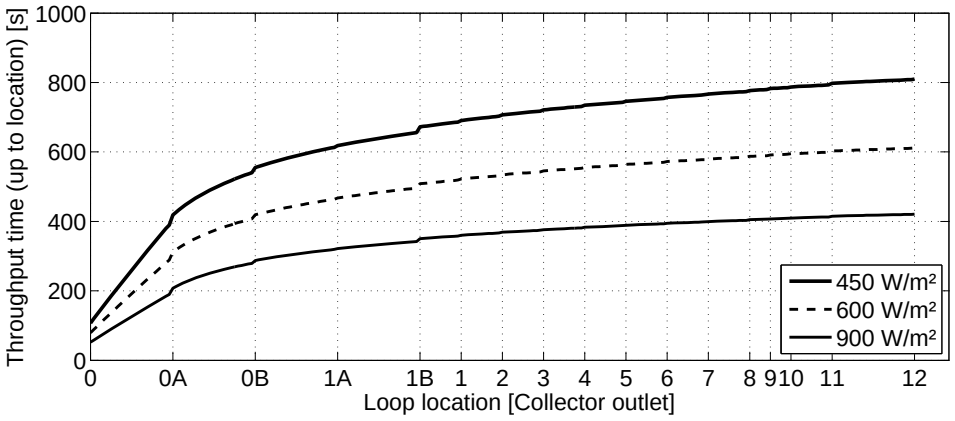

Figure 4.1: Residence time of fluid along the loop for different load situations at DISS test facility; steps after the collectors are due to long crossover pipe sections.

In a DSG system, the mass flow and temperature at the outlet cannot be influenced directly by the inlet mass flow. The steam volume in the loop provides a kind of buffer, such that the fluid cannot be treated as incompressible. On the one hand, this is a significant drawback from the control point of view, since long delays must be considered. On the other hand, it shows an advantage compared to large solar fields with oil as heat transfer fluid. The latter line focus plants with synthetic oil show anti-resonance modes for fast changes/high frequencies in irradiation or mass flow [166, 167, 278]. The plant gain changes extremely, if only a minor change in disturbance happens. These resonances are in the range of periods of 30 s or faster [278], and can affect the real system. Because of the compressibility of the steam, such resonance modes do not exist for DSG systems. Critical frequencies are found in the range of 1 s^{-1} or faster [57], which is not a typical frequency of cloud intermittence during operation. Thus, they affect neither the real plant nor the controller design.

A drawback compared to solar fields with oil is the unobservability in the two-phase flow section. Enthalpy or steam quality cannot be measured and, as a result, no information about states is available. One might argue that the temperature slightly decreases because of the pressure loss in the system and that this pressure loss depends on the energy input and the current mass flow distribution along the loop. Thus, a guess on the states may be possible. This is true theoretically, but in practice, saturation temperature/pressure sensors are not accurate enough and pressure loss correlations are not known precisely enough to provide any useful information. Another option is to measure the steam void fraction [57, 279], from which a steam quality could be derived. Such systems are expensive, very complex and not precise enough at the moment. In consequence, the only option to gain more insights is irradiance measurements along the loop, which also is very expensive. The latter option can be used beneficially for feedforward and MPC. Nevertheless, it is not considered here to be available.

Typical step responses for inlet mass flow, injection mass flows, DNI on the complete loop and inlet temperature are shown in Figure 4.2 for the DISS test facility. Inlet mass flow and homogeneous DNI disturbances show the same shape and nearly the same gain, with the mass flow reaction being slightly slower than the DNI reaction. Both are based on a misbalance between heat input to the system and water/steam content in the system. Slow changes in DNI could thus be controlled by the inlet mass flow. Due to the long delay of the responses, a short variation of DNI would be visible by temperature measurements a few minutes later. A corresponding controller response of the inlet mass flow would again be delayed by various minutes. During this time, a DNI/cloud disturbance is likely to have vanished again and the delayed control reaction does not counteract the former disturbance, but result in another disturbance. The system might become instable. In consequence, the feedback reaction of a controller on a DNI disturbance would not be very good. Only feedforward action would be able to compensate most of a DNI disturbance, if the DNI can be measured. Injection mass flow reactions are faster than DNI disturbances on the loop. Thus, they are able to reject those disturbances effectively, if the working range is chosen high enough. This is true for all loads (compare Figure 4.2 left and right).

Changes in inlet temperature, which are comparable to changes in energy input at the loop inlet, show steeper gradients than DNI disturbances and a non-minimum phase response with strong undershoots. Again, feedforward action of the inlet mass flow might be able to compensate this. However, it must be a transient compensation due to the non-minimum phase character. Since model uncertainty is very high, such feedforward compensation by the inlet

mass flow may not be able to fully cope with such a disturbance. Again, only the injection mass flows offer this possibility.

Local changes at the end of the evaporation section (collector 6) and the loop outlet (collector 12) are shown in Figure 4.3 for the DISS facility. In the evaporation section, the injection before collector 6 shows a similar system response than the disturbance by collector 6. However, this is different for the injection before collector 11 and a disturbance at collector 12. Even feedforward compensation cannot handle such a situation completely, as the collector disturbance results in a much faster response. Only the focusing of the collector itself can quickly compensate a loss of irradiance input to the collector. This example illustrates the limits of every temperature control system. Local reduction of DNI in the superheating section will always result in a reduction of outlet temperature at the beginning. In the case shown in Figure 4.3, the disturbance would have reached 61 % of its final value (1.5 K of 2.5 K deviation) before the perfect (steady-state) feedforward control of the injection would be able to counteract. No control strategy can perform better than this physical limit. There are only two possibilities to overcome this limitation: a) a very reliable local DNI prediction is available (which is not true in reality at the moment) or b) additional mirrors of the last collector can be focused. The latter option b) is possible, but means that the last collector is defocused to some degree at nominal conditions – or, for the case of linear Fresnel collectors, that some mirror facets are defocused at nominal conditions. This obviously results in a loss of efficiency or heat output, respectively. Whether this is economically promising, must be evaluated for each project. For parabolic troughs, it is unlikely due to their large and relatively expensive collector module areas. For linear Fresnel collectors with independent mirror facet control, it might be interesting. As this work concentrates on parabolic troughs, such an option is not covered for the main control schemes.

Note that there exist fundamental differences between recirculation mode (RM) and once-through mode (OTM) control. RM has a fixed end of evaporation by the steam drum. The latter separates the steam mass flow generation of the evaporation loops from the steam temperature increase in the superheating section [24]. This is advantageous for long irradiation disturbances. However, it is a challenge to the design of such a system. The ratio of evaporation to superheating collector area is fixed and must be optimized for a nominal operating point. Due to different irradiation levels and collector efficiencies, the optimum ratio is already different in part load. The superheater injection of the RM field is not only needed for control during transients, but also for balancing different steady-state operating points. In consequence, RM fields without SHI must always be defocused to some degree in part load, even at a clear sky day. If the SHI is installed, the imbalance of evaporation and superheating areas may be-

come disadvantageous, if a certain amount of collectors is out of work in the evaporation section. The achievable temperature at the outlet of the superheating section is affected and some superheater collectors might have to be defocused because of those imbalances as well. Therefore, the OTM configuration offers a lot more flexibility in real plant off-design situations. The price to pay is the lack of water/steam mass buffer.

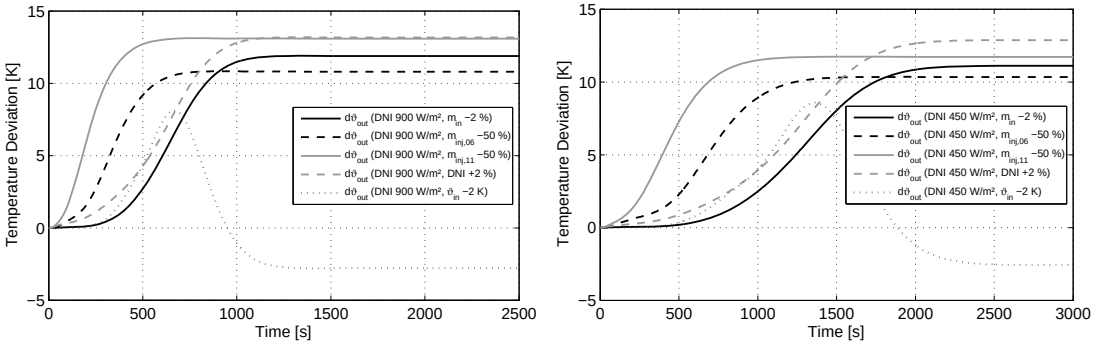

Figure 4.2: Comparison of outlet temperature step responses at DNI levels of 900 W/m² (left) and 450 W/m² (right) for changes of mass flows, DNI on complete loop and inlet temperature simulated with DFEM.

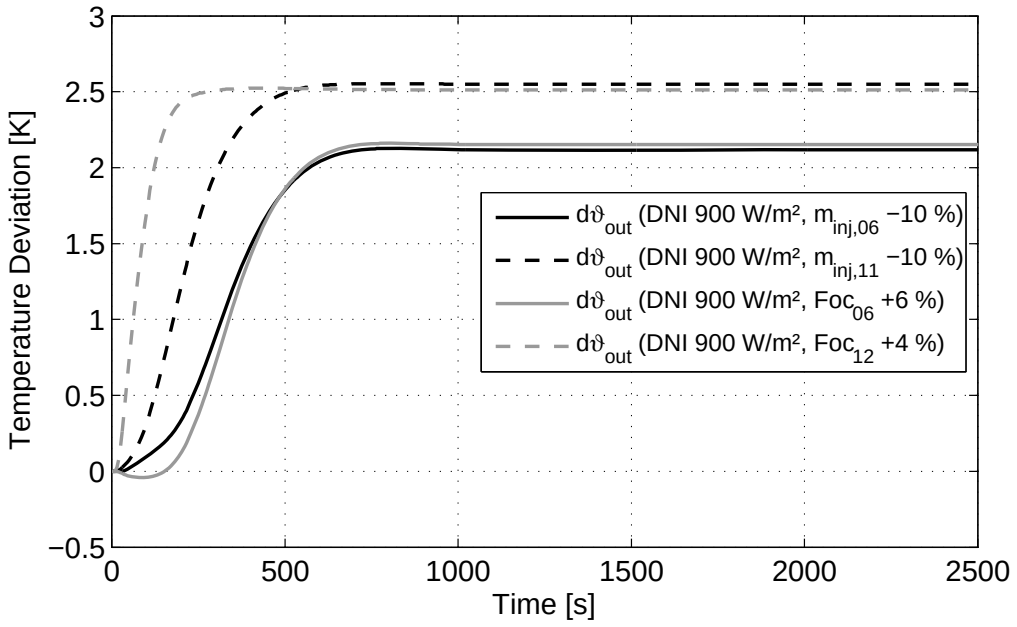

Figure 4.3: Comparison of outlet temperature step responses at a DNI level of 900 W/m² for changes of injection mass flows and energy input to collectors 6 and 12 of DISS facility simulated with DFEM.

4.2 Compilation of state-of-the-art control strategies

The following subsections summarize the control background for the newly developed concepts. Control of conventional fossil steam generators can partly be transferred to solar boilers. Many papers on control of distributed solar fields with single-phase flow exist as well. Some of the approaches can be applied to DSG solar fields, while others are not applicable because of different system characteristics. Finally, some papers on the particular topic of this work, i.e. solar once-through mode control, with the current state-of-the-art control concepts are presented.

4.2.1 Control of conventional once-through boilers

There is a vast variety of papers analyzing the control of conventional steam generators. Lindsley [149] or Flynn [85] provide a good overview; Dolezal, Klefenz and Profos [51, 53, 136, 137, 198] can be considered authors of fundamental books on the topic.

Remember that the main difference to solar plants is that the fuel input can be controlled in fossil boilers. An overview on standard approaches for superheating control provides Figure 4.4. The outlet temperature of the superheating section is usually controlled by a simple PI controller. This controller is supported by additional proportional control on the temperature directly after the injection. This is called a PI-P cascaded structure (Figure 4.4, left). The same is possible for two injections, if the superheating section is very long (Figure 4.4, middle). The temperature before the second injection is controlled by the first injection; the outlet temperature is controlled by the second injection. Both can then work in a PI-P structure. The setpoints and controller parameters may be adapted to the load and other structures like PI-PI structures are possible.

State feedback is another very wide-spread and useful control approach for superheater sections [85, 104]. The superheater model is transformed to a linear time-invariant state-space model [11]:

$$\begin{aligned} \dot{x}(t) &= Ax(t) + Bu(t) \\ y(t) &= Cx(t) + Du(t) \end{aligned} \tag{4.1}$$

The controlled variable is y, usually the outlet temperature, the manipulated variable is u, mainly the injection mass flows, and the current system state is x, e.g. temperature measurements along the superheating sections. The matrices A to D fully describe the dynamic behavior. A state-feedback controller can then be established by [11]:

$$u_{\mathrm{sfb}}(t) = -k_{\mathrm{sfb}}x(t) \tag{4.2}$$

The controlled variable u_{sfb} is updated by proportional feedback to all system states by a gain matrix k_{sfb}. If the states are only temperatures along the su-

perheating sections and all these temperatures can be measured, a perfect state feedback can be established [104] (Figure 4.4, right). However, the order of the state space model is high and not all – or even none – of the temperatures in between are measured. In these cases, the state must be estimated by a state observer. As this is a common approach in control theory, it is not described here in more detail. The reader is referred to [11] or other text books on advanced control. In general, one can say that the input to the system is considered to estimate the current system state. Note that by only using the knowledge/estimate on the input, the control can already be improved even without measuring the system states.

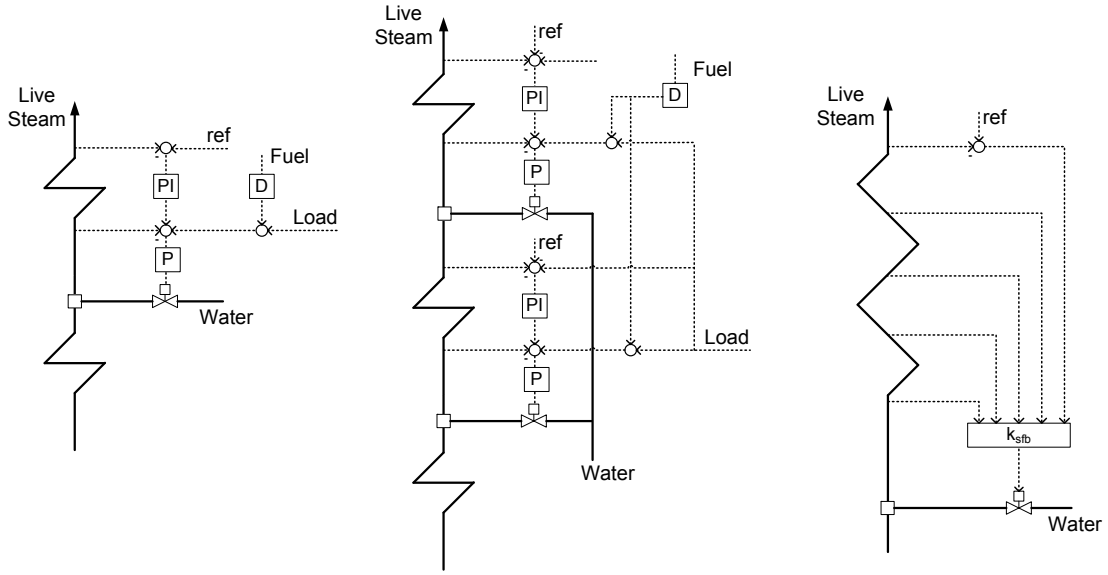

Figure 4.4: Control approaches for conventional superheating sections of fossil power plants based on [137] and [104]; PI-P cascade (left), PI-P cascade with two injections (middle); state feedback controller (right).

The control of the evaporator, i.e. the inlet mass flow, in a once-through boiler is usually based on a temperature measurement in the superheating section, shortly after the evaporation section. As the load and fuel input is known in conventional plants, this is used for feedforward action on the inlet mass flow [85, 136, 137].

Pioneering work on MPC for steam generators was published by Richalet [207] and Lecrique [147]. They paved the way for many other works on multivariable optimization of the complete steam generator. For example, MPC was used on supervisory level for improving existing PI controllers in [85, 180, 183, 187, 188, 196]. Moelbak [174] developed an adaptive superheater controller based on general predictive control. Recently, Franke [89, 90, 142] applied nonlinear MPC for the start-up of fossil-fired steam power plants. A lot more con-

cepts have been analyzed in literature and a detailed overview would be out of proportion to this section. Nevertheless, the most important concepts that can be transferred to solar once-through boilers have been mentioned.

4.2.2 Control of distributed solar fields with single-phase flow

The control of large distributed solar collector fields with synthetic oil as heat transfer fluid is covered by many research papers with all varieties of control concepts. Camacho [35, 36] provides a good overview on them. Modeling and classical control strategies are presented in [35], while advanced schemes such as adaptive control, gain scheduling, MPC, artificial neural networks, fuzzy control and optimal control are summarized in [36].

The concept of gain scheduling, which is described later on in more detail, shows promising results for such plants and is analyzed in [2, 120, 192, 193]. Irradiation, mass flow and inlet temperature are the main scheduling parameters. The delays of the system mainly depend on the oil mass flow such that in discrete time systems the discrete dead time shall be adapted or scaled [224, 278].

MPC schemes such as gain scheduled general predictive control [33, 34] are advantageous to simple PI controllers, if the internal model is accurate and if the DNI can be predicted, both of which is not necessarily the case. Nonlinear control is suggested in [13]. An interesting option, if the process is understood well by the designer, is the use of fuzzy control [84, 213]. Several works on the related linguistic equation control [121-123] have also been published. Most of the mentioned approaches have been tested at a small-scale test plant at PSA.

A more transparent design approach and robust performance are achieved based on internal model control as suggested by Zunft [278].

The influence of cloud patterns passing over a solar field was analyzed in various studies for other CSP technologies, e.g. in [105],[128],[152], but have not been considered explicitly in control papers on synthetic oil plants so far. This might be due to two reasons. First, the ACUREX test facility [34], which is used as reference in most of the related papers, was very small compared to typical collector areas of large-scale commercial plants – in fact, it had only about 0.5 % of a commercial collector area for a 50 MW_{el} plant [225]. Second, the oil solar field has a very distributed and high thermal inertia, such that local cloud patterns have a significantly smaller effect compared to a DSG loop.

4.2.3 Control of solar once-through boilers

The control of solar once-through boilers has not been analyzed in many papers before. The first paper is probably the theoretical work by Lippke [152] based on [150]. He already foresees a loop with up to two injections for good control. It is demonstrated that local irradiation disturbances are an extreme

challenge. They are worse, the slower the disturbing clouds move and the larger they are. General control propositions for mass flows are made based on transient simulations. An additional –high risk– control is suggested based on de-/re-focusing of the first collectors at certain disturbances. Although theoretically logical, such a strategy requires a very detailed knowledge of the transient behavior and current cloud positions. Thus, it is not recommended for robust control. Lippke [150] also suggests to use fixed pressure mode for turbine operation instead of sliding pressure mode. Fixed pressure mode shows better behavior during transient conditions and allows for a smooth temperature control [150]. It is also favorable during charging and discharging of a phase change material storage system [23, 25].

Control concepts for DSG operation modes have been developed and tested by Valenzuela [253, 254]. She demonstrated the general feasibility of DSG control at the old 500 m long DISS facility. The main control schemes for RM and OTM are introduced in [254]. The scheme for controlling the outlet temperature by the feed water valve at the loop inlet is shown in Figure 4.5 for OTM. The inner loop, comprising the PI/anti-windup controller and the plant, describes the valve control, which is rather fast. The mass flow setpoint for that inner loop (m_{in_dem}) is generated by an outer PI controller with a dominating feedforward action. This feedforward action is based on reference outlet temperature, current irradiation, inlet temperature, ambient temperature, injection water temperature and injection mass flow setpoint. An interpolation scheme from pre-calculated energy balances is used to determine the feedforward mass flow from the input variables. The same scheme is used for the injection controller, of which only one is foreseen before the last collector of the loop. Inputs to the feedforward action are steam temperature before injection, injection mass flow, loop outlet mass flow of the steam and injection water temperature [253].

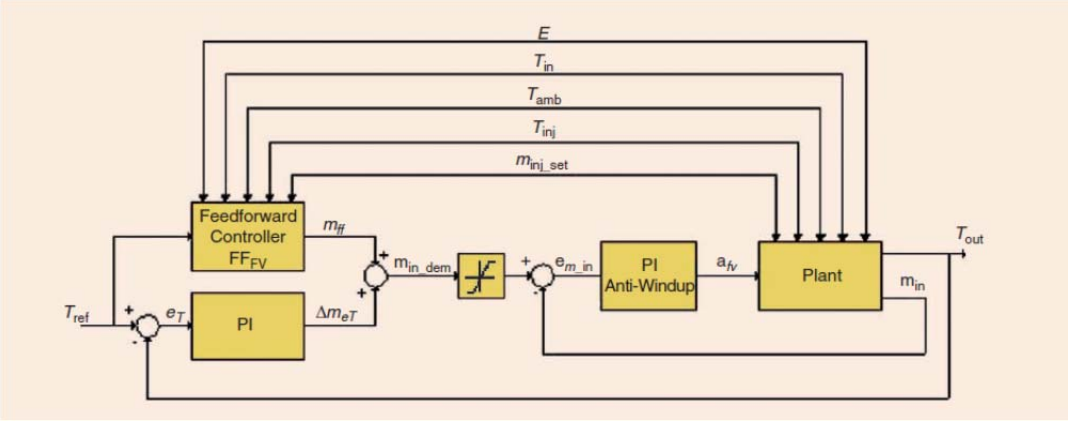

Figure 4.5: Outlet temperature control scheme via loop inlet valve as suggested by Valenzuela for once-through mode [254].

The transfer functions of inlet and injection mass flows to outlet temperature are approximated from experimental data by a first order delay element with dead time, including uncertainty assumptions. The PI controller parameters are designed such that each uncertainty model shows a minimum gain margin of 2 dB and a minimum phase margin of 60° for inlet and 90° for injection mass flow [253]. One controller is used for the complete operating spectrum. Its performance is shown in [254] for two clear sky days (April 22, 2002; July 27, 2002) and for one day with disturbances (April 26, 2002). Operation was performed at 30 or 60 bar, respectively. During clear sky irradiation, the temperature can be controlled very well. However, if drops in DNI occur, the temperature cannot be stabilized quickly. In [255], an additional clear sky day at 100 bar (May 21, 2003) and a day with short DNI drops at 30 bar (May 15, 2003) are shown. The latter article also includes experimental data for recirculation mode. [256] is dedicated to recirculation mode solely. It can be seen that the challenge of once-through mode is temperature control, while for recirculation mode, level control in the steam drum is crucial. The latter is analyzed for various control concepts in [256].

The control of the superheating temperature is relevant for all DSG modes. Eck [57, 59, 64] provides an approach for adapted PI controllers for the superheating injection. The model parameters are calculated online based on analytical equations and measurements. The adaptation is performed based on [9] by mapping one open loop point of the frequency response locus (Nyquist plot) to a predefined one by changing the PI controller's gain and time constant. The selection of the predefined point must be chosen from various simulations. This procedure is able to handle a wide range of plant parameters. The PI controller design for the evaporation injection is performed similarly in [57]. Based on this approach, a similar procedure is followed by Trebing [248], not resulting in one point, but rather in an area of predefined points. In [59], a superheater controller based on internal model control (IMC) is designed with the same analytical LTI models. Its control performance is described as worse than the adapted PI controller.

Koch [139] suggests an adaptive PI-PI cascade structure from conventional steam generators for superheating control. He uses an intermediate temperature measurement for fast inner loop control, while the outer control loop defines a setpoint for the intermediate temperature. This improves the performance of [64], but relies on additional temperature measurement and additional irradiation measurements in the sections before and after the intermediate temperature sensor.

Tanner [242] suggests an MPC scheme for once-through boilers of a special type of linear Fresnel collector systems. The receiver consists of a bundle of small parallel tubes. The collector loop has no injections and a small header at

the middle of the loop, which connects all parallel tubes of each loop. The layout is very similar to conventional boiler design, but differs in flow directions. Water/steam flows from the inlet to the middle header in only about half of the tubes, while it has the counter-direction from the middle header to the outlet in the other parallel tubes. A linear MPC concept is suggested and tested at a pilot plant. The resulting temperature can barely be stabilized even during rather constant irradiation conditions. This is no surprise when looking at the system characterization of section 4.1, especially the non-minimum phase behavior. The MPC scheme is favorable, but the loop layout does not allow for effective control. Further note that the receiver design does not guarantee a homogeneous flow distribution within the parallel receiver tubes, as demanded implicitly in section 2.3.

4.3 New robust control strategy

This section suggests a new outlet temperature control concept for solar once-through boilers based on PI controllers. These must be accompanied by feedforward, gain scheduling and non-linear control action because of the long time delays and various operating conditions of the system. The aim is not to provide optimal control in all operating conditions, but to enable the reader to easily design and tune a reliable, robust controller. Implementation is easily possible in every control environment and basic design rules are derived. This shall serve for short-term implementation in large-scale commercial solar fields. The control loops are simplified to single input-single output (SISO) systems as far as possible. All methods are exemplified by the design for the DISS test facility.

4.3.1 Selection of control structure

The basic loop layouts are shown in Figure 2.1 on page 12. These comprise

A) Evaporation injection (EVI) and superheater injection (SHI)
B) Only EVI
C) Only SHI
D) EVI with central superheating injection (CSHI) in the live steam header.

The loop control structure of variant B is identical to variant D. Only the setpoint of the loop outlet temperature is higher for variant D in order to provide a buffer for the central injection. In consequence, only variants A, B and C are discussed in the following.

It is advisable to control the outlet temperature by the last injection of the loop in order to reduce the time delays as much as possible. This is done by the SHI for variants A and C. The temperature before the SHI is almost independent from load for all steady states (see chapter 2). In consequence, this temperature is suggested as control variable for the evaporation mass flow. For variant

C, this is the loop inlet mass flow (IMF). For variant A, the fast control shall be done by the EVI, while the IMF can be used for slow tracking of the working points of EVI and/or SHI. If inlet temperature varies significantly during operation, the desired temperature before the SHI might not stay constant for all loads. In those cases, the reference value for the temperature before the SHI must be adapted such that a good working range of the SHI is assured. When the temperature before the SHI is close to its reference, the SHI will have a sufficient working range during all loads, unless significant plant failures are present (e.g. collectors in the superheating section being out of work). Both control loops (SHI to outlet temperature and EVI to temperature before SHI) can then be treated separately for control design. Those schemes are depicted in Figure 4.6. The temperature before the SHI is used as feedforward signal for the SHI controller. This is not possible for the EVI controller, since the enthalpy before the EVI cannot be measured. A PI-P cascade or state feedback are two options for variant B. A PI-P cascade is suggested for variant C. Only variant A is analyzed in detail here, the other structures are covered in a more general way.

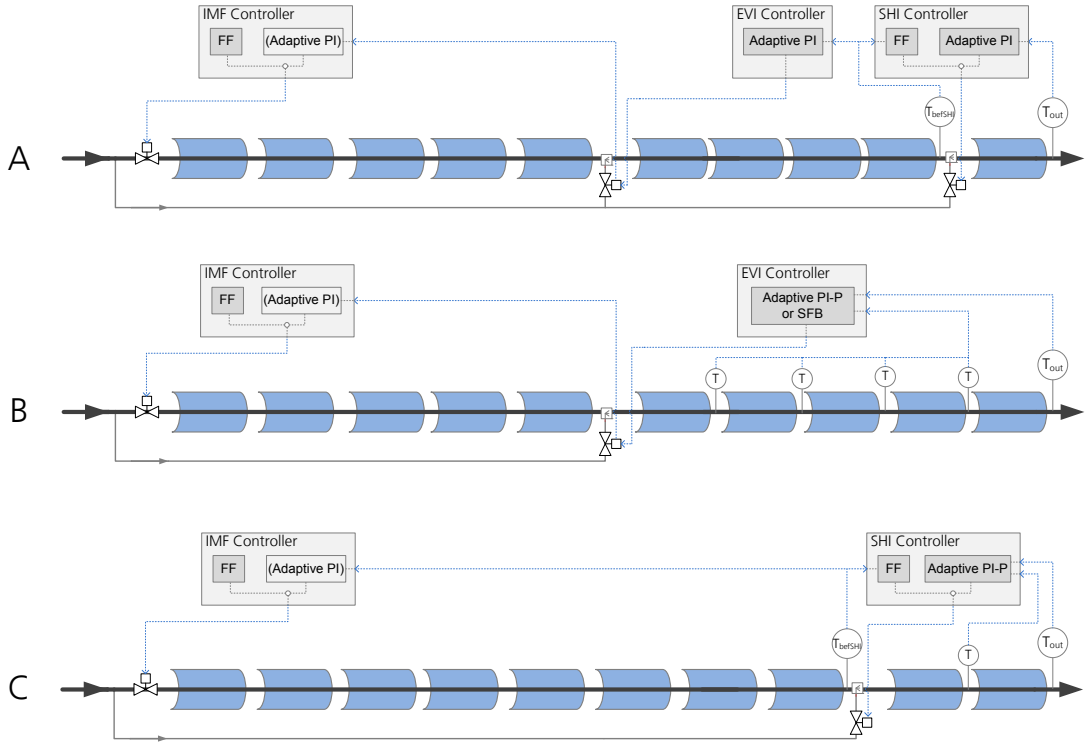

Figure 4.6: Overview on control structure for the three main loop layout variants with IMF adaption by PI structure; FF indicates feedforward action, IMF inlet mass flow, EVI evaporation injection, SHI superheating injection, PI-P indicates a PI controller with additional proportional action on temperatures along the plant.

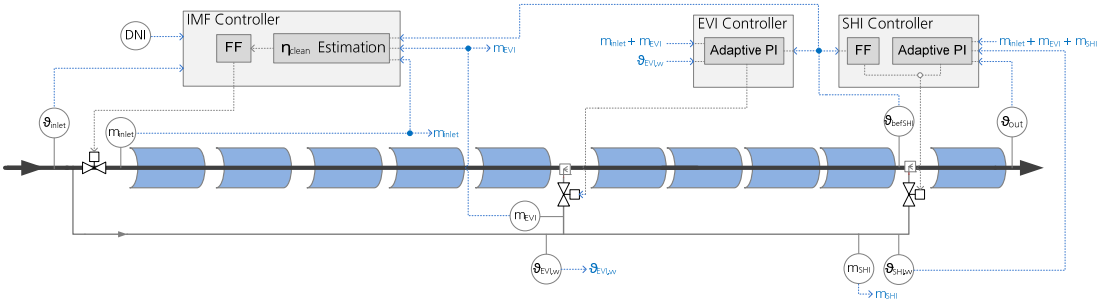

Figure 4.7: Detailed control set-up for the recommended basic control of variant A with online estimation of the optical efficiency or cleanliness, respectively; dashed lines indicate signals; solid lines indicate water/steam line.

The IMF control is very slow in all cases such that disturbance rejection is ineffective. In consequence, the IMF is predominantly determined by the feedforward term for the average irradiation on the solar field. This is explained in section 4.3.3. The IMF provides the main mass flow to the loop, while the injections cope with fast and local disturbances. The IMF controller needs feedback if a plant-model mismatch exists in the efficiency of the loop, which is very likely in real life. If loop efficiency is overestimated, the feedforward term of the IMF is too high and, in consequence, the EVI will have a lower mass flow share compared to the design. This leads to a lower buffer, if fast irradiation disturbances appear. Two options can be used to overcome this problem. One option is to use a PI controller on the working point of the EVI, e.g. a constant EVI mass flow, as illustrated in Figure 4.6. This controller may not adapt the mass flow as the manipulated variable, but shall correct the efficiency of the feedforward term. The better second option is to directly estimate the current efficiency of the loop and adapt the feedforward term for irradiation accordingly. The latter option requires online estimation of the efficiency. Although this is more complicated, the information is useful for both plant operation and maintenance. The reason behind the estimation is that the efficiency is valid for all the sun positions and transients in the morning and in the evening, which is not necessarily the case for the PI variant. Thus, it is highly recommended to apply the efficiency estimation. In the simplest variant for a small plant, online estimation for each loop could even roughly be performed by the operator. This proved to be sufficient for DISS facility. In any case, it must be considered that especially the PI control may only be used during clear sky periods in order not to provide misleading output. Its design must also be very slow to avoid oscillations. Further note that the successful application of a PI structure requires a very good prediction of the clear sky DNI curve in the feedforward of the IMF. Only in this case, the PI structure could be designed to have a similar effect as a simple Kalman filter estimation. Nevertheless, it will usually perform worse than the online estimation. In this work, good efficiency estimation is assumed

for the basic control concept. This recommended variant is shown in detail in Figure 4.7 with the most important sensors and signal paths.

For robust control of first commercial plants, it is recommended to apply variant A with two injections. This configuration allows good disturbance rejection during all situations. Its controller design is divided into three parts that can be solved independently:

1) Design of SHI control
2) Design of EVI control
3) Design of IMF control.

These steps are described in section 4.3.2. For variant B, the EVI controls the loop outlet temperature together with IMF control. Variant C is designed analog to the SHI and by a mixture of EVI and IMF.

Variant B poses significant problems to PI control design, since the delay from the EVI to the outlet is very large. The basic controller must then at least be accompanied by additional feedback from temperatures along the superheating section. This corresponds to a PI-P cascade structure from fossil superheaters [136, 137]. It is illustrated in Figure 4.6 and described in section 4.3.5. This is the minimum requirement, but it is advisable to directly use a model predictive controller as presented in section 4.5. Note that PI control via the IMF on outlet temperature would be very slow and become useless for disturbance rejection. Thus, the EVI working range is chosen as control variable.

For variant B, a fast EVI control of a temperature shortly after the evaporation section can be suggested as well. Its setpoint is then adapted by an integrator on the deviation of the outlet temperature. Due to the rather homogeneous heat input in fossil plants, this works well and is comparable to a PI-PI structure. However, for solar plants, the integrator would be too slow to effectively reject local disturbances at the end of the superheating section. During cloudy situations it can even destabilize the plant. The PI-PI structure is thus not considered here.

The IMF control of variant C constitutes a SISO system for the temperature before the SHI (see Figure 4.6). It is faster than using the loop outlet temperature. The SHI can be improved by additional proportional action on temperatures after the last superheating collectors. Depending on the degree of superheating before the SHI, such a PI-P cascade might also be useful for the IMF controller.

All PI controllers do not work sufficiently solely. There must be feedforward action (section 4.3.3) and adaptation of the parameters (section 4.3.4), which in the end establish a non-linear controller for the basic control scheme. Especially the SHI must include feedforward on the temperature before the SHI. Some special operating situations must be foreseen separately for robustness in

commercial plants (section 4.3.6). The basic controller design of variant A is then summarized in section 4.3.7.

There are a lot of additional variants, if the defocusing of collectors is taken into account for nominal control. For example, one might foresee variant B or D with the last collector acting on the outlet temperature via a PI controller or via a simple threshold hysteresis. The most important drawback of such configurations is that they do not offer any buffer during fast reductions of irradiation. Thus, they are only recommended for variant D. The outlet temperature will drop rapidly during these disturbances, which might lead to higher stress cycling in the absorber tubes or, if all loops suffer the same disturbance at once, even to trips of the turbine. Another important drawback of such options is the loss of energy during nominal operation. Theoretically, the collector can be defocused in very small steps in order to almost continuously control the temperature. Then, the resulting loss of energy might be negligible. However, with current precision of parabolic trough collectors and collector tracking units, it is very difficult to implement this in a real commercial plant [117]. In consequence, large shares of the collector are defocused all the time or at least periodically. Whether this can be outweighed economically by saving installation costs of the SHI, is a project-specific analysis. Linear Fresnel collectors with independently controllable facets or short mirror units have an advantage here. For the latter systems, defocus control should be analyzed in more detail in the future. In this work, the defocus control is only considered for special operation conditions as described in section 4.3.6.

4.3.2 Basic controller design procedure

The design of the underlying PI controllers is now analyzed. LTI models are derived for various load conditions and used for controller design. The procedure is accompanied by the example of the DISS test facility. Nine different loads are used in section 3.4 to do so. Thus, the LTI models are assumed to be available in the following. The first subsection introduces the design methodology and exemplifies it by the SHI controller design. The subsequent sections show the results for the other relevant controllers for variants A to C at the DISS test facility.

4.3.2.1 Design Procedure and example of SHI control

Figure 4.8 shows a classical feedback control structure in which measurements and noise are ignored for simplicity. The control variable (y) is the output of the plant section (P) under disturbances (d). The negative feedback is compared to the reference value (ref). The resulting error (err) is the input to the controller (C) with the manipulated variable (u) as output. The manipulated variable and possible deviations of it (u') are then taken as plant input. The

control variable y corresponds to a temperature, e.g. the loop outlet temperature, while the manipulated variable u corresponds to a mass flow, e.g. the injection mass flow. The transfer function μ(s) of the reference to the control variable is [175]:

$$\mu(s) = \frac{y}{\text{ref}} = \frac{C(s)P(s)}{1 + C(s)P(s)} \tag{4.3}$$

The transfer function from the disturbance to the control variable can be expressed by [175]:

$$\epsilon(s) = \frac{y}{\text{d}} = \frac{1}{1 + C(s)P(s)} \tag{4.4}$$

The transfer function $\epsilon(s)$ is called sensitivity function [175]. The sum of both functions always equals unity, which is why μ(s) is called complementary sensitivity function. The sensitivity function shall be small in order to effectively reject disturbances. However, it can be shown that $|\epsilon(s)| \to 1$ for $s \to \infty$. Thus, for high frequencies, disturbance rejection and controller performance is limited. One can interpret sensitivity as a measure of controller performance ($\epsilon(s) \approx 0$), while complementary sensitivity is a measure of robustness ($\mu(s) \approx 0$) [175].

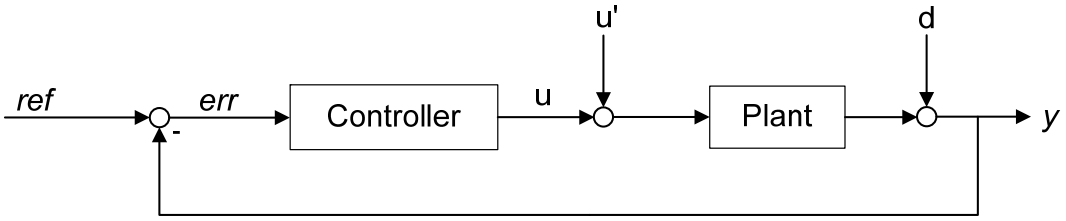

Figure 4.8: Classic feedback control structure based on [175].

The concept of internal model control (IMC) suggested by Morari [175] provides the background to design excellent controllers as trade-off between the two requirements. The resulting controllers usually are of high order and explicitly include the plant model and disturbance models. However, it can be shown that for systems of first or second order, the optimal IMC controller is nearly equivalent to a PID controller [175]. For higher order systems, as for DSG plants, the ideal IMC controller will always perform better than a simple PI controller. Nevertheless, a simple approach shall be derived here. The main idea of IMC, that a robust controller may not be faster than the underlying process, is transferred to the PI controller design.

The PI controller to be designed has the following form:

$$C(s) = k_\text{c}\left(1 + \frac{1}{\tau_\text{I} s}\right) = \frac{k_\text{c}}{\tau_\text{I}}\frac{(\tau_\text{I} s + 1)}{s} \tag{4.5}$$

Time constant τ_I and gain k_c must be chosen for each operating condition. The approach can be illustrated by a very simple example. The plant to be controlled is of first order:

$$P(s) = k_P \frac{1}{(\tau_p s + 1)} \tag{4.6}$$

An IMC controller for step inputs $(1/s)$ would result in the PI parameters [175]

$$\tau_I = \tau_{c,imc} = \tau_p \quad and \quad k_c = \frac{\tau_I}{\lambda\, k_P} \tag{4.7}$$

The controller's time constant is identical to the characteristic IMC time constant of the process, which has already been determined in chapter 3.4. The filter time constant λ can be interpreted as dominating time constant of the closed loop transfer function. The same idea is also valid for higher order systems. In consequence, the design of the PI controller can be reduced to searching for one parameter, the closed-loop time constant λ. For non-minimum phase systems, the controller gain k_c also depends on the zero τ_z in the right half plane. Consider the plant

$$P(s) = k_P \frac{-\tau_z s + 1}{\tau_p s + 1};\ \tau_z > 0 \tag{4.8}$$

Then a good choice from IMC methodology for the controller gain is

$$k_c = \frac{\tau_I}{(2\tau_z + \lambda)\, k_P} \tag{4.9}$$

The non-minimum phase character of the system reduces the gain and, in consequence, the controller performance.

If a high order controller can be implemented, it is recommended to follow the two-degree-of-freedom approach in [175]. However, the main success of the design is in the consideration of realistic disturbances. Consider *D'(s)* as a disturbance scenario on the output (comparable to d in Figure 4.8). Former approaches [36, 57, 254] used the sensitivity function for design purposes – more or less explicitly – which is equivalent to defining a step for design (*D'(s)* = $1/s$). This is a good approach for reference tracking or output step responses. However, both scenarios are usually not decisive for solar plants. The main disturbance from a control point of view is irradiation. Irradiation disturbances are slow, when acting homogeneously on the loop, or fast, when acting locally near the plant outlet. During nominal operation, *D'(s)* is better represented by irradiation disturbances and their transfer functions (compare sections 3.4.6 and 3.4.8). Other disturbances from inlet temperature and injection water temperature can be treated in the same way. The problem for the controller is the variety of disturbance scenarios *D'(s)* that can act on the system.

One approach is to define a robust performance objective based on the infinity norm such that all possible disturbances are rejected fulfilling a minimum controller performance requirement [175]. Although this sounds logical at first, the problem for solar plants is to define all possible disturbances. Therefore, further simplification would be needed. Note that all irradiation disturbances must pass through the system at least partly. System characterization in section 4.1 promotes that the relevant system response on irradiation disturbances can be very similar to mass flow disturbances. For the SHI, homogeneous disturbances on the loop are very slow, while disturbances on the last collector are very fast. As a compromise, it is suggested here to use mass flow disturbances for nominal controller performance. This can be interpreted as irradiation disturbance on the relevant plant section, which is the last superheating section for the SHI. At the DISS facility, this considers DNI disturbances on collectors 11 and 12. For a commercial plant, the SHI can be placed before the last collector, such that both collector and SHI response are nearly the same. In consequence, the design objective is simplified to find a good controller for mass flow disturbance rejection. The resulting transfer function of the closed loop is

$$\gamma(s) = \frac{D'(s)}{1 + C(s)P(s)} \approx \frac{y}{u'} = \epsilon(s)P(s) = \frac{P(s)}{1 + C(s)P(s)} \tag{4.10}$$

Two advantages promote this approach: it is already a compromise for all disturbances and no additional irradiation transfer function is explicitly needed for nominal controller design. The time constant of the controller is fixed by the mass flow or load, respectively, as derived above. Thus, the controller gain must be found as a good compromise between disturbance rejection $\gamma(s)$ and robustness $\mu(s)$.

An intuitive choice for the gain is to let the closed-loop system be as fast as the plant. This implies $\lambda = \tau_I$. A corresponding controller $C_1(s)$ is defined and the tuning factor f_λ is introduced as the ratio of integration time and λ. The controller can then be represented by:

$$C(s) = k_\mathrm{c}\left(1 + \frac{1}{\tau_\mathrm{I} s}\right) = \frac{\tau_\mathrm{I}}{\lambda\, k_\mathrm{P}}\left(1 + \frac{1}{\tau_\mathrm{I} s}\right) = f_\lambda \frac{1}{k_\mathrm{P}}\left(1 + \frac{1}{\tau_\mathrm{I} s}\right) = f_\lambda C_1(s) \tag{4.11}$$

Figure 4.9 shows the closed-loop system responses of an input disturbance step $\gamma(s)$ (left) and a reference step $\mu(s)$ (right) for various values of the tuning factor for a DNI level of 900 W/m². A small tuning factor leads to a smooth, but slow system response. On the other hand, a large tuning factor results in a fast disturbance rejection, but strong oscillations. The controller $C_1(s)$ with $f_\lambda = 1$ shows a smooth response for both steps. The peak of the disturbance rejection, the maximum control deviation, is at about 0.5. This means that about 50 % of an uncontrolled disturbance will still be effective on the controlled plant. It is

suggested to limit the tuning factor to values for which system responses become negative at some point. This is reached by increasing the tuning factor to 2, resulting in a peak at about 37 %. A better disturbance rejection would cause robustness problems with very high overshoots in the reference step response.

With lower loads, the system tends to oscillate stronger and to have a more distinguished non-minimum phase behavior. This is illustrated in Figure 4.10. Tuning factors must be chosen more conservatively. A tuning factor of 1.05 reaches the limit of non-negative values in the disturbance rejection response. A tuning factor of 3 would destabilize the whole plant. It is useful to recall equation (4.9). The nominal model has a characteristic time constant of 473 s and two right half plane zeros at 326 s. If $\lambda = 0$ is chosen, the factor $\tau_I/2\tau_z$ is 0.73. The shape of the corresponding step response in Figure 4.10 resembles the one with a tuning factor of one for higher loads in Figure 4.9. Also note that the peak in disturbance rejection is significantly higher for low loads. A rather aggressive tuning factor of one still has a peak value of about 0.55. This can be interpreted as a system immanent performance limitation.

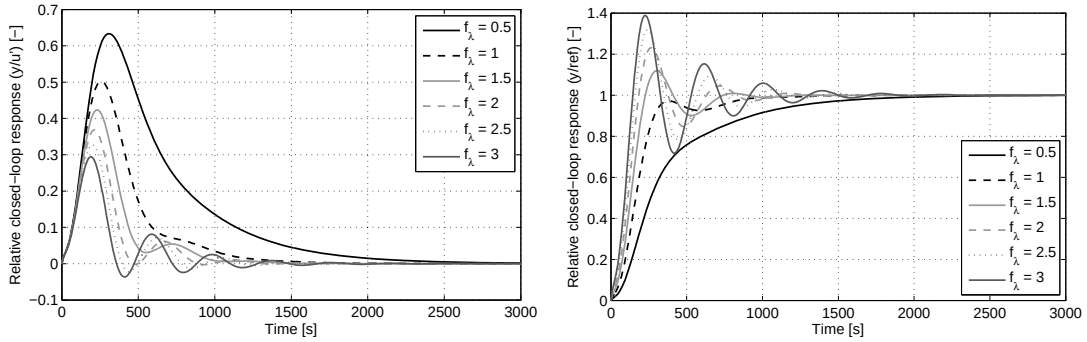

Figure 4.9: Closed-loop system responses to step inputs of input variable (u'; left) and reference (ref; right) for the nominal LTI model of the SHI to outlet temperature at 900 W/m².

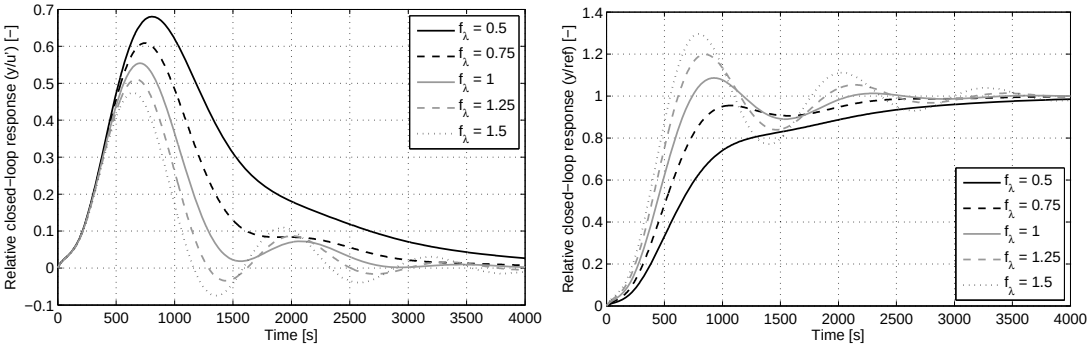

Figure 4.10: Closed-loop system responses to step inputs of input variable (u'; left) and reference (ref; right) for the nominal LTI model of the SHI to outlet temperature at 375 W/m².

For an automated calculation of controllers and for a more concise description, an objective function for the choice of the gain can be developed. The objective chosen here is comparable to a weighted H_2-optimal controller design [175]. The perfect controller shall have no setpoint deviations for input disturbances, which means $\gamma_{ideal}(t) = 0$ for all times t, and perfect robustness against noise, which would mean $\mu_{ideal}(t) = 0$ for all times t. This is obviously not possible in reality, but allows for comparing the step responses to the ideal value. The step response of the reference is weighted by a factor w_μ to choose the desired shape. The objective function J is minimized in order to find the optimal tuning factor f_λ^* :

$$\min_{f_\lambda} J$$
$$s.t. \quad J(f_\lambda) = \int_0^\infty \gamma(t)^2 dt + w_\mu \int_0^\infty \mu(t)^2 dt \tag{4.12}$$

The objective function is linked to the tuning factor by equations (4.10) and (4.11). It is formulated for the tuning factor, but of course, can also be formulated directly for the controller gain, which leads to the same results. Figure 4.11 shows the closed-loop system responses for two optimal tuning factors. Weights of 0.2 lead to smooth results and weights of 0.25 to more aggressive ones. With lower loads, the weights should be reduced to achieve the same shape of the response. Note that the relative variation of the tuning factor is significantly reduced with lower loads as well.

Robustness must not only be considered for the nominal plant model, but also for deviating models considering uncertainty. Figure 4.12 shows that, even for high uncertainty, the controller performance remains in a good range. The systems considered in the figure are all LTI models with the same DNI level (14 in total), a faster LTI model with a more than 30 % higher gain and a slower LTI model with an about 25 % smaller gain. Experimental data suggests a slightly faster system with higher gain compared to the DFEM and LTI models. Thus, this model uncertainty leads to an even better closed-loop performance than the nominal case.

Stability is not explicitly mentioned during the design procedure here, but must be assured, of course. The objective function J can be interpreted as a Lyapunov function [2, 11] of the system output. If the plant is stable and if any stabilizing controller with the chosen IMC time constant exists, the solution of the optimization is stable as well. Both assumptions hold for the models and solar plants considered here.

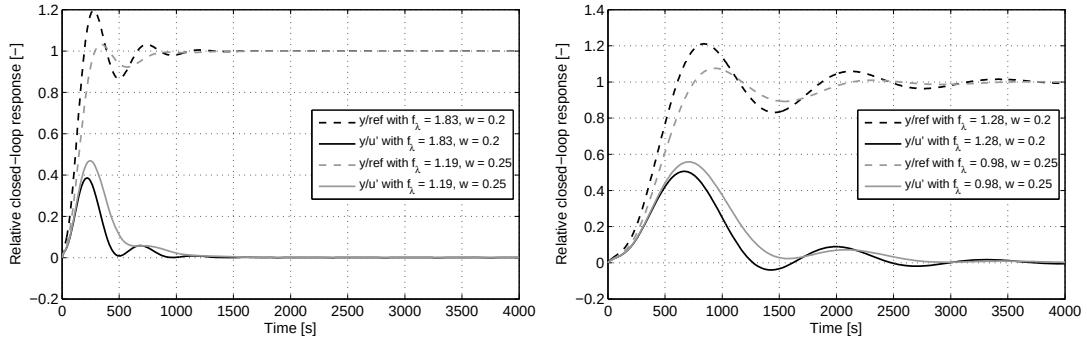

Figure 4.11: Closed-loop system responses to steps of input variable (u') and reference (ref) simulated with the nominal LTI model for optimized tuning factor at a given weight at 900 W/m² (left) and 375 W/m² (right).

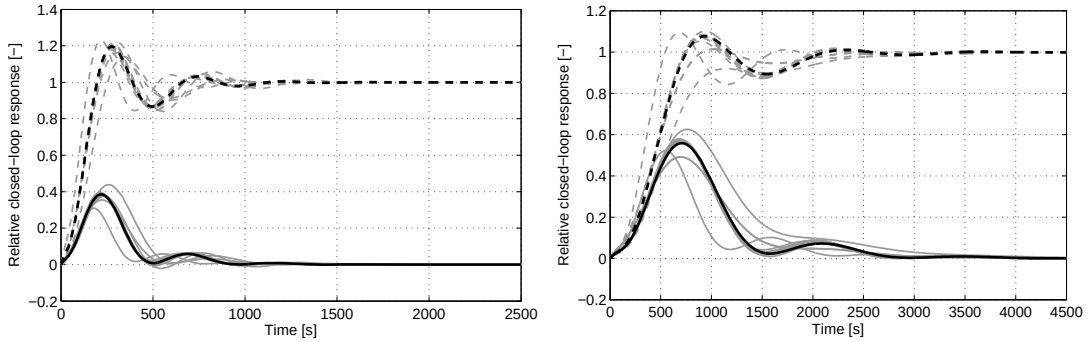

Figure 4.12: Closed-loop system responses to steps of input variable (u') and reference (ref) for optimal controller gain by weight 0.2 at 900 W/m² (left) and weight 0.25 at 375 W/m² (right), simulated with nominal model (black) and various other (grey) LTI models in the range of 0.92...3.1 of nominal characteristic time and 0.76...1.36 of the nominal plant gain.

Note that the approximation of the IMC time constant (see Figure 3.15 on page 65) is very good for all models and was not changed for the controllers. The gain optimization can then also be interpreted as a kind of pole placement strategy. This is illustrated for the nominal controller at 900 W/m² in Figure 4.13. The controller introduces an open-loop zero on the real axis at the inverse of the IMC time constant (1/200 s^{-1}). Thereby, the root loci lines are fixed and the gain of the controller moves the additional closed-loop poles along the lines in the direction of the zeros. A good compromise between speed and smoothness is usually achieved, when the additional slow closed-loop poles are close to each other. A minimum damping must be considered for pole pairs in order to avoid extensive oscillations. More aggressive pole placement strategies would place the controller zero closer to the inverse of the characteristic times $\tau_{c,rp}$ or even $\tau_{c,sl}$. This can lead to a less oscillating and only slightly slower closed-loop response for the nominal models, but at the price of a higher first peak (e.g. compared to y/u' in Figure 4.11 left). Detailed descriptions can be found e.g. in

[11, 132]. Robustness against uncertainty is usually smaller compared to the IMC approach taken here [175].

The resulting controller design is depicted as Bode plot in Figure 4.14. Cloud disturbances can happen at various and random frequencies. Ideally, the controller should be able to reject disturbances in the range of 10^{-3} s^{-1} to $4 \cdot 10^{-2}$ s^{-1}. These values correspond to cloud patterns with a period of about 25 s to 1000 s, respectively. Low frequencies indicate large, but slow moving clouds. High frequencies indicate very small and fast clouds that periodically cover the plant. At high loads with relatively short delay, the magnitude peak of the disturbance rejection in the Bode plot can be shifted to high frequencies. For both the conservative and aggressive controllers the peak has a magnitude smaller than one. In consequence, the resulting system response is able to at least reject some part of the disturbance, although it amplifies the disturbance more than an uncontrolled plant – of course, only at those frequencies. For lower loads and longer time delay, the peak is shifted to lower frequencies, making it more likely to be met at relevant operating conditions. Care must be taken during such weather conditions. If they happen regularly, adapted, i.e. detuned, controller parameters for these conditions may be a good option. This topic is briefly discussed in section 4.3.4 on adaptation.

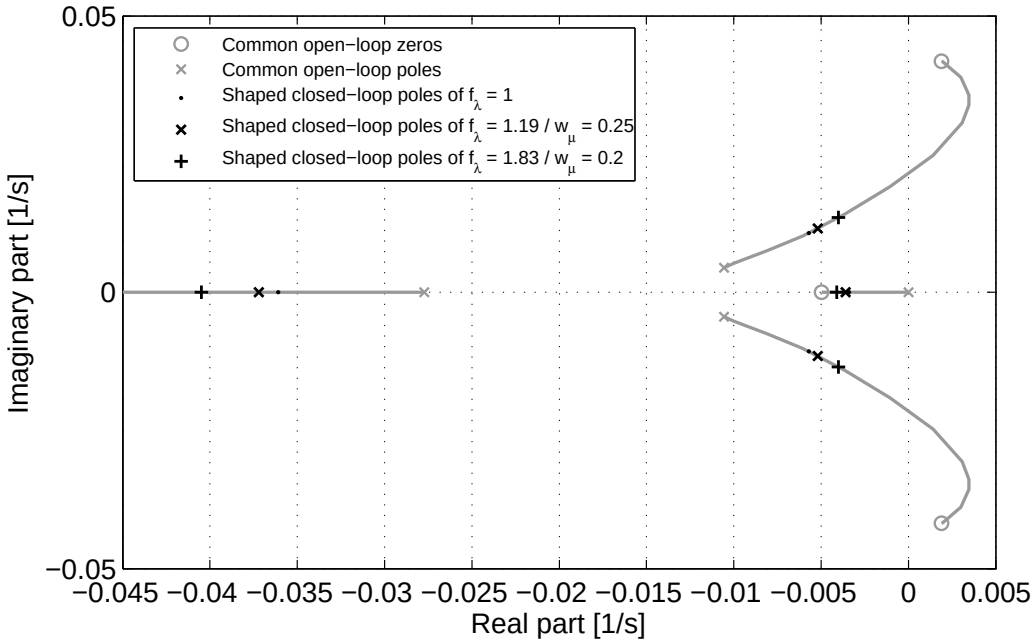

Figure 4.13: Root locus plot of the closed loop system μ(s) for various tuning factors with the nominal LTI model at 900 W/m².

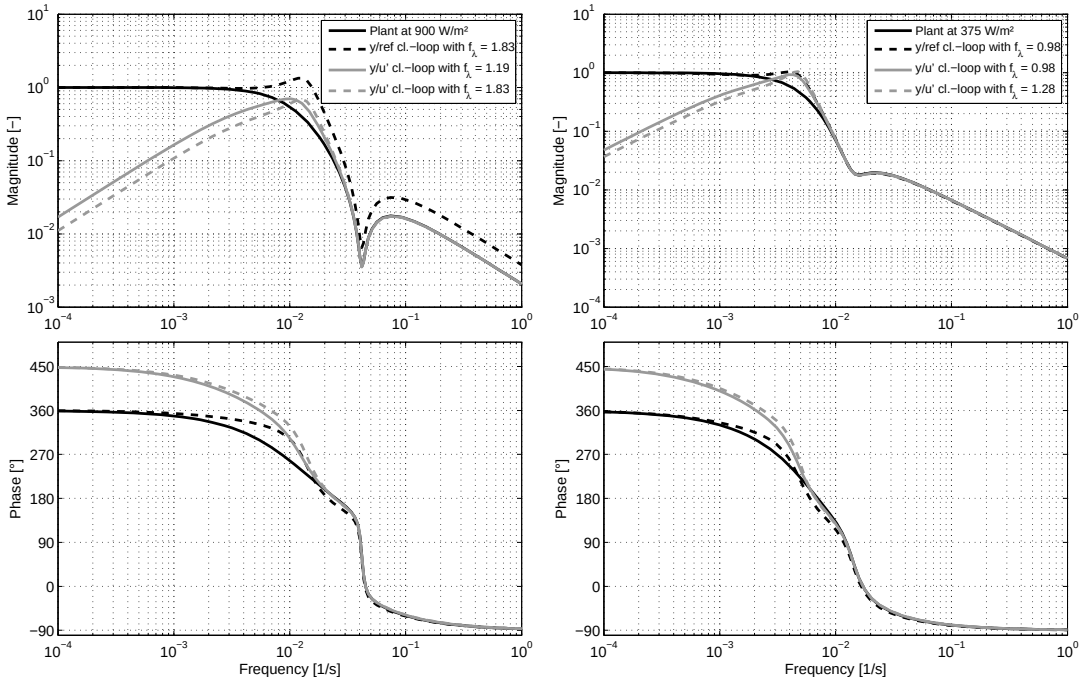

Figure 4.14: Bode plots for the nominal LTI plant model and the closed-loop system for SHI to outlet temperature at 900 W/m² (left) and 375 W/m² (right).

From optimization or pole placement, the optimal values for the controller gain can be calculated. This is performed for each LTI model and the resulting values are plotted against the steam mass flow after the superheating injection in Figure 4.15. For high and low loads, the clustering is very good, while for medium loads, there are high deviations. A simple linear approximation is one solution that is more aggressive for high loads and gets more conservative for lower loads. This leads to an easily implementable gain scheduling scheme, which is described in more detail in section 4.3.4.

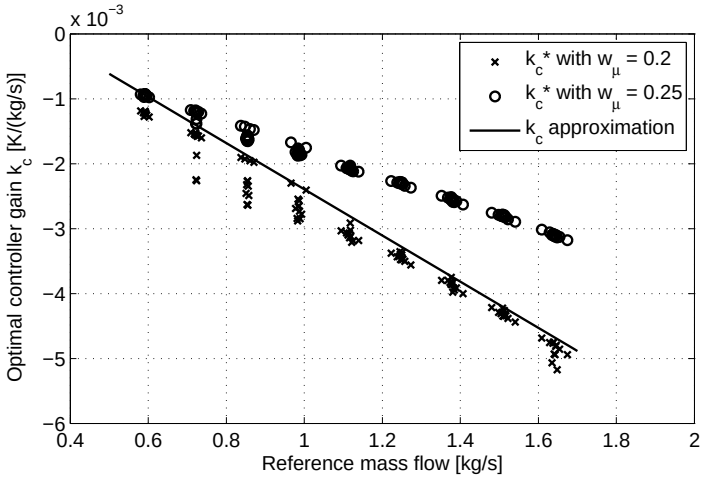

Figure 4.15: Optimal SHI controller gain calculated by objective function for different weights and its approximation for controller implementation.

The same approach is used for all other PI controllers here. Therefore, it is useful to summarize it again:

1. Set the controller integration time constant equal to the approximation function of the characteristic IMC time constant from section 3.4, i.e. $\tau_I = \tau_{c,imc}$.
2. Find a tuning factor f_λ such that the shape of the closed-loop response to an input disturbance step (y/u') shows a good compromise between small first peak and low oscillations. This can be automated either by solving an optimization problem (4.12) or by defining desired poles in the root locus curve (Figure 4.13).
3. Calculate the controller gain k_c from the optimal tuning factor.
4. Repeat steps 1 to 3 for all LTI models or for at least all nominal LTI models.
5. Define an approximation of the controller gain k_c as dependency of the main mass flow (after the manipulated valve).

An important aspect is the saturation of the manipulated variable. If the minimum or maximum of the manipulated mass flow is reached, an anti-windup [2] for the control signal and the integrational term must be activated. This is standard in commercial control systems and not described here in detail. Additional anti-windup must be foreseen for the case when the controlled temperature falls to saturation, i.e. there is two-phase flow instead of superheating.

The following sections summarize the results achieved for the other plant sections to be controlled.

4.3.2.2 Evaporation injection to temperature before SHI

The control of the temperature before the superheating injection by the evaporation injection is very important for commercial plants. The influence of the crossover piping is reduced compared to the transfer behavior of the SHI to the outlet temperature of the DISS facility, which was considered in the sections above. Thus, the resulting controllers of this section are very similar to the ones in commercial plants for controlling a superheated temperature by an injection. The same objective function (4.12) is applied with weights of 0.24, 0.2 and 0.15. The resulting step responses at 900 W/m² are shown in Figure 4.16 (left). Note that the maximum control deviation in the input disturbance rejection response (0.5 at weight 0.20) is greater compared to the response of the SHI (0.4 at weight 0.20). This is due to the longer collector section of 200 m for the EVI and the reduced thermal inertia by the shorter crossover piping. The system response also tends to oscillate more. This can cause problems for the downstream SHI controller as well. Little oscillations are thus desirable for the

EVI controller response. The corresponding approximations for controller gains are depicted in Figure 4.16 (right) for the two conservative weights.

In principal, the system response to the EVI depends on the designed reference temperature or, more precisely, on the share of evaporation length to superheater length of the controlled plant (between EVI and SHI in this case). As the system is almost isothermal in the evaporation section, the damping of the piping's thermal inertia is negligible in that part [59]. Note that this adds to the model uncertainty. A longer evaporation share implies a faster response, which should still be manageable by the controller. This further supports the choice of the conservative weighting.

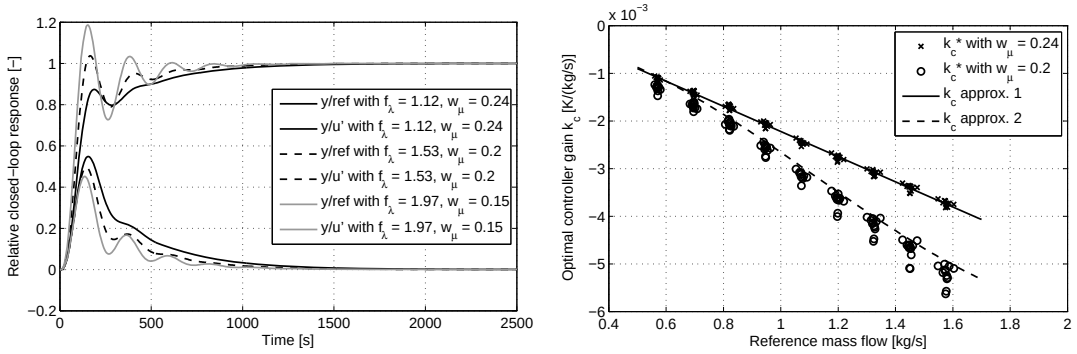

Figure 4.16: Optimal results for the EVI controller gain for temperature before SHI; resulting step responses for reference (y/ref) and input disturbance (y/u') steps at 900 W/m² (left) and optimal controller gains with possible approximations (right).

4.3.2.3 Evaporation injection to outlet temperature

The control of the outlet temperature by the EVI is less effective than the control of the temperature before the SHI because of the long distance between injection and outlet. For the DISS facility, the distance is a collector length of 350 m plus additional crossover piping of about 70 m. The long time delay requires the tuning factors be lower than in the before mentioned cases. Acceptable system responses are achieved by higher weights of 0.3 and 0.25 now (Figure 4.17, left). The maximum control deviation increases to about 0.65 for a weight of 0.25 at 900 W/m². Corresponding controller gains are depicted in Figure 4.17 (right).

It is important to take a look at the Bode plots of the resulting closed-loop systems, as shown in Figure 4.18. The amplitude peak of the disturbance rejection is at the relevant frequencies between $3*10^{-3}$ s^{-1} (period of 330 s) and 10^{-2} s^{-1}. This indicates that certain periodic cloud combinations at those frequencies cannot be compensated by the controller. In fact, at low loads, they are even amplified. This is a limitation of the plant and there is no PI controller that could shift the bandwidth to higher frequencies. Thus, the performance of

the controller is very limited and effective disturbance rejection is not possible. In consequence, such a controller must be accompanied by controller parameter adaptation, additional state feedback, reliable feedforward action – which is complicated, as will be discussed in the next sections – and by additional collector control. The corresponding loop layout of variant B, only equipped with the EVI, shows significantly worse performance than variant A during cloudy weather conditions.

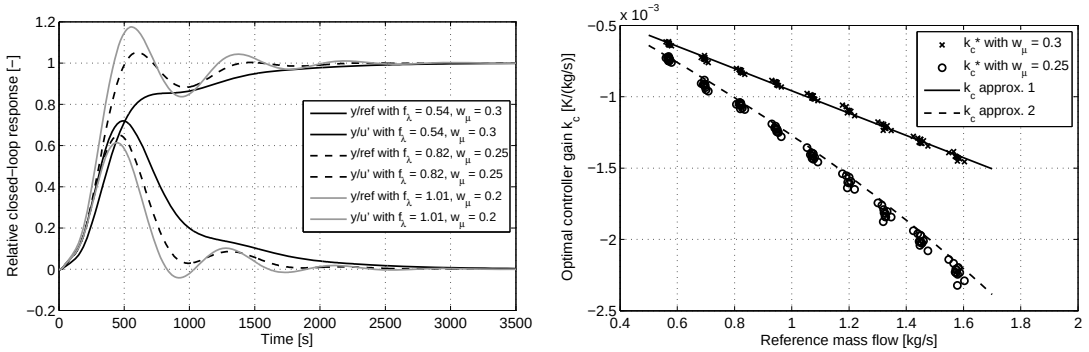

Figure 4.17: Optimal results for the EVI controller gain for outlet temperature; resulting step responses for reference (y/ref) and input disturbance (y/u') steps at 900 W/m² (left) and optimal controller gains with possible approximations (right).

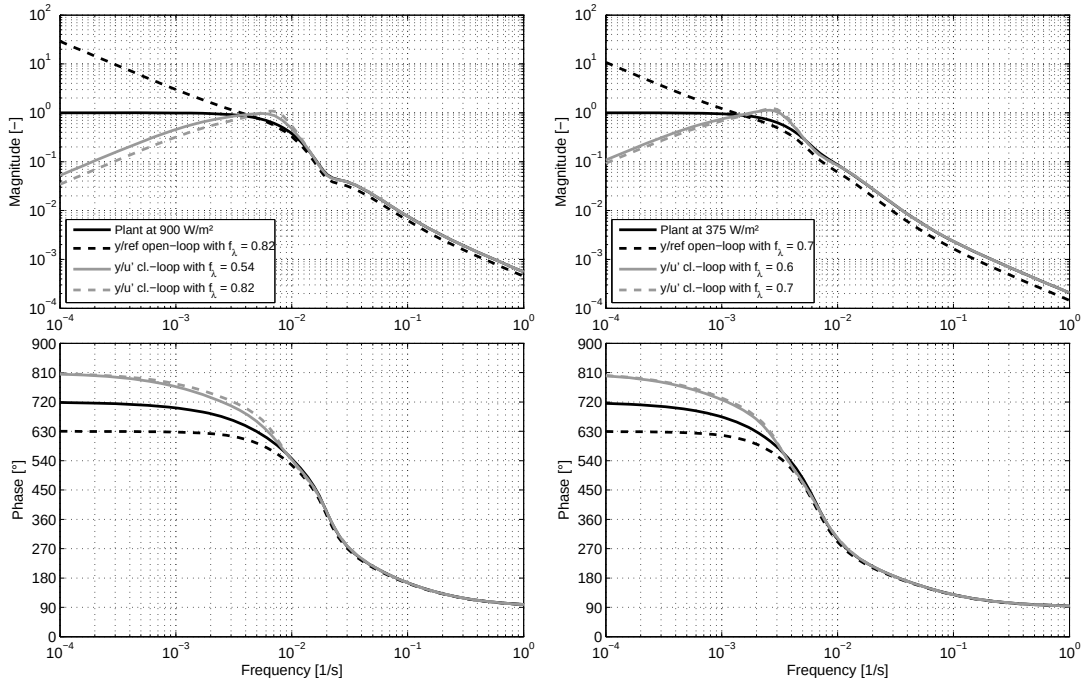

Figure 4.18: Bode plots for the nominal LTI plant model and the closed-loop system for EVI to outlet temperature at 900 W/m² (left) and 375 W/m² (right).

4.3.2.4 Inlet mass flow to the temperature before injection

The control of the temperature before the SHI by the inlet mass flow is discussed now. System characterization reveals very long step responses that are in the same range as homogeneous DNI variations along the loop. Any faster disturbance cannot be rejected in an acceptable time. Even DNI disturbances cannot be rejected well, as there will always be a delay between the controller recognizing the disturbance and a significant controller answer. This can be seen in Figure 4.19 (left). The maximum control deviation is in the range of 0.9 after about 900 seconds. Within this period, the disturbance is likely to already have disappeared. Then the controller action leads to even worse results. Thus, even under ideal step response conditions, the controller takes more than one hour at 900 W/m² to counteract the disturbance. At lower load, such ideal conditions result in more than two hours for complete disturbance rejection. This is unacceptable for control. Note that the disturbance rejection as shown in the figure is only valid for homogeneous DNI disturbances along the loop. Short local DNI disturbances in the superheating section rather act as an output step (mirrored y/ref response). Such disturbances are rejected slightly better, but still very slow. High oscillations during the response must be avoided, since a small fluctuation in the inlet mass flow already results in high temperature variations at the outlet. The injections may then have to use their complete operating range to counteract inlet oscillations – or run out of range. Weights of the objective function must therefore be chosen high to smooth the response. Controller gains are shown in Figure 4.19 (right) and must be considered for reference tracking rather than disturbance rejection. Weights should be increased for lower loads. Bode plots are shown in Figure 4.20. Input disturbance rejection is not successful, but worsens the situation by the controller in the relevant frequencies for all loads. It is thus better not to implement this kind of controller and to only use the injections.

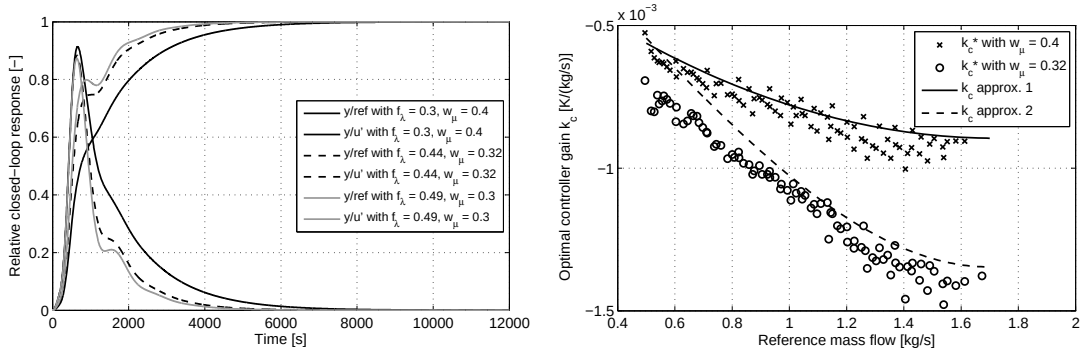

Figure 4.19: Optimal results for the IMF controller gain for outlet temperature; resulting step responses for reference (y/ref) and input disturbance (y/u') steps at 900 W/m² (left) and optimal controller gains with possible approximations (right).

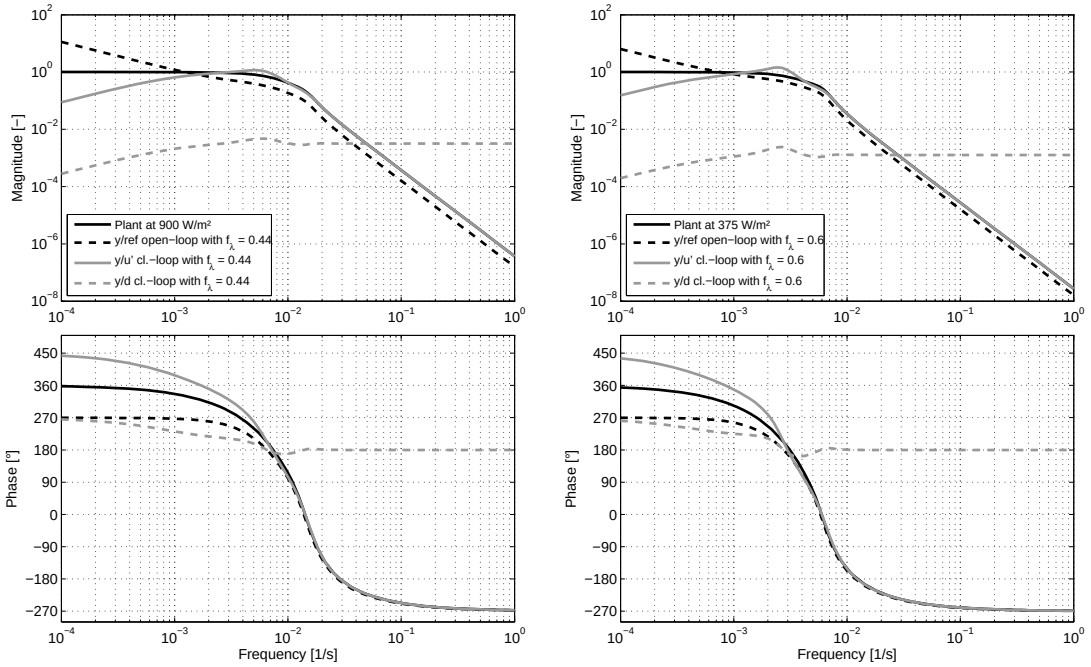

Figure 4.20: Bode plots for the nominal LTI plant model and the closed-loop system for inlet mass flow to temperature before SHI at 900 W/m² (left) and 375 W/m² (right).

4.3.2.5 Conclusions for different loop layouts

Concluding the basic controller design, a methodology to design PI controllers for solar once-through boilers is suggested. Good disturbance rejection is only achieved along short distances, e.g. from the EVI to the SHI and from the SHI to the outlet. Disturbance rejection by the inlet mass flow is ineffective and very slow due to the long time delay involved. In consequence, variant A with two injections is the only variant able to effectively reject disturbances by the suggested PI controllers. The inlet mass flow is based on pure feedforward action with the help of average DNI measurements. Variant B and D (only EVI) may only be used for short superheating sections. Otherwise the same effect as for the inlet mass flow appears, i.e. the control action can even worsen the performance. Variants B and D can significantly be improved by additional proportional feedback or MPC approaches. Variant C (only SHI) can work with PI control and additional proportional feedback for the SHI controller. Its inlet mass flow is again only based on feedforward control. Due to its robustness, the recommended control should be performed by variant A. Therefore, the following sections focus on this variant. The other variants are only briefly described.

4.3.3 Feedforward

The main controller's task is to reject disturbances during operation and keep a constant temperature. If a disturbance happens, the system needs a certain time to react to it. Then, the controller needs additional time to react and, after that, the system needs additional time to respond. This can take a lot of time due to the long delays of the system. If disturbances can be measured, it is thus helpful to let the controller counteract it already before the system reaction is apparent. This is called feedforward control.

Feedforward action must be applied with caution. If the dynamics or the measurements of the variable are uncertain, a misleading feedforward term acts as an input disturbance.

There are many disturbances that can appear, e.g. changes in inlet temperature, irradiation, ambient temperature, injection water temperature. A perfect controller should consider all of them. In fact, former DSG control concepts foresee a variety of feedforward actions [57, 152, 254]. However, this perfect controller is limited by design and model effort as well as by measurement accuracy and effort. Furthermore, some disturbances happen very slowly, such that the new PI controller can easily handle them without prior action.

Table 4.1 provides an overview on the most important system disturbances and their consideration in feedforward control for the SHI. In its simplest version, the SHI controller only uses the temperature before the SHI as feedforward variable. In contrast, the state-of-the-art concepts use eight or more different terms. The differences result from assumptions for large scale solar fields and the more aggressive design of the PI controller in this work. They are explained in more detail below.

The EVI controller in its basic version has no feedforward at all. However, it would be desirable to measure the enthalpy before the EVI. This would significantly improve the performance – analog to the temperature before the SHI for the SHI controller. Measurement techniques for steam void fraction are available [59], but they are very expensive, require a lot of extra process effort and show high uncertainty [57, 279]. The subsequent calculation of enthalpy further increases this uncertainty. In consequence, enthalpy before EVI cannot be used for feedforward at the moment. Nevertheless, it can be considered as the most important missing sensor for DSG technology.

Table 4.2 provides the same overview for the feedforward of the inlet mass flow controller. Differences to former approaches are small. The most important differences, however, are the consideration of a clear sky DNI model together with the IAM. The following paragraphs explain the differences and significance of the single disturbances.

Table 4.1: Disturbances considered for feedforward control of superheater injection (SHI).

Variable	*SHI Simple*	*SHI Advanced*	*Former approaches [57, 254]*
Current DNI	Not used	Recommended (if measured for superheater)	Yes
Temperature before SHI	Important	Important	Yes
Temperature after SHI	Not used	Not used	Yes
Inlet temperature	Not used	Not used	Yes
Injection water temperature	Not used (see adaptation)	Not used (see adaptation)	Yes
Steam mass flow before SHI or at outlet	Not used	Not used	Yes
Outlet pressure	Not used	Recommended	Yes
Ambient temperature	Not used	Not used	Yes
Wind speed	Not used	Not used	Some
IAM	Not used	Recommended	Yes
Clear sky DNI model	Not used	Recommended	Not used

Table 4.2: Disturbances considered for feedforward control of inlet mass flow (IMF).

Variable	*IMF Basic*	*IMF Advanced*	*Former approaches [57, 254]*
Current DNI	Important	Important	Yes
Inlet temperature	Recommended	Recommended	Yes
Injection water temperature	Not used	Not used	Yes
Steam mass flow before SHI or at outlet	Not used	Not used	Sometimes
Outlet pressure	Recommended	Recommended	Yes
Ambient temperature	Not used	Helpful	Yes
Wind speed	Not used	Not used	Yes
IAM	Important	Important	Yes
Clear sky DNI model	Recommended	Important	Not used
Collector focus state	Recommended	Important	Yes

4.3.3.1 Temperature before the superheating injection

If the dynamics are minimum phase, correspond to the dynamics of the manipulated variable and a good model exists, the feedforward action can be based on the static gain of the transfer function. This gain can be calculated from steady-state energy balance. Those for the superheater section can be formulated to calculate the outlet enthalpy of the loop h_{out}:

$$h_{\mathrm{out}} = \frac{\dot{m}_{\mathrm{bi}} h_{\mathrm{bi}} + \dot{m}_{\mathrm{inj}} h_{\mathrm{inj}} + Q_{\mathrm{eff}}}{\left(\dot{m}_{\mathrm{bi}} + \dot{m}_{\mathrm{inj}}\right)} \tag{4.13}$$

The subscript “bi” indicates states before the injector in the main steam line. The subscript “inj” indicates states of the injection water and “out” the loop outlet condition.

The change in outlet temperature by a change in injection mass flow is given by its derivative:

$$\frac{\mathrm{d}\vartheta_{\mathrm{out}}}{\mathrm{d}\dot{m}_{\mathrm{inj}}} = \frac{\dot{m}_{\mathrm{bi}} h_{\mathrm{inj}} - \dot{m}_{\mathrm{bi}} h_{\mathrm{bi}} - Q_{\mathrm{eff}}}{\left(\dot{m}_{\mathrm{bi}} + \dot{m}_{\mathrm{inj}}\right)^2 c_{p,\mathrm{out}}} \tag{4.14}$$

Note that enthalpy is approximated by heat capacity c_p and temperature. For the case of a disturbance of the steam temperature before the injection, the resulting (steady state) change in outlet temperature can be described by the following derivative:

$$\frac{\mathrm{d}\vartheta_{\mathrm{out}}}{\mathrm{d}\vartheta_{\mathrm{bi}}} = \frac{\dot{m}_{\mathrm{bi}} c_{p,\mathrm{bi}}}{\left(\dot{m}_{\mathrm{bi}} + \dot{m}_{\mathrm{inj}}\right) c_{p,\mathrm{out}}} \tag{4.15}$$

The change in injection mass flow and in temperature before the injection must give the same outlet temperature change for an ideal feedforward control. The differential equations are now considered as difference equations, solved for outlet temperature and set equal. The resulting equation is:

$$\Delta\dot{m}_{\mathrm{inj}} = \frac{\left(\dot{m}_{\mathrm{bi}} + \dot{m}_{\mathrm{inj}}\right)\dot{m}_{\mathrm{bi}} c_{p,\mathrm{bi}}}{\left(\dot{m}_{\mathrm{bi}} h_{\mathrm{inj}} - \dot{m}_{\mathrm{bi}} h_{\mathrm{bi}} - Q_{\mathrm{eff}}\right)} \Delta\vartheta_{\mathrm{bi}} \tag{4.16}$$

This equation can be used as additional feedforward signal for the injection mass flow ($\Delta\dot{m}_{\mathrm{inj}}$) depending on the temperature before the SHI ($\Delta\vartheta_{\mathrm{bi}}$). The effective heat input Q_{eff} can be estimated by the absorbed heat and the heat losses in the superheating section:

$$Q_{\mathrm{eff}} = Q_{\mathrm{abs}} - Q_{\mathrm{loss}} = w_{\mathrm{ap}} \Delta z \, G_{\mathrm{b}} \eta_{\mathrm{opt}} - q_{\mathrm{loss,L,mean}} \Delta z \tag{4.17}$$

The heat terms are taken from equations (3.14) and (3.16). The variable Δz in this case denotes the length of the superheating collectors between injection and loop outlet. The length-specific heat loss should be averaged over the su-

perheating section, e.g. by a simple equation for high temperatures as suggested in [265]:

$$q_{\mathrm{loss,L,mean}} = \frac{1}{\vartheta_{\mathrm{out}} - \vartheta_{\mathrm{in}}}\left(\frac{1}{2}c_1\left(\vartheta_{\mathrm{out}}^2 - \vartheta_{\mathrm{in}}^2\right) + \frac{1}{5}c_4\left(\vartheta_{\mathrm{out}}^5 - \vartheta_{\mathrm{in}}^5\right)\right) \tag{4.18}$$

The temperatures of the inlet and outlet of the corresponding section are considered here. The coefficients c_1 and c_4 are as described for equation (3.16).

Equations (4.16) to (4.18) together provide a good estimate of the feedforward correction. Note that they are different to the linearized equation used in [57]. The equations here assume that various system parameters are measured, which would result in a lot of sensors. For large scale plants, significant reduction is needed.

It is recommended to measure the injection mass flow as a minimum requirement, since this measurement is not only needed for SHI feedforward, but also for controller adaptation. In addition, the mass flow is a manipulated variable that should be checked to work properly and it can be an input to energy balances for performance evaluation. Considerations of other measurements are covered within the following sections.

4.3.3.2 Temperature of injected water

The temperature of the injected water should be known for equation (4.16). However, it is usually not necessary to measure it in all loops as it changes slowly. The injected water is taken from the main feed water line, whose temperature is measured for control and performance evaluation anyway. There is a deviation to this feed water temperature, since the injection line is separated at some point and has different thermal inertia and flow velocities. This can be corrected, if the temperature is measured at two or more loops of the plant, e.g. the last and the first loop of a subfield. The water temperature can then be modeled or estimated, respectively. This estimation can reduce the temperature measurements significantly for large scale plants. Note however, that these measurements may be required by an operating company or owner for reliable performance evaluation of the plant.

When changes in injection water temperature shall be compensated, a formulation analog the one above results in:

$$\Delta\dot{m}_{\mathrm{inj}} = \frac{\left(\dot{m}_{\mathrm{bi}} + \dot{m}_{\mathrm{inj}}\right)\dot{m}_{\mathrm{inj}}c_{p,\mathrm{inj}}}{\left(\dot{m}_{\mathrm{bi}}h_{\mathrm{inj}} - \dot{m}_{\mathrm{bi}}h_{\mathrm{bi}} - Q_{\mathrm{eff}}\right)}\Delta\vartheta_{\mathrm{inj}} \tag{4.19}$$

As the injection mass flow (as a factor in the numerator) is significantly smaller than the main steam mass flow, the influence of the water temperature on the mass flow change is rather low. It is thus only worth implementing, if very high gradients in water temperature are expected. This can be the case

during start-up procedure and/or if a hot wave is reaching the injectors with significant time delay after heating up. This phenomenon is especially observable at the DISS facility, but can be reduced by opening the injection lines early during the start-up phase. Even during high transients greater than 100 K, the resulting deviation of the steam temperature is smaller than 6 K, as e.g. shown in Figure 3.51. Experiments at the DISS facility promote this result and no significant influence even during higher transients was visible. In consequence, the water temperature is not used for feedforward in the new concepts suggested in this work.

There is one decisive aspect of water temperature that has been ignored so far. Although the feedforward, based on the overall energy balance, turns out to be negligible, the water temperature has a decisive influence on the injection gain. This must be considered by adaptation of the controller gain, as will be described in section 4.3.4.

4.3.3.3 Outlet steam mass flow

The mass flow before the SHI – or as an alternative the complete outlet steam mass flow – could be measured in principle. Nevertheless, such a sensor for steam mass flow is rather expensive and not very accurate. A simpler variant is to use the inlet mass flow into the loop added by the mass flows of the injection(s). By that, one assumes that the system is in steady state, which is of course not correct for highly dynamic situations. It is thus a trade-off between more accurate feedforward and higher investment. In the following, it is assumed that the sensor is not available.

The steam mass flow can be considered as feedforward signal itself. After sudden drops in irradiation, the steam mass flow falls rapidly. Using its derivate as feedforward signal can improve the controller performance [152]. Nevertheless, the LTI models from the simulations already consider such mass flow changes implicitly. Experiments showed that the controller reacts fast enough without this feedforward action. In consequence, it is a recommended option to save costs.

4.3.3.4 Mixing temperature after the SHI

The inlet temperature to the controlled section, that is the steam temperature after the SHI, could be measured. However, a long section for homogenization, which is necessary for an accurate measurement, is usually not acceptable between collectors in order to save costs and space. Thus, the measured temperature cannot be used as feedforward signal – as it is usually done in fossil plants. The calculation of the temperature by an energy balance is possible, but its result is already implicitly included in the feedforward term of the temperature before the SHI. Thus, no additional feedforward term is needed.

4.3.3.5 Local irradiation

The DNI is not assumed to be measured at all locations of a large solar field. Sensors are too expensive and cloud formations are random, such that a perfect covering with DNI sensors is unlikely. An averaged irradiation signal of the plant is used for equation (4.16), accepting that a cloud could pass over the superheating section and shortly lead to wrong feedforward signals.

If a better guess on irradiation is available, it should be used. At the DISS facility, pyranometers with two side plates are installed on the collectors and tracked with them. Although pyranometers measure the global irradiation, the side plates act like a shield and stress the direct character of the signal. The result is a barely defined mixture between direct and global irradiation. No exact absolute value of DNI can be derived from it. Nevertheless, if such signals are understood better or are further developed, they could offer additional information to control. Due to its improved direct irradiance character, the derivatives of the shielded pyranometer signal allow for guessing of current changes in DNI at that point. Such a gradient can serve as feedforward signal. A similar signal might be found from small photovoltaic cells. If they were measured distributed along the loop, a good guess of irradiation even in the unobservable evaporation section might become possible. Such ideas are proposed for future research and testing, since they offer very promising control improvements.

The controllers considered in this work do not employ such local irradiation measurements.

4.3.3.6 Average DNI and effective irradiation

The effective irradiation is the most important variable for the system. It is defined by equation (3.15) as the product of DNI, current optical efficiency and a focus signal. The current optical efficiency is assumed to be known, with the real cleanliness of the mirrors as dominating uncertainty. Note that for the DISS facility, the IAM is also a major uncertainty due to the variety of different collectors. The IAM uncertainty is assumed to be much lower for commercial plants with only one type of collector. The focus signal is usually known to the control system, assuming that a focused collector (signal is 1) is completely focused and a defocused collector has negligible heat input (signal is 0). Again, this assumption does not necessarily hold. A defocused collector that is tracking with a certain offset to its ideal focus will also generate a small heat input to the system. Diffuse irradiation and the low heat losses of commercial receivers is already sufficient (see e.g. [116] for more details). A good approximation from DISS experiments shows about 2 % “optical efficiency” for defocused collectors in the so-called “destir mode”. This is reduced to almost no heat input, if the collector is in stow position and the mirrors are facing the ground.

The main unpredictable heat input is the direct normal irradiance. The DNI is measured by pyrheliometers with a very small acceptance angle and an uncertainty of about 1 to 2 % [134, 262]. The pyrheliometers are directly facing the sun position by a two-axis tracker. Only few sensors are installed in a commercial plant because of the high costs of the complete measurement system, with the high-precision tracker being the main cost driver [135].

For equation (4.16), an averaged irradiation signal of the solar field is used. It is highly recommended to never base the average DNI signal on one sensor only. Experiments at the DISS test facility show very scattered clouds even for the single loop. The DNI sensor is mounted on top of the BOP building in the north of the loop. Various situations occurred with different DNI in the north and in the south. At least three or more sensors should be used and installed at different locations of a large solar field. Again, these could be accompanied by local substitutional irradiation measurements or cameras to improve the overall guess [218]. Nowcasting of the DNI from satellite and weather data or cloud cameras can also help to provide current DNI maps or predictions [109]. As such systems are not yet available commercially, they are not considered in this work, but can help to improve control in the future.

The inlet mass flow is set by the feedforward signal of the effective irradiation. A simple variant, as used in this work, is to pre-calculate the inlet mass flow as a function of the effective irradiation by steady-state heat balances. If operation conditions such as the inlet temperature and the outlet pressure are not varying much, it is sufficient to use only this dependency for feedforward. Otherwise, a more complex function considering significant influences should be used [254]. Another option is to solve the heat balances directly online during operation by using the desired outlet temperature and injection mass flows.

Note that this pure feedforward action is only justified, because of the long time delay of the inlet mass flow response, as derived in section 4.3.2.4 above. There is no effective rejection of any disturbance. The only chance of coping with DNI variations is to use it as feedforward, since it shows the same shape and delay of system response. By averaging the DNI signal over time, feedforward becomes more robust against noise and it is assumed that all cloud disturbances are much faster. This already suggests that the time constant of the filter of the DNI signal should be adapted to the weather conditions. This is analyzed in more detail in the adaptation section below.

Slow changes and deviations in effective irradiation over the day can usually be dealt with by the suggested feedforward scheme and the PI controllers of the injections. Problems arise when DNI and incidence angle change quickly in the evening. The feedforward term must therefore at least include a model of the mean incidence angle modifier (IAM) for the current throughput time of the loop. Note that this was not foreseen in former approaches such as [254] or

[152]. Especially in winter afternoons, the IAM is slowly increasing, while the DNI can already decrease rapidly. Only using the IAM for prediction thus leads to an imbalance in the loop, which can only be compensated by the injections for a short time. Additional advancement can be achieved, if a clear sky day is modeled and its characteristic curve of the DNI is used as reference for DNI changes. The prediction factor for clear sky f_{clsky} can be formulated by the help of the forecast horizon τ_{pre}:

$$f_{\mathrm{clsky}}(t_0) = \frac{1}{\tau_{\mathrm{pre}}\, IAM(t_0)\, DNI_{\mathrm{clsky}}(t_0)} \int_{t_0}^{t_0+\tau_{\mathrm{pre}}} IAM(t)\, DNI_{\mathrm{clsky}}(t)\, dt \qquad (4.20)$$

It calculates the expected relative change in energy input during the residence time of the fluid. The IAM must include the cosine of the incidence angle in this formulation. The forecast horizon should be in the range of the fluid residence time in the loop. Ideally, it is adapted based on the clear sky or current inlet mass flow. The clear sky factor is then multiplied with the feedforward signal from current effective irradiation to give the final inlet mass flow setpoint. Note that the clear sky factor can be pre-calculated for each day, if the forecast horizon is constant or set equal to the ideal clear sky mass flow. However, the clear sky model may have to be adapted during the day because of changing atmosphere conditions. Then, an adaptation scheme for estimation of the clear sky DNI can improve the forecast and feedforward performance. Very good results are already achieved by using the convex hull of the measured DNI of the day before as a prediction of the clear sky DNI function. An example of such a hull is depicted in Figure 4.41 on page 168. As equation (4.20) gives only a relative signal, small deviations of the DNI model are not significant. Only after severe atmospheric events, such as sand storms or rain, this approximation may be misleading and care must be taken.

4.3.3.7 Ambient conditions

Changes in ambient temperature have very slow dynamics and the influence on the system is negligible compared to other uncertainties. High wind velocities can lead to higher heat losses as well [32]. However, their impact again is negligible for a large scale loop. The modelling is more accurate taking ambient effects into account, especially for the feedforward of the complete loop. The result for control performance, however, is not significantly influenced. As not all ambient conditions – and other unusual ones might appear – can be foreseen, verification is recommended for each particular site.

4.3.3.8 Collector defocus

If problems with a collector occur and it has to be defocused, a feedforward action scheme should be designed to reject the resulting disturbances. As it is

an intended disturbance, it can be predicted quite well and feedforward action could be done jointly by the inlet and injection controller. This case is not critical, if it is foreseen in the operation scheme. Thus, it is recommended to design a feedforward scheme for failure/defocus of each individual collector of the loop. Especially for collectors close to the inlet, this is a very important safety requirement of a commercial plant.

The design of such a feedforward is not part of this work. Procedures for it can be found in various text books on control, e.g. [11]. Corresponding LTI models are derived in chapter 3.4.8.

This work concentrates on rejecting an unforeseen and mainly unmeasured disturbance. Let us consider that the first collector has a sudden failure, which is not known to the control system. A steep increase of superheating temperature is then followed by a steep decrease. The steep increase could be smoothened by defocusing one of the first superheating collectors. The steep decrease could be smoothened by focusing this collector again. From an energetic point of view, only the final energetic loss of the first collector must be compensated by a different inlet or injection mass flow. However, from a dynamic perspective, the defocusing of the first superheating collector also results in an additional decrease in steam mass flow. The problem at the loop outlet thus becomes worse. To counteract the inlet density disturbance, the de-/re-focusing of superheating collectors should ideally be concerted throughout all or various collectors, e.g. by defocusing all collectors by about 5 %. If such a gradual defocus is not possible, the first superheating collector is the best remaining option to be defocused in order to limit the temperature increase within the superheating section. The other collectors may then have to follow, if temperature further increases. It is thus beneficial if the defocus temperatures of the superheating collectors correspond to the desired temperature profile along the loop. A fast increase in temperature can thereby be compensated as early as possible to limit its impact on the downstream collectors.

4.3.3.9 Inlet temperature

Transients of the inlet temperature cause similar system responses as collector disturbances close to the inlet. In principle, there are two possibilities to reduce such disturbances by feedforward. One is to react in the same way as collector defocus events above. The second is to also involve the inlet mass flow for such disturbances. System characterization showed that the response to inlet temperature disturbances is faster than a response to inlet mass flow. However, in a large scale power plant, it may be possible to predict the behavior of the inlet temperature quite well before it even reaches the loop inlet, e.g. if it is measured at the outlet of the power block. Additionally, the gradient and speed of the response depends on the gradient of the inlet temperature change. This

is illustrated in Figure 4.21. In consequence, the inlet mass flow can be used to compensate some part of the disturbance for some selected situations, if a good header model is available. Note however, that this is limited by loop model uncertainty and header model uncertainty. If there is a strong mismatch between the prediction and the real plant behavior, the disturbance can be amplified. The idea is thus better used in an MPC framework, considering it as multivariable optimization problem, instead of using it in a simple predefined feedforward scheme. The basic control concept does not foresee such feedforward. The behavior of inlet temperature must be considered, however, for start-up procedures of the solar field.

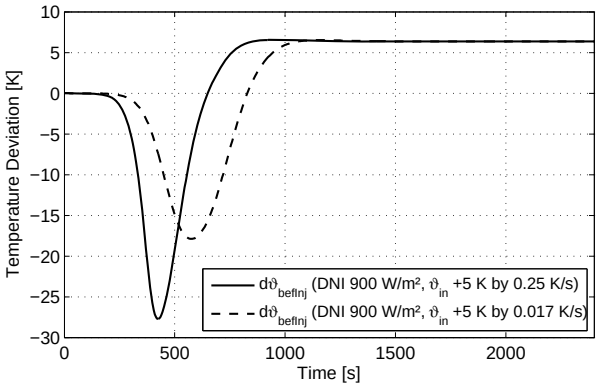

Figure 4.21: System response of temperature before SHI to inlet temperature ramps with different gradients for 900 W/m² simulated with DFEM.

4.3.3.10 Enthalpy before the EVI

The most desired feedforward for the evaporation injection would be using the enthalpy before the EVI. As it cannot be measured reliably at the moment, this kind of feedforward is not possible. However, the influence of the inlet mass flow on the enthalpy before the EVI or the temperature before the SHI, respectively, can be modeled. This compensates for measurable influences from the inlet and requires inverting the inlet mass flow LTI model. The procedures can be found in various text books on control theory, e.g. [11]. Such a feedforward is useful for clear days, during which the inlet mass flow changes are the dominating disturbances in the evaporation section. But it can also be useful for cloudy days, during which the input uncertainty is high, but the inlet mass flow varies strongly. For the sake of simplicity, the basic control scheme does not foresee such a dynamic compensation. Instead, the resulting small fluctuation of the temperature before the SHI is accepted. Note however, that it is a useful compensation, which is implicitly taken into account by any MPC scheme.

4.3.4 Adaptation

The notion of adaptation is used here to denote changes in controller parameters, i.e. time constant and gain, and changes in related equations or control algorithms. The dynamic behavior of the system can be predicted quite well with the available tools. The adaptation can thus be performed via precalculated relations. This is called gain scheduling [11]. It is easier to implement than classical adaptation, which implies that the controller parameters are changed by feedback to certain process conditions. For example, the current plant model is estimated online and an automatic controller design is performed and applied based on this new model [11]. The main and most important ideas suggested here apply gain scheduling. It can be interpreted as a feedforward schedule, which does not receive feedback whether the predefined changes are useful or not for the current system conditions. A block diagram of a gain scheduled controller is shown in Figure 4.22. The current measurements and states (*x*) from the plant are used as input to the precalculated scheduling. The controller parameters are then determined and applied to the controller.

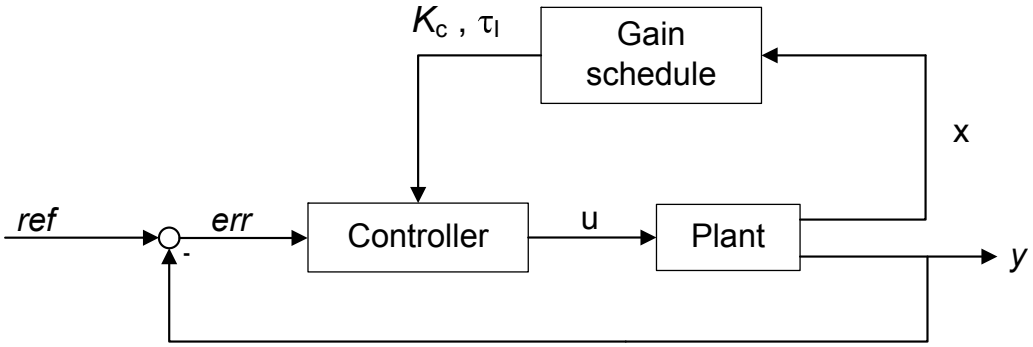

Figure 4.22: Block diagram of a gain scheduled controller, based on [11].

Such a scheme is applied for manipulating the controller parameters by mass flow, injection water temperature and control error. An extension to effective irradiation and clear sky DNI can be helpful for certain situations. Adaptation in its feedback form is suggested by estimating the current optical efficiency and the clear sky DNI model. All these suggestions, mainly derived from operational experience, are described in more detail in the following paragraphs. Although a variety of adaptions are made, each one is simplified as much as possible. The resulting control is then non-linear, which is necessary to successfully control the non-linear plant in a wide range of operating points.

4.3.4.1 Gain scheduling by mass flow and irradiation

The application of gain scheduling is not new for solar thermal power plants and an overview for solar fields with synthetic oil is given in [36]. Johansen [120] chooses a matrix of six operating regimes for scheduling. They are select-

ed based on three mass flow regions and two DNI regions. For each regime, a controller is designed based on a pole placement strategy. The resulting control scheme is good for high loads, but has poor performance for low loads. The reason is the rough scheduling matrix. The non-linearity of both oil and DSG solar fields becomes more pronounced with lower mass flow. Thus, a high resolution of underlying operating points/regions must especially be chosen at low loads.

The scheduling variable is of special interest. Various definitions for oil solar fields exist [2, 33, 120, 192]. They range from pure mass flow or DNI to ratios of mass flow and inlet temperature. Eck [57, 59] also suggests gain scheduling for the controllers of an injection mode DSG system. He uses an interpolation area based on various process conditions like pressure, inlet and outlet enthalpies, mass flow and DNI. The controller can be applied for a variety of different operating points. However, in a commercial plant, these operating points are – or should be – rather limited. A simpler scheme is thus suggested here.

As shown in the LTI identification section, the process gain and characteristic time constants can be well linked to the main mass flow at the inlet of the controlled section. Therefore, the section's mass flow seems suitable as scheduling variable of a once-through mode controller. However, the mass flow is also the manipulated variable, such that at certain excitations the system could become unstable in theory [2]. This concern can be confirmed for once-through boilers neither by simulations nor by experiments. This time, it is an advantage that there is only a delayed coupling between inlet mass flow and superheating temperatures. As the inlet mass flow is mainly dependent on irradiation by feedforward, there is no signal path to destabilize it by the injections or temperatures. On the other hand, the main mass flow, i.e. the main influence on PI controller scheduling, is the inlet mass flow. Unstable conditions can only occur if a) the scheduling is chosen wrong or b) the irradiation causes the system to fluctuate strongly. Case a) is a problem of any gain scheduling scheme and must be avoided by good design and on-site tuning. Case b) should be avoided by a good DNI signal filter for the feedforward control. In consequence, the simplest and preferred way is to choose the measured mass flow as scheduling variable.

The procedure for scheduling of the PI controller parameters of the injections can be summarized as follows:

1. The IMC time constants are determined to be a function of the mass flow at the inlet of the controlled section by simulations, e.g. the steam mass flow after the SHI defines the IMC time constants for the SHI controller.
2. A regression is performed to find an explicit, smooth function for this relation.

3. The IMC time constant function is implemented as schedule in the controller and directly defines the reset time of the PI controller.
4. For each analyzed operating point from step 1 (now with mass flow and corresponding time constant), a good controller gain is determined.
5. The controller gains are approximated by a smooth function only depending on the corresponding mass flow.
6. The gain scheduling is implemented in the control system.

After these steps, the basic pair of controller gain and time constant is defined solely by the mass flow. As mentioned above, the steam mass flows are not measured, but the inlet (water) mass flows are used as scheduling variable. The approximations are already shown in the chapters on model identification (IMC time constants) and basic controller design (controller gain). They are not repeated here. Note that the resulting performance is much better than using regimes with constant controller parameters. Further note that there is no need in using a scheduling regime matrix for DNI and mass flow as in [120]. For steady states, there is only one optimal combination of effective irradiation and mass flow. Furthermore, a scheduling of the time constant by irradiation is not useful, as they do not correlate. Only the gain is depending on both irradiation and mass flow.

Slight improvements for strong irradiation disturbances are possible, if the effective irradiation or the clear sky irradiation is also considered for scheduling of the controller gain. This is true for a measurable and fast increase in irradiation after a long period of cloud cover. A simple (weighted) interpolation scheme is then possible. The current effective irradiation is used to calculate the ideal corresponding steady-state mass flow. This mass flow is used as input to the same scheduling function as the real mass flow. The two different outputs of the function are then weighted. Tests at DISS facility with a weighting of 90 % on real mass flow and 10 % on ideal mass flow showed good results. These values have not been optimized, though, and also depend on the loop configuration.

Note that the dominating inlet mass flow is already influenced by the irradiation via the feedforward term. The extra scheduling with DNI is only useful, if significantly different time-filters of the DNI signal are used for feedforward and scheduling.

Some definitions for oil systems use the stationary heat balance and solve it for the mass flow. Then, not the mass flow, but the determining variables are used for scheduling. This is not recommended because of the complexity, the uncertain measurements of involved states and the inconsistency of the heat balance for transient situations. The performance is either equivalent or usually worse with such a scheduling scheme.

4.3.4.2 Gain scheduling by injection water temperature

It has been shown that the feedforward compensation based on the injection water temperature is not needed. However, the injection gain depends on its enthalpy flow, i.e. the product of mass flow and enthalpy, relative to the steam enthalpy flow before the injection. If the injection temperature is reduced, the difference of enthalpy compared to the steam is increased. In consequence, the injection mass flow must be varied less to achieve the same result. The gain is higher than its design value. The resulting control will show more oscillations compared to the nominal design. The gain deviation can be calculated from steady-state heat balances and is shown in Figure 4.23. The relative deviation of the gain is rather linear and almost the same for all loads, which is a very good characteristic for gain scheduling.

The best way to compensate for deviating injection water temperatures is to consider various deviations and repeat the design procedure for the gain as for the basic controller. However, a simpler option is possible. Since the controller gain is proportional to the inverse of the process gain, as shown in equation (4.11), the nominal controller gain can be divided by the relative deviation of Figure 4.23. This implies using the same tuning factor as for the nominal model. This scheme was successfully applied at DISS test facility and is recommended due to its simplicity.

Note that it is in general not recommended to inject cold water into superheated steam in order to avoid material stress and corrosion by water droplets in the steam flow.

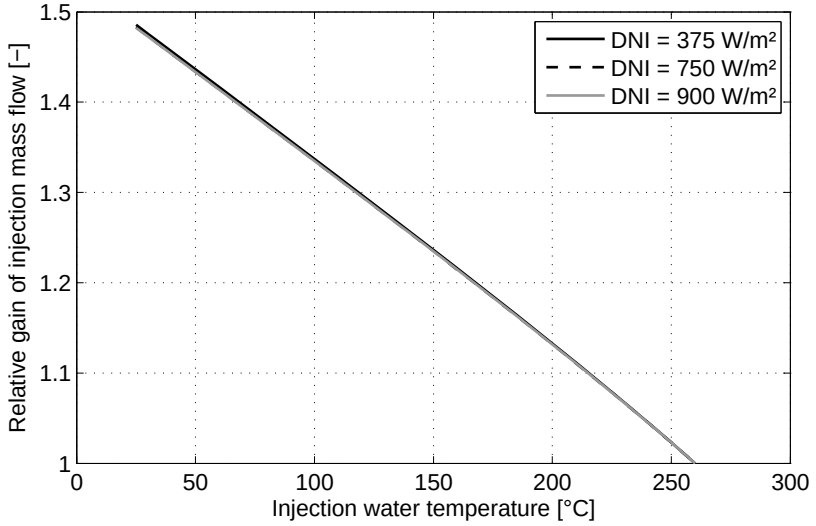

Figure 4.23: Variation of injection mass flow gain as a function of the injection water temperature; from steady-state heat balances for the SHI of the DISS facility.

4.3.4.3 Error-based gain scheduling

The main drawback of linear PI controllers has been illustrated in the controller design section. The controller gain is limited, because the final system response shall not oscillate significantly. In consequence, maximum control deviations are very high.

One option to overcome this problem is to leave the path of constant controller gain during disturbances. If the control error, i.e. the difference between measured and reference temperature, is high, one can assume that a disturbance is currently acting on the system. In this case, it makes sense to increase the controller gain to reduce the resulting maximum control deviation. The general framework of such a concept is called soft variable-structure control and is described in [3, 87, 88, 100]. The particular case of adapting PI parameters based on the control error is elaborated by Song [226] for a second order system. It is introduced as error-based adaptive control. A very similar approach is suggested here, with the difference of only varying the controller gain. It can be denoted by error-based gain scheduling (EBGS) or, from the impact point of view, gain acceleration.

The tuning factor approach of the basic controller design can be used to establish the EBGS. A tuning factor with smooth control at rather constant conditions is selected to define the basic gain. Then, a greater tuning factor with a lower maximum control deviation is chosen for disturbance rejection. During operation with large disturbances, the gain is increased from its basic value to higher values, dependent on the actual control error. Figure 4.24 (left) illustrates two possibilities to implement such a scheduling scheme. A maximum gain acceleration factor is defined, which limits the gain of the controller. The resulting controller must still stabilize the system. A threshold error should be foreseen to start the gain adaptation.

A different option is shown in Figure 4.24 (right). The derivative of the absolute values of the control error is used to adapt the controller gain.

$$f_{\mathrm{GA}} = f_{\mathrm{GA}}\left(\frac{d|e|}{dt}\right) = f_{\mathrm{GA}}\left(\frac{d|y_{\mathrm{ref}} - y(t)|}{dt}\right) \tag{4.21}$$

Note that positive gradients indicate that the error increases. The main objective of the gain acceleration is to reduce the maximum control error. A maximum gain acceleration factor f_{GA} is defined for a certain gradient (e.g. 2.5 at 4 K/min as shown in the figure). The maximum control error is reached when the gradient is zero. If only disturbance limitation is desired, a simple linear interpolation is possible, which reaches a gain acceleration factor of one at a gradient of zero (see Figure 4.24, right). An additional possibility arises from this gradient approach. A desired, ideal shape of the system response can be defined. From this ideal response, the ideal gradients can be derived as a function of the absolute control error. The desired error gradients are negative and, ide-

ally, should be located at a gain acceleration factor of one. The gain adaptation is thus continued to negative values. This is illustrated as well in Figure 4.24 (right) for a very simple linear interpolation.

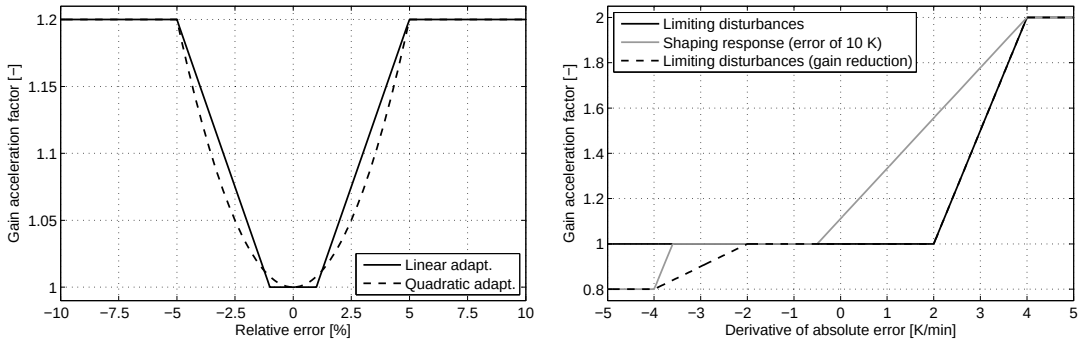

Figure 4.24: Variation of relative controller gain as a function of the relative control error (left) or the derivative of the absolute error.

The result of the closed-loop system response for the superheater injection at 900 W/m² is shown in Figure 4.25. The nominal controller exhibits the largest control deviation of about 44 %. The adaptation based on the control error is slightly better, but has the drawback of more oscillations at the end. The gradient-based adaptation is significantly better. Its gain acceleration factor can be increased more strongly. This is due to different stability characteristics. While the error-based method requires the maximum controller gain to give a stable system, the gradient-based method is less restrictive. As a rule of thumb, which must be checked for each case, only the controller gain at the intersection with the zero gradients must be stabilizing. The goal of limiting the maximum control deviation is reached easier. Only 33 % of the original disturbance takes effect in closed-loop with gradient-based control (Figure 4.25), during which the maximum factor of 2.5 is used. In the example, the response shaping action is clearly visible in the graph of the gain acceleration factor. A simple first order element with $\tau_{\mathrm{PT1}} = 1.5\,\tau_{\mathrm{c,imc}}$ is used as ideal response. This corresponds to an exponentially decreasing error with the ideal derivative of $de/dt = e/\tau_{\mathrm{PT1}}$. Due to the non-minimum phase characteristic and the high order of the plant, it is not possible to force the real response to this ambitious ideal shape. Nevertheless, the response is already significantly smoother than the nominal one. A threshold of 2 K of absolute error is used in the simulations in order to provide a smooth control range around the setpoint. Improvements could be achieved by strictly designing the adaptation of both controller parameters by pole placement, similar to approaches in [11, 226].

In practice, both simple gradient approaches (with and without response shaping) offer significant advantages compared to the nominal PI controller. Thus, it is highly recommended to implement them in a real plant. If the plant

dynamics are well-known, the simple scheme of disturbance limitation is sufficient. If there is high uncertainty or strong oscillations in the nominal controller design, the response shaping offers the possibility to automatically correct the controller gain. This brings it close to a real adaptive controller in the classical sense.

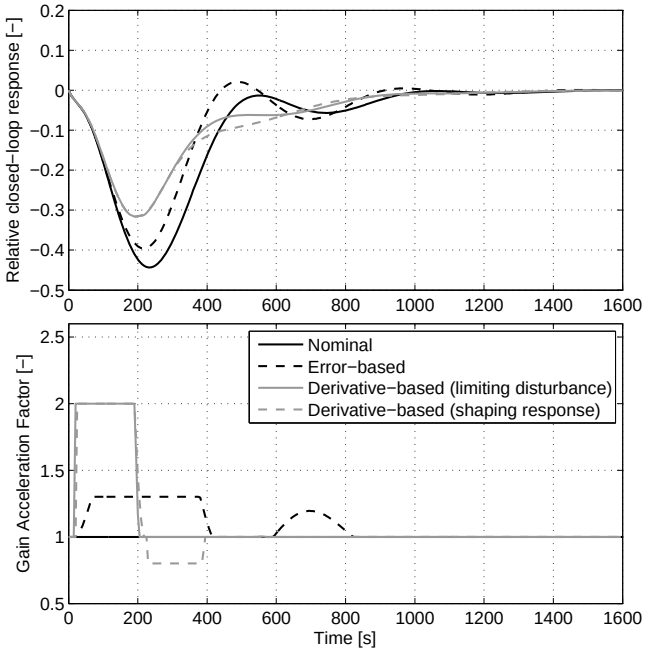

Figure 4.25: Closed-loop disturbance rejection with nominal controller and different types of error-based adaptive control for SHI at 900 W/m².

4.3.4.4 Disturbance frequency adaptation

The design of the basic controllers for the evaporation injection and especially the inlet mass flow show resonance peaks at frequencies of realistic disturbance scenarios, as e.g. shown in Figure 4.18 on page 120. Shifting those magnitude peaks to higher frequencies is not possible without severe oscillations during normal operation. Thus, the only option to use a PI controller during such frequencies is to detune the controller gain, obviously only as long as the clouds appear in the critical frequency range. This requires estimation of the current cloud frequencies. The concept for the design of such controllers is equivalent to the procedure described for the basic controllers. The difference is in considering a periodic DNI disturbance instead of a single input step disturbance. This frequency design is not elaborated here, but can be an option for improvements. Note that the EBGS scheme based on gradients and response shaping, as discussed above, offers a different solution to this problem. Although the nominal controller might lead to oscillations, the gradient-based adaptation already reduces these effects. The frequency adaptation is therefore not elaborated here for the PI controllers.

4.3.4.5 Adaptation for DNI feedforward

Disturbance rejection is very slow by the inlet mass flow. Furthermore, steep gradients of the inlet mass flow result in very high temperature gradients in the superheating section. Such high gradients are a challenge to the injection controllers. On the other hand, the inlet mass flow must be used to counteract imbalances between main inlet mass flow and injection mass flows. Such imbalances can arise from a wrong estimation of optical efficiency or other plant parameters. In consequence, it is recommended to use the inlet mass flow for very slow tracking of reference mass flows of the injections. As the effective use of this is limited to rather clear sky conditions, it is equivalent to use a state estimator to estimate the current (optical) efficiency of the collector loop. As this efficiency is a dominating factor in the feedforward action, it should be slowly adapted to the current estimate, e.g. by a first order hold with the current IMC time constant. The advantage of efficiency adaptation, rather than temperature/injection mass flow adaptation, is the validity for the complete day – at least ideally. A wrong pre-defined optical efficiency in the feedforward action for a clear sky day with variant A (two injections) is assumed as an example. The working range of the EVI is controlled via a PI controller on the inlet mass flow. At constant effective irradiation, the inlet mass flow slowly changes and adapts the working range of the EVI. A change in effective irradiation again results in an imbalance between inlet mass flow and injection, which then again must be compensated slowly. In reality, such constant conditions cannot be expected even during clear sky days due to the variation of the sun position. Estimation of the optical efficiency also requires time. However, once a good estimate is reached, the feedforward action can already compensate DNI and sun position changes in advance. The imbalance is reduced to the level of plant-model mismatch at the beginning of the day. Note however, that the simple predefinition of parameters is then sacrificed for the sake of online estimation and performance here. Alternatively, a day-to-day adaptation may also be possible manually by the operators. It could as well be performed after operation and by including cleaning schedules. The online estimation is especially useful for control, if a good feedforward model exists. If the latter model does not ensure accurate feedforward, the efficiency estimation will not offer significant advantages.

Online estimation of the optical efficiency can be performed using the LTI models in combination with standard observer algorithms, e.g. a Kalman filter [11, 126]. The same can be done with the help of the MBM or the DFEM. Note however, that more detailed state estimation is not easily possible with the MBM or DFEM. Standard observers use a derivate of the system, which usually cannot be derived numerically for the stiff MBM or DFEM models [215]. In the latter cases, more complicated non-linear estimation schemes like moving hori-

zon estimation or particle filters must be applied. More details on state estimation of once-through loops can be found in [215]. The online estimation is helpful for performance evaluation as well.

If the estimation of the loop efficiency and the feedforward model are accurate, an interesting case related to cloud frequencies arises for the inlet mass flow as well. There is no effective rejection of any fast disturbance. The only chance of coping with DNI variations is to use it as feedforward. By averaging the DNI signal over time, feedforward becomes more robust and it is assumed that all cloud disturbances are much faster. This already suggests that the time constant of the filter of the DNI signal could be adapted to the weather conditions. A more elaborated adaptation arises, if the clear sky DNI is taken into account. The feedforward inlet mass flow is derived not only from measured DNI, but also from ideal maximum clear sky DNI.

$$\dot{m}_{\mathrm{FF,in}}(t) = \left(1 - w_{\mathrm{clsky}}\right)\dot{m}_{\mathrm{FF,meas}} + w_{\mathrm{clsky}}\dot{m}_{\mathrm{FF,clsky}} \tag{4.22}$$

The feedforward (index “FF”) from clear sky model (index ‘clsky’) is weighted by w_{clsky} to correct the mass flow based on the measured DNI signal.

The advantage can be illustrated by an example. Consider a clear day with only few small but thick clouds. If a small cloud covers the DNI sensor, its signal is reduced to almost zero irradiation. The resulting influence on the feedforward is the reduction to minimum mass flow. This causes a strong increase in the superheating temperatures of the loop, since only few of them are really influenced by the cloud. It is thus better, to limit the cloud influence. This can be achieved by increasing the weight w_{clsky} to almost one. The small cloud has a minor effect on the feedforward signal and the injection mass flows can be used to effectively counteract the short disturbances. A weighting scheme depending on the cloud situation is therefore recommended. It also offers the chance of limiting the lower mass flow at the loop inlet depending on the clear sky DNI. This can be an important feature, because it offers the chance of operation at low loads with thick clouds, while still guaranteeing safe operation, even if the DNI is suddenly recovering

In combination with the online estimation of the efficiency, it is possible to shift the working range of the EVI depending on the cloud situation. High cloud frequencies can usually be anticipated by the operator. The EVI mass flow share can be increased beforehand, to offer more buffer against the resulting transients. A similar adaptation is possible to increase the working range of the SHI. This is achieved by increasing the setpoint temperature before the SHI. The latter again implies a different feedforward function or weighting for the inlet mass flow. In consequence, a complex scheduling scheme for the setpoints and feedforward action arises. Such a scheme can be elaborated by simulations of the corresponding conditions. It may also be a playground for fuzzy controller

design. As the basic control system works without these complex adaptations, such innovations are left for future research and operation experience.

4.3.5 State feedback

Loop variants with only one injection have the drawback of slow disturbance rejection. It is thus essential to detect disturbances as fast as possible. This improvement is achieved, if the feedback of a temperature located between injection and loop outlet is measured. This measurement can be considered as a state of the superheater (model) and reveal disturbances before they reach the outlet. Thus, this state feedback further improves the overall response. A concept, which considers this kind of feedback, is described in [138]. It is especially important, if the superheating section to be controlled is very long, i.e. longer than 150 m or one collector. There exist two possibilities to include such measurements. One is by introducing a state feedback controller; the other is to let a proportional controller act on the intermediate temperature. The action in the real plant is equivalent for both approaches.

Classical state feedback suggests using a certain controller design approach, but in the end also puts a proportional gain on the temperature state as well. Its main advantage is the additional consideration of plant inputs and the systematic gain balancing of the different states. In combination with a state observer, the state feedback control already includes the feedforward action, which must be separately derived for the PI controllers. Nevertheless, note that a pure state feedback approach for the complete superheating section without using a PI controller shows a temperature offset even during nominal conditions, such that an additional integral part must act on the outlet temperature. These control schemes are well-known for conventional steam generators and can be found in e.g. [85, 104]. It is also applied by Zapata [269] for a solar steam generation system using dish-stirling technology. A direct proportional controller is suggested and simulated in [138] for superheating sections of a parabolic trough plant.

The installation of a temperature measurement after each collector is state of the art in parabolic trough plants. Thus, such a control structure is possible without additional sensors and should be used, if the superheating section comprises various collectors. However, the added value for short superheating sections or Fresnel collector fields must be analyzed specifically and might turn out not high enough to justify an additional installation effort.

Variant C is suggested to use an additional proportional controller on the temperature before the last collector (one collector after the injection). Variants B and D could already justify a controller design based on state feedback. Note however, that a state space model is needed for such an approach. This could be generated from plant specific transfer functions or by the use of the analyti-

cal superheater model as presented in [57, 139]. Then, an additional state estimator for the superheating section is recommended. This is helpful from a control point of view, but increases the effort in design and tuning significantly. Therefore, it is a rather individual or project-specific trade-off. Following the notion of simplicity, even for variants B and D the proportional controller approach is feasible and would lead to very similar results. The controller design is not pursuit here, as its performance is in between the basic PI controller and an MPC scheme. The latter two controllers are analyzed in this work.

4.3.6 Handling of severe disturbances

For severe disturbances, even the second injection might not be sufficient. This is the case for a long defocus of the complete inlet collector (maybe due to failure) or the shadowing of a loop inlet section only. This can be described as a severe imbalance between evaporation and superheating section. A loss of energy at the inlet results in a steep increase of temperature in the superheating section, followed by a steep decrease after a maximum (see section 4.1 on system characteristics for details). In these cases, it is favorable not only to maintain the outlet temperature, but rather to maintain the temperature profile along the loop. This guarantees to keep all collector coatings and tubes at safe conditions, while allowing a fast transition back to steady state. Therefore, not the last collectors should be defocused, but the collectors at the end of the evaporation and the beginning of the superheating section. Not the design temperature is then relevant for defocusing, but a temperature about 15 to 30 K above the nominal collector outlet temperature should be chosen as defocus signal. If possible (like e.g. for Fresnel collectors), a stepwise defocus is favorable to avoid high gradients for the tubes as well as for the superheating injection downstream. When a certain lower temperature (e.g. nominal temperature) is reached, the collectors can be focused again. Even a severe inlet disturbance such as a slowly passing cloud can be controlled smoothly with such a control scheme.

A different critical situation is a large step increase (not decrease) in energy input near the loop inlet, e.g. the focusing of a collector or a harsh increase in inlet temperature. This is considered an extraordinary disturbance, since a good operation strategy does avoid such situations, e.g. by only very slowly focusing the collector and/or by accompanying it with corresponding feedforward action of the mass flows (see section 4.3.3.8). The resulting transient of the disturbance is a steep drop in superheating temperatures. This cannot be recovered by the focused collectors and injection mass flows might run out of range. In consequence, the outlet temperature can drop uncontrollably. The necessary measure is to reduce the steam mass flow. A harsh reduction in inlet mass flow is not fast enough, as the stored mass in the loop is too high. The only way to

actively reduce the steam mass flow is the partial defocus of one of the first evaporation collectors. Note that this can hardly be called control, since there is a very high uncertainty in the response. However, it allows for decreasing the steam mass flow and for providing a control range for the injection mass flow. After the original disturbance, the partially defocused collector must very slowly be focused again to stay in a controllable range. A similar option is mentioned in [152], who suggests to use deviation limits between feed water mass flow and outlet steam mass flow as a signal (control variable) for defocusing one or more complete inlet collectors. His results for an ideal control show potential of the method. However, with uncertainty in mind, an automatic control is very risky, as the deviations might also come from a different disturbance, which might be even intensified by the collector defocus. Furthermore, the outlet mass flow measurement of each loop is avoided in the basic control scheme to save costs and an absolute value from the measurement shows high uncertainty. A better indication might come from different signals: outlet temperature under a certain threshold, combined with a high decreasing temperature gradient along the loop and rather constant irradiation conditions. Only under those three prerequisites, it is likely to have an inlet disturbance of the mentioned kind. For large power plants, a more robust option is to allow two-phase flow at the outlet. As such disturbances seldom appear in all loops at once, the two-phase flow of one loop can be compensated by the normal operation of the others. The preferred control option must thus be evaluated depending on the particular boundary conditions of the power plant configuration.

4.3.7 Summary of design rules

The design of the suggested 'basic control scheme' from the former sections is now briefly summarized.

PI controllers are used for all the injections. The underlying integrational time constant τ_I is chosen as the IMC time constant, as derived in section 3.4. For each operating condition of the derived LTI models (injection mass flow to superheating temperature), a controller gain k_c is chosen by optimizing a weighted disturbance rejection response (section 4.3.2). During operation, the PI parameters are adapted by a scheduling scheme based on the corresponding mass flow of the controlled plant section (section 4.3.4.1). This can also be calculated with a weighted mass flow including the clear sky conditions, which avoids slow reactions after sharp drops of irradiation. Additional adaptation of the controller gain is foreseen depending on the injection water temperature (section 4.3.4.2). In order to effectively reduce the maximum control deviation, an additional adaptation of k_c is recommended based on the time gradient of the control error (section 4.3.4.3). Feedforward action on the temperature before the SHI is required. All other feedforward terms can be omitted. Feedfor-

ward on the enthalpy before the EVI cannot be measured, but can be estimated to some extent. Using this estimation offers a significant improvement. Due to the higher effort, it is not part of the basic control scheme. The resulting injection controllers are fast and offer reliable performance during all operating conditions.

There are various differences to former approaches by [57, 139, 254]. The controllers are designed for disturbance rejection instead of reference tracking. A simple scheduling scheme based on internal model control time constants is used, which is very intuitive and easy to implement. Injection water temperature is used for gain scheduling instead of ineffective feedforward. All other feedforward terms and measurements (up to eight in former concepts) are omitted as well, with the exception of the only important temperature before the SHI. In consequence, only water mass flows to the loop, (some) water temperatures and two superheating temperatures are needed for control, which reduces the equipment costs significantly. The error gradient-based control developed in this work offers very good disturbance rejection results, which were not achieved by former concepts.

The inlet mass flow control is designed considering its poor disturbance rejection quality. The mass flow is defined by feedforward action on averaged DNI signals of the whole plant. This defining function should take into account the IAM, the working condition of the injections, the cloud situation and the clear sky DNI model. Feedback is considered by estimating the optical efficiency of the loop and adapting this parameter in the feedforward function. The resulting inlet mass flow guarantees good control results during all normal operating conditions. The feedforward approach is also beneficial for the operation of parallel loops, since most of the control valve action is performed in all the loops at the same time. Mass flow imbalances between the loops can thus be reduced. As an alternative to the efficiency estimation, feedback can be established by a slow PI controller on the working condition of the EVI (loop variants A, B and D) or the temperature before the SHI (loop variant C). However, this kind of simple PI control leads to possible disturbance amplification and is only suggested for good days with very small fluctuations of the DNI.

By this basic control scheme, the task of developing a robust controller for solar once-through boilers is achieved. The next section provides experimental results from the DISS test facility. Better control is possible, but more complicated. The potential of MPC schemes is shortly illustrated in the subsequent section to indicate possible future improvements.

4.4 Experimental validation of new concept

The following paragraphs discuss exemplary test results from the DISS facilty for different control variants and DNI conditions.

Control system implementation at DISS facility

The new control concept has been implemented at the DISS test facility to validate its performance. All sensors are connected to the main control system of the plant, which is based on an ABB Bailey Infinity90 ™ system. To allow for more flexibility in the controller testing, all control tests of this work have been performed via a Matlab® environment. The data exchange between the ABB and the Matlab® system is performed by an OPC (Object Linking and Embedding for Process Control) interface, which is an OPC server by RoviSys linked with the Matlab® OPC Toolbox.

Controller design has been done for continuous systems. The discrete time parameters for the real system are chosen equal to the ones derived for continuous time. This can be done, because the applied sampling time τ_{sam} of 5 seconds is very small compared to the dominating time constants of the system. The discrete time instant k is used for continuous time t; k+1 indicates $t + \tau_{\mathrm{sam}}$. The implementation of the PI controllers is done in state space with the following transformation from the continuous parameters [248]:

$$x(k+1) = x(k) + \tau_{\mathrm{sam}} e(k) \tag{4.23}$$

$$u(k) = \frac{k_{\mathrm{c}}}{\tau_{\mathrm{I}}} x(k) + k_{\mathrm{c}} e(k) \tag{4.24}$$

The variable u denotes the manipulated variable (mass flow) and e denotes the error, which is the reference minus the current measurement ($e = y_{\mathrm{ref}} - y$). The variable x denotes the controller state.

The control concept tested at the DISS facility mainly comprises the features as described in section 4.3.7 above. Exceptions are that both the gradient-based adaptation and the clear sky model for DNI are not used.

The tests were performed using the injections before collector 11 (index “inj11” in the following) and before collector 6 (“inj06”). The pressure was kept at a constant level of 80 bar, imitating fixed pressure mode of a turbine. The outlet temperature shown was measured directly after the last receiver of the last collector, with less than one meter of piping between sensor and receiver outlet. The DNI signal is measured on the roof of the building that houses the balance of plant. It is located in the north-west of the collector loop. The effective irradiation G_{eff} is the DNI corrected by the cosine of the incidence angle and the IAM (see equation (3.15) on page 39). The efficiency of the loop was estimated by the operator without further correction, i.e. without online estimation.

Steam temperature stability requirements

The experimental facility does not have a steam turbine for testing. Nevertheless, the measured data can be used to assess, whether a steam turbine would have worked with the provided live steam from the collector loop. Requirements of turbines are listed in the IEC 60045-1 standard for steam turbines [114]. A summary is presented in [24]. The following limitations for the turbine inlet can be derived, with ϑ_{LS} and $\vartheta_{\mathrm{LS,ref}}$ indicating the actual and the reference live steam temperature:

- $\vartheta_{\mathrm{LS}} < \vartheta_{\mathrm{LS,ref}} + 8\ \mathrm{K}$:
  No limitations
- $\vartheta_{\mathrm{LS,ref}} + 8\ \mathrm{K} \leq \vartheta_{\mathrm{LS}} < \vartheta_{\mathrm{LS,ref}} + 14\ \mathrm{K}$:
  Limited to 400 hours/year in total
- $\vartheta_{\mathrm{LS,ref}} + 14\ \mathrm{K} \leq \vartheta_{\mathrm{LS}} < \vartheta_{\mathrm{LS,ref}} + 28\ \mathrm{K}$:
  Limited to 80 hours/year in total or 15 minutes per event
- $\vartheta_{\mathrm{LS}} \geq \vartheta_{\mathrm{LS,ref}} + 28\ \mathrm{K}$:
  Not allowed
- $d\vartheta_{\mathrm{LS}}/dt < 5\ \mathrm{K/min}$:
  Usually possible for turbines at a rated power of 150 $\mathrm{MW_{el}}$ or smaller, higher gradients limited by manufacturer [24].

As a result, the rated temperature can be exceeded by up to 8 K without limitations. Exceeding the rated temperature by 8 K up to 14 K is restricted to 400 hours per year, which is more than one hour per day. Short overshoots in temperatures up to 14 K are thus acceptable for control. There is no explicit limit of temperature gradients at the turbine inlet, because the value is usually a particular characteristic of the turbine. To ensure safe operation, the control objective is to maintain the loop outlet temperature below 8 K above the set-point and with smaller gradients than 5 K/min. Note that these are conservative criteria, since a large plant consists of various loops and a long live steam header line. The effect of one loop is damped by the piping and smoothened by a shift in time for clouds passing the solar field.

There is no explicit lower limit for the live steam temperature. A commonly described requirement is too guarantee a minimum wet steam quality at the last low-pressure turbine stage in order to limit erosion by water droplets. Such a limit can be re-formulated for the inlet temperature. The value is again dependent on the turbine design. A minimum of 25 K is chosen here as objective for the loop [234]. Note that this only applies to constant pressure operation. If the pressure at the turbine inlet is reduced, the inlet temperature can also be reduced until a minimum superheating temperature difference is reached. The latter limit is again particular for each turbine; a good estimate may be in the range of 10 to 30 K above saturation temperature.

Test A: Variant C with SHI only, IMF control by temperature

Figure 4.26 shows the test results of September 5, 2014. The inlet mass flow is defined by feedforward as well as by a PI controller on the temperature before the superheating injection. This corresponds to a loop layout of variant C. The irradiation is very smooth and can be considered a clear sky day. The outlet temperature can be stabilized in the desired range. The only difficult event arose around 16.5 h (16:30 h). The desired injection mass flow was too small to be effectively established by the subcontroller of the injection valve. This results in two strong mass flow peaks, which influence the controller gain and integral state. A short overshoot can be seen in the outlet temperature.

Another characteristic is observable in the data of Figure 4.26. The temperature before the injection cannot be stabilized well between 15.5 h and 16 h due to former inlet disturbances. There is only a slow correction of the inlet mass flow with a slow response. In consequence, it takes about 25 minutes to correct the high overshoot. This is acceptable for the test plant, since it is designed for temperatures up to 500°C. For a commercial plant, the defocus of a superheating collector may be the consequence. Nevertheless, because of the SHI's static feedforward on the temperature before the SHI, the outlet temperature can be stabilized without problems. This is the main task of the SHI controller at this day, which can be seen by the rather parallel curves of the SHI mass flow and the temperature before the injection.

Test B: Variant A with two injections, small clouds, low injection temperature

Figure 4.27 shows experimental results for variant A with two injections. The sky was cloudier with thicker clouds around 17.5 h. Even this situation can be handled by the controller with the outlet temperature deviating less than 5 K from its setpoint. The temperature before the injection is oscillating slowly because of two effects. First, the injection water temperature is about 30°C compared to 250°C design temperature, which had not been compensated by adaptation in this experiment. Thus, the process gain is significantly underestimated and the controller gain is too aggressive, resulting in an oscillating response. Second, the drop of DNI results in two short drops of the inlet mass flow by about 8 % around 17.5 h. This is not compensated by a weight on DNI clear sky model, since the latter one is not used for control during the experiments. The resulting disturbance is compensated by the evaporation injection. Note that the SHI control is less affected by the low injection water temperature, because its measured value is included in the feedforward term acting on the temperature before the SHI.

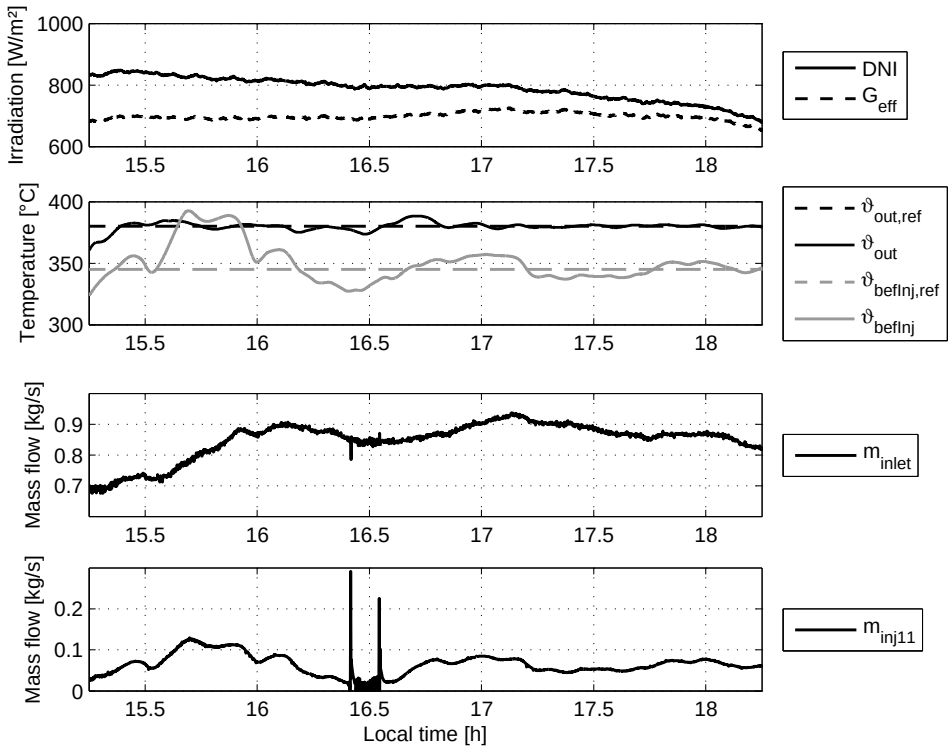

Figure 4.26: Test A: Control experiment at the DISS test facility with variant C (only superheater injection before collector 11) on September 5, 2014.

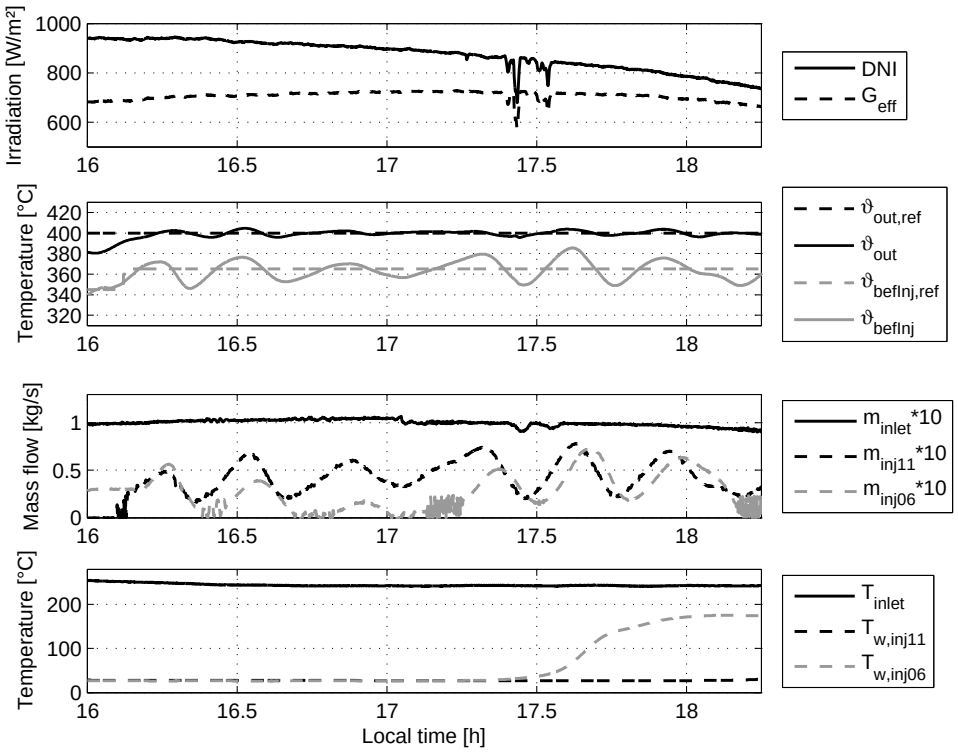

Figure 4.27: Test B: Control experiment at the DISS test facility with variant A (two injections) on October 8, 2014.

Test C: Variant A, thick cirrus clouds

Another experiment of interest for commercial plants is the one on October 9, 2014, which is illustrated in Figure 4.28. The DNI indicates a clear sky day. However, the picture of the actual cloud situation (Figure 4.29) reveals fields of cirrus clouds with varying thickness. The outlet temperature is therefore fluctuating more than expected. Nevertheless, it remains well between ±8 K during the whole experiment. The influence on the injection water temperature is also illustrated. With low temperature, oscillations are high. After the water temperature had risen, the controller was shortly re-initialized and then started again. The subsequent oscillations were smaller than before.

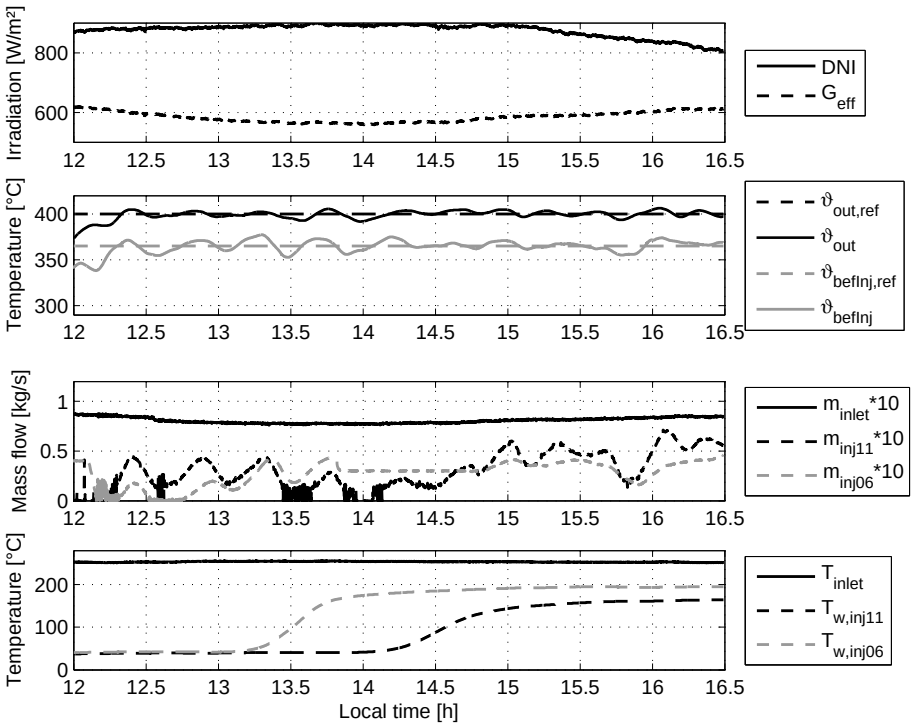

Figure 4.28: Test C: Control experiment at the DISS test facility with variant A (two injections) on October 9, 2014.

Figure 4.29: Test C: Sky image with cloud situation of October 9, 2014, taken from DISS control room in west direction; picture taken at 16:46 h.

Test D: Variant A, high minimum inlet mass flow, DNI imbalance on loop

The experiment of November 10, 2014, is shown in Figure 4.30. The whole day is dominated by a minimum mass flow restriction at the inlet at 0.65 kg/s imposed by the operator. The effective irradiation is around 450 W/m², which requires a lower mass flow for good control. This restriction was only released after 15 h, but too late for effective control. Note that the minimum mass flow is not limited because of process restrictions. The operation at a lower mass flow would have been possible without problems for a loop of this type. As described above, the restriction of the mass flow based on the effective clear sky irradiation would have indicated a significantly lower minimum mass flow. The set-points for outlet temperature and temperature before the SHI had to be reduced to 350°C and 330°C, respectively, to allow for at least a small control range of the SHI. As a result, the EVI mass flow is zero between 13 h and 14 h. Thus, only the SHI is able to control the outlet temperature. The evaluation of the resulting temperature response must take this limitation into account.

Although the DNI measurement does not reveal any disturbance at 13 h, the outlet temperature shows a strong drop shortly after that. This situation shows the response to an imbalance between the evaporation and superheating heat input. A photo of the DISS test loop at 12:54 h is shown in Figure 4.31. It exhibits a shadowing of 40 % of the total loop in the south. This is a typical event of an inlet energy disturbance. The outlet temperature shortly rises, before it steeply falls to a preliminary minimum and then recovers again. The EVI mass flow is already zero due to the inlet limitation. Thus, it cannot contribute to counteracting the disturbance. In consequence, the SHI controller quickly reduces the SHI mass flow to zero, but has no buffer for further reduction. The outlet temperature drops by more than 30 K. This could be critical, if the disturbance was the same in all loops of a large plant. Since such an imbalance event is usually shifted in time and only affects a few loops, it is unlikely that even this unfavorable combination would have caused the turbine of a real plant to trip.

Another disturbance happens during this day at 15 h. A stronger DNI disturbance acts on almost the whole loop. The SHI controller is able to cope with this disturbance without problems. At 15.4 h, the controllers were deactivated and the plant was shut down because of a large cloud field covering the whole sky.

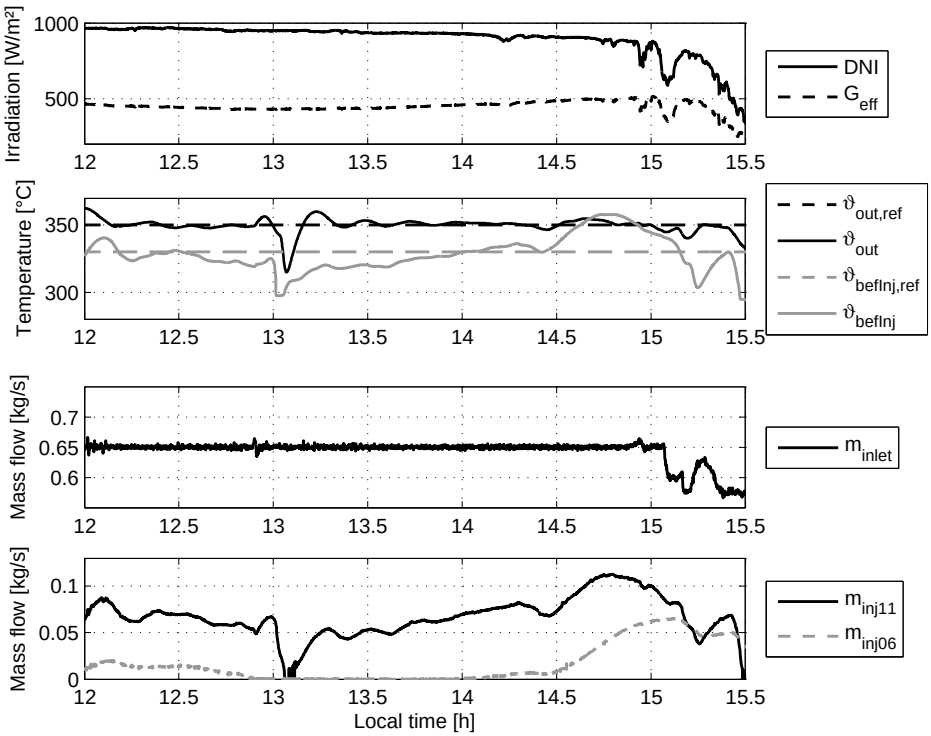

Figure 4.30: Test D: Control experiment at the DISS test facility with variant A (two injections) with lower mass flow limitation at the inlet on November 10, 2014; evaporator/superheater imbalance around 13 h; injection water temperatures around 210°C.

Figure 4.31: Test D: Sky image with cloud situation of November 10, 2014, taken from CESA-1 shadow cam in eastern direction at 12:54 h; cloud over southern collectors 1A to 4 (Source: DLR, PSA).

Test E: Variant A, EVI detuned, long drop of DNI

The test situation on November 5, 2014 is shown in Figure 4.32 and can be used to derive a variety of aspects. The controller of injection 6 (EVI) was detuned by a factor of 0.5 from about noon on, assuming completely clear sky conditions. The PI part of the inlet mass flow controller is active and shall control the mass flow of injection 6. Due to this influence, the inlet mass flow is

slowly increasing until 14 h. Then, a sharp drop in DNI occurs with a complete shadowing of the loop for six minutes. The inlet mass flow is quickly reduced to its minimum value, which in this case are 0.575 kg/s and only 15 % less than before. The gradient catcher of injection 11 is active and gives a constant factor 1.5 for outlet temperature gradients greater than 1.5 K/min. It is therefore very quickly brought to zero, which saves the temperature profile as long as possible along the superheating part. The controller of injection 6 only reacts very slowly on the disturbance, as it is detuned and does not have any other active feature. The situation is therefore comparable to variant C, although a slight influence of injection 6 exists. The outlet temperature falls to a minimum of 310°C, which is 40 K less than the setpoint. Such a situation may lead to a short low temperature trip of the turbine in a power plant, if the header has only a low thermal inertia and the disturbance is not somehow distributed along the collector field. Nevertheless, if the controller of injection 6 would have been in normal mode or even featured by a gradient catcher, this trip could have been avoided successfully. This is even more remarkably when considering the relatively high inlet mass flow. Similar cases are discussed below for the assessment of disturbance classes.

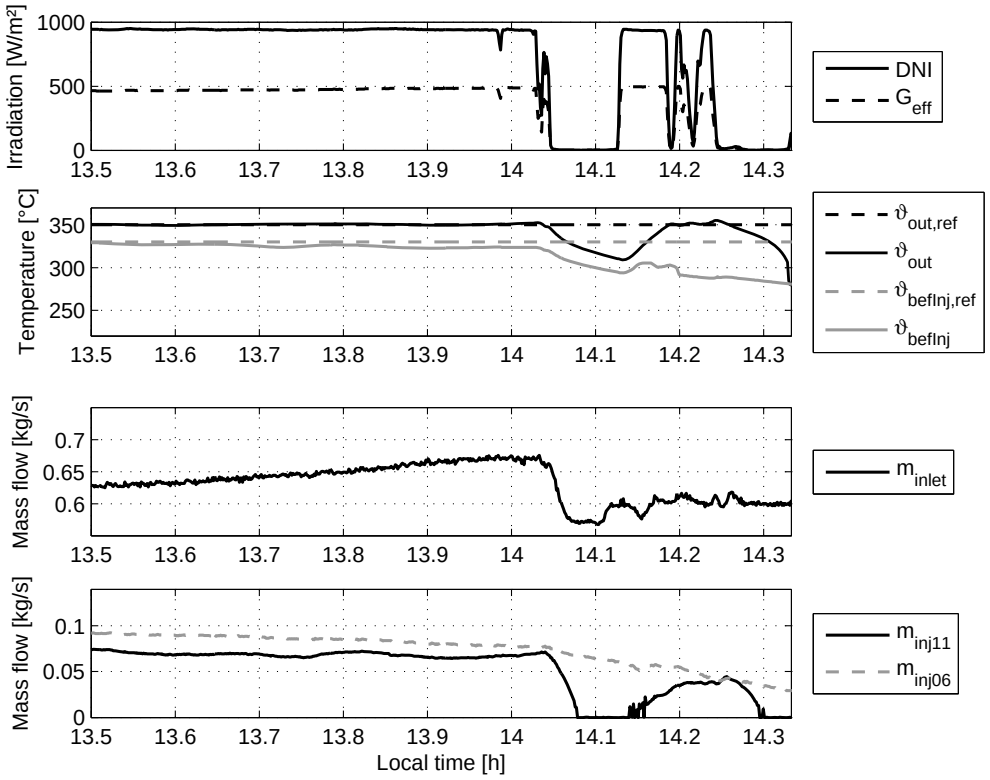

Figure 4.32: Test E: Control experiment at the DISS test facility with variant A (two injections) with lower mass flow limitation at the inlet on November 5, 2014; controller injection 6 detuned, controller injection 11 with active gradient catcher (factor 1.5); injection water temperatures around 210°C.

Conclusions on control experiments and comparison

In total, control experiments have been performed on eleven days in 2014. The results reveal that the SHI controller works very well and as expected during all disturbance situations. The EVI controller had to be slightly detuned, even after taking the injection water correction into account. A factor of about 0.85 showed good results. This detuning is caused by the uncertainty of the model, which must always be corrected during commissioning, as well as by the different setpoint temperatures. Due to the mixed plant section with evaporation and superheating, the setpoint temperature before the SHI has a significant influence on the relevant transfer function and process gain. The EVI controller design for 340°C was used during all experiments, even when lower setpoints were used in some experiments. Overall, the experiments support that the general controller design, with the additional adaptations suggested in the sections above, provides a robust control strategy for commercial plants.

The direct comparison with former control concepts is difficult, since former experiments were performed for the old DISS facility and at lower loads. Control performance is exemplified by Valenzuela in Figure 10 of [254] for April 26, 2002. For brevity, only the main transients are described here: A defocus of collector 6 (10 % of loop energy at that time) was induced for about 5 min and led to a reduction of -21 K in outlet temperature. After the recovery, an overshoot of about 10 K happened. After that, a drop of the DNI from about 910 W/m² to about 620 W/m² (-32 %) happened for about 15 min. The resulting outlet temperature was reduced by about 60 K and recovery to the reference temperature of 300°C took more than 30 min after the disturbance had disappeared. Figure 4.32 (Test E) shows the experiment performed in this work for a drop of -100 % for 5 min. It can be supposed to be more severe than the published case, and only leads to a reduction of 40 K under the disadvantageous conditions mentioned above. Although the situations are not strictly comparable, it already indicates the faster responses of the new concept.

4.5 New control strategies based on model predictive control

The sections on classical controllers above clearly show the limits of the system under consideration. Due to the long response and delay times, the PI controllers must be slowed down for robust performance. This can only partly be compensated by additional means such as feedforward or adaptive control. A powerful control strategy to deal with these problems is model predictive control (MPC). This field of control was pioneered by Richalet [207] and Cutler and Ramaker [40] together with Prett [197] and Martin-Sanchez [162]. Similar ideas to MPC can be traced back to the 1950s [159]. Good introductions to the topic can be found in [6, 50, 93, 159, 165, 202].

This section briefly introduces the idea of MPC, shows some illustrative examples to motivate its application and outlines a useful MPC scheme for solar line focus boilers. The latter is done for a linear MPC with different parallel LTI models. Some aspects are added for non-linear MPC.

4.5.1 Introduction to MPC

An MPC algorithm is performed in the following main steps [159]:

- The future behavior of the plant is predicted based on the current states, inputs and, as far as available, disturbances.
- An optimizer is used to estimate the optimal trajectory of the manipulated variables to reach the desired setpoint under certain constraints.
- The first value of the optimal trajectory for the manipulated variables is applied to the system.
- The steps above are performed for each sampling instant again, which makes it a so-called receding horizon control.

This conception is illustrated in Figure 4.33. The discrete time instant k indicates the current time, $k+1$ indicates the current time plus one sampling time of the system etc. The internal model is used to predict a free response y_{free} of the output to be controlled. This is done along the prediction horizon H_{p} and under the condition of keeping the former input $u(k-1)$ constant. The optimization problem is to find a combination of future inputs that lead to the optimal possible trajectory of the output $\hat{y}^*$. The hat indicates that it is an estimate of the internal model; the star indicates that it is the solution of the optimization. The optimal inputs $\hat{u}^*(k+j|k)$ can be varied along the control horizon. The first index $k+j$ indicates the future time at which the value is first applied, while the second index k denotes the time of the optimization. Although it is possible to optimize a trajectory for each sampling instant, this is computationally not efficient. The reason is that only the first optimal input estimate is applied to the system, i.e. $u(k) = \hat{u}^*(k|k)$. The rest of the inputs are not needed, since the whole procedure is repeated at the next sampling time. For large multivariable systems and non-linear optimizations, it can be useful to store the trajectories to have a good initial starting point for the coming optimization as well as to have a back-up trajectory in the case of optimization failure. For linear quadratic programming, i.e. quadratic optimization as performed during most of the linear MPC algorithms, this is usually not needed. Attention must be paid when designing the control horizon, since the interactions of control horizon and prediction horizon can be interpreted as tuning parameters of the MPC [159] and a wrong choice can even destabilize a stable open-loop plant [199].

There is no integrator included in the MPC. However, the predictions are compared to the real system output and the free response is corrected by the prediction error. In this manner, constant disturbances can quickly be rejected with the same effect as an integrator [93].

The main advantages of MPC are the explicit modeling of the plant, the inherently consideration of multivariable interactions and the inclusion of constraints like actuator limitations. All three items play a significant role in a DSG line focus system, as has been shown above. The main drawback of MPC is the necessity of online optimization and the resulting computational effort. This aspect is especially relevant for non-linear MPC. In addition, the tuning effort to achieve a reliable MPC configuration may not be underestimated – though it is much easier than separately designing the same control via different concepts.

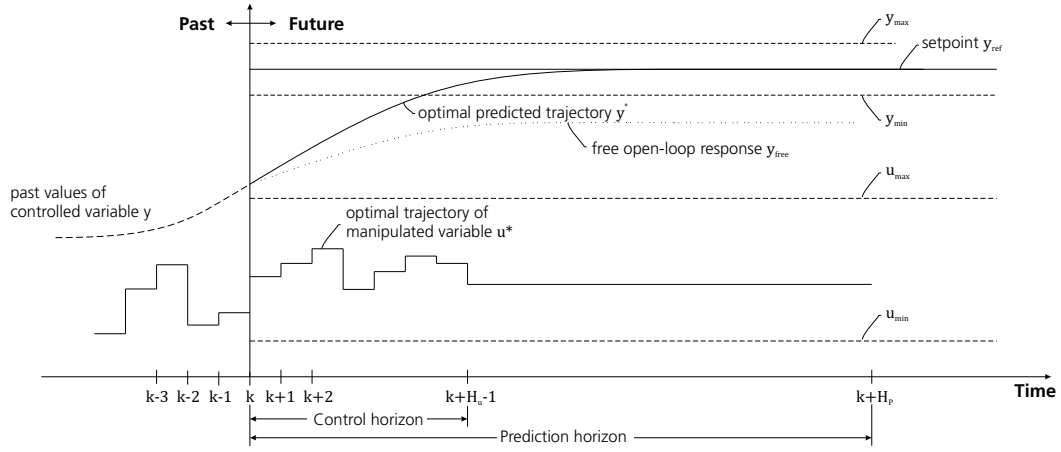

Figure 4.33: Basic scheme of model predictive control, based on [50].

In the case of CSP systems, the main disturbance is the change of the DNI. During a clear sky day without clouds, the DNI varies slowly and can be well – or at least sufficiently– predicted. Such a clear sky model serves as a disturbance model for the MPC. The performance of MPC thus depends on how good the DNI prediction is and how well the MPC algorithm can cope with deviations between real and estimated DNI. The ideal case is shown Figure 4.34 for the example of August 9, 2013. The exact almost clear sky G_{eff} curve is known to the controller. From this curve and the disturbance model, which is the transfer function of the DNI to the temperature before the SHI in this case, the disturbance is predicted in terms of temperature deviation. This is indicated in the upper graph of Figure 4.34. With the ideal prediction, an optimal inlet mass flow can be calculated. The optimal mass flow is shown in the lower graph and the optimal temperature deviation result is depicted in the upper graph. The maximum temperature deviation is about 1 K. Note that this is comparable to pure feedforward action, since all disturbances are known in this scenario.

Such a simulation can, and in fact should, be used for the basic controller in order to provide the optimal clear sky trajectory for the inlet mass flow.

Unfortunately, the more realistic scenario is that the DNI behavior is not known for the whole day. The prediction of the DNI is a current field of research to improve the operation of CSP plants, especially for electricity scheduling [109, 264]. The term nowcasting usually indicates the forecasting or prediction of DNI in a time frame up to 6 hours [109] – though there is no strict definition yet. The relevant time frame for MPC applications considered here is even shorter in the range of 1 to 45 minutes. So far, the reliable online nowcasting of DNI for a solar plant is not possible. Nevertheless, it is essential to know, if nowcasting can be useful for the system in the future, what the quality requirements would be and what benefit can be expected. Therefore, emphasis is put on the particular advantages and limits of MPC applied to solar line focus once-through boilers in general. Some aspects have already been discussed for line focus systems with synthetic oil [36]. But the DSG process shows different system characteristics, which leads to different MPC designs and results.

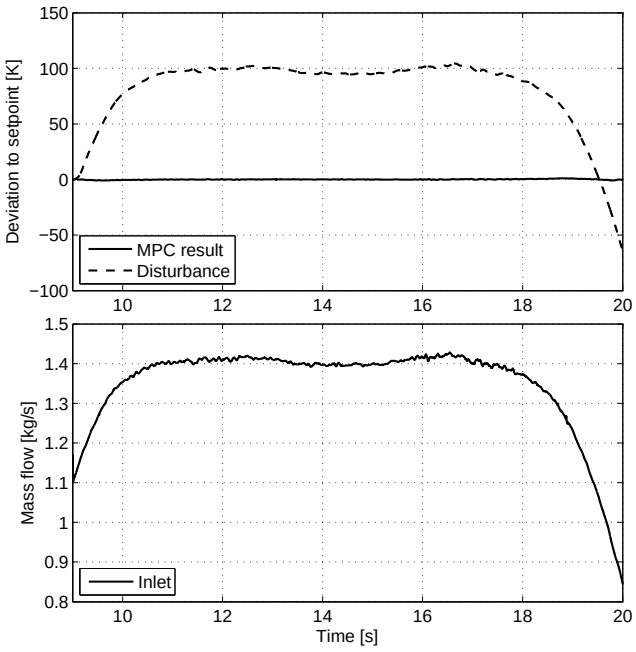

Figure 4.34: Temperature deviation in superheater section without control and with perfect MPC (top) and optimal MPC inlet mass flow (bottom); simulated with LTI model for 900 W/m²; manipulated variable: inlet mass flow, controlled variable: temperature before the SHI.

4.5.2 Linear MPC

The sections on basic control showed that there is a problem for the PI controllers, if the controlled plant section is very long and time delay is high. Such sections appear at the inlet and for variants B to D with only one injection. Note

that MPC cannot change the plant dynamics, nor can delays be removed from the physical system. However, MPC uses an internal model to predict the future behavior. In consequence, the dynamics are known to a large extend and MPC can act on a (constantly adapted) feedforward basis. If disturbances can be anticipated by a good disturbance model, MPC can use this feedforward strength to significantly improve the controller performance.

An illustrative example is discussed now. As shown during the experimental validation, the short shadowing of an evaporation collector causes a strong reaction of the superheating temperature. Collector 0B of the DISS test facility is assumed to be shadowed for two minutes and the response of the temperature before the SHI is analyzed. The peaks of the open-loop disturbance are about +20 K and -23 K before the steady state is reached again. Figure 4.35 shows the optimal results for a possible MPC configuration. The ideal case with a perfect disturbance prediction is shown on the left hand side together with the open-loop disturbance reaction. The shadowing starts at 50 s and ends at 170 s of the simulation. The perfect prediction is available from the start, i.e. a perfect nowcasting of 50 s ahead is assumed. The resulting temperature deviation is less than 3.5 K. This is possible due to the strong variation of the inlet mass flow. In fact, almost the complete working range between 0.55 kg/s to 1.55 kg/s is used. The detailed constraints are listed in Table 4.3, of which only the input constraints are applied. Note that such a strong reaction as well as the various mass flow oscillations would hardly be accepted by the plant operators. The inlet mass flow fluctuation should therefore be penalized by a higher weight in the objective function of the optimizer, which will be illustrated later on. Simulation starts from steady state with mass flows of 1.1 kg/s at the inlet and 0.07 kg/s at the EVI. The response of the MPC and the basic PI controller of the EVI are shown on the right hand side of Figure 4.35. The PI controller is quickly guiding the EVI mass flow to its maximum. The influence of the inlet mass flow is not considered here, as it would even slightly worsen the response due to the time delay. Only feedforward can help to improve the situation. The MPC has a prediction horizon of about 1200 s, i.e. three times the IMC time constant. At each sampling time, it finds an optimal open-loop trajectory to compensate the current error, by using the inlet and the EVI mass flow. In consequence, even without a disturbance prediction, the first peak of the temperature response is much lower than the one of the PI controller (at about +8 K). The second peak is close to the PI result and then there is a third peak before steady state is reached again. Note that a PI controller with a higher working range and without saturation would look very similar to this MPC result, but with slightly more oscillations at the end. The inlet mass flow is less fluctuating than before. By this, the potential of MPC is already visible, even if no accurate prediction is available.

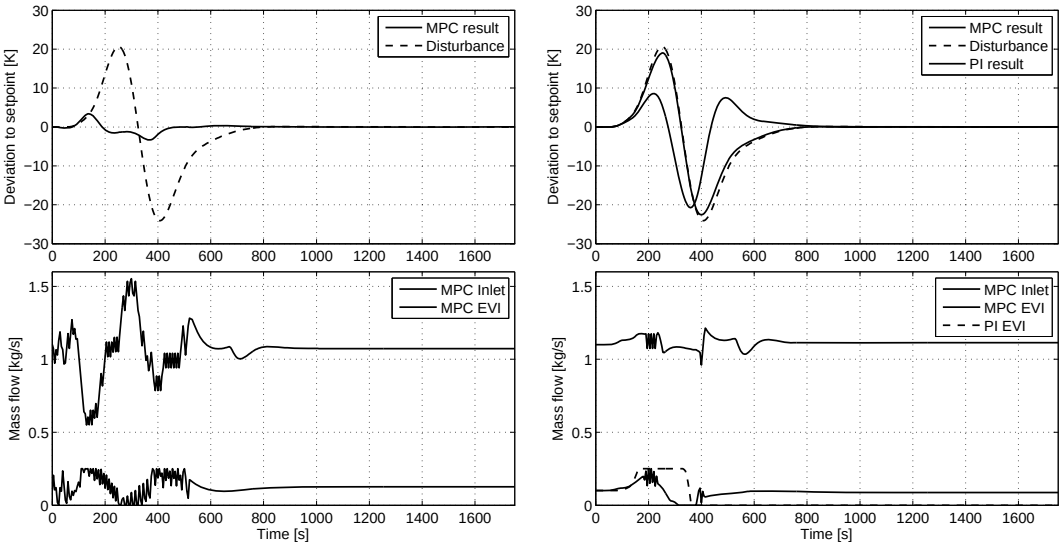

Figure 4.35: MPC performance with perfectly known disturbance (left) and unknown disturbance compared to basic PI controller (right); simulated with LTI models for 900 W/m²; manipulated variable: inlet mass flow and EVI mass flow, controlled variable: temperature before the SHI.

Table 4.3: Assumed constraints of MPC optimization problem.

Variable	*Minimum*	*Maximum*
Inlet mass flow	0.5 kg/s	1.6 kg/s
EVI mass flow	0 kg/s	0.25 kg/s
SHI mass flow	0 kg/s	0.25 kg/s
Inlet slew rate	-0.1 kg/s	0.1 kg/s
EVI slew rate	-0.15 kg/s	0.15 kg/s
SHI slew rate	-0.15 kg/s	0.15 kg/s
Outlet temperature	$\vartheta_{\mathrm{out,ref}} - 20\ \mathrm{K}$	$\vartheta_{\mathrm{out,ref}} + 8\ \mathrm{K}$
Temperature before injection	$\vartheta_{\mathrm{befInj,ref}} - 30\ \mathrm{K}$	$\vartheta_{\mathrm{befInj,ref}} + 20\ \mathrm{K}$

Unfortunately, the more realistic scenario is that the DNI behavior is not known or that only a certain guess can be made. Figure 4.36 illustrates the influence of the disturbance guess. It is assumed that the disturbance can be detected with a delay of four minutes after the initial shadowing, i.e. two minutes after it has vanished. The percentage of the guess indicates to which extend the disturbance is known to the MPC prediction. This is comparable to the reliability of the guess, although in a real system it would not be that simple. The initial response is the same for all delayed predictions. This can be explained by the fact that a faster reaction is not possible anymore. The guess then only influences the lower peak and the path to steady state. All assumptions lead to a

better result than without prediction (compare Figure 4.35, right). Therefore, a good qualitative assumption on the disturbance already improves the result, even if the disturbance has already vanished.

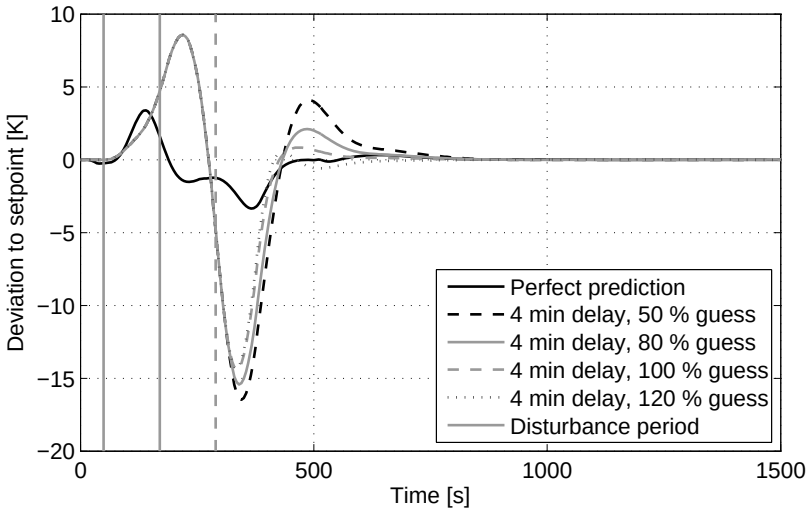

Figure 4.36: MPC performance with different guess qualities; simulated with LTI models for 900 W/m²; manipulated variable: inlet mass flow and EVI mass flow, controlled variable: temperature before the SHI; vertical lines indicate the disturbance (-) and the delay of the guess (--).

Besides the quality of the guess, the time at which the guess is made available is very important. Figure 4.37 provides an impression on that influence. Note that the disturbance starts at $t_{d0} = 600$ s and that the nowcasting availability is given relative to this time instant. An interesting result is that the temperature deviations are barely influenced by the prediction availability between -10 min and +1 min. In fact, the temperature stability is better for the latter case. The reason is that the mass flow deviations of the inlet mass flow are highly penalized in the objective function of the optimizer in this configuration. A long nowcasting horizon enables the inlet mass flow to vary less and slower and, thereby, to shift the higher control action to the EVI. The resulting inlet mass flow is shown in Figure 4.38 for two examples. The optimal nowcasting horizon cannot be determined independently from the MPC objective function. If the input variables are highly restricted to reduce the valves' wear and the fluctuation of the steam production, the nowcasting horizon should be longer. Nevertheless, a short-term nowcasting in the range of a few minutes is already very helpful for temperature stabilization. Note that the optimal nowcasting horizon also depends on the load. A reasonable requirement to the nowcasting seems to be the availability of the disturbance estimate in the range of one IMC time constant in advance. For the system of Figure 4.37, with the maximum IMC time constant defined from the inlet to the SHI, this is in the range of six minutes (compare Figure 3.31 on page 75).

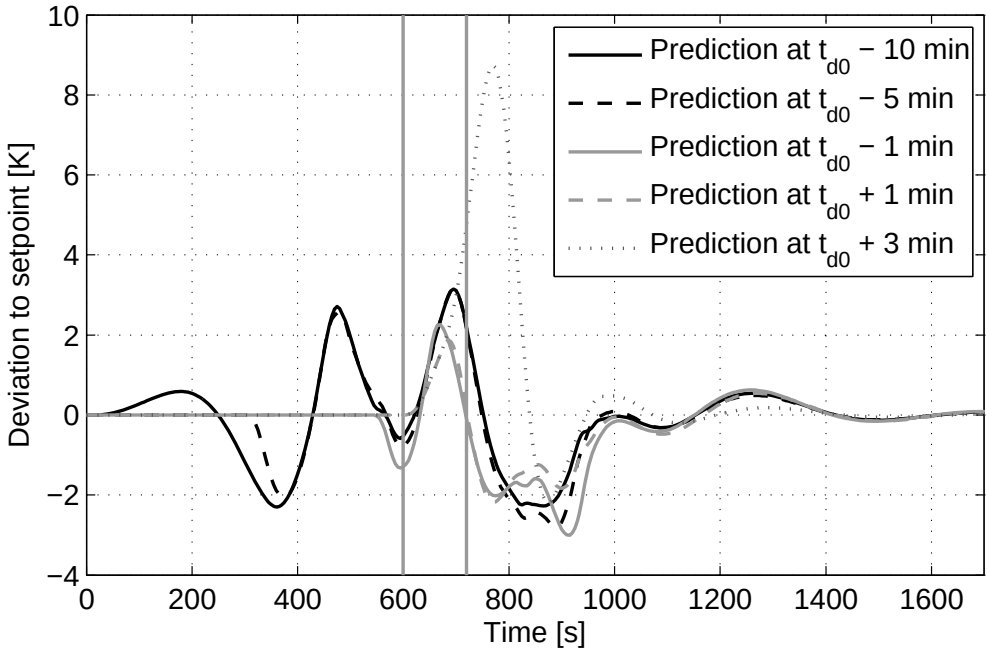

Figure 4.37: MPC performance with different nowcasting lead times; simulated with LTI models for 900 W/m²; manipulated variable: inlet mass flow and EVI mass flow, controlled variable: temperature before the SHI; left vertical line indicates start of the disturbance at time t_{d0} = 600 s.

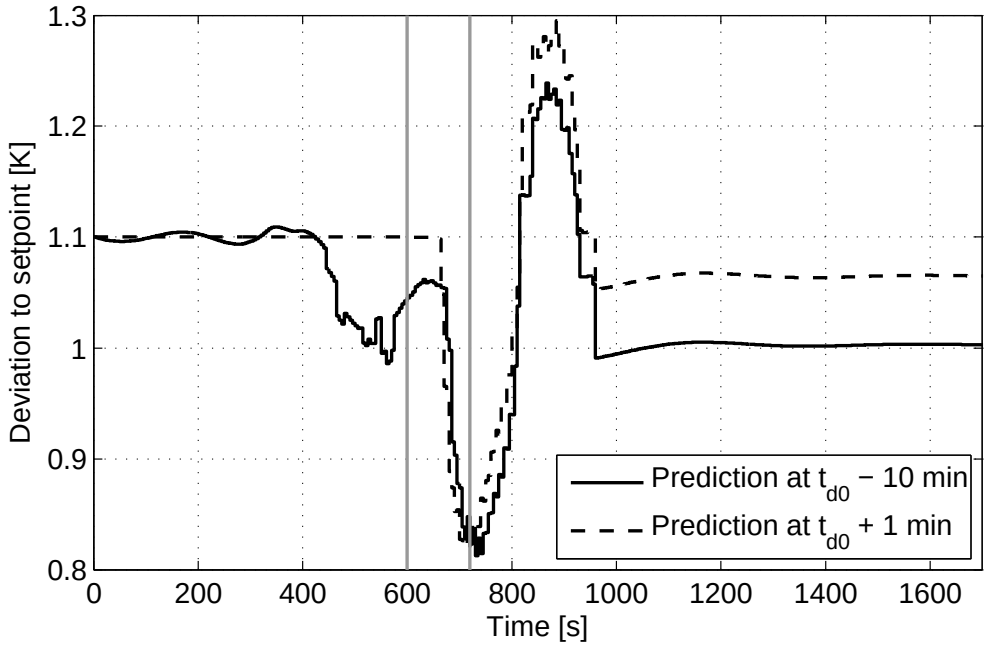

Figure 4.38: MPC performance with different nowcasting lead times; simulated with LTI models for 900 W/m²; manipulated variable: inlet mass flow and EVI mass flow, controlled variable: temperature before the SHI; left vertical line indicates start of the disturbance at time t_{d0} = 600 s.

The following paragraphs provide first qualitative recommendations for the design of an MPC scheme. The linear time-invariant models of the plant are only valid in a small operating range. Thus, as derived in [248], a linear MPC scheme should consist of various parallel LTI models. These models should then be selected depending on the current operating point. A pre-scaling of the gain while using the same time constant seems possible from identification and resembles a Hammerschmidt modeling approach [260]. One reasonable choice is to use five or six models for nominal conditions of 900 W/m², 750 W/m², 600 W/m², 525 W/m², 450 W/m² and maybe 375 W/m². Since the transient behavior gets more distinct with lower loads, a higher resolution must be used there. Similar to the scheduling of the basic controller, the selection could be based on inlet mass flow, taking into account that this should be a very slow change to guarantee stability. The regions, in which the models are applied, should then also be overlapping. Another possibility is to interpolate the free responses and the optimized trajectories between the two neighboring regions/models. A Kalman filter can be used to estimate the current state of the plant for each model in parallel. This allows for having a reasonable starting point when switching models.

The nowcasting can be accompanied by an augmentation of the model states for estimating the current disturbances. According to [159], the qualitative estimate of a certain disturbance and its inclusion in the internal model already help to significantly improve the MPC performance. This is promoted by the examples shown above.

An interesting option is also to use scenario-based MPC, e.g. similar to [21, 155, 220]. The free response is not only simulated for constant inputs, but different disturbance scenarios are generated, e.g. various energy disturbances at the loop inlet or fluctuations of the DNI on the whole field. The optimal trajectory is then defined by fulfilling all scenarios to a minimum extend. Weighting of the scenarios is then recommended. However, it is computationally expensive to generate and optimize many possible disturbance variants and weight them via probabilities. It will still be unclear, if the real disturbance is met, if no other measurements are available. Furthermore, various very conservative scenarios would most likely lead to a poor nominal performance. A more promising concept would be to combine the operator experience and other available information with the scenario MPC approach. Thus, it is suggested here enabling the operator to enter one or more disturbance scenarios manually when needed. For example, if a collector is defocused without the control system/MPC ‘seeing’ it, the operator might notice it. Then he/she can provide a guess of the disturbance, i.e. when the collector was de- and re-focused. The MPC can then consider the disturbance and react on the input accordingly. This operator support is especially helpful, as the disturbance might happen in the unob-

servable part of the plant. The 'ignoring' MPC reaction might otherwise take the wrong means or longer time for counteracting the disturbance.

It is also reasonable to change the weights of the input variables and the setpoints depending on the weather conditions. This can be done either explicitly, by providing different values to the MPC. Alternatively, the same can be achieved by changing the underlying disturbance scenarios, e.g. putting more weight on a scenario with high DNI fluctuations on cloudy days.

The application of the MPC is especially helpful for the multivariable interactions of inlet mass flow and evaporation injection, since for the latter no sensor for feedforward control exists. The improvements for the superheating injection are smaller due to the feedforward by the measured temperature before the SHI. Nevertheless, the overall performance could be improved by also integrating the SHI into the MPC.

Hard constraints on the output, e.g. maximum limit of the outlet temperature, should usually be avoided [159]. It is more advisable to put a higher penalty on such violations by the objective function. Exceptions are the physical limits of the system. This is usually the design temperature of the absorber tubes and their selective coatings. For an optimal exploitation of the working range, some superheating collectors should be integrated into the MPC such that an alternative to the hard constraints can be found by the optimizer. First preliminary simulation studies showed that even with a higher number of manipulated inputs, such as the collector focus values, the optimization can be realized within a sampling time of 5 seconds in a Matlab® and office PC environment (Intel Core i7 with 2.8 GHz). Using more efficient programming and hardware, such an MPC configuration could be applied to a large power plant as well.

Preliminary simulation studies also showed that there is a good agreement of the pure LTI simulations, as shown above, with simulations that use the MBM or DFEM as plant model, while keeping the LTI models for the internal optimization. Experimental validation and details of such an MPC strategy are not part of this work and must be left for future studies.

4.5.3 Non-linear MPC

Non-linear MPC (NMPC) has the advantage that only one internal plant model must be used. Predictions are more reliable compared to the LTI models, which can improve the overall performance. The main drawback of NMPC is usually that the simulations require more time and the internal optimization cannot be formulated as a computationally efficient quadratic programming problem. Good overviews can be found e.g. in [6, 45, 83]. For the system analyzed here, another problem arises from the fact that the optimizer tries variants that are physically not feasible or that do not fulfill the boundary condi-

tions of the model. This is a problem especially associated to the MBM, because the boundaries of the model must be fulfilled. This is not the case during high transients, which require strong changes of the input variables. Even if the complete range of the loop's operating conditions could be represented, the numerical stability and physical limits of the simulation would still be restricting this approach. Simulating the free response with the non-linear model and optimizing the trajectory with the linear models as suggested in [20] for parabolic trough plants with oil does not seem reasonable for DSG solar fields. A deeper analysis of NMPC for solar once-through boilers can be found in [215].

To overcome these numerical problems, it seems to be more useful to preestimate a good trajectory by linear MPC and then further optimize this trajectory by NMPC. The higher computational effort must then be weight against a slightly better trajectory.

Another difficulty for the MBM and DFEM arises from its numerical stiffness and the strong coupling with algebraic constraints. Classical state estimation is not applicable for large solar boilers, as described in detail in [215]. A state estimator such as the Kalman filter modifies the initial system state for the next simulation. Such a modification is usually not consistent with the algebraic constraints. Furthermore, due to the stiffness of the equation set, a numerical linearization cannot be found reliably. Extended Kalman filters, e.g. as applied to a solar dish system with a similar MBM [270] are therefore not reliable enough for the large distributed OTM. As this is the result of the different dynamics, the same holds for a linearization of the DFEM. In consequence, the state estimation should be performed by moving horizon estimation or particle filter techniques [215]. These are computationally demanding, although numerical tools and complex online applications already exist [46, 91, 98].

Concluding, the implementation of an NMPC scheme requires more reliable models, probably by further model reduction, or at least special integration algorithms for stiff algebraic systems. State estimation is also more demanding. It is a very interesting example for academia. Detailed studies are needed to evaluate, if such a development path is worse going for real plants.

4.6 Comparison and evaluation of control approaches

The comparison and evaluation of control approaches is performed in two steps. First, typical DNI disturbance classes are defined. Then, the control strategies are applied on days with these disturbances. The advantages and disadvantages of the controllers are thereby illustrated. All simulations are performed for the DISS test facility, since a validated model is available and the corresponding transfer functions and characteristics have already been introduced above.

4.6.1 Definition of reference disturbances

The main disturbance imposed on CSP systems is the fluctuation of the DNI. The course of the sun can be predicted very well and so can be the corresponding changes in incidence angle. If the collector's IAM is known, a good feedforward control can be established to compensate for these slow changes. Difficulties arise with clouds. It depends on the location, if there are cloud patterns or disturbance patterns that can be selected as typical ones. Such an approach is developed in the following for the site of the PSA. DNI data of the complete year 2013 is analyzed from measurements with a resolution of 10 seconds provided by PSA's high precision meteorological station [200]. Typical DNI patterns were visually identified and shown in Figure 4.39. The DNI and the effective irradiation must now be distinguished. The three top graphs show both the DNI and the effective irradiation. In winter (2013-01-06), the incidence angles are very large, resulting in an effective irradiation that is only in the range of 50 % of DNI and that reveals two peaks in the morning and in the evening. In summer (2013-06-24), the effective irradiation is almost the same as the DNI. The typical DNI patterns are valid for all seasons such that the effective irradiation is omitted in the other graphs. A typical situation of 2013 is an almost clear day with a short, but intense drop in DNI. This is represented by 2013-04-17 in the first row of Figure 4.39. Such a disturbance is caused by a small cumulus cloud – better known colloquially as "sheep cloud". These clouds are small, thick and very distinct. Figure 4.40 illustrates some typical cloud types. At PSA, cumuli often appear very scattered such that one location of the solar field might be shaded only once or twice per day, although the clouds are visible in the sky for a long time period. About 14 % of the days in 2013 were very similar. Additional 13 % of the days showed few but more than two drops with a significant time period between them. Depending on the height, thickness and velocity of the cloud as well as the sun position, the shading duration and intensity can vary. The DNI curves of 2013-07-13, 2013-05-18 and others provide corresponding examples.

With increasing cumuli density, only small clearings are left and the DNI oscillates strongly, e.g. on 2013-06-20, 2013-10-09 or partly 2013-10-06. In fact, data of 2013 revealed that about 15 % of the days showed significant time with similar cumuli field DNI patterns throughout the year, i.e. a sudden strong decrease of more than 80 % in DNI for various times within a short period of time. Similar patterns for cumulus humilis clouds have been described and mathematically analyzed for PV systems for a location in Tallinn, Estonia by Tomson [247]. The cloud cover pattern is highly stochastic and may be described by approaches such as Markov processes [176, 177] or lattice models with certain probability functions [4, 5].

Only about 3 % (10 days) could be identified as complete clear-sky days from the DNI data. 8 % of the days showed very small fluctuations of the DNI on a high level, which suggests the presence of thin cirri. This can be seen especially during noon on 2013-02-16, 2013-01-31 and many others. This pattern dominates for about 25 % of the days, which includes a significant share of the days with single cumuli events. On various other days, cirri are also present, but do not significantly contribute to the main cloud cover or disturbance, respectively.

One important example are days with cirrocumuli or fields of thick cirrocumuli layers. Such phenomena seem to appear frequently in the morning and in the afternoon at PSA, which is exemplified by 2013-03-15, 2013-07-03 or 2013-10-25. Bad DNI conditions are very likely to be caused by this kind of cloud type as well. From pure DNI data, it is not possible to distinguish unambiguously between thick layers of cirrocumuli fields and pure cumuli fields. About 4 % of the days showed comparable situations with drops by less than 20 % and being the dominant disturbance of that day. Days, for which this kind of disturbance appeared, but was not dominating, were not counted in this work.

Another phenomenon at PSA is the formation of cumulonimbi. This cloud type is very high, very thick and usually moves very slowly. It may also not move at all, but form up and disappear at nearly the same place. DNI disturbances are characterized by a long drop to zero, e.g. on 2013-04-02 in the morning or 2013-03-09 at noon and in the evening. This is probably due to meteorological low-pressure areas on the plateau of Tabernas [128, 150]. Such situations are unlikely for the Middle East or Californian deserts. However, for evaluating the likelihood of such situations, it is recommended to use local high resolution weather data and the expertise of local meteorologists.

For the assessment of control strategies and typical situations, a more general description of disturbances is desired. It is thus suggested here to normalize the DNI patterns to a relative time series. Ideally, one could use a clear sky DNI curve for comparison. The problem is that atmospheric conditions, necessary for a good clear sky prediction, are not available in historic DNI data and specialized equipment for measurement is needed. Therefore, an easier approach is used here, taking the convex hull of the DNI data of each day. The hull is initialized at sunrise and terminated at sunset. The relative DNI is then defined as ratio between DNI data and its hull. More precisely, it can be denominated hull-normalized DNI. This is illustrated in Figure 4.41 for May 18, 2013. The relative DNI provides a good impression on the occurring events. In the morning, some cirrocumuli clouds are present. Then, cirri prevail and additional cumuli appear in the afternoon.

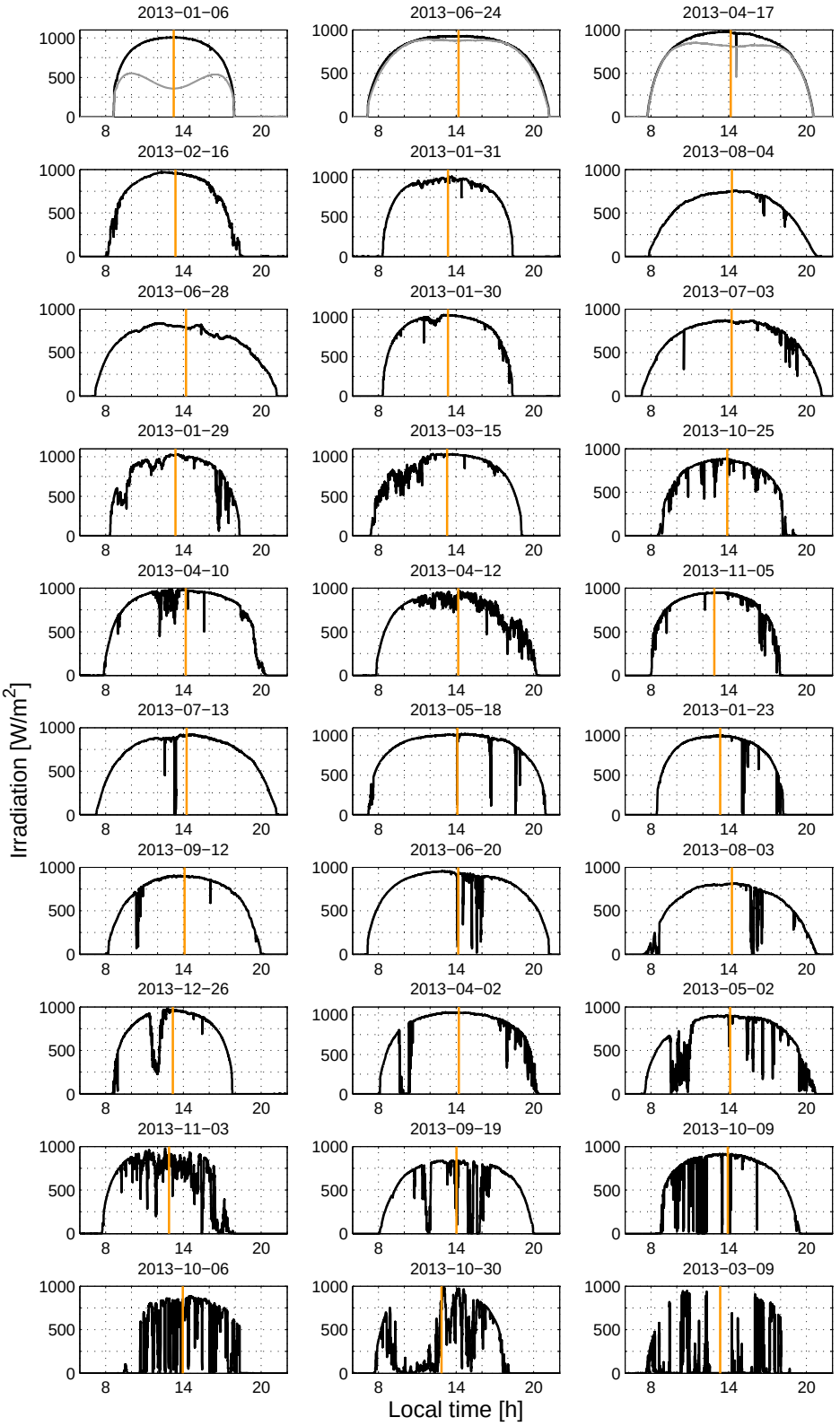

Figure 4.39: DNI data for 33 selected days at PSA in 2013 with 10 seconds resolution, showing all relevant occurring DNI patterns of that year; grey line in the top graphs: DNI*IAM including cosine losses; vertical line: solar noon.

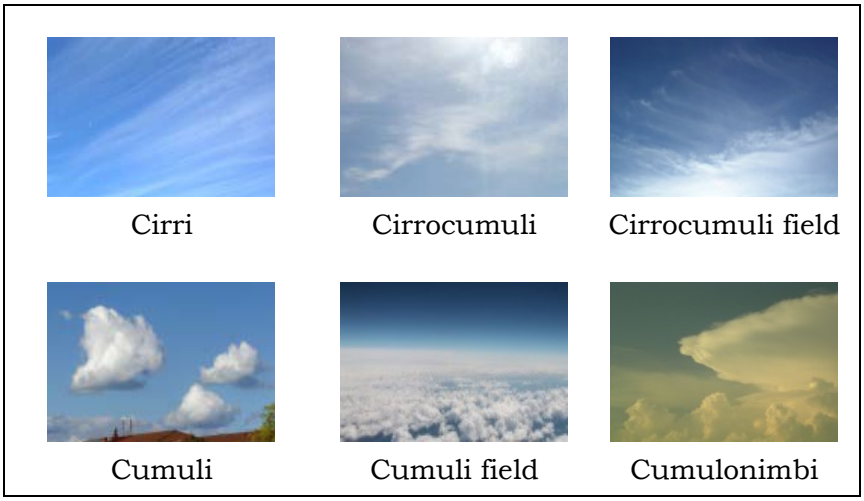

Figure 4.40: Cloud types for analysis of DNI characteristics (source: [261] and own pictures).

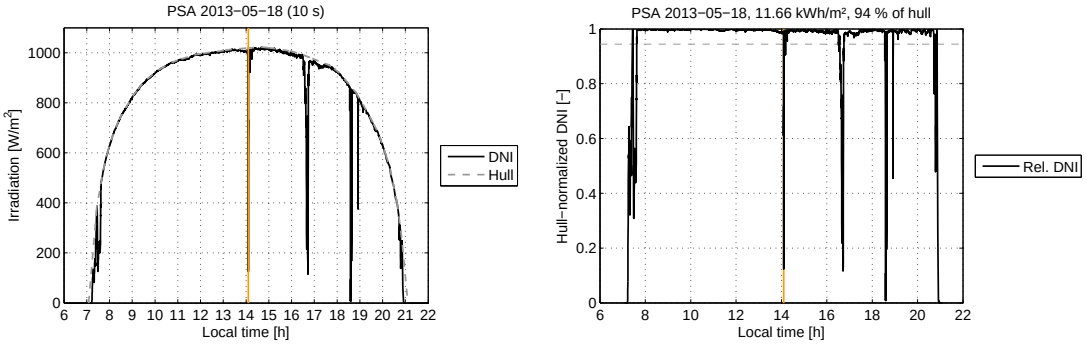

Figure 4.41: Normalized DNI exemplified for May 18, 2013; DNI and convex hull (left) and resulting ratio of DNI and hull (right) with integral mean value.

The integral of the relative DNI can be used to characterize how much energy is lost because of clouds. Since it is scaled to one, taking the mean value is equivalent. It is 94 % for the example and indicated as horizontal line in Figure 4.41, right. Note that it obviously does not give information about the absolute energy input. It is thus useful to include this value to the graph as well, which gives 11.66 kWh/m² in the example. The normalized DNI is shown in Figure 4.42 for all the representative days.

The scaled DNI is a very good means to assess typical patterns of a year, of cloud formations or of a power plant site. However, it lacks information on what might be critical situations for the solar field. To close this gap, typical transient characteristics or a system filter, respectively, are applied here to the normalized DNI. With respect to the once-through loop, the fastest system time constant is the one of the last superheating collector. One can apply the typical

LTI transfer function from defocusing of the last collector to the outlet temperature. Such an LTI function was derived in chapter 3.4.1 and a scaled version with a gain of one can be applied to the normalized DNI patterns. The results are shown in Figure 4.43 (grey lines). The same can be done for the slowest time constant, which is represented by the transfer function of a change in DNI on the complete loop to the outlet temperature. The results are also depicted in Figure 4.43 (black dashed lines).

The different influences are now better visible. Small fluctuations in DNI are smoothed by the fast and the slow system filters. It can be expected, that those do not cause difficulties for control. Drops visible only in the fast filter only affect the outlet temperature and the superheating control. They are almost negligible for the complete system, which acts as a low-pass filter. For drops of the slow system response, two cases are apparent when compared to the fast (superheater) response. High oscillations of the fast response are likely to cause high fluctuations of the outlet temperature. Thus, superheating control will be very ambitious. If the oscillations are small, the low-pass effect dominates and the superheating control can rather contribute to a fast adaption of the complete system. Difficult situations arise if the difference of both filters is large. The injection mass flow is usually in the range of 10 to 20 % of the overall mass flow. If differences in the filtered system responses (right column of Figure 4.43) are greater than this share, the injection controllers may reach their limits and no effective control may be possible. The system is considerably non-linear, such that the limits are not that strict. However, the general assumptions already provide a good impression on critical situations. As a result, 10 load classes are defined. These are based on relative DNI data. An overview is provided by Figure 4.43 and details are given in Table 4.4.

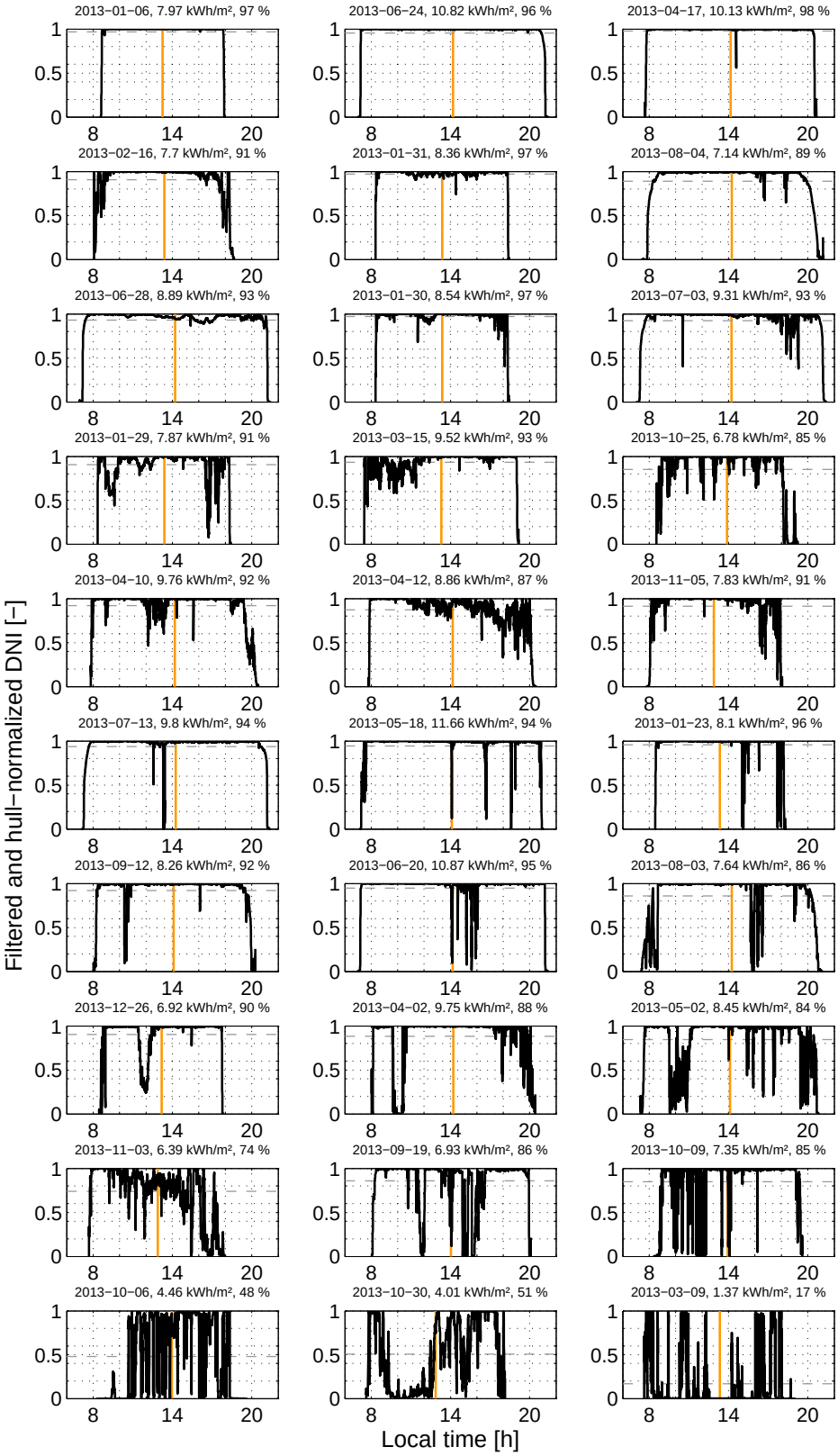

Figure 4.42: Hull-normalized DNI for 33 selected days at PSA in 2013 with 10 seconds resolution, showing all relevant occurring DNI patterns of that year; grey dashed horizontal line: mean/integral value of that day; vertical line: solar noon.

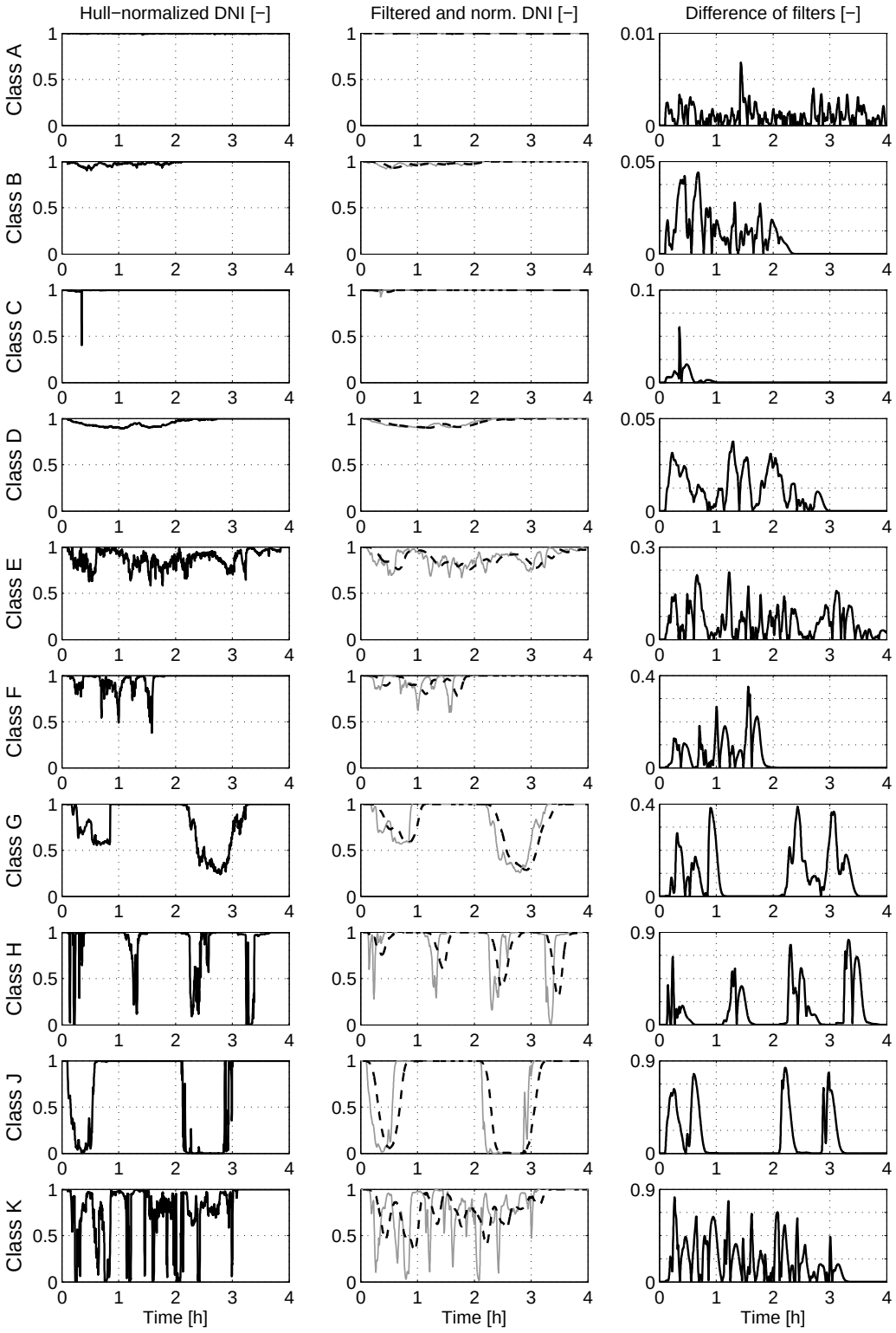

Figure 4.43: Definition of disturbance classes used as test cases for control strategies; filtered signals are from the fast system (grey line, defocus coll. 12 to outlet temperature at 900 W/m²) and the slow system (black dashed line, loop DNI to outlet temperature at 900 W/m²); filter difference is in absolute values; 5 seconds resolution.

Table 4.4: Overview on defined DNI disturbance classes; *minimum values of relative DNI, fast filter and slow filter; fractal lengths scaled to 1 hour for relative DNI, fast filter, slow filter and filter difference.

Class	*Original data (2013-MM-DD)*	*Hourly mean*	*Minimum**	*Hourly fractal length*	*Maximum filter difference*
A	06-24: 11-15 h	0.997	0.98/0.99/0.99	1.0/1.0/1.0/1.0	0.01
B	01-31: 11-13 h	0.97	0.91/0.92/0.93	1.4/1.05/1.01/1.06	0.04
C	07-03: 10-11 h	0.99	0.4/0.93/0.98	2.2/1.1/1.01/1.1	0.06
D	06-28: 15-18 h	0.95	0.89/0.89/0.90	1.1/1.02/1.01/1.02	0.04
E	03-15: 8-12 h	0.88	0.58/0.67/0.76	2.4-7.8/1.4-2.3/ 1.1/1.9	0.22
F	07-03: 18-20 h	0.93	0.38/0.60/0.77	4.3-5.8/2.0/1.2/2.3	0.35
G	01-29: 8-10 h	0.80	0.55/0.57/0.58	2.8/2.0/1.4/2.4	0.38
	12-26: 11-13 h	0.55	0.24/0.26/0.29	5.4/1.8/1.4/1.7	0.39
H	01-23: 15-16 h	0.95	0/0.28/0.76	8.3/3.3/1.3/3.4	0.66
	05-18: 16-17 h	0.93	0.12/0.29/0.61	4.6/2.4/1.5/2.8	0.55
	09-12: 10-11 h	0.86	0.93/0.16/0.41	8.9/3.4/1.8/3.6	0.78
	07-13: 13-14 h	0.86	0/0.01/0.30	5.6/3.1/2.0/3.9	0.83
J	09-19: 12-13 h	0.64	0.01/0.02/0.06	4.2/2.9/2.4/3.5	0.77
	04-02: 9-11 h	0.23	0/0/0	11.6/4.1/2.3/4.7	0.83
K	10-06: 11-15 h	0.73	0/0.02/0.33	11-23/6.2/2.1/7.0	0.82

The standard load case A is a clear sky day. The relative data is equal to one, with only small fluctuations within about -1 % from the hull data. The filters applied in Figure 4.43 (second column) are the same as before at the same effective irradiation level of 900 W/m² for the DISS test facility. These are the relevant filters for a summer day. If winter days with low effective irradiation or other OTM loops are to be analyzed, a different filter must be chosen. For illustration, results discussed here only include summer days.

The disturbance type is important for the evaluation of control. Some differences of the classes are therefore discussed in the following. Control results are presented in the next section.

A day with cirri (e.g. classes B or D) can have the same mean value as a period with sharp drops in DNI (e.g. class H). However, the outlet temperature can be held within its desired boundaries much easier for cirri than for the sharp drop, which will be shown later. Therefore, another measure is introduced. It is inspired by Khenissi [133], who applied fractal indices to characterize the energetic performance of a solar-thermal power plant. One of the first to introduce the fractal dimension to natural science was Mandelberg [160] based on the analysis of Richardson [208]. Richardson examined that the length of the coast

line of Britain cannot be determined, as it depends on the length of the ruler. If the coast line is measured by a ruler of 1 km in length, it is different, i.e. shorter, to the measured length by a 1 meter ruler. The length thus increases with a smaller ruler. This scaling influence is still denotes as Richardson effect. Although not the classical fractal dimension is applied here, the same idea is used for analysis of DNI signals. If a 10 seconds resolution of DNI measurements is considered, the length of the curve is longer than the length of the filtered or averaged signals. The fractal length L_{fract} of a curve is defined here as the total length connecting all points (t, y) of a time series chronologically. It can be calculated by the formula:

$$L_{\mathrm{fract}} = \sum_{i=1}^{N-1} \sqrt{\Delta t_{\mathrm{rel},i}^2 + \Delta y_i^2} \tag{4.25}$$

The arithmetic length within one sample time Δt_{sam} can be calculated by the change in time Δt_{rel} and the change in signal Δy. Note that the time scale $\Delta t_{\mathrm{horizon}}$ must be fixed to get comparable results:

$$\Delta t_{\mathrm{rel}} = \frac{\Delta t_{\mathrm{sam}}}{\Delta t_{\mathrm{horizon}}} = \frac{1}{N-1} \tag{4.26}$$

As a result, the ideal length of an unchanged signal during the time horizon is always one, with N being the number of samples within the time scale horizon. Table 4.4 provides values of the fractal lengths from the load classes scaled to a horizon of one hour. Note that not the time resolution is changed, which would be the equivalent of a changed ruler size for the coast line, but that the signal is changed by the characteristic filters. For an ideal clear sky day, the fractal length is equal to one. The ratio of the fractal lengths of the two filters already provides a first impression on the oscillations. If the ratio is close to one, changes are rather slow or oscillations are rather low. If the ratio is large or close to zero, respectively, sharp drops can be expected in the DNI and in the outlet temperature. Note that the absolute difference of the filters, as plotted in Figure 4.43, is also a good measure for sharp drops. Its fractal length is usually in the range of the fast filter signal, which is not surprising considering its calculation.

A certain time period can in general be assessed by the provided measures of fractal lengths of the filters, mean value of the relative DNI and maximum of the filter differences. In addition, the minimum values of the slow filter signal play an important role when real operating points are analyzed. For summer days, a relative minimum of 50 % may not cause problems, while it may for winter days due to the absolute minimum mass flow of a plant. Four values can thus be used as a good estimation of how critical operation may be in a certain time period.

4.6.2 Control quality criteria

The outlet temperature does not stay constant even during perfect clear sky conditions. There are two main requirements for successful operation. First, the operating conditions of a steam turbine must be met in all situations. Second, further restrictions of the loop, if they are more demanding, must also be fulfilled. The turbine limits are already listed in section 4.4. The most important boundaries of the rated life steam temperature $\vartheta_{LS,ref}$ being

- $\vartheta_{\mathrm{LS,ref}} + 8\ \mathrm{K} \leq \vartheta_{\mathrm{LS}} < \vartheta_{\mathrm{LS,ref}} + 14\ \mathrm{K}$:
  Limited to 400 hours/year in total
- $\vartheta_{\mathrm{LS,ref}} + 14\ \mathrm{K} \leq \vartheta_{\mathrm{LS}} < \vartheta_{\mathrm{LS,ref}} + 28\ \mathrm{K}$:
  Limited to 80 hours/year in total or 15 minutes per event

This is the minimum requirement stated in the IEC 45-1 standard [114] for steam turbines. It is taken as conservative limit here.

A temperature of 28 K above rated temperature is not allowed. This is usually not necessary as separate requirement, since the loop outlet temperature also has restrictions. In practice, there exist temperature limits to evoke an automatic defocus event of each collector. This temperature depends on the design temperature of the subsequent piping and the design temperature of the receivers. The latter is either limited by the absorber tube material or by the selective coating on it. High temperature coatings already exist for 550°C or even higher. At lower temperatures, the absorber tube material is more likely to be the limiting factor. As there is no general limit, three different temperatures are considered here. The same two limits as for the turbine are taken, i.e. 8 K and 14 K above the setpoint outlet temperature. Additionally, a higher deviation of 20 K also seems reasonable. The goal of the injectors is to reduce the defocus events as much as possible. On the other hand, a higher outlet temperature is beneficial when considering mixing effects of various parallel loops. If one loop can be operated close to the high limit, the low limit of the other loops is relaxed. This is an important aspect during periods with high oscillations of DNI.

The turbine limits are not important for the temperature before the SHI. In principle, the same design temperature as for the outlet temperature is valid. It may therefore be possible to simply restrict it to the setpoint of the outlet temperature. However, this would require the SHI to provide a very high mass flow, which usually is not possible due to the design limits of the injection valve. It is therefore assumed here that the limit of the temperature before the SHI is 20 K above its setpoint.

There are no strict limitations of the temperature gradient in the loop, in the header piping or in the turbine. Acceptable gradients for turbines are at least 5 K/min according to [24]. Considering mixing and thermal inertia effects in the header piping, a higher gradient may be acceptable for the loop temperatures. The limit considered here is chosen to be 8 K/min. If such a gradient is

critical must be determined by detailed studies for the receivers and especially for the header piping [26]. Such a study is not performed here and the gradient must be taken as an estimate for the loads on the system. The variables mentioned above are analyzed for the different disturbance classes and various control concepts for comparison in the following section.

4.6.3 Comparison of control strategies

The basic control strategy can now be analyzed based on the different disturbance class situations. The relative DNI can be multiplied with the clear sky curve or hull of any day. All simulations are performed here with a summer day. The original DNI data of June 24, 2013 is used, which is an almost perfect clear sky day. For the disturbance periods, the hull data of that day is multiplied with the relative DNI of the corresponding disturbance class. All simulations are brought to the same or at least comparable initial conditions before the disturbances start. Small deviations cannot be avoided, since different controllers are applied. The DISS facility is used as an example with injections before collectors 6 (EVI) and 11 (SHI). The corresponding figures are compiled at the end of the section for a better visual comparison.

Classes A to D

On a perfect clear sky day, all controllers are equivalent. Thus, class A is not shown separately. The system response of the new basic controller is directly shown for classes B and C in Figure 4.44. As expected from the filtered signals for these classes, the disturbance is negligible. A relatively fast drop followed by a fast increase in temperature is seen for class C around 13.3 h. The variation in outlet temperature is less than 6 K. After 14 h, the DNI slightly decreases and the temperature before the SHI falls to about 360°C. The mass flow of the EVI is reduced accordingly. The reduction in inlet mass flow, caused only by the decrease in DNI, makes the temperature before the SHI increase with a short time delay, which is then again compensated by the EVI. The result for class D, depicted in Figure 4.45, shows the same behavior over a longer period. It can be concluded that operation during disturbances of classes A to D does not cause any problem for control. When class C is imposed only on the evaporation part of the loop, the temperatures fluctuate more, but not in a critical manner. Such an effect would also be distributed and evened out for a large collector field.

Class E

DNI of class E is fluctuating with a high frequency and with jumps of up to 40 %. Temperature control is therefore more difficult than in the former classes. The differences in the control strategies now become visible. The basic control concept serves as a reference in Figure 4.46. Its outlet temperature can be

kept within 380°C and 426°C. Table 4.4 summarizes the time periods related to the temperature limits derived in the former section. If the basic concept is applied, the limit of 8 K above the setpoint is exceeded for about 30 min. The 14 K limit is exceeded for about 5.5 min and the defocus temperature is exceeded for about 2.7 min. The latter event is due to the steep jump in DNI level of +30 % at 12.5 h. Other strong increases of outlet temperature happen after 13.5 h and 15 h. An initial drop of DNI is catched by a fast reduction in SHI mass flow. The jump back to normal DNI then occurs before the former disturbance is settled and the delay in SHI reaction is too long to allow for a fast intervention. This kind of disturbance is critical for all controllers. Note that none of the shown concepts uses the DNI for feedforward of the injections, but only for the inlet. If a reliable local DNI signal was available, the disturbance could be reduced significantly, although a steep increase would still be visible.

The basic control strategy can be combined with the state-of-the-art approach of using a slow PI controller on the steam temperature [254]. This variant is represented here by the very similar control on the working range of the EVI. Note that all the rest of the controller design does not correspond to the state-of-the-art control, but is the same as the new basic concept as well. This case is called 'PI Inlet'. The disadvantageous effect for disturbance rejection is as expected from the control design sections above. The long time delay between the DNI disturbance and the effect of the inlet mass flow amplifies the temperature peaks during oscillations. This can be easily seen at the temperature before the SHI (lower left graph of Figure 4.46). It exceeds the 20 K limit for 39 min, which is about 16 % of the disturbance time of 4 h. During this time, 16.8 % of the accumulated DNI of the disturbance period, which is 3.2 kWh/m² between 12-16 h, is incident on the loop. A collector defocus at DISS facility corresponds to 50 m collector length or 5 % of the loop length. For longer collectors, it can be expected that the temperature is reduced quickly and stronger after defocus and it can be focused again after a short time. However, this will most likely again lead to another defocus event. The assumption of using an average of about 50 % of the collector area seems reasonable in this case. For a 100 m collector, this also leads to about 5 % loss of the loop area. The latter value is thus used as a loss factor for defocus events. In consequence, the PI control of the inlet mass flow causes a loss of about 0.168*0.05 = 0.84 % due to defocusing before the SHI. Sensitivity studies showed that the temperature behavior and the loss value are not significantly influenced by the actual setpoint of the inlet PI controller. The PI parameters obviously have a large influence, but simulations are already performed with beneficial values. With the basic control concept, the loss value is only half of it, with about 0.44 %. An innovative concept for a more reliable control was introduced in the adaptation section on page 141 with equation (4.22). The feedforward mass flow at the inlet is ad-

justed by a weight on the expected clear sky DNI. The result for a weight of 40 % is also shown in Figure 4.46 (with $w_{cs} = w_{clsky}$ for brevity in the graphs). The inlet mass flow is in general higher compared to the basic concept, which leads to smaller gradients and a higher buffer in the collectors before the SHI. This innovation completely avoids defocus events for this disturbance class after 12.6 h, if a value higher than 30 % is chosen. Lower values at least reduce the need for defocusing. The energetic loss associated to the first strong overshoot at 12.5 h is about 0.1 % of the total irradiation for a weight of 40 %. This shows the effectiveness for efficiency of the improved concept.

Note that such defocus events are very likely to happen for other CSP technologies as well, be it line focus or point focus systems. Line focus fields with DSG in recirculation mode (RM) have the advantage that they decouple steam mass flow generation in the evaporator part from the increase in temperature in the superheating section. The average mass flow in the superheating section is therefore more constant than for OTM. However, the temperature before the SHI, which is supposed to be installed in RM as well, cannot be controlled separately in recirculation mode. Thus, high DNI oscillations will have a comparable, maybe even worse, influence. For parabolic trough plants with synthetic oil, only a subfield mass flow is controlled. The exact control strategy is not known and depends on the actual plant operator. The high heat capacity of the fluid reduces the impact of the fluctuations in DNI. Nevertheless, the heat capacity of the tubes is smaller, there is no individual adaptation of the loop mass flow and the defocus temperature threshold is closer to the setpoint (about 7 to 10 K) due to the fluid's stability limitations. It is thus very likely that an oil plant also suffers from defocus events during class E disturbances. The exact share cannot be determined reliably in this work.

Class F

Class F disturbances are very similar, but show more distinct minima in relative DNI. The difference of the filtered signals is in the same range or slightly higher (compare above in Figure 4.43). The effect of increasing disturbances is illustrated in Figure 4.47. First, the basic control concept is analyzed. The first increase in DNI at 13.3 h showed a filtered difference of less than 0.15 and can be controlled well without any defocus event. The increase at 13.9 h has a filtered difference of 0.23 and an overshoot of more than 20 K of the temperature before the SHI is provoked for 6.5 min. The last stronger DNI step at 14.5 h has a filtered difference of 0.29 and an overshoot with defocus is likely for about 9.3 min. These values show a clear trend that the difference signal is a promising indicator for control performance. However, there is no direct correlation between overshoot and filter difference due to different initial system states before the decisive DNI step. PI control by the inlet mass flow significant-

ly increases the defocus time, while a weight on the clear sky mass flow significantly improves performance.

Class G

Class G is a difficult case for control. The minimum of the slow filter reaches values of 0.58 and 0.28 for the two different disturbances, which correspond to an effective irradiation of 530 and 250 W/m² derived from the DNI hull data. At an irradiation level of 250 W/m², a minimum mass flow at the inlet of 0.4 kg/s is needed in steady-state. The safety margins at DISS facility usually foresee a minimum mass flow of 0.4 to 0.55 kg/s. The simulations performed for class G are depicted in Figure 4.48 and consider two different minimum mass flows, namely 0.525 kg/s, as standard for simulations, and 0.25 kg/s, for exemplifying the corresponding system response. The mass flow of 0.525 kg/s requires an effective irradiation of 320 W/m² or a relative irradiation of 0.35 for the data of the summer day, respectively. The minimum of the slow filter already provides a good estimate on what happens. The first decrease in DNI is handled without problems by the control. All limitations are satisfied until the sudden step in DNI of +50 % at 12.75 h. Then, a longer overshoot compared to class F happens due to the lower initial mass flow. This overshoot lasts for about 20 min after the DNI step. It is very high and suggests defocusing two collectors before the SHI. Thus, an energetic loss of two times 5 % for the overshoot period is assumed, which is a rather conservative estimate. The outlet temperature has a long overshoot as well. Its initial cause is the DNI step for about 3 min, but then, the overshoot is only due to the high temperature before the SHI, which cannot be handled because of the SHI mass flow limits. For an energetic evaluation, only the initial 3 min must be considered. Further note that it is unlikely that any CSP technology would be able to cope with such a DNI step without defocusing. The difference is mainly in the overshoot period, which can be smaller for incompressible fluids like synthetic oil. Defocusing of 3 to 10 min is probable for these, which is about half of the energetic loss.

The second disturbance of class G, denoted G-2 in the following, shows a lower minimum of the relative irradiation. It is about 25 min below the required 0.35 for the normal minimum mass flow. The slow filter suggests that the minimum is violated for about 15 min, while the simulation results show a violation of the lower temperature limit (375°C) for 37 min. If the inlet mass flow can be reduced to 0.3 kg/s, a superheating temperature of 320°C can be maintained, while otherwise saturation shortly appears at the outlet. The size of the field and the operating strategy are decisive factors now. The mass flow of 0.3 or 0.4 kg/s could theoretically be applied safely at low DNI conditions. Only the increase in DNI requires a higher minimum mass flow. If the field and the thermal inertia are large enough to keep the turbine running, a reduction in minimum mass flow seems acceptable. More conservative loop operation would

probably lead to a trip of the turbine and to condensate entering the life steam header. Both events contribute to a certain life time reduction of the components. Furthermore, the re-start of the turbine will take additional time and cause additional losses. If the overall loop suffers from the same disturbance, the pressure of the solar field also decreases. This is not represented in the simulations, but the effect is rather small for the OTM due to the small mass in the loop. For recirculation mode with a central steam drum, experience from the TSE1 plant [141] suggests that the disturbance can be handled by operating the turbine at low load in fixed power mode. The steam drum provides a continuous mass flow at decreasing pressure, which can still be slightly superheated by the superheating section. Turbine operation is thus maintained, although at a lower efficiency. Recirculation mode thus offers decisive advantages for class G-2 disturbances.

The subsequent increase in DNI after 14.8 h is slower than for the first disturbance, such that the resulting overshoot period for the temperature before the SHI is only 21 min for one collector. A defocus in the last superheating section may be needed for only about 3 min, if the collector before the SHI is defocused.

Class H

Four different drops of DNI belong to class H. They differ in the minimum of their filtered signals, but can all be characterized by a fast drop followed by a fast increase of DNI. Figure 4.49 (left) shows the corresponding simulations. Due to the steep changes in DNI, the integration accuracy was relaxed by a factor of two. Various simulations with similar accuracies were performed and yielded the same results. The results of class G can be reproduced with the relaxed accuracy as well. This is mentioned here explicitly, since the results of class H look surprisingly well compared to class G. Differences between fast and slow filter reach values between 0.68 and 0.86 for class H, while remaining below 0.4 for class G. Nevertheless, the overshoots of class H are very small compared to class G. This can be explained by two effects. First, the last DNI step of class G-1 is 500 W/m² within 5 seconds. For the steepest step of H-4 at 15.3 h, it is 700 W/m² within 60 seconds (H-2: 520 W/m² in 45 s), which is much less and leaves time for controller reaction. Second, the step increase of H-4 is further interrupted by a short drop of about 150 W/m² which is hardly visible in the graph. Similar intermediate drops exist for the other DNI recovery curves of class H. The first pattern of class H is not critical for an OTM plant and the loop outlet stays within its desired limits. The second pattern (H-2) shortly falls below the desired turbine limit at the outlet of the loop. Nevertheless, this does not cause problems for a large solar field because of mixing effects. These might not be sufficient for the other two patterns of class H, for which saturation occurs at the outlet for a short time. The extent of energy loss

again depends on the operating strategy. For recirculation mode, it is likely that saturation is avoided by the same means as mentioned for class G.

Class J

Disturbances of class J can be described unambiguously. The quick and long reduction in DNI cannot be compensated by the system. After 7 to 15 min, saturation is reached at the outlet. Temperature is recovered quickly after DNI appears again, but even for large fields, it is unlikely that turbine operation can continue without further means like storage or co-firing. Note that periods without DNI can be bridged by the steam drum in recirculation mode. Half an hour or even longer is possible, e.g. as shown in TSE1 [141]. This is a clear disadvantage of the once-through concept, but an expectable result from omitting the installation of the steam drum, which otherwise serves as a short term storage.

Class K

Class K represents extreme oscillations of DNI. The results for the basic control concept are shown in Figure 4.50. Saturation appears for about 12 min of the three hours of disturbance. During about one hour, the outlet temperature is below the desired minimum temperature of 375°C (54 min for basic control, 64 min for weighted mass flow example). A collector before the SHI needs to be defocused for about 19 or 36 min, depending on the control chosen. Ideally, only the latter 1 or 2 % of the energy are lost due to defocusing. If violations of the low temperature limit cannot be compensated, additional 25 to 30 % of the solar energy is lost. If the turbine trips and needs to be restarted three times for about 20 min (hot start), about 40 % of the energy are lost in total. These values are based on operation of one loop and the assumption that the complete loop has the same local DNI distribution. Both assumptions do not hold for a large solar field. The mixing effect during such weather conditions can be very advantageous, such that the turbine may not trip. A reduced pressure operation can be foreseen for this. If such weather conditions are very often, a large thermal inertia for buffering seems a very promising option. It is also possible to reduce the feedforward mass flow and defocus more collectors. This can reduce the temperature variation, although it cannot avoid the saturation events unless the minimum mass flow is reduced. The distribution of the DNI can have positive and negative effects on temperature stability. It is a highly stochastic process and is therefore not analyzed here in detail. In summary, operation on a class K day seems possible, but a high energetic loss is very likely. A loss of 2 to 10 % seems possible for large collector fields due to thermal inertia and mixing effects. Without these effects, a loss of about 40 % may be expected. The high temperature cycling at the outlet may significantly contribute to the life time reduction of the material. Three temperature cycles of about

110 K and three of about 70 K can be assumed from Figure 4.50. In a worst case scenario, it might be economically better to not operate at all considering the component cost and life time. Such analyses can only be performed for particular plants and with all information available. A general case is therefore not analyzed here.

Table 4.5: Time periods of exceeding limitations of outlet temperature and temperature before SHI, all values in minutes; GA = gain acceleration; w_{CS} = weight of clear sky mass flow.

Class	*Case*	ϑ_{out} $> \vartheta_{ref}$ + 8/ 14/ 20 K *[min]*	ϑ_{befSHI} $> \vartheta_{ref}$ + 20 K/ $< \vartheta_{sat}$ + 20 K *[min]*	$\frac{d\vartheta_{out}}{dt}$ / $\frac{d\vartheta_{befSHI}}{dt}$ > 8 K/min *[min]*
A-D	All	-	-	-
E	Basic	29.9 / 5.5 / 2.7	19.6 / -	3.5 / 14.9
(4 h)	w_{cs} = 20 %	25.6 / 5.3 / 2.2	9.4 / -	3.5 / 10.2
	w_{cs} = 40 %	20.5 / 3.3 / 1.2	3.7 / -	2.8 / 4.9
	w_{cs} = 20 %+GA	21.3 / 3.9 / 1.6	9.4 / -	3.5 / 10.1
	PI Inlet	35.9 / 5.3 / 3.0	38.9 / -	3.3 / 15.7
F	Basic	15.3 / 7.3 / 2.7	15.8 / -	4.7 / 11.8
	w_{cs} = 10 %	14.8 / 6.8 / 1.8	11.9 / -	4.3 / 10.6
	w_{cs} = 30 %	13.8 / 2.1 / -	5.8 / 1.2	3.5 / 9.0
	PI Inlet	34.4 / 23.0 / 17.1	38.3 / -	7.5 / 16.6
G	Basic	24.4 / 19.8 / 16.8	19.9 / -	2.7 / 6.7
(1.5 h)		10.4 / 8.5 / 6.6	21.1 / 35.6	10.2 / 7.6
	Low min	24.4 / 19.8 / 16.8	19.9 / -	2.7 / 6.7
		21.0 / 16.3 / 12.8	25.9 / 28.6	8.9 / 8.3
H	Basic	2.3 / 0.0 / 0.0	12.0 / 1.6	2.7 / 7.7
		12.4 / 5.6 / 3.7	12.9 / 5.7	5.3 / 7.3
		6.4 / 4.3 / 1.3	14.8 / 11.3	7.8 / 5.5
		1.1 / 0.0 / 0.0	6.6 / 13.2	5.8 / 6.3
	w_{cs} = 30 %	0.0 / 0.0 / 0.0	4.2 / 1.9	2.3 / 7.6
		4.4 / 0.0 / 0.0	5.3 / 7.2	6.1 / 8.0
		2.3 / 0.0 / 0.0	3.5 / 13.5	7.6 /6.2
		0.0 / 0.0 / 0.0	4.8 / 14.2	5.6 / 6.2
J	Basic	9.0 / 4.4 / 0.0	12.3 / 30.1	4.6 / 7.3
K	Basic	35.5 / 24.8 / 16.7	47.1 / 37.7	40.7 / 58.6
	w_{cs} = 20 %	19.0 / 11.5 / 4.5	34.3 / 48.1	43.3 / 52.3

Table 4.6: Energetic considerations for the different disturbance classes and control strategies; GA = gain acceleration; w_{cs} = weight of clear sky mass flow.

Class	*Case*	*DNI share during high-T events bi/out [%]*	*DNI share during too low outlet temperature [%]*	*Expected energy loss due to defocus relative to solar resource bi/out [%]*
A-D	All	-	-	-
E	Basic	8.79 / 1.20	-	0.44 / 0.06
(3 h)	w_{cs} = 20 %	4.17 / 0.98	-	0.21 / 0.05
	w_{cs} = 40 %	1.63 / 0.52	-	0.08 / 0.03
	w_{cs} = 20 %+GA	4.17 / 0.72	-	0.21 / 0.04
	PI Inlet	16.79 / 1.34	-	0.84 / 0.07
F	Basic	13.98 / 2.38	-	0.70 / 0.12
	w_{cs} = 10 %	10.55 / 1.63	-	0.53 / 0.08
	w_{cs} = 30 %	5.08 / -	-	0.25 / -
	PI Inlet	33.46 / 15.17	-	1.67 / 0.76
G	Basic	25.05 / 21.65	-	2*1.25 / 1.08
(1.5 h)		31.20 / 9.44	23.3	1.56 / 0.47
	Low min	25.05 / 21.65	-	2*1.25 / 1.08
		37.41 / 18.32	17.8	2*1.87 / 0.92
H	Basic	20.57 / 0.00	3.26	1.03 / -
(1 h)		23.10 / 6.50	8.47	1.16 / 0.33
		27.11 / 2.20	15.15	1.36 / 0.11
		12.51 / - ?	16.70	0.63 / - ?
	w_{cs} = 30 %	7.27 / -	3.69	0.36 / -
		9.40 / -	10.54	0.47 / -
		6.77 / -	17.93	0.34 / -
		9.19 / -	18.75	0.46 / -
J	Basic	31.74 / -	29.80	2*1.59 / -
K	Basic	30.48 / 11.71	25.85	1.52 / 0.59
			4.80 (sat.)	
	w_{cs} = 20 %	22.05 / 3.23	30.34	1.10 / 0.16
			6.06 (sat.)	

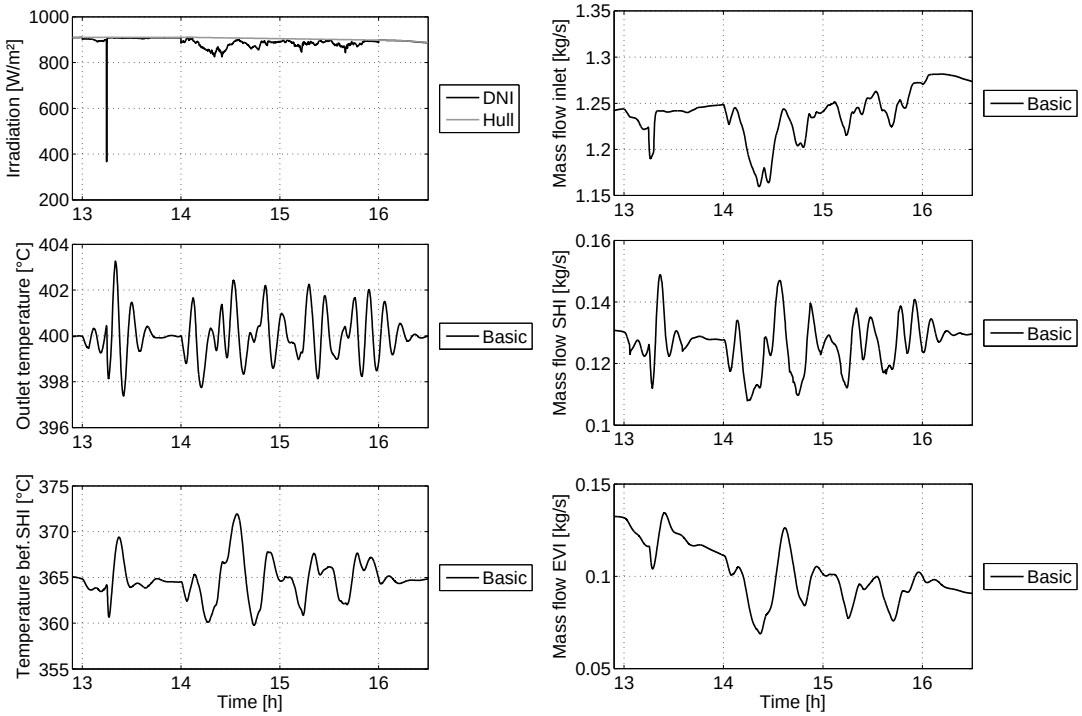

Figure 4.44: Control simulation of disturbance classes C (13-14 h) and B (14-16 h) with loop variant A for DISS test facility.

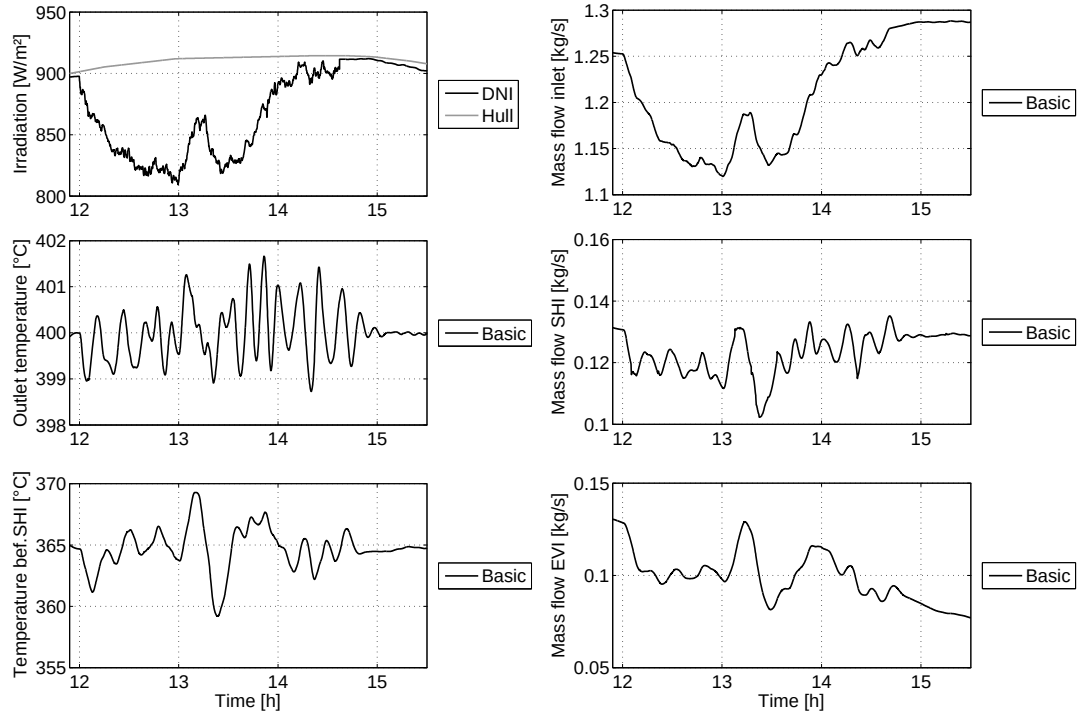

Figure 4.45: Control simulation of disturbance class D with loop variant A for DISS test facility.

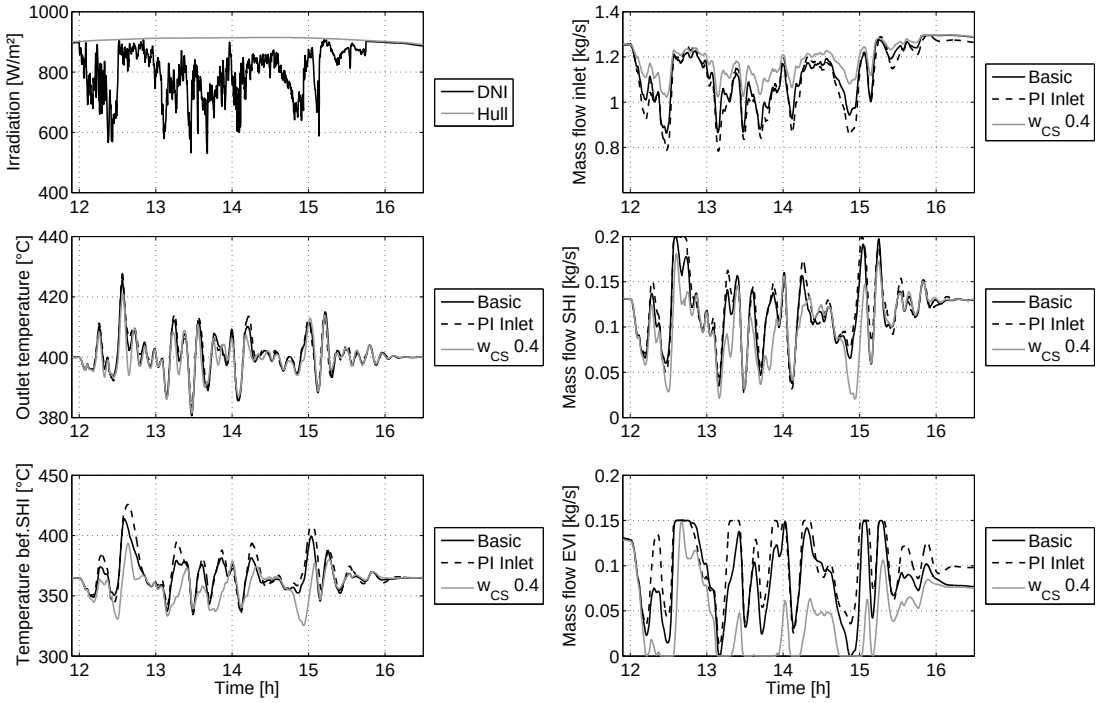

Figure 4.46: Control simulation of disturbance class E with loop variant A for DISS test facility.

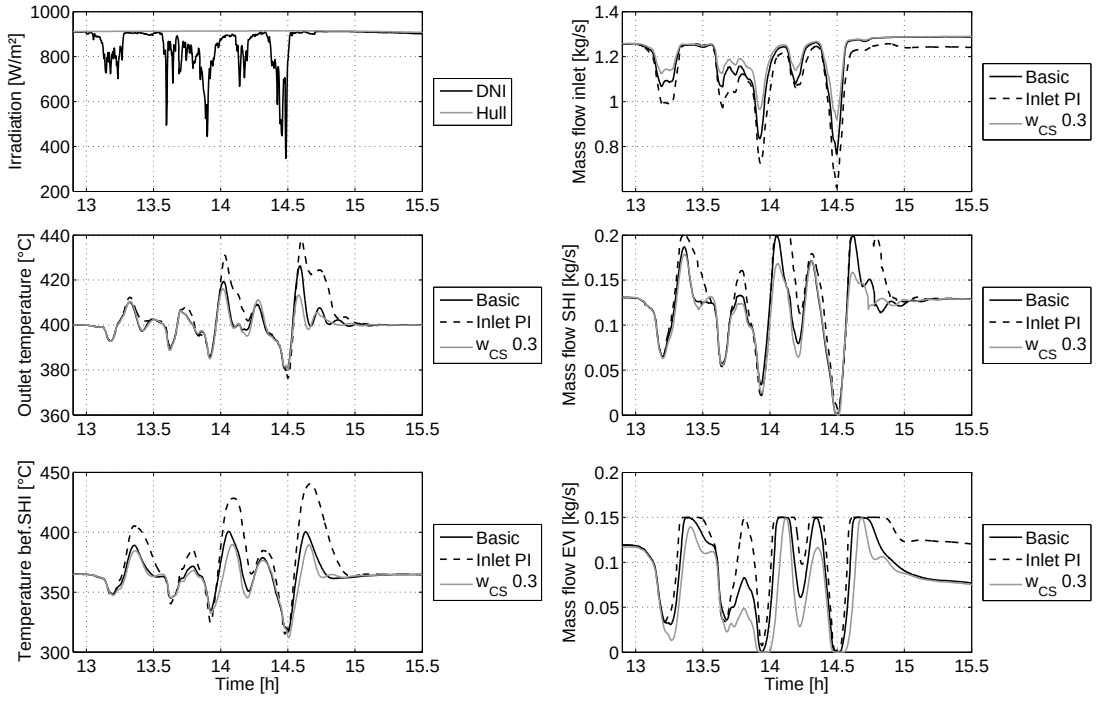

Figure 4.47: Control simulations of disturbance class F with loop variant A for DISS test facility; inlet PI controller with mass flow setpoint of 0.12 kg/s for the EVI.

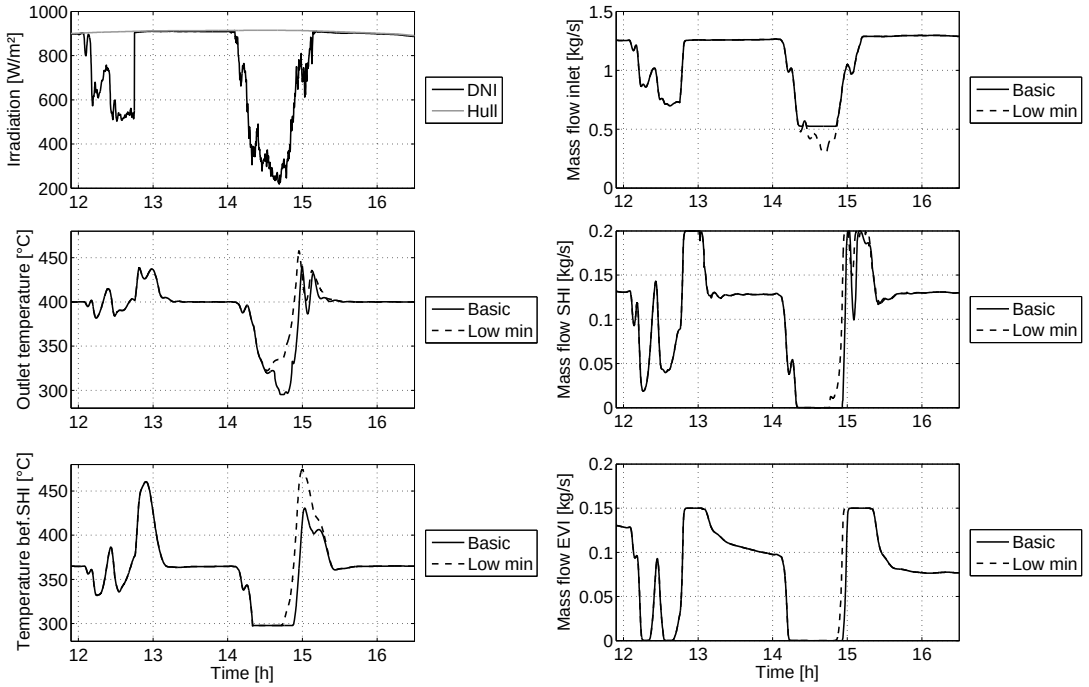

Figure 4.48: Control simulations of disturbance class G with loop variant A for DISS test facility; minimum mass flow at inlet is 0.525 kg/s (basic) and 0.25 kg/s (Low min).

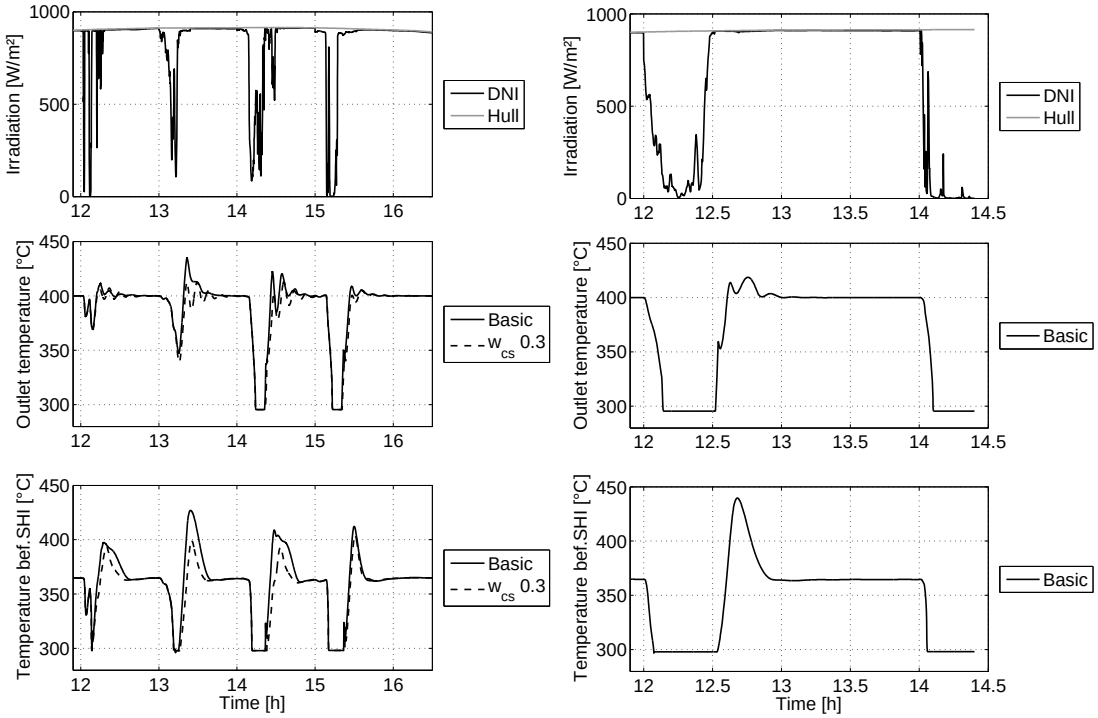

Figure 4.49: Control simulations of disturbance classes H (left) and J (right) with loop variant A for DISS test facility; minimum mass flow at inlet is 0.525 kg/s.

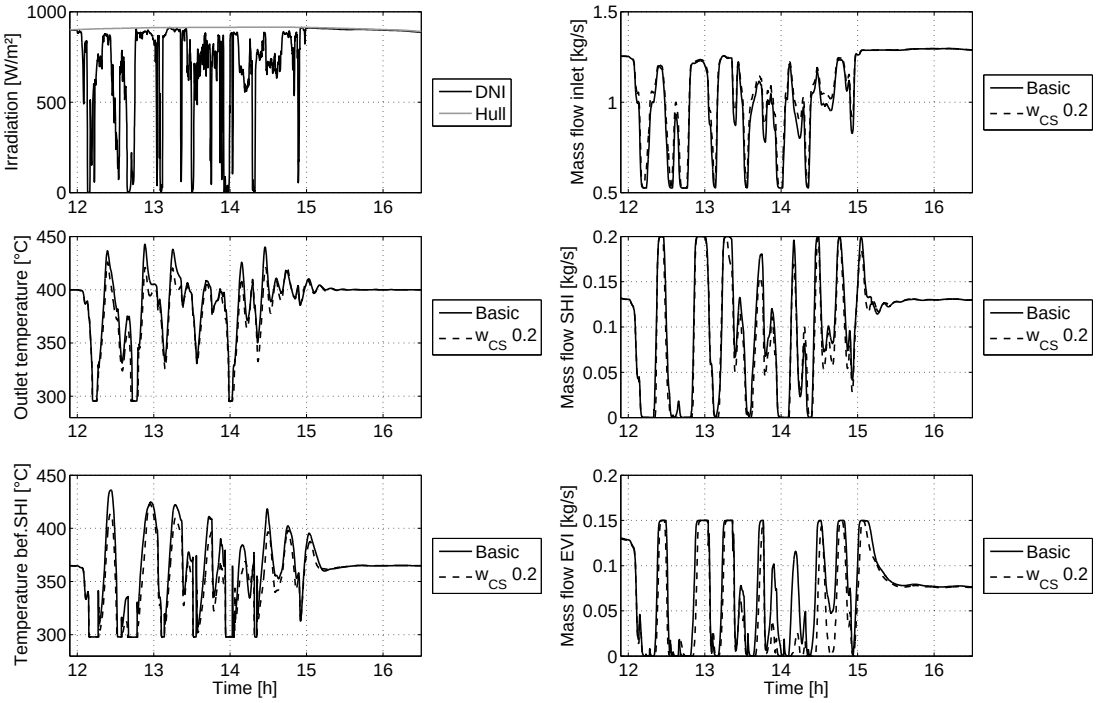

Figure 4.50: Control simulations of disturbance class K with loop variant A for DISS test facility; minimum mass flow at inlet is 0.525 kg/s.

4.6.4 Evaluation of controllers

The chapter on control shows the consequences of the transient system characteristics. The inlet mass flow is not able to compensate for quick changes of DNI and worsens the situation. Therefore, the state-of-the-art PI control of the inlet by a steam temperature is not recommended. A more reliable feedforward scheme has been suggested instead. The division of the loop in three parts, represented by variant A, is the best option for control. The evaporation injection and the superheating injection work independently and reliably with the suggested control design based on time constants derived from internal model control. Variant A guarantees good control results during most of the analyzed disturbances. As a result of these developments, the application of the once-through mode is feasible for commercial power plants.

From a control perspective, variant A is clearly recommended. Variants B (only EVI) and C (only SHI) are not shown explicitly in the figures of section 4.6.3. Their performance is usually worse than the one of variant A with PI inlet control, even when the PI inlet control is not active for those variants. Energetic losses must at least be doubled compared to the basic control of variant A. Class C and D disturbances also lead to defocus events, while these disturbances can be handled without problems by variant A. Losses are only comparable for class J, during which saturation dominates and operation is not possible

anyway. Only a very high installation cost of the second injection may shift this preference economically to variant B or C. The control characteristics of variant B then promote its application for loops with low superheating shares. This stabilizes the single end of evaporation, while the delays are still acceptable. Variant C is favored for high superheating shares to keep an acceptable delay for outlet temperature control. If low outlet temperatures are acceptable for some periods during a disturbance, variant B in combination with a smart defocus control of the outlet collector is another option beneficial for control.

A classification of DNI disturbances of the particular project site is recommended for the selection of the loop variant. This has been exemplified in the former section and can be followed adding information about the classes' frequencies throughout a typical year. In general, a large share of clear days from classes A to D favors the application of the once-through mode and a variant with only one injection may be an option. With a shift to classes E to H, variant A becomes more reliable and enables the application of the OTM. With a high share of class J and K disturbances, OTM suffers from the lack of thermal inertia, which must be compensated by storage or co-firing for continuous turbine operation. Otherwise, recirculation mode with its inherent steam buffer tank is favorable.

The control design derived here clearly enables the OTM to be applied in commercial plants under the mentioned conditions. Defocus control can contribute to quickly react during fast disturbances of class K. This option seems worth analyzing in more detail in the future, especially for Fresnel collector fields. The only feasible option to further improve temperature stability with better efficiency at the same time is the application of more complex control schemes. Model predictive control can be used to allow the inlet mass flow to contribute to control of the steam temperatures. This may lead to the economic feasibility of variant B or C. The intrinsic feedforward action of the MPC could also be used for more aggressive action of the injections during fast increases of DNI to avoid defocus events. It also has the potential to optimize the combination of mass flow, predicted mean DNI and defocusing by including focus signals to the MPC algorithm. This can especially be beneficial for days of class K. A deeper analysis seems worth the effort for the medium and long term.

5 Methodology for absorber tube stress analysis

The components of a power plant must be designed to work reliably during their whole life time. Design codes exist for conventional pressure vessels such as steam generators to guarantee this requirement. These are important for the safe operation of the plant and for the security of all people involved. It is obvious that a reliable design must be demanded from solar once-through boilers as well. The normal way of design is either to use empirical guidelines for particular components or to generate certain load scenarios and their associated influence on life time. For solar once-through boilers, some empirical estimates can be taken from conventional steam generators. However, the dimensions are significantly different with longer pipes, larger inner diameters and greater wall thicknesses. The heat flux incident on the absorber tubes is different as well, usually much lower than in conventional steam generators. Daily start-up and shut-down cycles impose further loads on the system. The main resulting questions are which load scenarios are realistic for a solar plant, how high their impact is on material life time and how often one can assume them to happen during the plant's life time. These aspects are important for the design of a component. They can also be used for its monitoring during operation in order to compare design and operating conditions.

On the one hand, the component must withstand high static loads, e.g. the high pressure of the steam inside a receiver tube. The wall thickness should be increased to withstand these higher loads. On the other hand, temperature fluctuations within the wall of components cause alternating (thermal) stress. Such stress increases with the temperature deviation as well as with the inhomogeneity of the components' shape. The wall thickness should be decreased to better withstand such transients. In consequence, a good compromise must be found for the design.

The aim of this chapter is to provide a methodology to derive boundary conditions for a reliable design of the solar field components. This methodology is exemplified by a receiver tube. The emphasis is put on the influence of low cycle fatigue on the life time, since this is the most relevant mechanism associated with solar plants in the range of up to 500°C [26]. Fatigue can be described as material weakening due to frequently occurring loads. The influence of creep is not considered here because of the, for creeping, rather low temperatures in line focus systems. Three relevant impacts exist for a solar once-through boiler. One is the daily start-up and shut-down cycle of the solar field, which leads to very high temperature changes in the superheater section of the solar field. The second impact is steam temperature fluctuation in the superheating section. This is usually caused by high irradiation gradients or disturbances and should

be reduced by a good temperature control. The third aspect is the fluctuation of the end point of the evaporation and certain stratification or dry-out phenomena that might appear close to it. Start-up cycles can be estimated well and design is in principle similar to current coal-fired steam generators. Thus, the remaining two aspects are analyzed in more detail in the next sections.

5.1 Outline of methodology

The methodology is outlined here and then exemplified in the subsequent sections. This methodology can be applied to all CSP technologies and is summarized by the following procedure:

1. Identification of critical locations and components
2. Identification of typical load classes
3. Estimation on boundary conditions for thermal stress analysis at critical components/locations for each load class
4. Estimation on cyclic thermal stress at critical components/locations for each load class
5. Estimation on frequency of each load class for one year or whole desired life time
6. Estimation of the stress rupture strength for each critical component based on appropriate design standard
7. Evaluation of life time dependent on stress strength, frequency extrapolation and weighting of load classes for each critical component.

1) Identification of critical locations and components

The identification of critical locations or components must be evaluated in detail. Welding of small pipes to thick-walled pipes is in general critical. One example is the connection of the loop outlet to the life steam header. The receivers at the loop outlet and before the SHI are prone to high temperatures with the smallest heat transfer coefficients (HTC). They are additionally cycled during defocus events or when the sun is covered by clouds. This might be critical as well. Thus, the receivers before the SHI and at the loop outlet shall be considered. The fluctuation of the end of evaporation is supposed to be critical due to certain dry-out phenomena and quickly changing heat transfer coefficients. One shall analyze receivers shortly before, at and after the EPE. These can also be treated as one to add conservatism. The fluctuation of the EPE during strong disturbances must be considered as well. It might be the case that the EPE moves before the evaporation injection or after the SHI. The latter event is a standard load during start-up and shut-down of the solar field. The design of the header line and the steam attemperators must include this load as well. For recirculation plants, especially the steam drum is an additional

critical component. The receivers at the loop inlet have low temperature gradients around the circumference and high heat transfer coefficients. It is thus unlikely that these components suffer from additional critical loads. Nevertheless, this should be verified especially during start-up procedures and for the initial point of boiling.

2) Identification of typical load classes

The identification of different load classes is decisive for analysis. Start-up can probably be seen as the most critical event for life time due to the high temperature change. The combined increase of temperature and pressure is very important to avoid high loads [26, 140]. Furthermore, typical load classes must be identified for nominal operation. The new approach of hull-normalized DNI can be applied to identify corresponding operating conditions. It is explained in detail in section 4.6.1 above and is applied in the following. It allows for a standardized treatment of DNI situations with respect to load calculation for the first time. Other load classes can be necessary depending on the component or operating conditions.

3) and 4) Estimation on thermal stress

Simulations of each identified DNI situation and other load classes are then used to estimate its transient temperature characteristic with corresponding heat transfer coefficients and heat fluxes. They also depend on the control strategy chosen, as has been illustrated in detail in section 4.6.3.

With the boundary conditions from the transient simulations, a thermal stress analysis can be performed. A finite element model (FEM) can be applied considering the geometry, material properties and fluid boundary conditions to derive the resulting thermal stress. The maximum stress amplitude for each coordinate or the combined maximum equivalent stress amplitude is a typical result for each load class. The DNI disturbance classes defined above usually cover a certain period in time. Therefore, certain stress amplitudes may also appear more than once during a typical disturbance class situation.

5) Estimation on frequency of each load class

The stress analysis per class provides the bridge to the subsequent step, namely the estimation of the load class frequency. The identified typical situations are characterized by certain indicators. For OTM, some indicators are suggested in sections 4.6.1 and 4.6.3. These are the integral value of the hull-normalized DNI, the maximum difference between fast and slow system filter signals, the ratio of the fractal lengths of slow and fast system filter as well as the slow filter minimum in combination with the effective hull irradiation and the minimum inlet mass flow. These indicators are identified for typical time periods of a class, e.g. one hour. They are applied for selection, if the time peri-

od is feasible for operation, e.g. if enough energy is available in a certain hour. This approach allows for assigning a typical disturbance class to each operating period of a year with the help of annual DNI data. As a result, the expected frequency of each disturbance class can be estimated and, thereby, the frequency of the stress amplitudes is available. Note that classical load classes only include one particular cycle, for which the frequency is estimated, e.g. by a rainflow algorithm [42]. This is not possible for CSP plants, since there is no direct transformation from DNI to thermal stress. Only the daily start-up cycles may be simple to estimate. The disturbance classes, as suggested here, can be derived by the indicators for a certain period and different stress cycles are associated to one period. The frequency of the periods within one year is then used to extrapolate the stress loads for one year or the plant's life time.

6) Estimation of the stress rupture strength by appropriate design standard

A design standard must then be chosen for estimation of the material strength. Values for rupture strength can be derived from appropriate standards, e.g. DIN EN 10028-2 [43], DIN EN10216-2 [44]. These are modified depending on the application, shape and installation of the material by further standards, e.g. by the ASME Boiler and Pressure Vessel Code [8], DIN EN 12952-4 [42] or FKM Guidelines [86]. A typical result may be the characteristic line for the stress strength versus the number of cycles-to-failure, which is known as S-N curve in English or Wöhler diagram in German literature.

7) Evaluation of life time

The last step is the combination of the S-N curve, or similar characteristics, with the stress amplitudes and load frequencies derived from the disturbance classes. A simple linear extrapolation may be sufficient, if there is only one major load. Otherwise, a more complex calculation considering the order of the loads may be necessary [86, 169]. As a result, one gains an estimation of the component life time. It can also be learned which component and, especially, which load class is the most critical one. Counter-measures may then be developed to increase the corresponding life time, e.g. by an improved component design or by an improved control strategy.

The following sections exemplify this methodology. However, it must be understood as a preliminary example. Detailed analysis is needed for each plant, but is not performed in this work.

5.2 Temperature variation in superheating section

The temperature profile along the superheating section varies with time depending on occurring disturbances. At the DISS facility, temperature measurements around the circumference are used to determine the actual tempera-

ture gradient within a cross-section. Details are described in section 1.3. An exemplary measurement of a cross section of collector 11 close to the outlet is shown in Figure 5.1 for August 7, 2013. A variety of tests has been performed on that day, e.g. a defocus of collector 10 at 15.1 h, an inlet mass flow reduction at 15.4 h and an inlet temperature reduction at 16.4 h. Thermocouple A (lowest line in upper graph of Figure 5.1) is on the non-irradiated side of the absorber tube and gives a good estimation on fluid temperature. The maximum temperature gradient around the cross-section is shown in the lower graph. Only small variations with fluid temperature are visible around the cross-section. The highest value at 16.65 h is about 38 K. This fits very well with the design data from the FEM model by Uhlig [19, 62] as shown in Figure 2.8 on page 21 (compare with a mass flow of 1.1 kg/s and 880 W/m²). Even during high transient conditions between 16.6 and 16.75 h, the temperature gradients change smoothly. This indicates two important aspects. First, there are no critical temperature gradients during defocus or inlet energy disturbances. Second, temperature gradients of the cross-section can be modeled well with the stationary FEM tool even for fast fluid temperature transients. This is also in agreement with other studies considering even faster transients [127]. As a result, modeling of the thermal stress with the stationary FEM tool seems reasonable.

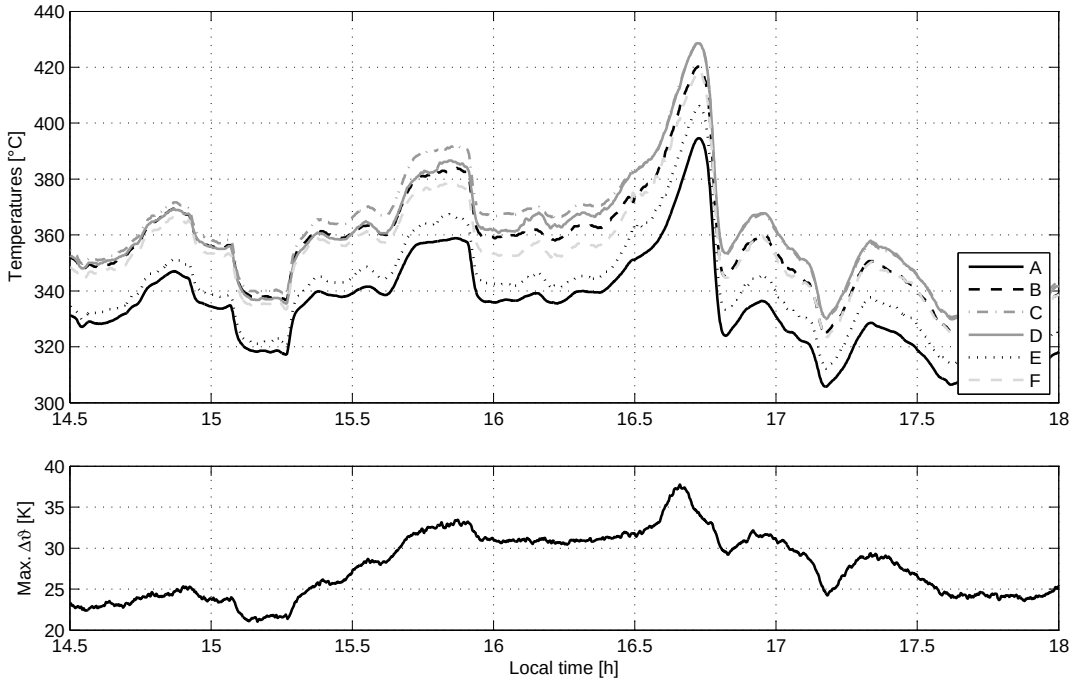

Figure 5.1: Temperature measurements of cross-section 611-40 close to the outlet of collector 11 of DISS test facility (top) and their maximum difference (bottom) on August 7, 2013; inlet mass flow 1.1 kg/s; G_{eff} about 880 W/m².

The controlled simulations for each disturbance class, as shown in section 4.6.3, are used to estimate the stress and frequencies of the different loads. Figure 5.2 illustrates an example for class H at a pressure of 110 bar. The DNI, the outlet temperature controlled by the basic control concept and the resulting stress series are depicted. The stress series have been derived by Rosselló [211] with the help of the mentioned FEM tool. The drops in DNI reduce the temperature difference around the cross-section and thus the equivalent stress level within the absorber tube. It can be learned that the irradiation level is the dominant influence of stress variations. Nevertheless, stress peaks are detected after a sudden increase of DNI at a mass flow significantly below the steady-state design value. It is thus important that the injection control quickly recovers the desired mass flow level, although the actual temperature has only a minor influence on the stress result. The stress series is also shown for a winter day, for which the hull of January 6 (compare Figure 4.39 on page 167) is used. The outlet temperature (not shown) and the stress behavior are very similar to the summer day, but the maximum stress level is lower due to the lower irradiation level of about 450 W/m². A conservative estimate can therefore be derived from summer data. The maximum stress fluctuation is about 16 MPa for the disturbances after 12 h and 15 h. For life cycle counting, e.g. by the rainflow algorithm, a stress cycle must be closed to fully contribute to life time reduction [26]. The largest closed cycle does only have a stress variation of 12 MPa here. This corresponds to a stress amplitude of 6 MPa. However, further conservatism is added by assigning two closed cycles of 10 MPa to one hour of disturbance class H. Note that a defocus of a collector during normal operation would be comparable to a stress cycle between the normal DNI level (about 88 MPa for the summer day at 110 bar) and the zero DNI level (about 75 MPa at 110 bar). The pressure level usually shifts the absolute values, but not the variation bandwidth [211]. If the collector was defocused directly after the sudden increase of the DNI, the stress peak would be lower and could ideally be reduced to a normal defocus event. On the other hand, a defocus control strategy for normal temperature control, in contrast to injection control, may impose such stress cycles regularly.

The same assumptions as for class H are made for all other classes. Table 5.1 summarizes the conservatively estimated stress cycles for the basic control for FEM simulations of Rosselló [211]. Stress amplitudes below 4 MPa are ignored due to their insignificance for life time estimation. Classes A to D do therefore not contribute to additional life time reduction.

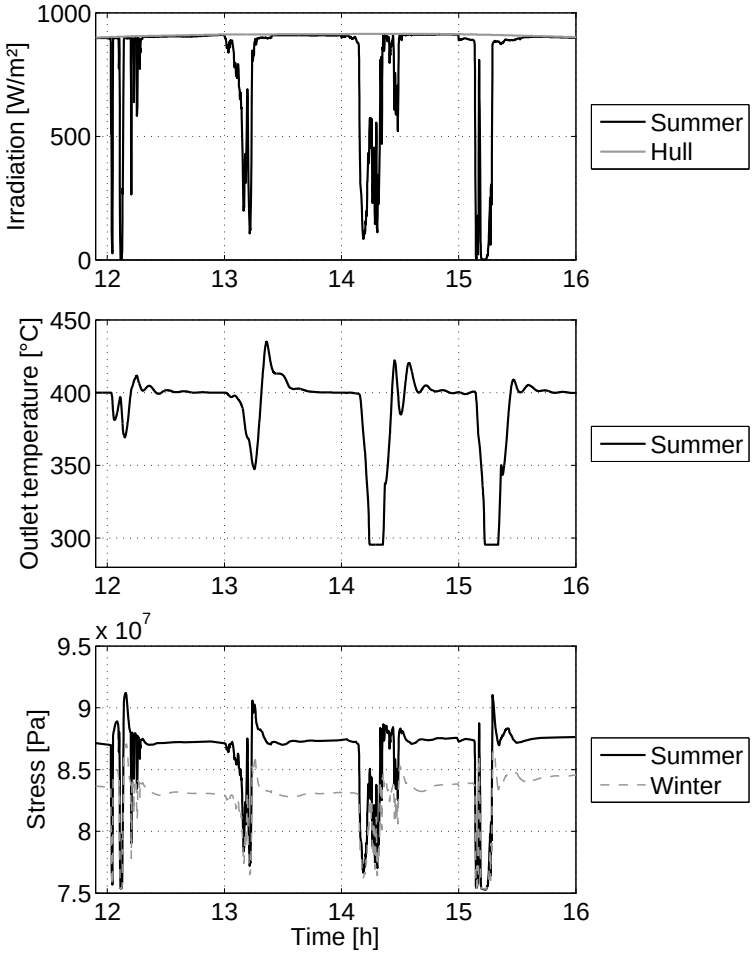

Figure 5.2: Stress series for the controlled simulation of class G, Temperature measurements of cross-section 611-40 close to the outlet of collector 11 of DISS test facility (top) and their maximum difference (bottom) on August 7, 2013; inlet mass flow 1.1 kg/s; G_{eff} about 880 W/m².

Table 5.1: Stress amplitudes and their frequencies per hour for different disturbance classes and a summer day based on FEM simulations.

Class	*10 MPa*	*8 MPa*	*6 MPa*	*4 MPa*
A to D	-	-	-	-
E	-	-	-	1/h
F	-	-	1/h	1/h
G	-	-	1/h	-
H	2/h	1/h	-	-
J	1/h	-	-	-
K	2/h	2/h	2/h	-

5.3 Fluctuation of the end of evaporation

The end of the evaporation in a once-through boiler is not fixed to a certain location. It varies with the available irradiation and the mass flow in the evaporation section. Former studies by Steinmann [230] revealed the main challenges of this fluctuating EPE. The HTC in the evaporation section is very high, while it is much lower in the superheating section. Two phenomena can be distinguished, one being caused by an overall mass flow to irradiation imbalance and the other one resulting in high frequency changes of the wall temperature gradients. Both phenomena are explained and analyzed in the following.

Mass flow to irradiation imbalance

A decrease of irradiation or an increase of mass flow causes the EPE to be shifted downstream into the former superheating section. The receiver in the superheating section is then cooled by the evaporating water film. As a result, the material stress of the tube is changed. These disturbances are a result of the overall energy and mass balance of the system. They can be predicted very well by both the DFEM and the MBM. Thus, simulations can be used to estimate the frequency and influence of it.

Depending on the value of the steam's HTC, severe stress amplitudes may result [230]. For a Eurotrough collector, a rule of thumb is to assume a temperature increase in the superheating section of 0.4 to 0.7 K per meter. A shift of 50 meters of the EPE can thus cause axial temperature gradients of about 20 K to 35 K. This increases the axial stress. In addition, the temperature of the formerly superheated receivers is quickly decreased. A slow shift of the EPE slowly changes the stress level and is comparable to the behavior of the superheating temperatures, while a fast shift of the EPE can result in transitional stress peaks. Such fast variations of HTC and temperature at once should be simulated with a transient FEM tool. Therefore, Rosselló [211] has adapted the steady-state FEM tool to perform transient simulations. Grid studies are performed that show the high influence of the element resolution in radial direction, i.e. in how many elements the tube wall thickness (5.6 mm) is divided. While for steady-state only one element is needed, an accurate transient simulation requires four elements in radial direction [211].

Selected simulation results of [211] are depicted in Table 5.2. A transition from superheated steam of 400°C to evaporation is considered. The variants differ in the speed of transition, the two-phase flow regime and the track angle. Annular flow or stratified flow with half the inner circumference being wetted is assumed. A realistic scenario during a strong disturbance may be the shift of the EPE to the injection before the superheating injection or even to the outlet of the loop. A conservative assumption for such a shift from experimental data is in the range of 30 seconds or longer. Variant S1 considers such a transition

from superheated steam to annular flow within 30 s. The maximum stress amplitude is negligible with about 6 MPa. Note that this scenario can be interpreted as fast disturbance in the superheating section, e.g. by suffering from two-phase flow at the outlet of the loop. It is thus comparable to the situation of disturbance class G-3 in Figure 5.2 after 14 h. Its stress amplitude is in the same range of 6 MPa. Ideally, the slow shift of the EPE would already be covered by the superheating analysis.

Table 5.2: Maximum stress variation range of receiver tube from strong shifts of EPE by single ramp changes at 800 W/m² from superheated steam (Sh) to evaporation at 320°C with annular (An) or stratified (St) flow; HTC steam of 2000 W/m²/K and HTC liquid of 17000 W/m²/K; rounded data from [211].

	Var. S1	*Var. S2*	*Var. S3*	*Var. S4*	*Var. S5*	*Var. S6*
Flow transition	Sh-An	Sh-An	Sh-Str	Sh-Str	Sh-Str	Str-Sh
Initial temperature [°C]	400	400	400	400	400	320
Temperature change $\Delta\vartheta$ [K]	-80	-80	-80	-80	-80	+80
Slope time Δt_{rise} [s]	30	3	30	3	3	3
Track angle [°] (0° for sun in zenith position)	0-90	0-90	90	90	0	90
Max. stress amplitude of inner/outer tube [MPa]	5 6	24 7	7 12	26 15	27 14	8 7
Max. temperature difference at outer cross-section [K]	27	27	46	59	28	28

Nevertheless, if the final flow regime is stratified flow, the stress amplitude is increased to about 12 MPa (variant S3). This increase justifies a more detailed analysis of the EPE to get an impression on the sensitivity of the results. A theoretical transition time of 3 seconds results in significantly higher stress amplitudes of up to 27 MPa (variant S5), which is caused by a high transition stress peak. There is a strong dependency on the transition time. A good estimation of it is thus important for the accuracy of the life time analysis. Note that the back-shift of the EPE from stratified flow to superheating (variant S6) does not impose significant stress loads on the receiver, even if its transition time of 3 s is chosen very fast. The influence of irradiation level does not change the results significantly either [211].

Considering experimental data of transition times, the 30 s variant S1 seems a reasonable scenario for life time estimation. However, it is already covered by the superheating scenarios of the disturbance classes. All other variants would add conservatism to the analysis and corresponding scenarios would have to be defined for their frequency estimation per year.

High frequency wall temperature oscillations

Another phenomenon observable at the DISS facility is a high frequency oscillation of the temperature gradient within the cross-sections close to the EPE. Similar phenomena are already described in [205] and [68]. Such oscillations are illustrated in Figure 5.3. The sensors A to F are aligned as shown in Figure 1.4 on page 10, with A facing the sun and D facing the middle of the collector. The track angle (see Figure 5.4, left) was about -25°, i.e. the receiver was rotated such that sensor E was at the bottom. The temperature gradients within the cross-section vary between the evaporation (around 10 K) and the superheating case (around 25 K). A steady-state analysis with the FEM tool (Figure 5.4, right) shows that the temperature gradient becomes higher with a decrease of wetted inner circumference, i.e. an increase of the dry zone with steam. For the conditions of the experiments, there is no critical temperature gradient exceeding the value for a cross-section with steam only during such an increase of the dry angle φ_{dry}. A transition of the dry angle close to the EPE is then likely to result in a smooth transition of the cross-sectional temperature gradients. In that sense, the experimental results (Figure 5.3) suggest a stall of the annular flow with a continuously decreasing wetted inner wall surface. The stall position is varying slightly. The maximum and minimum values of one cross-section can well be estimated by the HTC of the completely wetted and dry surfaces. The transition period between peak and minimum is about 15 to 30 s for the example. This phenomenon is visible during the majority of the experiments, although some days exist with very little or negligible oscillations.

Fluid temperatures downstream the corresponding cross-sections with wall temperature oscillations did not reveal any significant fluctuations during the experiments. Therefore, the high frequency oscillations cannot be modeled by the DFEM or the MBM and must thus be considered as a stochastic disturbance. Its influence on outlet temperature is negligible.

Siphon instability or severe slugging was thought to cause these oscillations [205]. However, recent developments [112] suggest that it is unlikely to be the case at the DISS facility at the high pressures of the experiments.

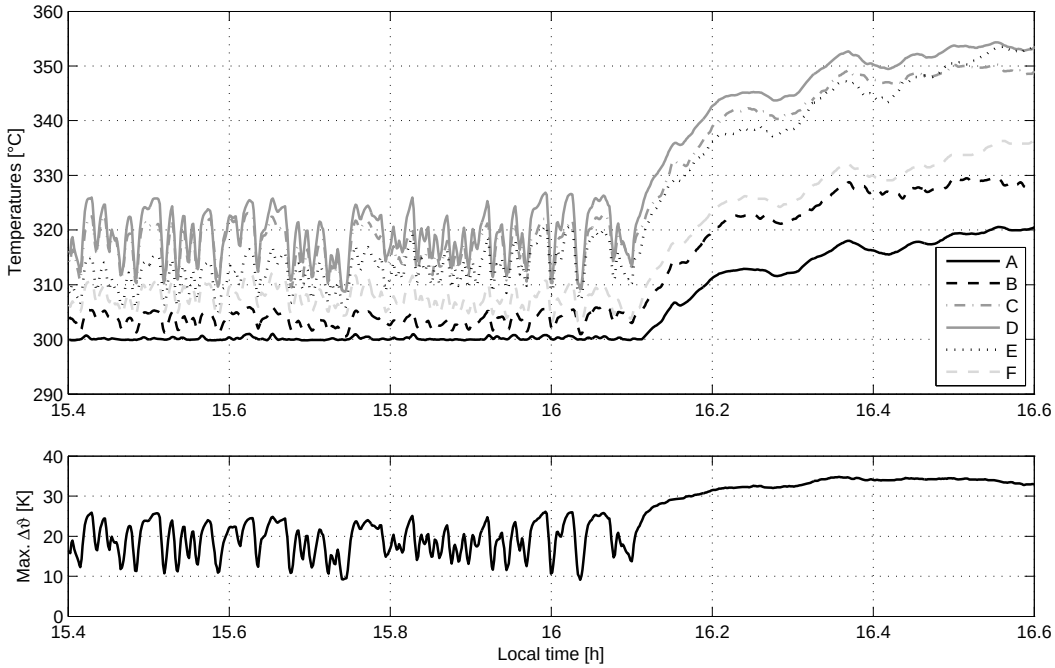

Figure 5.3: Temperature measurements of cross-section 609-20 close to the outlet of collector 9 of DISS test facility (top) and their maximum difference (bottom) on July 26, 2013; inlet mass flow 1.0 kg/s; G_{eff} about 730 W/m².

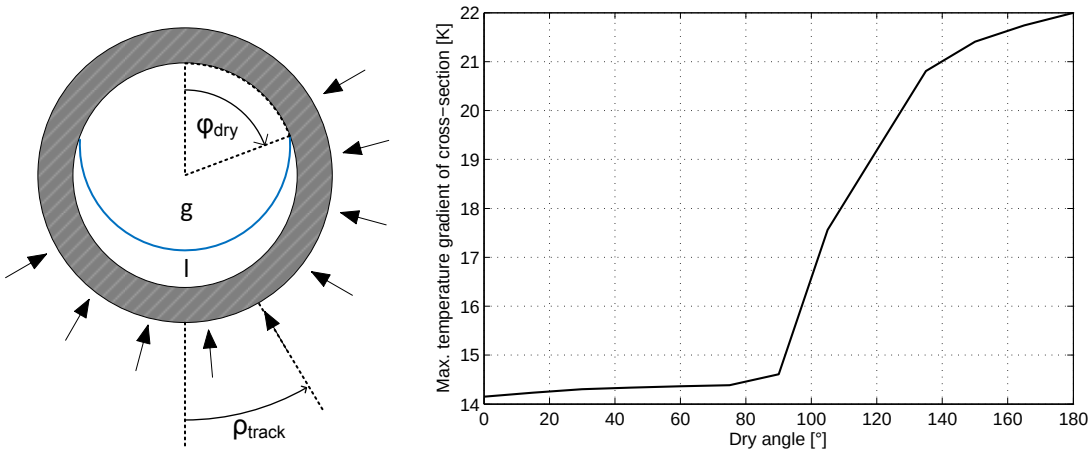

Figure 5.4: Receiver cross-section view with angle definitions (left) and dependency of cross-section temperature difference as a function of dry angle (right) for a track angle of 30° at DISS test facility; based on [211] with scaling to 325°C steam temperature.

An investigation of small, high frequency temperature oscillations for nuclear steam generators is available in [127]. It is assumed there that such fluctuations exist due to flow instability in parallel tubes. Though this is not the case for the single-loop DISS facility, the assumption of small mass flow variations may be realistic due to other reasons. The installed collectors might induce dis-

turbances by imperfect tracking, either close to the EPE or already at the inlet of the loop. During high wind loads, the mirrors themselves oscillate quickly with a very small magnitude, which might also contribute to temperature oscillation. The loop's inlet control valve induces very small variations in mass flow due to unavoidable imperfection of its control. A detailed analysis of the cause of the temperature oscillation phenomenon is recommended for future research on the once-through concept.

The cross-section measurements at DISS facility are installed within 12 m or 24 m in distance close to the EPE. The temperature oscillation is usually measured only at one cross-section. Thus, the phenomenon is likely to be limited to ±12 to ±24 m around the EPE. In a commercial plant, this would allow for keeping it within one collector during normal operation, if the boundary conditions would induce the phenomenon at all.

Conclusions on EPE oscillations for design and stress analysis

It is important to note that, on the one hand, dry-out phenomena at the EPE can be very critical with very high temperature gradients within a cross-section and very high stress loads, but that, on the other hand, the dry-out becomes less critical with higher mass flows and higher heat transfer coefficients of the steam phase [230]. Furthermore, the location of the stall of annular flow close to the EPE can vary such that oscillations of the possible dry-out zone may occur. In consequence, a well-designed once-through loop must foresee a high HTC of the steam phase in order to achieve a smooth transition between evaporation and superheating as shown in Figure 5.4 (right). This requirement is likely to be met when considering the suggested design as in chapter 2.2. Nevertheless, it is highly recommended to check it for the particular boundary conditions by generating the temperature gradient versus dry angle curve for nominal and part load as well as for the relevant track angles.

A transient FEM analysis can reveal the possible impacts of the EPE oscillations. Rosselló [211] simulated the transition from superheated steam to evaporation similar as described above (e.g. in Table 5.2). The results for the small EPE fluctuations now consider a much lower initial superheated temperature of 325°C, which is 5 K above the evaporation temperature. This assumption seem justified from the experimental results, as they do not show significant variations of the downstream fluid temperature. The temperature and heat transfer coefficient is then quickly changed by a linear ramp to meet the evaporation conditions. The stress and temperature gradient results are listed in Table 5.3. Variant F1 considers a transition to stratified flow with a dry angle of 90° within 3 seconds and irradiation from the side. Especially, this irradiation condition is the most critical and usually results in the highest temperature gradients within a cross-section. Nevertheless, a significant stress peak does not appear and stress amplitudes of only 3 MPa are estimated. A fast transition of the HTC

within 1 second from steam to annular flow does neither reveal critical stress amplitudes (variant F2).

As a result, the transient FEM analysis suggests that the wall temperature oscillations close to the EPE only induce negligible stress amplitudes.

Table 5.3: Maximum stress variation range for small EPE oscillations by single ramp changes at 800 W/m² from superheated steam at 325°C (Sh) to evaporation at 320°C with annular (An) or stratified (St) flow, according to [211].

	Var. F1	*Var. F2*
Flow transition	Sh-Str	Sh-An
Initial temperature [°C]	325	325
Temperature change $\Delta\vartheta$ [K]	-5	-5
Slope time Δt_{rise} [s]	3	1
Track angle [°] (0° for sun in zenith position)	90	0-90
Max. stress amplitude of inner/outer tube [MPa]	3	4
	3	3
Max. temperature difference at cross-section [K]	22	22

A comparison with the assumptions of Steinmann [230] promotes that the experimental results are less critical than assumed. The thick receiver walls in combination with the low HTC of the steam assumed in [230] cause a change in maximum stress location from radial to circumferential stress. This corresponds to a change from location B to A, when compared to Figure 2.6 on page 20. As a result, a very high peak stress occurs at the instantaneous change of the HTC in [230]. A change from 500 W/m²/K to 3'000 W/m²/K is assumed in [230], while a change from 2'000 W/m²/K to 17'000 W/m²/K is likely for the new DISS facility and was applied for Table 5.3. The HTC for the new DISS facility is already high for pure steam, such that there is neither a change in location nor in the cause of the maximum stress. In consequence, high transition peaks of the stress, caused by a fast change of the HTC during the fluctuation of the EPE, are not expected. This result holds for all part loads, since a change in the stress profile occurs at about 750 W/m²/K (Figure 2.7), which corresponds to a steam mass flow below 0.45 kg/s at 30 bar. Such low steam mass flows were avoided already during loop design and by a minimum mass flow setting for operation. Note however, that the results from stress analysis change significantly with different boundary conditions such as outlet pressure, receiver material or loop length. Thus, the results must be checked again for new loop designs.

General assumptions for load cases

Different loads can be established to represent the thermal stress behavior of a receiver in the evaporation section. From the sections above, two conclusions can be drawn. First, strong shifts of the EPE put a stress load on receivers in the superheating section. Depending on the velocity of the EPE during the simulations of the disturbance classes, stress amplitudes can be increased when two-phase flow suddenly enters the receiver, e.g. at the loop outlet of disturbance class G-3. This stress increase should be integrated in the superheater analysis of disturbance classes.

Second, the stress loads at the nominal location of the EPE can be estimated by a permanent oscillation of the wall temperatures between evaporation and superheating conditions. The transition with only partly wetted tube walls must be considered in such an analysis. An oscillation frequency of about 40 changes per hour seems reasonable from experimental data. The latter oscillations should be considered as a separate load or disturbance class, which always occurs during operation of the solar field.

Comparison to other load estimation study

A different concept of load estimation corresponds to a study of the Material Testing Institute of the University of Stuttgart (MPA) [163]. It particularly deals with once-through receivers in parabolic troughs. Four load types are distinguished, representing four different situations. These situations are specified by Table 5.4 in combination with Figure 5.5. The receiver is symmetrically divided into a lower, irradiated part, which comprises 120°, and an upper, unirradiated part of 240°. Load type I represents the mentioned oscillations close to the EPE with a conservative approach. The lower part of the receiver tube experiences a periodic change of the HTC between steam (4700 W/m²/K) and boiling (40’000 W/m²/K). The upper part of the inner tube circumference always has an HTC of steam. Changes in HTC occur almost immediately within one or a few seconds. Furthermore, the circumferential temperature gradient is continuously high due to a steam temperature of about 25 K higher than evaporation temperature. This condition would rather be associated with stratified flow in combination with a severe slip, i.e. the phase velocities are very different such that the steam may reach significantly higher superheated temperatures than the condensate at the receiver bottom. These are very conservative or unrealistic assumptions, respectively, when compared to experimental data. Load type I must therefore be seen as a worst case estimation of thermal stress. Types II and III also start from the stratified flow case. The HTC of steam is then imposed on the lower side of the tube and the fluid temperature is increased by 40 K or 80 K, respectively. The upper fluid temperature remains at the highest temperature level of the load type, while cycles are only imposed on the lower

part of the tube. This can be interpreted as liquid water film being swept into the superheating section. Type IV shall represent a typical start-up case.

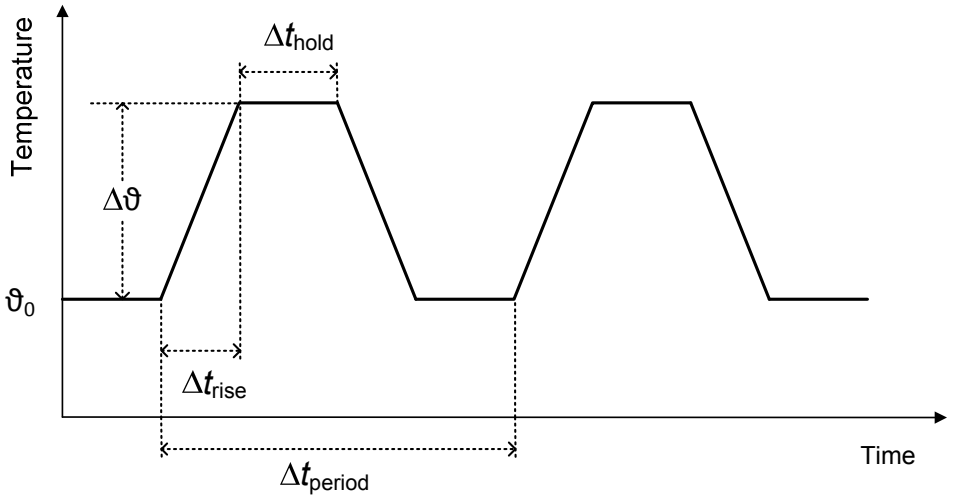

Figure 5.5: Nomenclature for boundary conditions of analysis close to the EPE.

Table 5.4: Load type definition for analysis close to EPE.

	Type I	*Type II*	*Type III*	*Type IV*
Period Δt_{period} [s]	60	600	1200	> 3600
Temperature change $\Delta\vartheta$ [K]	+25	+40	+80	-250
Slope time Δt_{rise} [s]	30	30	40	1800
Hold time at peak Δt_{hold} [s]	0	400	800	> 3600

Table 5.5: Thermo-mechanical stress amplitudes associated with load types for the evaporation section; values taken from [163].

	Type I	*Type II*	*Type III / IV*
Austenite, circumferential stress [MPa]	47	20	102
Austenite, axial stress [MPa]	40	32	88
Ferrite, circumferential stress [MPa]	25	13	55
Ferrite, axial stress [MPa]	22	23	50

The resulting stress amplitudes are listed in Table 5.5. Types III and IV were found to be very close to each other and only the higher values are listed. Two different materials are considered. Austenites such as ANSI type 321H usually

show a low heat conductivity of about 19 W/m/K, while ferrites such as ANSI type P11 (also known as 13CrMo4-5 or 1.7335, respectively) have about double the heat conductivity. The heat expansion coefficient is significantly higher for the austenite, with $1.7 \cdot 10^{-5}$ compared to $1.2 \cdot 10^{-5}$/K of the ferrite [163]. The ferritic receiver has a wall thickness of 5.8 mm, while the austenitic receiver has a wall thickness of 6.5 mm. Both axial and circumferential stress amplitudes are significantly higher for the austenite, while the rupture strength is slightly lower for the ferrite. Thus, it can already be concluded that a ferritic absorber tube would be beneficial for the reduction of thermal stress impacts.

The circumferential stress is dominating for types I and III/IV, mainly due to the assumed stratified flow. The axial stress is dominating for type II and is about 80 % to 90 % of the circumferential stress for the other types. It must not be excluded from a general stress analysis, because it may become dominating, if the assumption of stratified flow is not applied. The values are derived for a high mass flow of 1.4 kg/s and high irradiation of 900 W/m². A strike of the EPE in the superheating section is assumed to have the same stress amplitude as type I.

There are significant differences in the assumptions, modeling and results of the EPE disturbances between the MPA study [163] and Rosselló [211]. In [211], the boundary conditions are chosen as realistic scenario from experimental data. The validated FEM tool is applied for one receiver (4 m) that can expand in axial direction. The number of elements was 4 in radial direction and 36 in tangential direction for the transient analysis. On the other hand, assumptions in [163] provide first guesses on worst case situations. A length of 5 receivers including their collector supports is modeled. One end is fixed, representing the middle pylon of a collector, while the other end can expand in axial direction. A shell model is used for the receivers such that there is only one wall element in radial direction and 18 in tangential direction. The axial resolution is not provided. The same austenite is considered by the studies, but [211] uses a wall thickness of 5.6 mm, the original dimensions of the new Schott PTR70-DSG receivers, while [163] analyzes a wall thickness of 6.5 mm. Furthermore, the receiver is divided into a lower and an upper part in [163]. The steam temperature of the upper part remains at maximum temperature, while only the lower part is cycled. In consequence, much higher temperature gradients exist and the transitional stress peak is much higher than in simulations of [211], which assume a rather homogeneous temperature change along the loop.

In consequence, the assumptions and results of [211] seem realistic from experimental data and for a good loop design. Results of [163] represent rather unrealistic worst case assumptions.

Final choice of stress loads and frequency

Despite the unrealistic scenarios, the stress amplitudes of [163] are used in the following section to derive an estimate of the receiver life time and illustrate the methodology. The reason for that choice is trivial. Stress loads of the realistic scenarios of [211] are below any critical limit and detailed life time estimation would not be needed.

For extrapolation of results, a frequency for each load type I to IV of [163] must be associated to the different disturbance classes A to K. Table 5.6 summarizes the assumed distribution. The stochastic disturbances of the EPE are associated with load type I and are estimated to happen 40 times per hour during normal operation. Load types II and III are linked with significant mass flow and irradiation imbalances. A first guess for start-up is assumed by load type IV, but highly depends on the start-up procedure, which shall not be analyzed here. The same holds for other values given in brackets. Two scenarios of [211] are chosen for illustration as well. Variant F2 is a realistic case for EPE fluctuations and the same frequency as for type I is chosen.

Variant S5 is chosen for a fast cooling of superheater receivers. The scenario is for an 80 K temperature shock within 3 seconds, which does not happen at all in any simulated or tested operating condition. Nevertheless, its frequency is derived from disturbance class simulations by counting the number of temperature drops of the temperature before the SHI. A situation is counted, if the temperature falls more than 30 K within 5 minutes. For simplicity, this variant replaces all former, and less critical, superheater loads from Table 5.1 in the following.

Table 5.6: Frequency of load types from [163] corresponding to disturbance classes for evaporation section; superposition of EPE and receivers nearby.

Class	*Type I / Var. F2*	*Type II*	*Type III*	*Type IV*	*Var. S5*
Start-up	(20/h)	-	-	1	-
A	40/h	-	-	-	
B	40/h	-	-	-	
C	40/h	-	-	-	
D	40/h	-	-	-	
E	40/h	1/h	-	-	1.5/h
F	40/h	1/h	(0.5/h)	-	2/h
G	40/h	1/h	1/h	-	2/h
H	40/h	1/h	1/h	-	2/h
J	(20/h)	-	1/h	-	1/h
K	40/h	3/h	2/h	-	5/h

5.4 Life time estimation

The estimation of life time depends on two aspects. First, the acceptable material strength is determined to be a function of the number of load cycles. Then, the expected number of load cycles and their corresponding stress amplitudes are compared to the acceptable ones. The exact approach depends on the design code to be applied. Amongst others, it differs in the value of rupture strength as a function of temperature, its correction factors and the final criteria for determining the life time.

Fundamentals of life time analysis

Figure 5.6 illustrates an exemplary stress versus number of cycles curve (S-N curve). The fatigue range starts at about 10^4 cycles and is characterized by a typical slope or slope exponent, respectively. The material can withstand a certain stress amplitude $S_{a,i}$ for $N_{a,i}$ cycles. Some codes, such as the ASME Boiler & Pressure Vessel Code [8], assume a permanent fatigue strength $S_{a,p}$ after about 10^6 cycles, which is indicated by the horizontal line in Figure 5.6. All stress amplitudes below this value do not contribute any more to fatigue and are ignored for life time estimation. Various studies [16, 169] suggest that even small stress amplitudes can contribute to fatigue, if the number of cycles is high enough and a crack with a critical initial length exists at the beginning. Some design codes, such as the EN 12952-4 [42], therefore extrapolate the acceptable stress by a certain slope. The extrapolation with the same slope exponent, also referred to as Miner elementary, or half the main slope exponent, referred to as modified Miner, are commonly used. In practice, stress amplitudes are often considered for pipe design, if they are greater than 80 % of $S_{a,p}$ [26]. Otherwise, they are ignored.

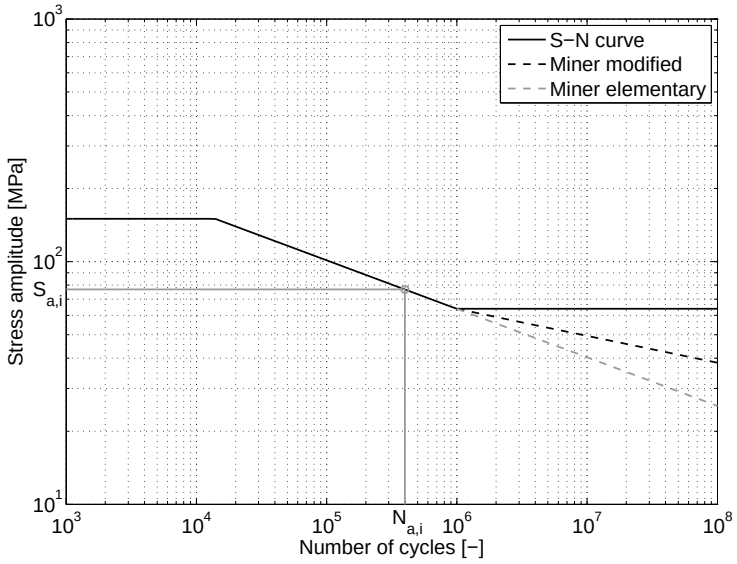

Figure 5.6: Exemplary S-N curve with extensions for high cycle fatigue.

An incremental damage ΔD_i of the pipe can be described by relating the impact of one cycle to the number of cycles-to-failure $N_{a,i}$ with the same stress amplitude [26]:

$$\Delta D_i = \frac{1}{N_{a,i}} \tag{5.1}$$

The overall damage D, also referred to as usage factor, is the accumulation of the incremental damages ΔD_i. High stress amplitudes thus contribute more to the overall damage than small ones [30]. The underlying idea is very intuitive. However, the simple additive increase in overall damage is far from being a realistic assumption [169]. In consequence, there is no reliable understanding on when the life time of a component is reached. A value of one sounds reasonable, but in practice, values around 0.4 are a common choice [26], although even values greater than one are possible [30]. The chronological order of the loads can be accounted for as well, e.g. by the FKM Guideline [86].

Acceptable and expected number of cycles

As a result from design codes, the acceptable number of cycles is determined for each load type and the S-N curve for the component can be drawn. The values in this work are derived from [163]. They are listed in Table 5.7 for an austenitic receiver and a ferritic receiver. The underlying material temperature for rupture strength correction is 400°C. The austenitic receiver can withstand the type I fluctuation of the EPE for more than 17 million times. If the scenarios of [211] from Table 5.3 are considered, the allowable number of cycles of the EPE fluctuations is even higher, in the range of $3.3 \cdot 10^{13}$ cycles.

Table 5.7: Acceptable number of load cycles for the corresponding load types in the evaporation section; based on values in [163] (type I to IV) and [211] (variants S5 and F2 as in tables above) with modified Miner approach.

	Type I *[10^5]*	*Type II* *[10^5]*	*Type III / IV* *[10^5]*	*Variant S5* *[10^5]*	*Variant F2* *[10^5]*
Austenite	174	5'000	1	23'700	$3.3*10^8$
Ferrite	15'463	39'912	14	-	-

The expected number of cycles remains to be estimated. A very common procedure is to generate a complete time series of stresses and then use an algorithm to categorize the stress loads. The rainflow algorithm [26, 42] is often implemented to do this. This concept is very useful, if a time series is available from data, e.g. from a plant's data acquisition system. For design, the data must be generated by simulations and it would be very ineffective to simulate data for a whole year or longer. The disturbance classes from section 4.6.1 are applied here to estimate the frequencies. Each hour with normal operation is

assigned to one class. Hours of start-up are assumed to have an access of mass flow and the identified loads may therefore overestimate their influence. The criteria for categorization are explained in Annex D. The characteristic values from the visual identification are sufficient for 90 % of the annual hours. A rigorous algorithm is used to assign the remaining 10 % to a suitable class. Figure 5.7 shows the result for the exemplary year 2013 at Tabernas, Spain. About 900 hours are found to be of nearly clear sky condition of class A. Class Z is introduced for hours with very low irradiation, which would not be suited for operation. The 'start' class does not only include successful start-up periods, but also days with irradiation not being sufficient for reaching normal operation. It must therefore not be confused with the number of start-up times. The categorization of class A to Z is performed starting from the time of successful start-up. Sun set is thus not reached exactly at the end of one hour. The remaining periods are accumulated as well and shown separately. A high uncertainty exists for those times. A decreasing DNI at the end of the day is usually assigned to class J or Z correctly. Note that the number of hours of classes J and Z are high, but that their energy content is in the range of 5 %. Corresponding details are provided in the next chapter. Table 5.8 lists the number of hours from Figure 5.7. A total of 3930 hours are categorized.

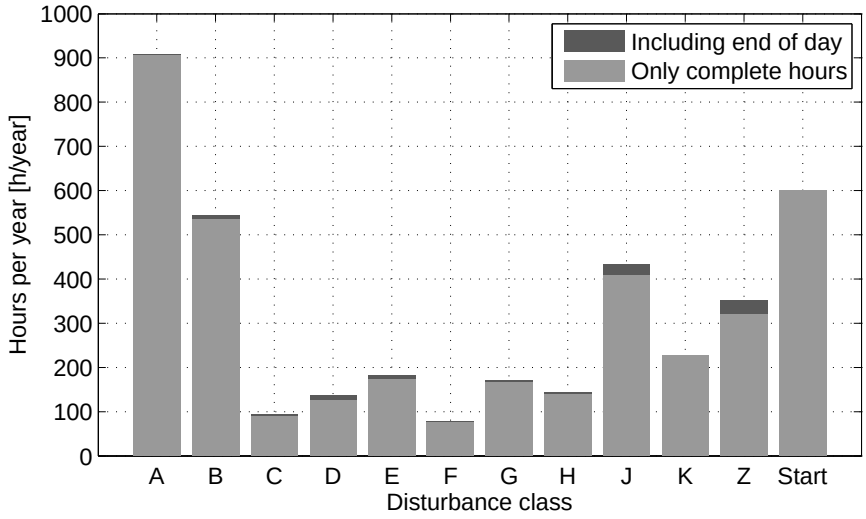

Figure 5.7: Graphical overview on number of hours assigned to one disturbance class for the year 2013 at Tabernas, Spain.

Table 5.8: Number of hours assigned to one disturbance class for the year 2013 at Tabernas, Spain.

	A	*B*	*C*	*D*	*E*	*F*	*G*	*H*	*J*	*K*
Hours per year	906	534	90	125	173	75	165	138	407	227

Results of life time estimation

The results of the various data are depicted in Figure 5.8 for an austenitic receiver. A superposition of superheater loads (type II-IV or S5) and EPE fluctuations (type I or F2) is assumed. The high number of cycles close to the EPE can gain significant influence on life time, depending on the underlying approach. An overall usage factor of 0.4 is reached after about 14 years with the modified Miner approach and the extreme assumptions of type I and III/IV of [163]. If the more realistic scenarios of [211] are considered (S5 + F2), their influence is negligible and below 50 % of the fatigue endurance limit. In consequence, the start-up loads dominate the life time estimation, which corresponds to results in [26]. With the assumed values of type IV, a life time of more than 40 years can be expected.

The detailed results for the superheater from section 5.2 are not shown separately. The maximum stress amplitude for temperature variations is about 10 MPa, which is securely below the permanent stress strength as well.

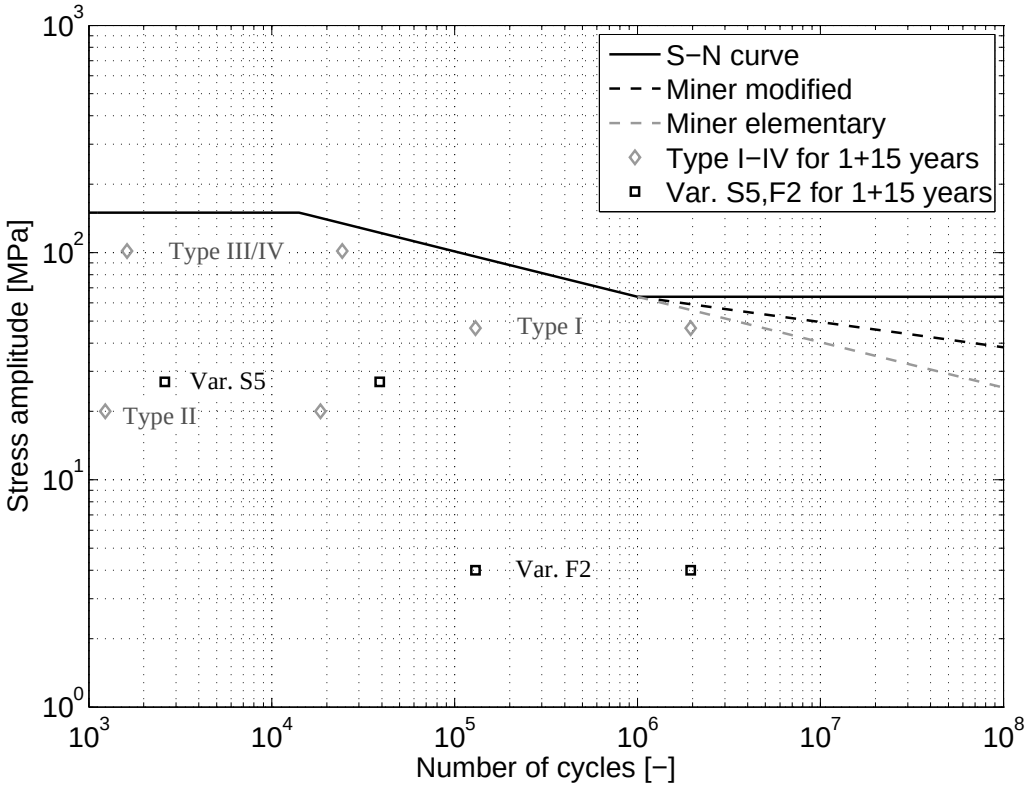

Figure 5.8: S-N curve of austenitic receiver with load types of the EPE and superheater.

Conclusions from life time estimation and recommendations

The results of this chapter may not be taken as exact values, but are rather meant as a first estimate. Nevertheless, they can be used to draw some important conclusions. The main result is that there is no fundamental obstacle for solar once-through boilers. Realistic operating scenarios for well-designed loops and their simulation with the transient FEM tool did not show any influence on life time. Only extreme and rather unrealistic scenarios showed a life time reduction, but would still allow for an operation of more than 14 years. Thus, an exchange of receivers may be necessary only once or twice throughout a plant's life time in a worst case scenario. This would increase the maintenance costs, but could still be cheaper than comparable solar field concepts in the end.

Another result is that the application of a ferritic receiver material would lead to lower stress loads in all sections of a once-through loop. It is especially helpful close to the EPE. The current state-of-the-art material is austenitic steel. The main reason is probably the coating process of the absorber tubes. Polished austenitic steel keeps a clear surface for a long time, such that the steel manufacturer can polish the tubes and the receiver manufacturer can spray the coating onto it at a different time and place. This is not possible for ferritic steel, such that the receiver manufacturer would have to polish the tubes directly before coating [58]. It thus depends on the receiver manufacturing process, whether a ferritic absorber may be available or not. For other components such as the superheating header piping, ferritic materials are recommended. This agrees with the current practice in fossil power plants. The ferrites 10CrMo9-10 and 13CrMo4-5 can be used up to 550°C and wall thicknesses up to 60 mm. The ferrite X10CrMoVNb9-1 (ANSI T-91), which has a smaller heat conductivity of about 26 W/m/K, can be used up to 560°C and wall thicknesses up to 120 mm [26, 44]. Both types are often applied for live steam headers and collecting headers in fossil plants.

Only the receivers are considered in this work. It is obvious that all components must be evaluated regarding fatigue during the design stage. It is suggested to include the influence on fretting and fatigue by the HCE supports in parabolic troughs or the expansion sliding shoes of the receivers in Fresnel collectors for such an analysis. Tube bends caused a high risk of failure in nuclear plants due to stress-corrosion cracking [38, 47, 158]. Corresponding design modifications must be taken into account especially for the particular case of Fresnel collectors with U-bend receiver tubes [170, 242].

Another issue is worth mentioning separately here. One loop may fall to saturation at the outlet, while the main header line provides superheated steam. This may be due to strong cloud fluctuations or a component failure in the single loop. The connection of the loop to the main superheating header

then has two very different temperature levels, which imposes high thermal stress in the material. This situation cannot be avoided in a once-through solar field. Thus, the header design must foresee it already in the design stage. An analysis in [26] suggests that such situations can be handled by ferritic pipes without a significant loss of life time. A corresponding header design is thus a solvable, but a very important task for thermo-mechanical analysis. Water droplets might also enter the live steam header in such a situation. Condensate traps should be foreseen at the outlet of each loop in order to reduce such events as much as possible.

A more detailed analysis of the latter situation and the EPE is recommended for future work regarding life time estimation. It will be especially important to monitor the loads during long term operation in a commercial plant. Such monitoring is a standard procedure for in-service steam turbines or thick-walled components in power plants [241, 258, 259]. It is also foreseen for critical components of solar tower plants [243]. A corresponding surveyance system can be used for two purposes. The real stress loads can be accumulated to estimate the current fatigue status. It can be compared to material inspections and a better estimate on an acceptable usage factor may be derived.

In-service inspections do not always reveal small cracks in progress, that might later on result in tube failures. This is a typical problem known from failures in nuclear power plants in the USA [169]. It is therefore recommended to foresee regular inspections at some representative loops of a plant, after a certain usage factor is reached. These inspections can provide more confidence in life time estimation. Note that they are easily implementable in solar plants, since the inspection of one loop does not require the plant to be shut down. Inspections can be done in parallel or at night without affecting operation.

The system monitoring should also be applied for verifying and improving the proposed methodology of load frequency estimation. A reliable prediction is important in order to foresee suitable maintenance periods and to associate certain costs to critical operating conditions. There must be a tradeoff between maximum energy output and life time reduction of the components. The operation on days with highly fluctuating DNI can provide electricity and revenue, but also causes costs for the auxiliary power consumption and fatigue. A share of life time reduction ΔD could be estimated and multiplied with the costs associated to the exchange of the related components, such as receivers or header piping at the loop outlet. By comparing those figures, an operating strategy can be developed and the operator can better decide on how to react on particular cloud situations or electricity market demands. The adjustment or optimization of operation depending on fatigue variables has been proposed for fossil plants e.g. in [125, 140]. This seems even more reasonable for solar power plants in the future.

6 Comparison of once-through and recirculation mode

The former chapters promote that the concept of once-through boilers is feasible in general. The main initial drawbacks associated to the concept, namely difficult temperature control and high thermo-mechanical loads, have been shown to be solvable. It is therefore a matter of economical evaluation, whether the once-through mode (OTM) or the recirculation mode (RM) is applied for a certain solar field or power plant project, respectively. A final evaluation on this aspect is not possible here and is not the objective of this chapter. The intention in comparing OTM and RM is rather to provide general aspects to be considered for choosing one or the other. An example is used to exemplify these aspects. Nevertheless, one must be aware that a change in boundary conditions can completely change the outcome of this comparison. Furthermore, as in most economic evaluations, figures must be treated as guesses with a certain probability rather than deterministic values. Under these conditions, the following chapter provides a preliminary comparison that must be checked for each individual project.

6.1 Reference power plants

A reference power plant is defined to estimate the potential of the OTM compared to RM. Various applications of a DSG solar field are possible. One option is solar augmentation of a fossil plant, i.e. steam produced by the solar field is used to reduce the amount of fossil fuel. The fossil part is usually dominating in such plants. The Australian coal-fired plant in Liddell is one example, which shows the potential for this kind of solar integration [190]. The requirements for the solar field are rather low. The total share of solar heat input is almost negligible, such that turbine requirements must not be met all the time by the solar steam. The emphasis is on cheap and efficient steam generation. This is an ideal application for DSG, especially OTM, solar fields without thermal storage. Existing plants could be upgraded by a solar field to reduce CO_2 emissions and, when assuming high fuel prices, to reduce costs. The same holds for process heat applications, in which the steam is not fed to a turbine, but is used for other purposes, such as food production or chemical processes.

In the long run, it is more desirable to have solar thermal power plants without or with a low share of fossil fuels. The DSG solar field must then provide steam that meets the requirements of a turbine. To increase the solar share, a thermal energy storage system (TES) can be foreseen. A large-scale power plant of this type is used as reference in this work. The nominal electric power output is set to 50 MW. A TES with a thermal storage capacity of eight

full load hours is assumed. A latent phase change material storage [145, 195, 277] is used for the evaporation/condensation of the water/steam. Sodium nitrate is a suitable phase change material, which has a melting point at 306°C [17]. The sensible heat for superheating is stored by a two-tank molten salt storage system. Such a TES and its meaning for power block operation are described in [23] and [81]. The TES is charged at a pressure level of 110 bar, which is also the nominal live steam pressure. It corresponds to a saturation temperature of 12 K above the melting temperature of the sodium nitrate. The TES can be discharged only at a lower pressure level, for which an evaporation temperature of about 13 K below the melting temperature of the sodium nitrate is assumed here. This results in a discharge pressure of 78 bar. The solar field is thus operated at a fixed pressure of 110 bar for nominal operation. Only during low part load below 50 %, the pressure is reduced to 78 bar in sliding pressure mode. At the low level, fixed pressure mode is activated again. Parallel steam production by the solar field and the TES is possible only at this low pressure level.

A schematic diagram of such a plant is shown in Figure 6.1. It is divided into four major parts, solar field, TES, fossil co-firing and power block. The focus is laid on the solar field here. It is depicted for RM in order to see the differences to OTM. The central steam drum or separator, respectively, divides the solar field into two parts. The recirculation line and pump are foreseen to feed condensate from the separator to the solar field inlet. The main pressure head is generated by the feed water pump, as for OTM. An injection in each superheater loop is foreseen, which is fed from the main feed water line. The feed water comes from the power block, where it is already pre-heated by bleed lines from the turbine. The TES and/or the co-firing can be used to keep the turbine running when the weather is cloudy or during the night.

The analysis here is closely related to the ones in [71, 72, 80, 81], which mainly focused on a comparison between DSG in RM and plants with synthetic oil as heat transfer fluid. These are extended by a more detailed comparison of RM and OTM. A live steam temperature of 500°C is assumed. The nominal gross power block efficiency at 500°C and 110 bar is estimated to be 40.6 % with dry cooling [81]. The nominal thermal power to the power block is thus 123.15 MW. The TES is designed to be charged at the same nominal power. As a result, the solar field provides about 246.3 MW at nominal conditions. The nominal effective irradiation is a degree of freedom, which is equivalent to choosing the solar field size. Usually, it is optimized to give the lowest levelized cost of electricity of the complete plant. Since the aim of this study is only the comparison of OTM and RM, this optimization is not performed. A reasonable value is between 800 W/m² and 900 W/m² for sites in Spain (rather lower) and

the south west of the USA (rather higher). A nominal value of 900 W/m² is chosen here.

Two solar fields are designed to meet the desired nominal 246.3 MW thermal power at an effective irradiation of 900 W/m². Note that these values cannot be met exactly due to discrete loop lengths and a desired symmetry of the solar field. The chosen collector is a scaled Eurotrough collector with 150 m length, 5.76 m aperture width and a nominal optical efficiency of 75 % based on an aperture area of 864 m², which is slightly higher than assumed in [72] and similar to [81]. It corresponds to a net optical efficiency of 79 % for its net aperture area of 817.5 m².

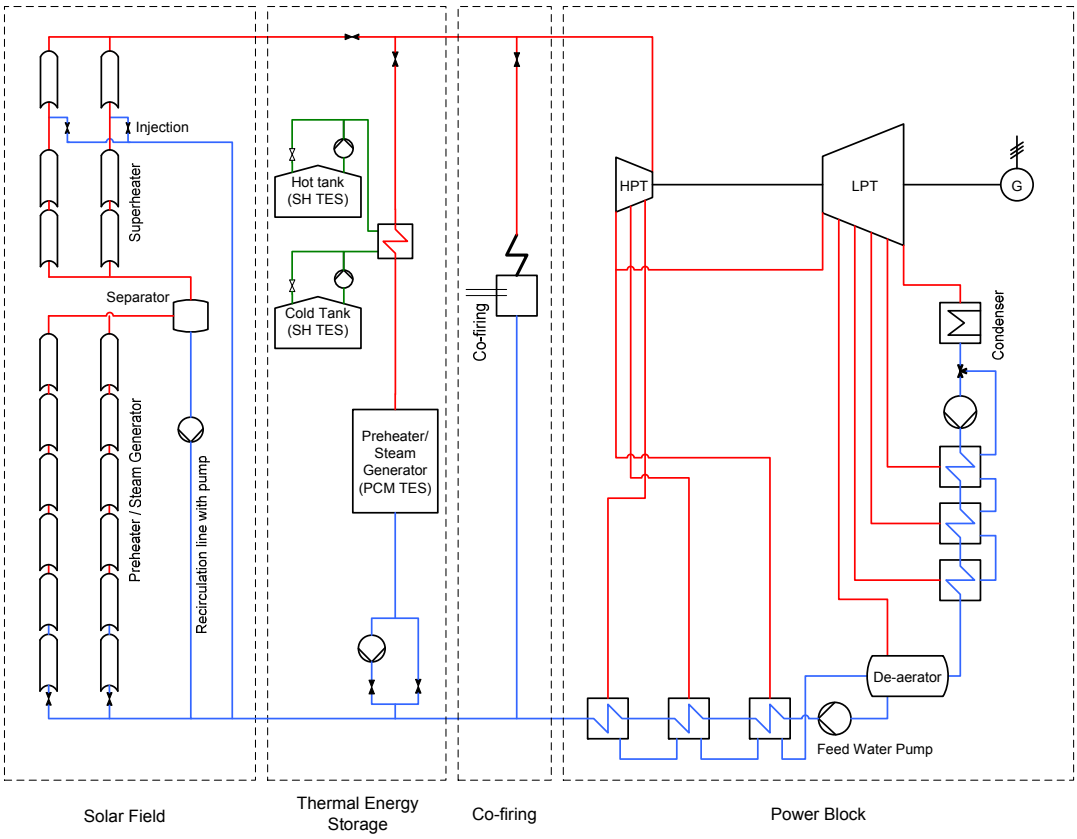

Figure 6.1: Schematic diagram of a DSG power plant with recirculation mode, thermal energy storage (TES), co-firing and power block; HPT = high pressure turbine; LPT = low pressure turbine; PCM = phase change material.

At nominal irradiation, the OTM loop then provides a thermal power of about 5'527 kW. A solar field with 44 loops is chosen to provide 243.2 MW, which corresponds to about 110 kg/s of live steam. Variant A with two injections is chosen, as derived in the examples of chapter 2. The reference case has a nominal temperature difference of 45 K over the SHI. The design foresees a constant temperature before the SHI of 475°C during part load. As a more effi-

cient variant, an OTM loop with a constant temperature difference of 25 K is analyzed. The main characteristic figures are summarized in Table 6.1.

In the case of RM, the decision of the solar field size is usually not that easy. In fact, the nominal case at 900 W/m² was chosen to allow for a design with four symmetric subfields and a nominal thermal power of 245.7 MW. Six collectors form an evaporation loop and three collectors form a superheating loop. This corresponds to the design suggested in [72]. This ideal RM solar field then comprises 48 evaporation loops and 52 superheating loops. This results in an aperture area share for superheating of 0.35, i.e. 35 % of the solar field are always used for superheating. The only feasible symmetric alternative for 500°C is a field with 48 evaporation loops and 56 superheating loops. The latter field would then provide 251.9 MW, with an aperture area share of 37 % for superheating.

Table 6.1: Solar field designs for comparison of OTM and RM for nominal live steam parameters of 500°C and 110 bar; EVL = evaporator loop, SHL = superheating loop; OTM with nominal temperature difference of 45 K (25 K) by the SHI; RM with 52 (56) SH loops.

	OTM	*RM*
Loop length	1500 m	900 m EVL 450 m SHL
Number of loops	44	48 EVL 52 (56) SHL
Injections per loop	EVI at 750 m SHI at 1350 m	SHI at 1200 m
Total solar field aperture area	380'160 m²	383'616 m² (393'984 m²)
Loop efficiency at 900 W/m²	71.08 % (71.22 %)	71.16 % (71.03 %)
Loop efficiency at 475 W/m²	68.03 % (68.31 %)	68.19 % (67.95 %)
Thermal power at 900 W/m²	243.2 MW (243.7 MW)	245.7 MW (251.9 MW)
Thermal power at 475 W/m²	122.9 MW (123.3 MW)	124.3 MW (127.2 MW)

The north-western subfield of the OTM solar field is sketched in Figure 6.2. The header lines for feed water and live steam are the same for the northwestern and the southwestern subfield. The solar field of the RM can have various alignments. It is assumed that the size of the total field requires the installation of a central steam drum within each subfield. Thus, a total of four steam drums

are needed. An alignment with only one central drum in the power block would have two drawbacks. First, the header lines of the live steam would be significantly longer, such that heat losses would increase. Second, a steam drum of the desired size would probably lead to significantly higher costs, if available at all. Since high pressures must be considered for design, the wall thickness would be very high. It is thus assumed to have four smaller steam drums. The alignment of the evaporators can then be chosen very compact for low pressure losses (left variant of Figure 6.3) or it can be designed with one simple long header (right variant of Figure 6.3). Other variants may be possible depending on the particular project and site. For simplicity, the variant with one long feed water distribution header is considered here. Nevertheless, the other variant is included in an additional sensitivity analysis. The OTM and RM solar fields are compared regarding efficiency and costs in the following sections.

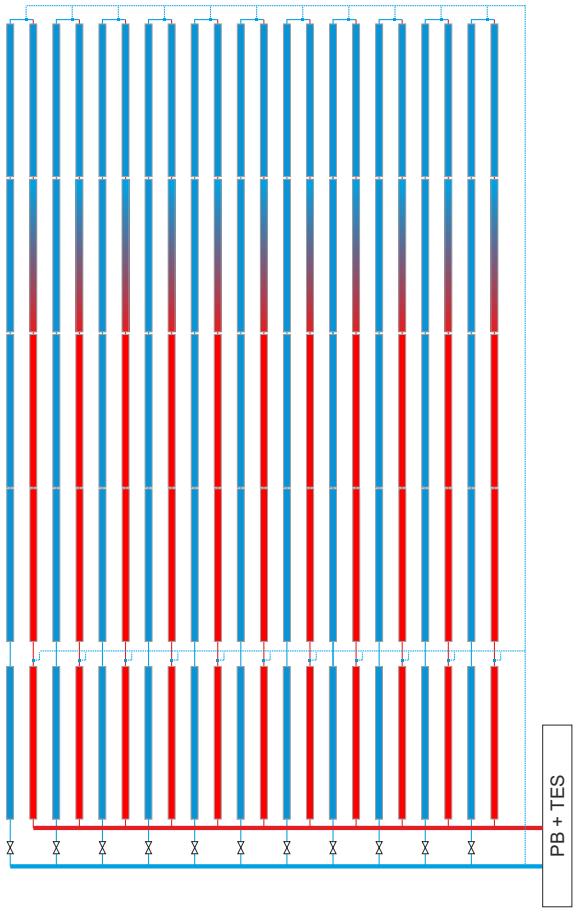

Figure 6.2: Schematic layout of an OTM subfield for variant A with two injections per loop.

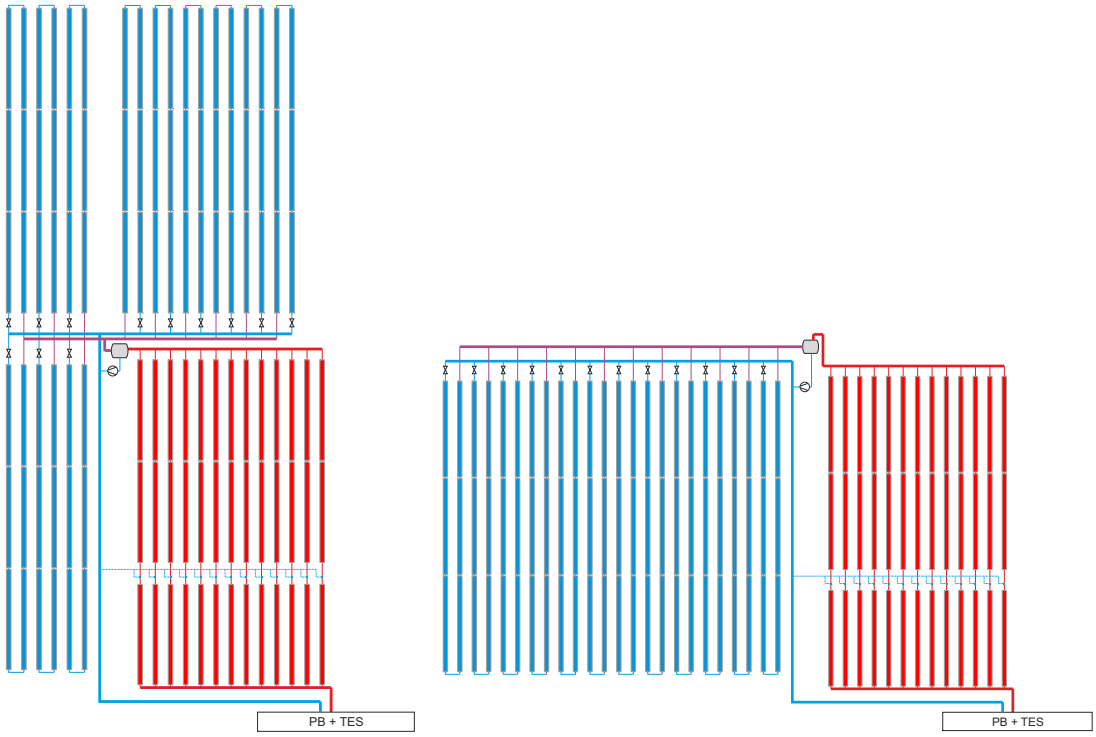

Figure 6.3: Schematic diagram of an RM subfield with central steam drum, recirculation pump and injection for each superheating loop; compact evaporator alignment (left) and simple evaporator alignment (right).

6.2 Efficiency potential of once-through mode

The efficiency and temperature profile of a once-through loop can be evaluated easily. This is not possible directly for RM due to the two different loop lengths and the different number of loops. A scaling approach is therefore used here to make them comparable. The temperature profile along the loop provides information about the loop's heat losses and gives an estimate on the controllability by the SHI. The RM profile is scaled by the total aperture area associated with the corresponding system state. The definition of the relative loop length z_{rel} distinguishes between an evaporation loop (EVL) and a superheating loop (SHL). The EVL length is L_{EVL} = 900 m and the SHL length is L_{SHL} = 450 m. The ratio of the number of the loops is $R_{\mathrm{EVL\text{-}SHL}}$ = 48/52 = 0.92 for the RM reference or 0.86 for its alternative. The relative loop length is then defined by

$$z_{\mathrm{rel,EVL}} = \frac{z_{\mathrm{EVL}} R_{\mathrm{EVL-SHL}}}{L_{\mathrm{EVL}} R_{\mathrm{EVL-SHL}} + L_{\mathrm{SHL}}} \text{ with } 0 \le z_{\mathrm{EVL}} \le L_{\mathrm{EVL}}$$
$$\mathrm{z_{rel,SHL}} = \frac{z_{\mathrm{SHL}}}{L_{\mathrm{EVL}} R_{\mathrm{EVL-SHL}} + L_{\mathrm{SHL}}} \text{ with } L_{\mathrm{EVL}} < z_{\mathrm{SHL}} \le L_{\mathrm{SHL}} \quad (6.1)$$

For OTM, a simple division by the loop length gives the same result. Note that these definitions assume the same collectors being used in the whole solar

field. If this is not the case, the integral of the aperture area must be used instead of the length definitions. The reference profiles along the scaled loop are shown in Figure 6.4. The OTM loop has a different profile depending on the chosen temperature difference by the SHI. The equivalent degree of freedom is the ratio $R_{EVL\text{-}SHL}$ for RM. The scaled temperature profile is very similar for both concepts. The inlet temperature to the loop is higher for RM, since the feed water is mixed with the condensate from the steam drum. At nominal conditions, the inlet temperature is 275°C for RM and 260°C for OTM. The relative position of the SHI is further downstream for OTM, which causes slightly higher relative heat losses. Nevertheless, the efficiency of the OTM loop can be varied according to the weather conditions. At clear sky conditions, the temperature difference by the SHI can be reduced, e.g. to 25 K, in order to achieve a better performance. This kind of variation is not possible for RM, since the temperature difference is fixed by the loop ratio $R_{EVL\text{-}SHL}$ and the current irradiation. It can only be influenced by defocusing of collectors, which reduces the efficiency. The steam quality profile reveals the assumptions for the evaporation sections. A steam quality of 75 % at the outlet of the EVL is considered for RM. Depending on the loop ratio, the relative position varies. The share of the EVI is assumed to be 7 % for OTM.

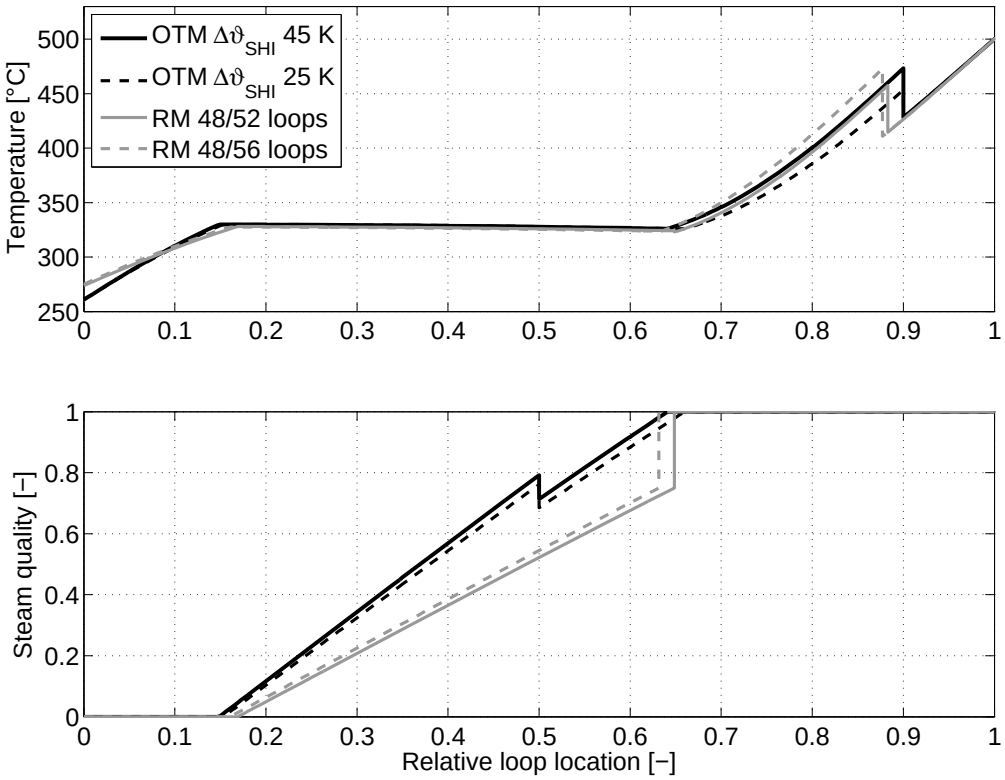

Figure 6.4: Scaled temperature and steam quality profile along the loop for two OTM and two RM variants.

The part load behavior of the loop is shown in Figure 6.5. The efficiency is very similar for all loops. It considers the effective thermal power to the fluid from each loop, which is scaled by the aperture area for RM. This loop efficiency does not include header losses or pumping power consumption. The nominal values are given in Table 6.1 above. The thermal power output is normalized to the number of loops for OTM and superheating loops for RM. At an effective irradiation of about 475 W/m² the solar field provides the nominal power to the power block and the storage cannot be charged anymore. The sliding mode is then active until a pressure of 78 bar is reached, which would be at about 70 % of the power block load [23, 79]. A linear transition between 110 bar and 78 bar is therefore assumed between 475 and 400 W/m². The loop efficiency slightly increases due to the lower saturation temperature. The EPE is shifted downstream in OTM. The different heat capacity of the steam results in an increased temperature difference at the SHI for RM, which cannot be influenced. At low loads, this temperature difference falls rapidly in RM, while it can be maintained longer for control by OTM. Note that the OTM reference loop reduces the temperature difference slightly in order to allow for an almost constant temperature before the SHI of 475°C. At very low loads, the operation of the RM at nominal conditions is hardly possible. The aperture area of the superheating section is not sufficient for reaching 500°C below 175 W/m². For OTM, it is possible with a low mass flow of about 0.35 kg/s. It may also be possible to reduce the outlet temperature in order to maintain a minimum mass flow in the loop. This depends on the turbine design and the operating strategy.

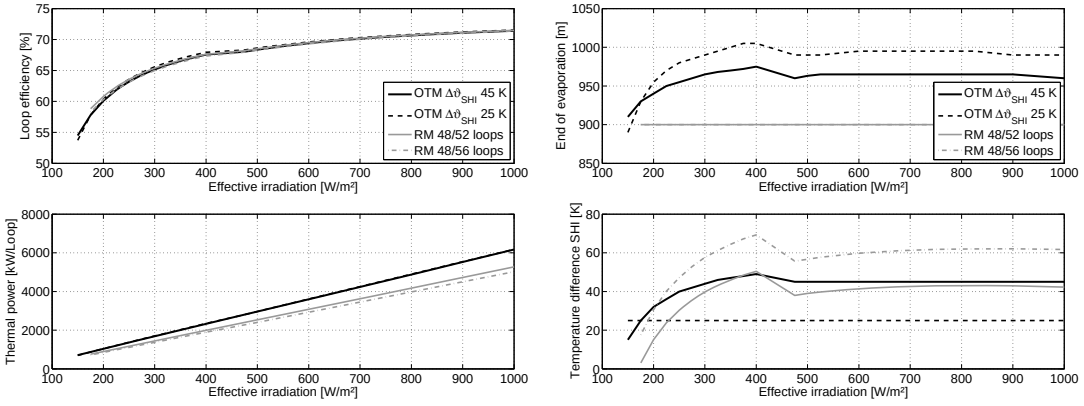

Figure 6.5: Part load behavior of the reference loops for OTM and RM; reference for thermal power is the number of loops (OTM) or superheating loops (RM); loop efficiency does not include solar field piping losses, but only loop piping and receiver heat losses.

The feed water pump compensates the main pressure loss of the plant for both modes. The recirculation pump additionally increases the pressure of the recirculated mass flow in the evaporation section. Figure 6.6 depicts the part load behavior of pressure loss and recirculation mass flow in the EVLs. For

OTM, the recirculation mass flow is zero and the pressure loss is calculated up to the EPE. These are only loop values, such that inlet control valves and header piping are not yet included. The total nominal recirculation mass flow is 0.71 kg/s (0.72 kg/s) per EVL or 34.2 kg/s (34.4 kg/s) for the complete solar field, respectively. The pressure loss is slightly higher for RM due to the recirculation mass flow.

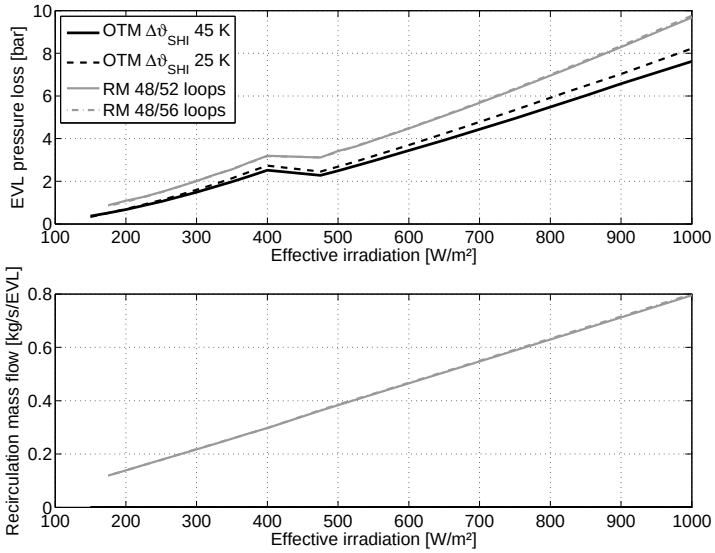

Figure 6.6: Pressure loss and recirculation mass flow per evaporation loop (EVL); inlet to end of evaporation for OTM loop.

The loops for OTM and RM have been designed such that no significant difference exists. It is thus necessary to look into the details of the solar field piping design. A row spacing of about three times the aperture width, i.e. 18 m, is assumed. The main distances for the header lines are listed in Table 6.2. Those indicate the net distances to be covered, but do not consider any piping bridge or thermal expansion bends. A rough estimation of the gross solar field dimensions is also included. The feed water line for RM is divided into two types, one type for the two east-west piping connections from the power block and the other type for the subsequent four north-south piping connections to the steam drum and recirculation line. The inlet distribution headers are different for the RM layouts with one header per subfield or with the compact design (compare with Figure 6.3).

The diameters of the solar field piping are determined by design standards for certain design conditions. Nevertheless, there are various degrees of freedom, such as the choice of the (discrete) standard design dimensions of a tube available on the market, the alignment of thermal expansion bends or the thickness of insulation. A general method for the comparison is chosen here. The mass flows at 1000 W/m² are used as design mass flow, i.e. as maximum mass flow for operation. The solar field is divided into design segments, e.g. the

feed water header of the OTM field has eleven segments between the loop inlets. The inner diameter of a pipe segment is calculated with the help of a design velocity. These velocities are 2 m/s for water, 15 m/s for two-phase flow and 20 m/s for pure steam. The outer diameter is defined to 1.2 times the inner diameter. This diameter factor is an average estimate from a design study for RM fields [234]. Different steel types have different diameter factors at different design pressures and temperatures. The factor suits well when applying steel type 16Mo3 for the piping of the feed water and saturation system and steel type X10CrMoVNb9-1 for the superheated steam headers [234].

The design velocity and the steel type have a significant influence on the cost of the system and a small influence on the thermal efficiency. A variation is thus only considered in the cost section below. However, the design velocity has a high impact on the pressure loss. Common velocities from conventional steam power plants are in the range of 2 to 6 m/s for feed water and 15 to 60 m/s for live steam [222]. Resulting pressure losses of the higher velocities would be in the range of 40 to 60 bar by the RM solar field piping without loops, which is not considered feasible here due to component limitations. The lower velocities as mentioned above are therefore chosen and induce a much lower pressure loss.

The insulation diameter or thickness, respectively, is ideally determined from an economic optimization as a trade-off between insulation cost and avoided heat loss. Such a choice is rather particular for each project and requires a large effort. Therefore, it is not considered useful here. Instead, the outer diameter of the insulation around the pipe is chosen to be two times the outer tube diameter for water lines and three times the tube diameter for steam lines. The same factors are used for OTM and RM to give a somehow comparable trend. The results must be interpreted with care because of the stated reasons.

With the general piping design, the corresponding heat losses and pressure loss can be estimated. Table 6.3 lists the resulting values and illustrates the trends. The heat loss can be significantly reduced by OTM. The total heat loss is about 2.2 MW for OTM and 4.5 to 6 MW for RM. This corresponds to a loss of 1 % or 2-3 % of the nominal thermal power, respectively. The specific heat loss of OTM per solar field aperture area is reduced to about 5.8 W/m², which is 60 to 70 % less than the RM field. The latter values for RM are in the range of oil fields, with about 15 to 20 W/m² [151]. The feed water temperature is assumed to be constant at 260°C. Thus, the specific heat loss is almost constant during operation for OTM. A variation of inlet temperature would slightly change the heat losses, but has a negligible impact on the results. The saturation level is only important for the RM piping to and from the steam drum. In consequence, there is a small difference depending on the load and the pressure level. The

distribution of the heat loss is very interesting for both solar fields and is depicted in Figure 6.7. The long loops allow for compact main headers of the OTM field. Only 27 % of the heat loss corresponds to the main feed water and live steam piping. The main loss is associated with the injection lines, since they are significantly longer and exist for each subfield. The EVI has the largest share of 39 % due to the long north-south connection. The SHI causes about 27 % of the losses. About 7 % are added by the loop piping, i.e. the losses associated by the connection of each loop to the next header. A length of 6 m is assumed for these pipes. In contrast, the two headers to and from the steam drum cause about 49 % of the heat loss in the RM field with compact layout. This includes losses by the recirculation line and the steam drum. This share is 60 % for the simple RM layout with only one evaporation and wet steam header. The feed water line requires a rather long north-south link per subfield, which results in additional 24 % of the heat loss. The influence of live steam header and injection lines is rather small for RM.

Table 6.2: Main characteristics of header piping for OTM and RM solar fields; RM reference with 52 SHL for layouts with one evaporation distribution header (and compact variant).

	OTM	*RM*	*RM compact*
Gross width (east-west) [m]	2 x 400	2 x 690	2 x 360
Gross height (north-south) [m]	2 x 770	2 x 480	2 x 940
Feed water line [m]	2 x 30	2 x 270	2 x 270
		4 x 490	4 x 490
Inlet distribution header [m]	2 x 396	4 x 396	4 x 324
Evaporator collection header [m]	-	4 x 452	4 x 354
Superheating distribution header [m]	-	4 x 264	4 x 264
Live steam collection header [m]	2 x 396	4 x 264	4 x 264
Live steam line [m]	2 x 30	2 x 30	2 x 30
Recirculation line [m]	-	4 x 20	4 x 20
SHI line [m]	4 x 160	4 x 10	4 x 10
SHI distribution header [m]	4 x 396	4 x 234	4 x 234
EVI line [m]	4 x 600	-	-
EVI distribution header [m]	4 x 396	-	-

The pressure loss induced by the solar field piping is also significantly reduced by OTM. At nominal conditions, the OTM header piping causes about 2.1 bar of additional pressure loss. The overall pressure loss including the loop is 20.7 bar. About 4 to 6 bar should be foreseen additionally in order to provide a good control range of the inlet valves. The pressure loss of the RM field is 7.2 to 9.4 bar, depending on the chosen layout. The two-phase flow header has a

significant influence. Its pressure drop could be reduced by choosing a lower design velocity. Nevertheless, especially the two-phase flow should have a high velocity to keep a good mixture of water and steam along the path. The RM field thus has a total pressure drop of 23 or 25.2 bar, which should also be increased by the control valve working range. As a result, the OTM has an 8 to 15 % lower pressure loss at nominal conditions. It can be expected that the power consumption of the feed water pump is also lower for OTM. For such a comparison, additional assumptions must be made. The pump efficiency is estimated as 78 % for the feed water pump and 70 % for the recirculation pumps. The lower feed water tank level is assumed to be constant at 20 bar. The total power consumption can then be reduced by 7 to 9 % at nominal conditions and by 4 to 10 % throughout all part load conditions. The relative part load behavior for OTM compared to RM is shown in Figure 6.8. The recirculation pump consumes about 130 kW at nominal conditions.

Table 6.3: Main trends of header piping for OTM and RM solar fields; RM reference with 52 SHL for layouts with one evaporation distribution header (and compact variant in brackets); pressure loss includes 5 bar by inlet control valve for all systems.

	OTM	*RM*	*Comparison OTM to RM*
Total nominal piping heat loss [MW]	2.2	6.0	-67 %
		(4.5)	(-56 %)
Heat loss per aperture area [W/m²]			
at nominal conditions	5.78	20.24	-71 %
		(15.26)	(-62 %)
at 78 bar	5.78	19.00	-70 %
		(14.53)	(-60 %)
Nominal pressure drop [bar]			
by field piping	2.1	9.4	-77 %
		(7.2)	(-70 %)
by evaporation section	12.2	19.6	-38 %
		(17.4)	(-30 %)
by complete solar field	25.7	30.2	-15 %
		(28.0)	(-8 %)
Nominal electricity consumption by feed water and recirculation pumps [MW]	2.0	2.26	-9 %
		(2.20)	(-7 %)

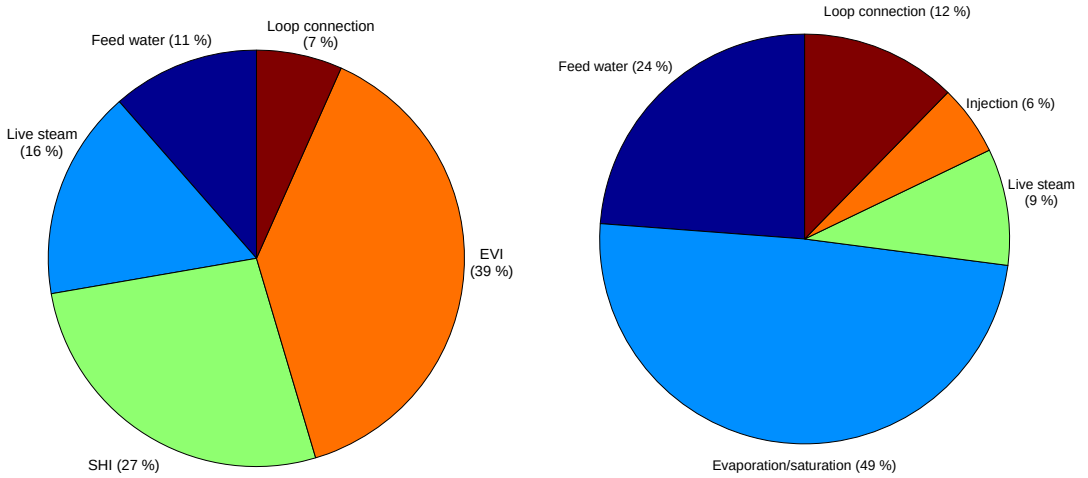

Figure 6.7: Shares of heat loss for the different sections of solar field piping of OTM (left) and RM (right; with compact layout) at nominal conditions.

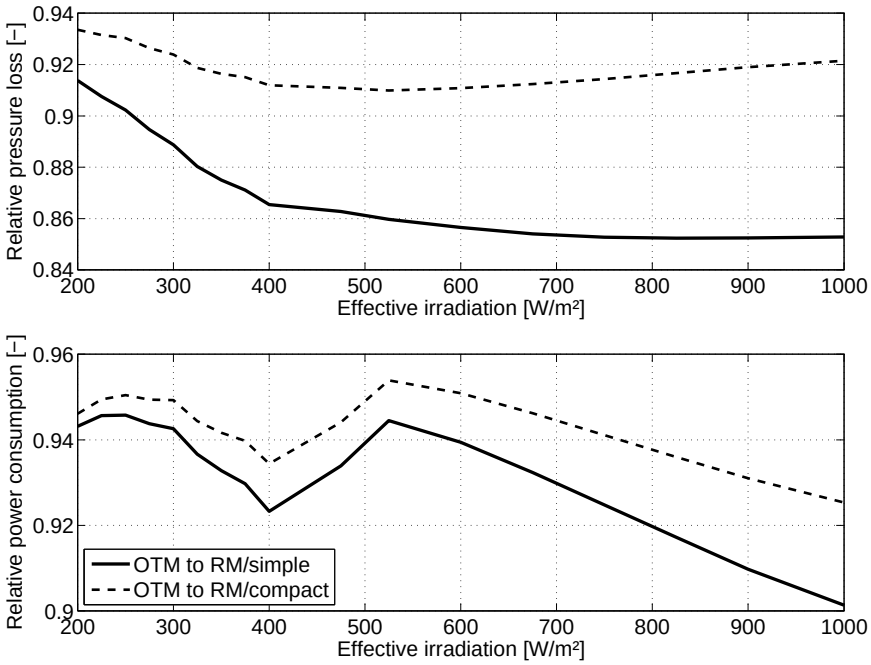

Figure 6.8: Relative values of OTM compared to RM solar fields; total pressure loss of solar field including piping and loops (top) and electricity consumption of feed water and recirculation pumps (bottom).

The more efficient solar field piping and the absence of the steam drum significantly reduce the required start-up energy of OTM solar fields. The same assumptions as for the heat loss analysis are taken regarding the solar field design. The start-up energy is calculated as the difference between two energetic states of the solar field. An analogue methodology to the one in [108] for synthetic oil plants is suggested here. The solar field is filled with water at a certain temperature in the morning. This water and the complete solar field piping

must be heated up to the final temperature levels. While the density of the oil does not change much during this process, the water is partly evaporated and the final thermodynamic state highly depends on the distributed profile of the water and steam mixture as well as on the temperature profile. A more complex procedure is therefore needed. At first, the pressure level of the loop is increased with a high remaining share of liquid water. At a certain pressure level, superheating is initiated to push most of the water content out of the solar field. Then, the remaining temperature rise can happen more efficiently with a reduced mass content. This procedure is assumed for both OTM and RM. The energetic difference is thus estimated via an intermediate state before the superheating is started. The chosen values are listed in Table 6.4. An increase from 80°C to 233°C/30 bar is chosen for the first step. The second step is then performed with the final mass content and a difference to the intermediate state. This procedure is rather easy for OTM. The loop is focused completely and the total heat input can be used for heating up the system. The header lines are calculated section-wise as for the heat loss and the loop is discretized with a resolution of 5 m to get the final mass content and temperature profile. The total start-up energy is determined to be 83 MWh for the complete solar field. This corresponds to a specific start-up energy of 0.22 kWh/m² when compared to the collector field aperture area.

The start-up procedure of the RM field is more complex. The superheating section requires a certain minimum mass flow, which must be provided by the evaporation section. In consequence, the evaporation section must be started significantly earlier than the superheating section, which causes a loss of solar energy. It is assumed that the superheating section is started after the intermediate level is reached. The intermediate level is thus only defined for the evaporation section and must be achieved only by the collector field of the evaporation section. Note that this intermediate level requires various assumptions on the energy content of the solar field piping and the steam drum as well. The same mass content of 90 % is chosen for the evaporation loop. It is further assumed that the first step heats up the distribution header line of the evaporator, but not the feed water line. The latter is included in the second step by the complete solar field. The specific energy is therefore divided into two parts. The required energy of the first step is normalized by the aperture area of the evaporation section, while the energy of the second step is normalized to the complete solar field area. As a result, this sum implicitly includes the losses of the superheating section during start-up. This is especially advantageous for annual yield calculations, which are usually based on the complete solar field area and for which a distinction is rather complex. The results of the start-up energy calculations are provided in Table 6.4. The compact field layout requires a total of 126 MWh, which is 0.33 kWh/m² based on the complete solar field

and similar to a synthetic oil solar field [108]. However, the effective specific start-up energy is estimated to be 0.42 kWh/m². This value is composed of 0.27 kWh/m² of aperture area in the evaporation section for the first start-up step, in which only the evaporation section is in focus, and 0.15 kWh/m² of total aperture area for the second step, in which the complete solar field is in focus. The effective start-up energy thus also considers the chronologically available aperture area. OTM requires about one third of the start-up energy (83 MWh), but only about 50 % of the solar heat input (0.22 kWh/m²) is needed to reach the final state. It can be seen that the fast focusing of all the collectors is a significant advantage during start-up.

Note that the start-up energy is calculated from one common level as in [108]. This assumption may not be realistic for some plants, since they may be able to maintain an advantageous temperature profile along the loops or may be started-up by a completely different procedure. The actual estimation of the start-up energy and the correction factors applied for annual yield analysis are a current topic of research and standardization [106, 108]. The values here must be treated as a first guess for comparison and have a high uncertainty.

Table 6.4: Assumptions and results of OTM and RM start-up comparison; * specific energy composed of evaporation part and complete solar field part; compact RM layout in brackets.

	OTM	*RM*	*Comparison OTM to RM*
Initial temperature	80°C	80°C	
Intermediate pressure level	30 bar	30 bar	
Intermediate temperature level	233°C	233°C	
Liquid share at intermediate level	90 %	90 %	
Resolution of temperature/mass level			
for loop	5 m	5 m	
for solar field piping	Section	Section	
Total start-up energy [MWh]	83	137	-37 %
		(126)	(-32 %)
Specific start-up energy [kWh/m²]	0.22	0.47*	-53 %
		(0.42*)	(-49 %)

An annual yield analysis is performed for the reference plants to estimate the combined impact of the various efficiency items presented so far. The site of PSA in Tabernas, Spain (latitude 37.09° North, longitude 2.36° East) is chosen. Data from the high precision measurement station of PSA are used. The data has a resolution of 10 s and is the same as used in previous chapters. The total sum of DNI is 2209 kWh/m² for that year. The sum of the effective irradiation is 1873 kWh/m². Average values of 60 min are used for yield analysis. The

start-up behavior is analyzed with a higher resolution of the data of 1 min, since it may have a significant influence on the result. Three requirements must be fulfilled for start-up. The specific energy must be accumulated by the effective irradiation. A constant thermal start-up efficiency of 71 % is assumed for this accumulation step. The theoretical start-up energies are multiplied by a correction factor of 1.1 to account for imperfect start-up [108]. A minimum duration is required for start-up to consider limitations of thermal gradients. A rather aggressive strategy is possible for the OTM field. Gradients of 10 K/min are assumed, such that 500°C can be reached after about 45 min. The steam drum of the RM must be treated with care due to its thick walls, such that maximum gradients of 5 K/min are allowed. The superheating section can have 10 K/min as well, if a high mass flow is available. As a result, a minimum start-up duration of 60 min is assumed. Furthermore, the minimum effective irradiation of 250 W/m² must be available for at least 15 min directly before the system is considered in normal operation. The assumed requirements lead to reasonable start-up times of the RM field compared to available data from the TSE-1 plant [141]. They are in the range of 70 to 90 min for the reference plant during clear sky mornings.

Once the system is in normal operation, the resolution of 60 min is used. The start of the hourly resolution of the DNI data thus depends on the start-up time. Although this might lead to inaccuracies, simulations showed that a shift of the hourly data does not change the results notably. The average effective irradiation of each hour is applied to calculate the steady state performance as discussed above in this section. The results of the yield analysis are shown in Table 6.5. The useful thermal energy of the OTM solar field is about 448.4 GWh/year. This energy could be used by a power block or any other steam consumer. The energy output is about 7.1 % better than the RM field with simple header layout. The advantage to the compact version is 4.4 %. If the whole year could be operated with a lower temperature difference of 25 K by the SHI, the OTM performance would be about 3 % better with an energy output of 461.9 GWh/year. This would be more than 10 % better than the simple RM design. Normalized to the aperture area of the solar field, the OTM is therefore between 6.2 and 11.4 % more efficient. Note that the listed yield and efficiency values do not consider any losses due to cleanliness or availability.

Especially the start-up performance is responsible for the greater energy yield. About 44 GWh of effective irradiation are needed for the start-up of the OTM field, while the RM fields require about double the irradiation. The electricity consumption is about 3 to 4 % lower for the OTM field. It depends on the price associated to the electricity, whether this is negligible (e.g. standard industry price) or whether it may be interesting (e.g. when it means a loss of a high feed-in tariff in some electricity markets).

In addition to standard yield analyses, each hour is categorized comparable to the suggestions made in section 4.6.1. Classes A to K are used for operation. An additional class Z is introduced for hours with low energy content, for which operation is unlikely. The procedure of categorization is described in detail in Annex D. The categorization is only performed for hours after start-up. The result of the OTM analysis is shown in Figure 6.9. The shares are robust against different start-up times and only vary within ±1 % of each class. The shares of the different classes can be used to interpret the uncertainty of the yield analysis. Classes A to C are joined and form the largest share of hours. As they do not pose limitations to operation, the more efficient OTM configuration could be used. Ideally, the 64 % share of classes A-C could be transferred to the additional 3 % of performance, which results in 1.9 % of additional energy gain. On the other hand, the OTM performance for classes H, J and K is not ideal. Details are described in section 4.6.3 above. The performance of the RM plant is neither perfect during these situations, but it might be better than the OTM performance. A reliable comparison for these situations is not possible. It would require a detailed analysis of both systems. Furthermore, the assumptions of the simulations do not necessarily hold in reality due to the distributed character of the irradiation. It also depends on the solar field size and turbine requirements, whether the whole plant could be operated or not. Only a rough evaluation can be done. If half of the energy of classes H, J and K could be used by the OTM, it would still be equivalent or slightly better than the RM field. For class K, operation is expected to be feasible with a more advanced control strategy and losses may be in the range of 20 % compared to the ideal value. A higher value can be expected for RM. Class J is characterized by long DNI interruptions. These could provoke a turbine trip and an additional loss by a subsequent re-start of the turbine. The definition of class J often includes the last hour of a day, which does not reduce the ideal performance. It is sometimes doubled, if the drop and recovery of DNI are splitted into two hours. The effective loss of energy may then be in the range of only 15 to 30 %. The examples show that a very detailed analysis would be required to reduce the uncertainty of the comparison.

As a conclusion, one can say that the potential of the OTM is up to 13 % in performance at sites with very good weather conditions, i.e. few days with fluctuating DNI and long drops in DNI. The performance advantage mainly results from the reduced start-up energy and to a small degree from the more flexible operation of the loops. If challenging weather conditions of classes H, J and K prevail at a site, the advantage can even turn into a disadvantage. The performance may then be equivalent or worse compared to the RM field, for which the thermal inertia of the steam drum is then a decisive advantage. Similar considerations hold for the size of the field, thermal storage or fossil co-firing. Large

solar fields offer the chance to balance the fluctuations in DNI. If the turbine can be kept running by auxiliary sources, the loss of irradiation can also be reduced significantly. The OTM offers the chance to preheat the solar field from the TES in the morning. This may increase the usage factor of the TES and further accelerate start-up. Such a preheating is not possible or very complex for RM due to its separated loops.

Another comparison is interesting from former control considerations. Certain energetic losses were assumed from simulations of the OTM loop variant A for the different disturbance classes (compare Table 4.6 on page 182). A reasonable control choice is a clear sky weight of 20 % for the inlet feedforward mass flow of variant A. The useful thermal energy of each category can be reduced by the corresponding losses to give a reference performance for control. This would reduce the energetic output to about 444.6 GWh/a. The application of a state-of-the-art PI controller for the inlet mass flow increases the duration of defocusing. Such a strategy may further reduce the result by at least 1 %. Although more detailed simulations must be performed for both systems, an estimate can be given for variant C. Its defocus duration is in the range of double the loss of the PI Inlet variant for best-case scenarios. A distributed variation of the DNI can significantly increase defocus times for variant C. Therefore, the reference yield of variant A could be reduced in the range of 2 to 5 % by variant C. A more detailed analysis is needed, which is out of the scope this work, but may be useful for the decision of investing in a second injection in the future.

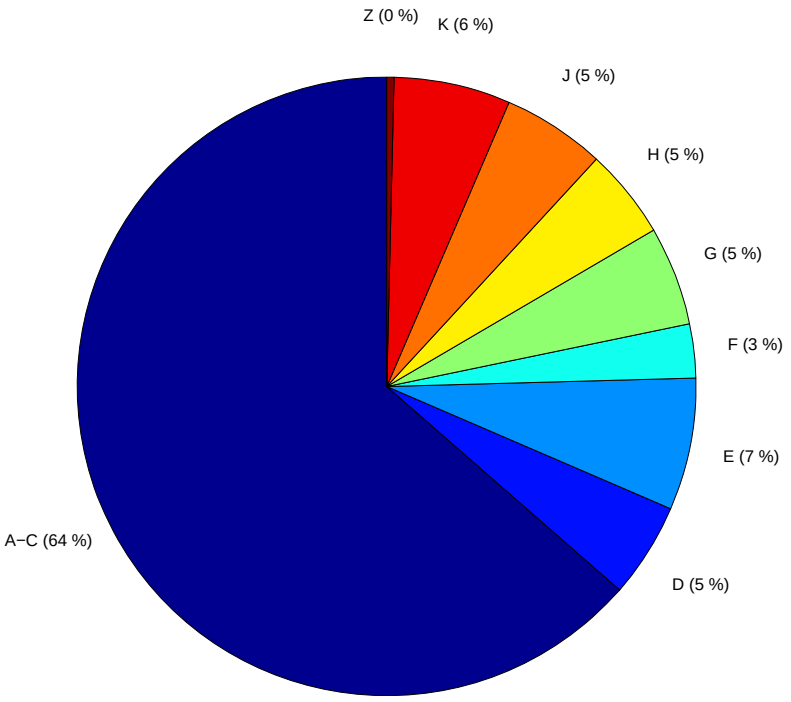

Figure 6.9: Categorization of useful thermal energy output by disturbance classes for operation hours of OTM solar field for data of 2013 at PSA.

Table 6.5: Parameters and results of annual yield analysis for OTM and RM; compact RM layout in brackets.

	OTM	*RM*	*Comparison OTM to RM*
Specific start-up energy [kWh/m²]	0.24	0.52 (0.46)	
Minimum start-up duration [min]	45	60	
Minimum effective irradiation [W/m²]	250	250	
Start-up thermal efficiency [%]	71	71	
Useful thermal energy [GWh/year]	448.4	418.5 (429.5)	+7.1 % (+4.4 %)
Specific useful thermal energy [kWh/m²]	1'180	1'091 (1'120)	+8.2 % (+5.4 %)
Efficiency to effective irradiation [%]	63.0	58.2 (59.8)	+8.2 % (+6.2 %)
Electricity needed by pumps [MWh/year]	3.62	3.78 (3.74)	-4.3 % (-3.3 %)
Effective irradiation for start-up [GWh/year]	44.1	89.5 (79.9)	-51 % (-45 %)

6.3 Cost reduction potential of once-through mode

The procurement cost of the solar field is a decisive factor for commercial projects. It depends on many particular aspects such as the CSP technology itself, component availability, piping design, labor costs, financing costs, financing schemes, supplier management and many others. In consequence, the cost assumptions of this section can only provide a rough estimation on the costs of a DSG solar field. The objective is therefore to identify trends between costs of solar fields with OTM and RM. These can serve as basis for detailed analyses in the future and for certain project decisions. Cost assumptions are mainly derived from two studies for recirculation mode fields, one performed during the DETOP project [79] and one provided by the engineering company Tiede- & Niemann in Hamburg, Germany [234]. Both studies are not open to the public and figures here are not identical. In fact, cost assumptions within the studies and other published data differ significantly at some points. Nevertheless, the assumptions are chosen to be consistent to the data. An uncertainty analysis provides an impression on the variety and effects of different assumptions in the next section.

The cost comparison uses the general solar field layout from the former sections. Specific costs are assumed in order to scale them to the current field layout. The reference values are provided in Table 6.6. The piping is divided into two parts. One is the low temperature piping below about 400°C, which is all the piping except the superheating and live steam headers. The latter ones usually require other steel types, which will lead to different specific prices of the tubes and installation. The diameter factor can vary significantly with the material and design temperature, between 1.1 and 1.9 in the case considered here [234]. Some steel types can be welded easily, while others require additional glowing after the welding to become stress-relieved. The final cost is therefore complex to estimate and must be found for each particular case. A study of the RM field [234] showed that the resulting costs vary significantly for a high temperature variant as considered here, while the final costs only slightly deviate for lower temperatures in the range of 400°C. For simplicity, only the specific costs of the piping are used and varied here, without details on its composition. The diameter factor is kept at 1.2 for the ratio of outer to inner tube diameter. The resulting steel mass is multiplied by the specific costs of 35 or 45 EUR/kg, respectively. The insulation cost is added by considering its outer insulation diameter. The recirculation pumps are divided into two times 75 % of the design volume flow, with an investment of 250'000 EUR per pump. All steam headers are equipped with condensate traps to avoid water droplets within the piping. The excess water during start-up must be fed to the power block during start-up. For RM, a flash tank is foreseen for each subfield to reduce the pressure of the condensate. Additional long piping and pumps must be installed from the steam drum to the power block to transport this condensate. For OTM, only the condensate traps of the superheating header are needed, which significantly reduces the costs. A total cost of the condensate and flash tank system is assumed for both systems. Safety valves are considered separately for each loop and control valves are foreseen at the inlet of each evaporation loop or OTM loop. The main sensor costs result from temperature and mass flow measurements. Not only the sensor, but also its installation and its connection to the control system are included in the cost estimation. The steam attemperators for injecting the water within the loop cost about 13'000 EUR per piece. This includes the injector itself, the control valve and related installation cost. In addition to the mentioned piping and equipment, the rest of the solar field installation is included by an overall estimate of 180 EUR/m². This includes the collectors with receivers, flexible joints, foundations and other costs. They are set equal for both OTM and RM.

Table 6.6: Cost assumptions including installation.

	OTM	*RM*
Low temperature piping [EUR/kg]	35	35
Live steam piping [EUR/kg]	45	45
Insulation [EUR/m² outer insulation surface]	115	115
Steam drum [EUR/kg]	-	9
Total steam drum equipment [10^6 EUR]	-	1.2
Recirculation pump (75 % flow) [10^6 EUR/pump]	-	0.25
Total condensate and flash tank system [10^6 EUR]	0.4	2.0
Wired connection to control system [EUR/channel]	2'000	2'000
Temperature sensor [EUR/piece]	1'300	1'300
Water mass flow sensor [EUR/piece]	3'500	3'500
Steam attemperator [EUR/piece]	13'000	13'000
Control valve [EUR/piece]	4'000	4'000
Safety valve [EUR/piece]	7'000	7'000
Collector field [EUR/m²]	180	180

The resulting total cost of the reference systems is itemized in Table 6.7. The OTM field requires an investment of about 89 million EUR, while the RM fields cost between 103 and 108 million EUR. Thus, a reduction of about 14 to 18 % can be expected. The breakdown of the shares is illustrated in Figure 6.10. The overall collector costs dominate the OTM investment with about 79 %. The main header piping accounts for about 15 % of the investment. Condensate system, control valves and safety valves within the loops together add another 4 %. The injections make about 5 % of the investment, when EVI and SHI are foreseen. The injection costs include not only the steam attemperators, but also the associated piping, a mass flow measurement, a temperature measurement and the required control system connection. Those sum up to 23'800 EUR per injection or 2.1 million EUR in total without piping. The north-south piping for the EVI injection accounts for additional 1 million EUR. The specific costs of the injections per aperture area can serve for an evaluation of their economic effectiveness. They must be compared to the overall collector cost, which gives about 3.6 % (6.4 EUR/m²) for the EVI and 2.6 % (4.7 EUR/m²) for the SHI. In other words, each loop could be extended by 54 m for the investment of the EVI and by 39 m for the investment of the SHI. This value must be interpreted in the context of the energetic and control effect of the EVI. If the total energy output is about 2 to 5 % higher with the EVI, as estimated above, its direct energetic and economic amortization is a matter of detailed analysis and cannot be evaluated in general. It will depend on the quality requirements of the outlet steam conditions and the robustness of the loop against significantly higher

fluctuations of the end of evaporation. It is therefore recommended to foresee the evaporation injection at least for first commercial parabolic trough plants with OTM. Furthermore, it is assumed that EVI and SHI cost the same. Since the differences between feed water and evaporation temperatures are low at the EVI, a detailed design might turn out to be much simpler with significantly lower costs. The design assumed here considers a complex injection with inlet tube and water spraying to reduce temperature shocks in the steam piping. An easier design might thus shift the economic advantage back to the EVI. A detailed analysis is needed to derive reliable recommendations. In general, the cost advantage is shifted towards a system without EVI or SHI in the long run when assuming a reduction of the specific collector costs.

The RM cost composition shows a significantly higher share of the main solar field piping and therefore a lower share of the collector field. The direct cost of the recirculation system is 4.9 million EUR including steam drums and recirculation pumps. This is about 5 % of the total investment. The overall advantage in the specific solar field costs of the OTM is about 13 to 18 % for the assumed specific costs. The reduction of collector costs is beneficial for OTM, since the share of the additional equipment is increased thereby as well.

Table 6.7: Cost comparison of OTM and RM; compact RM layout in brackets; injection costs including associated sensors and piping; sensors and valves without injection equipment.

	OTM	*RM*	*Comparison OTM to RM*
Collector field [10^6 EUR]	68.4	69.0	-
Main piping [10^6 EUR]	12.5	27.2	-54 %
		(22.7)	(-46 %)
Steam drums only [10^6 EUR]	-	1.7	-100 %
Total recirculation system [10^6 EUR]	-	4.9	-100 %
Condensate system [10^6 EUR]	0.6	2.0	-70 %
Sensors and valves [10^6 EUR]	2.8	3.4	-18 %
Injection [10^6 EUR]	4.2	1.5	+180 %
Total solar field [10^6 EUR]	88.6	108.1	-18.0 %
		(103.5)	(-14.4 %)
Superheating injection [EUR/m²]	4.7	3.8	+23 %
Evaporation injection [EUR/m²]	6.4	-	-
Total solar field [EUR/m²]	233	282	-17.4 %
		(270)	(-13.7 %)

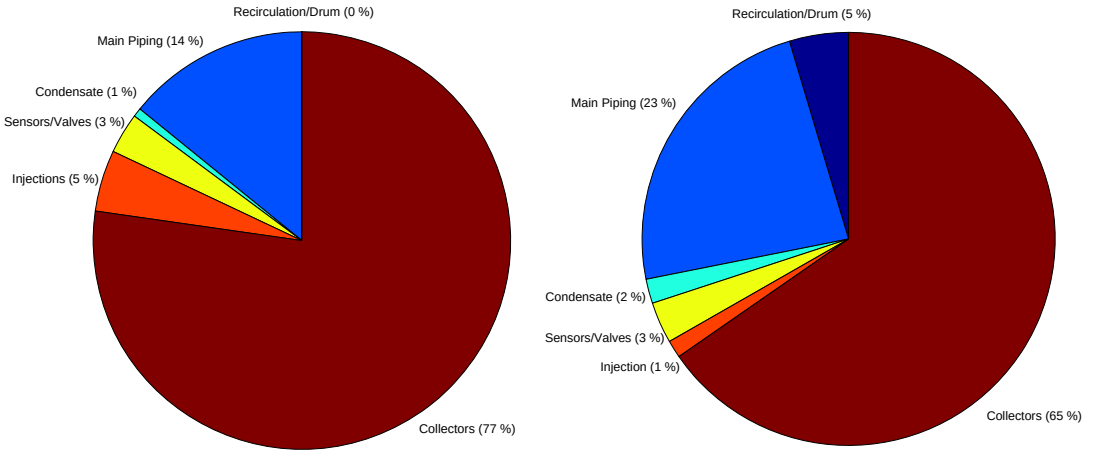

Figure 6.10: Cost breakdown of the OTM and simple RM solar field; injection costs including all associated sensors.

6.4 Overall comparison and evaluation

The results of the yield and cost analysis can be combined by a joint measure. The levelized cost of energy (LCOE) is used here for comparison. Since no project-specific requirements exist, a simple formula for the LCOE analogue to [81, 194] serves as criterion:

$$\mathrm{LCOE} = \frac{\mathrm{FCR} \cdot C_{\mathrm{inv},0} \cdot f_{\mathrm{epc}} + k_{\mathrm{O\&M}} A_{\mathrm{SF}}}{E_{\mathrm{th}}} \tag{6.2}$$

The fixed charge rate FCR [81] represents the annual financing cost as a share of the total investment $C_{\mathrm{inv},0}$. The latter is equivalent to the total solar field cost derived in the former section. It is increased by a surcharge for engineering, procurement and construction (EPC) of the project according to [41]. The chosen financial parameters are provided in Table 6.8. An FCR of 10 %/year is comparable to an annuity payment at an interest rate of 7.8 % for a duration of 20 years [72]. It also agrees well with assumptions in [41]. In addition, the operation and maintenance (O&M) cost is considered. A dependency $k_{\mathrm{O\&M}}$ on the solar field aperture area A_{SF} is used here. The chosen 4 EUR/m² agree with the assumptions in [41] for the RM variants. Nevertheless, the approach in [41] depends on aperture area, energy yield and investment. The resulting specific cost of the OTM plant is 3.7 EUR/m². It must be noted that there has not been a detailed analysis on the different O&M costs of both systems. The maintenance of the recirculation pumps and the steam drum may increase the costs compared to OTM, while the same might hold for increased injection maintenance. Since no reliable information is available, the area-specific costs serve as first estimate here and are the same for both systems. The O&M cost is therefore about 1.5 million EUR/year. The derived total annu-

al costs are divided by the useful thermal energy yield E_{th}, which is equivalent to the total thermal energy calculated in section 6.2. Note that LCOE is often used to give the cost of electricity; while it is defined for useful thermal energy of the solar field here.

Table 6.8: Cost comparison of OTM and RM; compact RM layout in brackets; injection costs including associated sensors and piping; sensors and valves without injection equipment.

	Nominal
FCR [%/year]	10
f_{epc} [-]	1.3
$k_{O\&M}$ [EUR/m²]	4

Main results

The values for total cost and thermal energy can be used for the LCOE calculation. The LCOE of the OTM solar field is 2.91 EUR-cents/kWh (thermal energy). The LCOE of the OTM reference system is 16 to 22 % lower than the one of the RM systems. The main results are summarized in Table 6.9.

The nominal assumptions suggest that the once-through concept can significantly contribute to a reduction of solar energy costs. The sensitivity of the assumptions must be evaluated as well in order to get an impression on the robustness of this result. Figure 6.11 therefore illustrates some aspects. The nominal case is shown as reference. The upper and lower limits in the chart result from the different RM field layouts.

Table 6.9: Main results of the OTM and RM comparison; ranges for RM from compact and simple field layout; LCOE for thermal energy.

	OTM	*RM*	*Comparison OTM to RM*
$C_{inv,0}$ [10^6 EUR]	88.6	103.5 .. 108.1	-14.4 .. -18.0 %
E_{th} [GWh/year]	448.4	418.5 .. 429.5	+4.4 .. +7.1 %
LCOE [EUR-cents/kWh]	2.91	3.49 .. 3.72	-16.7 .. 21.9 %

Impact of start-up assumptions

The start-up energies applied to calculate the annual yield of the solar field have been multiplied by a factor of 1.1 for the nominal case. If the theoretical value with a factor of one is taken, the LCOE potential changes according to the second bar in Figure 6.11. The lowest potential results from the compact RM layout, for which the solar irradiation can be used by the complete solar field

immediately, i.e. the first start-up step is already supported by the superheating collectors. The energy yield of the OTM is only 1.7 % higher in this case and the LCOE potential reduces to about 14 %. The upper limit considers a composed start-up of the simple RM field. On the other hand, correction factors for start-up can be much higher than assumed for the nominal case [108]. The potential of the OTM can increase up to 23 % for a start-up correction factor of 1.3. This corresponds to a specific start-up energy of 0.61 kWh/m² for the simple RM layout.

Impact of design velocity or pressure

The piping cost plays a key role in the comparison. An increase in design velocity reduces the overall steel mass and thereby reduces the piping cost. The RM field may benefit from this reduction significantly. However, it significantly increases the pressure loss of the system. An increase in design velocity of the RM field may result in the necessity to design the piping and the components for a higher design code level. This changes the assumed diameter factor and thereby again increases the steel mass. Such a change would require a complete re-design with different assumptions for the collector costs as well. A reliable estimate is not possible in this framework. Vice versa, a cost effective design of the OTM field would utilize the pressure loss difference to the RM field to increase its design velocities. The simple RM layout sets the maximum pressure loss and design code level of 148 bar/350°C for the following comparison. The OTM and the compact RM field are then changed to meet the same design pressure. The pressure loss of the OTM field can be increased by about 4.5 bar (compare Table 6.3 on page 222 for complete pressure loss). To achieve this, the design velocities can be augmented by a factor of 1.47 to 2.9 m/s for water and 29 m/s for steam flow. The EVI header line is kept at 2 m/s to avoid imbalances between loop and injection water pressure levels. The resulting investment is reduced to 84.4 million EUR. The theoretical start-up energy is reduced slightly to 0.20 kWh/m², by which the energy output becomes 450.4 GWh/year. The LCOE of this configuration is 2.77 EUR-cents/kWh, which is about 5 % lower than the reference. The compact RM field can allow for an increase by 2.2 bar to reach the level of the simple RM field. This results in an investment of 101.5 million EUR, a specific start-up energy of 0.41 kWh/m² and an energy output of 430.5 GWh/year. As a result, the OTM field could raise its LCOE advantage to a potential of 19 to 26 % compared to the RM design. Note that this option is probable, since the design engineer will try to exploit the limits and reduce the costs in any case. Increasing the design velocity is usually cost effective, as the increase in power consumption is negligible compared to the reduction in investment and LCOE. In fact, close to the nominal field design, the increase by 1 bar of pressure loss gives an investment reduction of almost 1 million EUR.

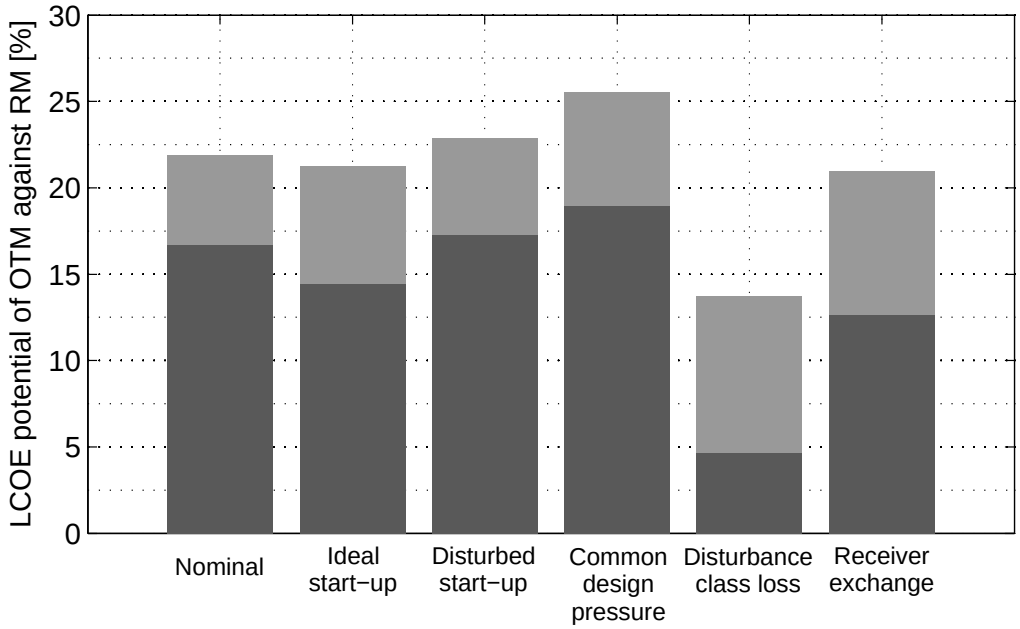

Figure 6.11: Potential reduction in LCOE by OTM compared to RM; upper and lower limits from simple and compact RM layout, respectively.

Impact of disturbance classes

The disturbance classes and the thermal output associated to them have been evaluated for one year at the site of Tabernas, Spain. Depending on mixing effects and the steam requirements, it might be infeasible to operate continuously during disturbances of classes H, J or K. These contain about 16 % of the total thermal energy output. As a worst-case scenario, it is assumed that 90 % of that energy is lost for OTM, while only 10 % of it is lost for RM. The LCOE potential remains positive and above 4 %, but is significantly influenced by those losses. The upper limit in Figure 6.11 is given by the simple RM layout with a loss of 20 % of the energy, while remaining at 90 % loss by OTM. A complete energetic loss of those classes by OTM and a complete usage by RM would result in a negligible potential of 0.8 % of the OTM system for that year. In consequence, the site and the control handling of disturbances must play a key role in the final evaluation of both concepts. A more detailed analysis may clarify these aspects in the future and show open development paths for OTM operation.

Impact of receiver life time

The life time of a receiver close to the end of evaporation cannot be predicted reliably yet. It is thus useful to estimate its influence on the comparison. As a worst-case scenario, the receivers of two collectors per loop might have to be exchanged after every five years. The receiver cost is estimated by

1'000 EUR/piece. This gives an additional annual cost of about 0.63 million EUR. Assuming an exchange of one collector after every ten years demands about 0.16 million EUR/year. The worst case is compared to the compact RM field and the better case to the simple RM layout in Figure 6.11. The potential LCOE reduction is still higher than 12 % for OTM even under the worst-case scenario. Note that, by comparing the latter result with the disturbance class loss, it might be beneficial to accept a regular exchange of the receivers due to high thermal cycling instead of conserving the solar field during strong cloud transients.

General sensitivities

Figure 6.12 shows the sensitivity of the LCOE potential, when only the OTM parameters are changed. Each parameter change is bounded by the two lines for either the compact or the simple RM layout with constant nominal conditions. The reference potential is 100 %, i.e. 100 % in the figure means either a reduction potential of 16.7 % compared to the compact RM layout or 21.9 % compared to the simple RM layout. If the relative OTM potential is reduced to 0 %, the LCOE of RM and OTM are equal and no potential in cost reduction is left. If the annual thermal energy yield of the OTM is reduced to 83 %, compact RM and OTM have the same LCOE. Compared to the simple RM layout, about 40 % of the potential would still be achievable. An increase of the OTM investment of more than 20 % would still result in an overall LCOE reduction of the OTM.

The O&M cost is small compared to the annual financial cost caused by the investment. Therefore, the relative influence is smaller. As proposed in [61, 110], a good impression on the significance of the parameters is achieved by comparing their sensitivity slopes. These are depicted in Figure 6.13. The RM variants are combined to an average LCOE, which is 19.3 % higher than the OTM value. The left bar chart is comparable to Figure 6.12. The slope of the energy yield is positive, such that an increase in yield results in an increase of the OTM potential. The absolute value of the slope is slightly higher than the absolute value of the OTM investment slope. Their ratio allows for an estimation of the economic effectiveness of the injections. The EVI accounts for about 2.75 % of the investment. An average economic benefit can be expected, if the gain in annual energy yield exceeds about 2.2 %.

The influence of the general assumptions can be interpreted with the right hand side bar chart of Figure 6.13. The cost parameters are equally varied for all systems. Their slopes are therefore much smaller than for the single OTM variations. The collector cost has the highest influence on the comparison with a negative slope. A decrease by 10 % to 162 EUR/m² would result in a 1.8 % higher reduction potential, i.e. an average potential of 19.65 %. This is a moderate change and indicates that the comparison result is rather robust against

the economic assumptions. The changes in FCR or EPC surcharge are equivalent to the investment change. A variation of availability or thermal energy yield of the plants does not influence the relative comparison.

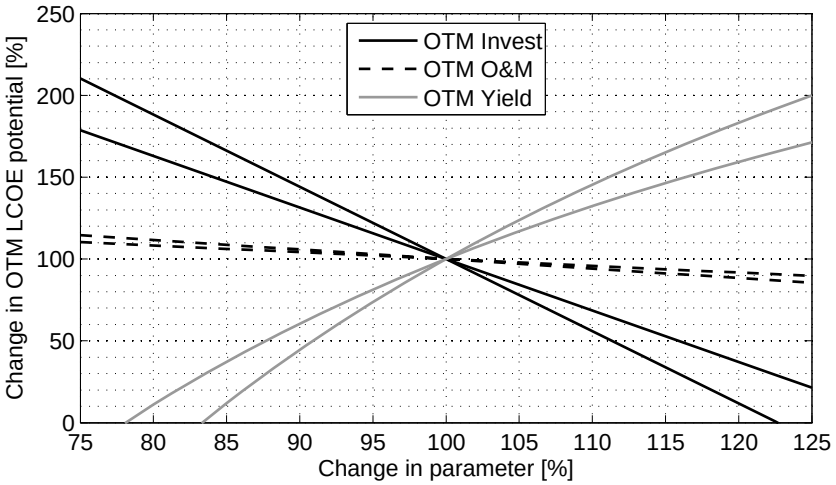

Figure 6.12: Sensitivity curves indicating the influence of different OTM parameters; one line for each RM layout, for which parameters are kept at nominal conditions; 16.7 and 21.9 % reference LCOE potential; zero on y-axis indicates loss of potential.

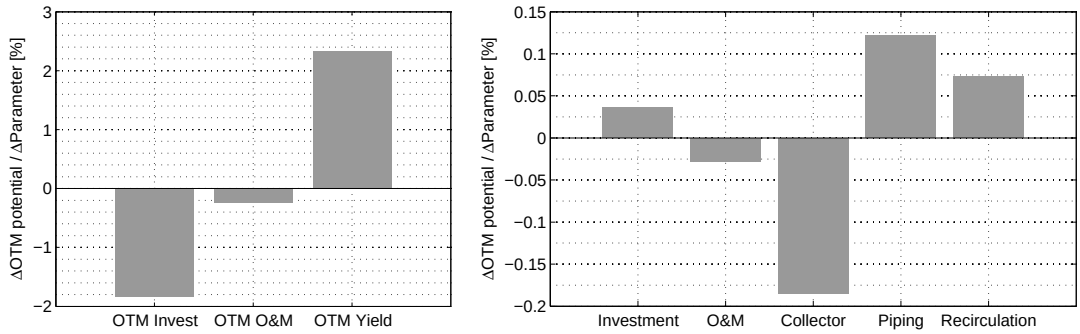

Figure 6.13: Sensitivity slopes indicating significance of cost influence of different parameters; change in OTM reduction potential by a change of 1 % of the parameter cost; 19.3 % reference LCOE potential; changes only in OTM parameter (left) and for both RM and OTM (right).

Conclusions of the comparison

Concluding, solar once-through boilers offer a significant potential for the reduction of the levelized cost of energy compared to the state-of-the-art solar recirculation steam generators. Two variants of RM systems are considered to illustrate the uncertainty by RM design and performance. The ideal OTM system can have an about 17 % lower LCOE than the ideal compact RM field vari-

ant. This value is only slightly changed, when considering that there might be solutions for a faster RM start-up on the one hand, but a higher design velocity of the OTM piping on the other hand. The overall design and modeling uncertainty suggests an OTM cost reduction potential between 14 and 26 %.

Two influences can change the main results and should be analyzed in more detail in the future. First, the OTM and RM performance on operation days with high DNI fluctuations and long drops in DNI needs to be compared. The case of DNI data of Tabernas, Spain, showed that the complete potential might be lost, if no operation during these situations was possible. The RM field has significant advantages due to its inherent steam buffer during these operating situations. The outlet pressure level can be reduced to discharge the steam drum and maintain a mass flow to the turbine during low irradiation periods. This has been operationally proven by the TSE-1 plant [141]. This operating strategy is not recommendable for OTM plants, since the reduction in pressure also leads to a discharge of the mass in the evaporation section. As the EPE is not fixed, it is shifted downstream significantly and, thereby, already reduces the achievable outlet temperature. This has been indicated in [150, 198]. To maintain full controllability during high irradiation disturbances, a fixed outlet pressure is therefore more favorable for OTM. Only a slow sliding of the pressure under controlled conditions is recommended. This operating strategy has not been proven yet, since conventional steam generators do usually not show such high disturbances, and will be important for the yield potential. The OTM performance also depends on the solar field size, the transient mixing effects of the piping system, the (stochastic) local DNI distribution and the requirements of the steam consumer, e.g. the steam turbine. Disturbance classes have been defined in this work and the resulting temperature curves have been derived by simulations for one OTM loop. Nevertheless, the real DNI distribution over a field is not reliably predictable at the moment and mixing effects are difficult to estimate. Detailed simulation studies and, especially, more experimental data is needed to eventually judge on this aspect.

The second major uncertainty of the comparison is the criticalness of the fluctuating end point of evaporation. Even if 20 % of the loop must be regularly equipped with new receivers, the OTM plant remains robustly cost effective compared to the RM plants. Analyses from thermo-mechanical loads suggest that an exchange of receivers might not be needed at all, such that the nominal potential could be confirmed. Nevertheless, not all aspects of a complete life time analysis could be covered here, as the emphasis was put on developing a methodology for estimation. This should be applied for future detailed life time assessments of all critical components. As the OTM potential remains high even under very conservative assumptions, it may be an option to build first OTM plants and continuously monitor their real loads. Non-destructive inspections

are available and can allow for a secure, regular evaluation of critical parts. A reliable evaluation will only be available after such long-term experience.

In general, RM offers more flexibility, or more complexity, during the solar field layout, which bears the chance to adapt more easily to unsymmetric restricted project sites. For example, some shorter loops for evaporation can be foreseen apart from the nominal loop length, in order to fill some gaps of the site. The imbalance between different subfields must then be considered, but is feasible in principle. The resulting ratio of superheating to evaporation is always fixed and cannot be changed anymore. OTM has the best and easiest layout for symmetric sites from scratch and then offers a high operational flexibility. This is especially beneficial for part load operation and if changes in the desired steam parameters may occur during the project or after changes of the power block. The nominal potential of the OTM is then very likely to be achievable at sites with few cloud transients. If a flexible auxiliary heat source like TES or fossil co-firing exists, it can compensate steam variations during difficult DNI situations. The quality requirements or the bandwidth of acceptable temperature fluctuations from the solar field, respectively, can then be released. As a result, it is probable that most of the OTM potential can also be harvested at locations like Tabernas, which show a significant share of difficult disturbances. Solar hybrid plants are an example of a perfect match for OTM applications, in which the solar part should be as cheap as possible and flexibility is available by a fossil or biomass co-firing. At locations with a very small share of cloud fluctuations, e.g. expectable in countries such as Jordan or Chile, solar-only plants are feasible as well.

One future development might be to have additional TES for shifting the solar energy to the peak demand times [223], without the necessity of 24 hour operation. These small storage systems could provide both the shifting of solar energy to demand times and the compensation of certain steam temperature variations by the OTM field. Former studies suggest that the solar field of DSG plants with recirculation concept are already about 10 % cheaper than plants with synthetic oil, but that the special high capacity TES is too expensive for DSG plants [81]. The further cost reduction by the OTM development might enable DSG technology to compete in the peak shifting market.

7 Conclusions

Direct steam generation (DSG) in parabolic trough power plants is a promising option for the generation of solar heat and power. Such power plants already exist in Thailand and Spain. In these plants, the state-of-the-art recirculation concept is applied, which separates the generation and the superheating of the steam by a steam drum. Analogue to the development in conventional boilers, the introduction of a solar once-through steam generator offers the potential to reduce the costs of the solar field. Before this work, only few experiments with the once-through concept had been performed at the Direct Solar Steam (DISS) test facility of the Plataforma Solar de Almería, Spain. Two main disadvantages of a once-through loop were identified. Temperature control was not successful during stronger cloud transients and the fluctuation of the end of evaporation was thought to severely damage the receivers, which would lead to a very short life time of the plant. In consequence, the comparison with other operating concepts suggested the initial development of the recirculation mode due to its robustness. With the experience and the confirmed safe operation of that concept in the commercial plants, the focus could be put on further cost reduction options of DSG. The objective of this work was to provide a profound technical and economic analysis of the potential of solar once-through steam generators. This task led the work to cover the whole range of steam generation aspects, such as design, modeling, temperature control, component life time estimation, energy yield analysis and economic assessment.

The design tools for parabolic trough loops with recirculation mode [62, 65, 66] have been adapted to the once-through mode. Criteria to maintain a favorable annular flow regime and to limit the temperature gradients within a receiver cross-section are applied. They guarantee a safe operation throughout the whole operating range. Three different loop layouts are suggested varying by the number and location of injections. These are necessary for a reliable and efficient temperature control. The most robust layout foresees one injection closely before the end of evaporation and one injection close to the loop outlet in the superheating section. The two other variants only use one injection either in the evaporation or in the superheating section. Design criteria for these injections have been derived and applied for the re-design of the DISS test facility. This facility currently has a loop length of 1000 m and was used for all experiments of this work. Special equipment is installed for the analysis of the once-through concept.

Simulation models are the basis for understanding the system dynamics and for developing control strategies. An axially discretized model was developed by Hirsch [105] for recirculation mode. It could be successfully validated

for the application of once-through boilers within this work. The steam temperature behavior and the main variations of the end of evaporation can be accurately simulated. For large simulation studies and as a preparation for real-time simulation, a new moving boundary model has been developed based on [203] as well. It combines fast computation of a concentrated model, while still offering insight into the distributed character of the once-through loop at selected locations. This model has also been validated successfully at the DISS facility. The models represent the temperature behavior during inlet disturbances of the loop especially well. If the inlet temperature is decreased or the heat input at the inlet is reduced, respectively, the outlet temperature shows a characteristic non-minimum phase behavior. It increases at first, due to a lower outlet steam flow, and then decreases to its lower final value after about one throughput time of the system. This reaction can take between 10 to 45 minutes, depending on the system states and inputs. The discretized model could be validated for various constellations of the direct normal irradiance (DNI), especially for inhomogeneous distributions along the loop. As a matter of model assumptions, the new moving boundary model does not reflect the smaller non-minimum phase fluctuations of these distributed disturbances. Nevertheless, most of the operating time is reproduced well with both models.

In contrast to fossil once-through steam generators, the heat source of the system, namely the sun light being influenced by passing clouds, cannot be controlled. The general goal of control is to keep the outlet temperature in a small bandwidth around the desired live steam temperature, e.g. 500°C, by adapting the mass flow to the loop. A fixed outlet pressure is assumed here for turbine operation and for charging a thermal energy storage system. The once-through loop shows a long delay of several minutes between inlet mass flow variation and the response of the outlet temperature. This phenomenon complicates the control of the system, since DNI disturbances caused by clouds are in the same range as this delay. It is also a decisive difference to solar fields with synthetic oil or molten salts. Control reactions may therefore lead to amplification of the disturbance. One important result is thus that state-of-the-art proportional integral (PI) controllers with steam temperature as controlled variable are not recommended for the inlet mass flow. One or two injections of feed water are foreseen within the loop to reduce the time delay. First control concepts for such injections had been developed and tested at DISS facility by Valenzuela [253] and Eck [57]. However, their control strategy was not suitable for the whole operating range or optimally adapted to the needs of large-scale power plants. Therefore, the main contribution of this work is the development of a robust, fast temperature control, which at the same time is easy to understand and implement in commercial plants. Linear time-invariant transfer functions have been derived from the discretized model for the whole operating range. PI

controllers are then designed for the injections in two steps based on those models and an internal model control approach [175]. The PI control parameters are adapted based on the current mass flow within the loop by a gain scheduling scheme. Feedforward action plays another important role. Former feedforward schemes have been modified and tested for their effectiveness in large commercial power plants. As a result, only one feedforward variable is maintained, namely the temperature before the superheating injection, which is measured anyway and therefore does not require additional sensors. A nonlinear steady-state feedforward is suggested and shows very good results in practice. The temperature of the injection water, formerly used as feedforward variable, was shown to be better used for an additional gain scheduling. The inlet mass flow is suggested to be based mainly on feedforward by an average DNI signal. This is ideally accompanied by a clear sky DNI model and estimation of the loop efficiency, which have been proposed here for the first time. Experiments at the DISS facility showed a reliable and very fast temperature control, which proved the suggested design. It was thus proven that temperature control of once-through solar fields is feasible and now readily available for commercial application together with steam turbines. The control is limited only by the physical boundary conditions of the system. That is, if no DNI is available for a period of 5 to 20 minutes, the outlet temperature may fall to saturation. In addition, high frequency fluctuations of DNI are difficult to manage and rely on mixing effects of the distributed solar field. It is thus advantageous to build once-through steam generators at sites with a low share of such situations. As an outlook, the potential of model predictive control strategies has been illustrated. It is a challenging task, but might lead to very advantageous control, especially in combination with local DNI measurements or nowcasting. The second injection might become unnecessary thereby in the future.

The notion of DNI disturbance classes has been proposed in this work to categorize irradiation situations. Criteria have been derived to identify certain critical control situations based on typical system filters. This categorization can be used as well for life time estimation and yield analysis. A classical method of life time estimation is the analysis of complete time series of stresses and the counting of cycles, e.g. via a rainflow algorithm [42]. By categorizing the DNI time series with the new methodology, load cycles can easily be identified for each class and the extrapolation for life time can be performed by multiplication of the class frequency. Preliminary life time analyses of receivers in the superheating section and close to the end of evaporation showed that there is no significant life time reduction due to temperature variations. The result for the end of evaporation depends on the design code and related assumptions, with variations between 16 and 60 years. It is thus necessary to detail this analysis in the future. It is also suggested to foresee a monitoring system for

critical solar field locations in order to track the real plant loads and gain experience for more reliable life time estimations.

Three reference plants have been analyzed for comparison of once-through and recirculation solar fields with 500°C and 110 bar live steam conditions at a nominal thermal power of 250 MW. The once-through loop can be aligned very compact and therefore significantly reduces the piping demand. Two types of state-of-the-art recirculation fields have been designed with four subfields and one central steam drum per subfield. The annual thermal energy of the once-through field is about 4 to 13 % higher due to a faster start-up and a more flexible operation. The overall cost of the once-through field is about 14 to 18 % lower, which is due to the more compact piping and to omitting of the recirculation components such as steam drum and recirculation pumps. The measure of levelized cost of thermal energy then shows that the average cost reduction potential of a once-through solar field is around 19 % compared to recirculation fields. Depending on the exact assumptions, it may reduce the cost within 14 and 26 %. The exact behavior of the outlet steam conditions depends on the local DNI distribution and the thermal inertia of the solar field. Worst-case assumptions on the performance were made for a year with an energetic share of 16 % of critical DNI situations. The result still suggests a remaining potential of more than 4 %. Nevertheless, the cloud conditions of the site as well as the quality requirements of the steam consumer have a significant influence on the comparison and must be analyzed carefully. If the end of evaporation would cause an increased worst-case exchange rate of receivers, which could not be answered eventually here, but seems unlikely, the potential in levelized cost reduction would remain above 10 %. A cost reduction of collectors further improves the relative advantage of the once-through configuration.

A much more complex control strategy was expected to be necessary for once-through boilers at the beginning. This turned out to be not true necessarily. From a practical perspective, the recirculation mode field is more flexible, but also more complex in the design stage, while the once-through system is much more flexible during operation and regarding changes in live steam parameters.

Future work may focus on advanced control concepts to reduce the number of injections and clearly elaborate critical cloud conditions and related control strategies. It must also be proven by long term plant data, whether or how challenging the varying end of evaporation is in reality. Even without exact information on the latter issues, solar once-through boilers already are a very promising option for commercial power plants and the reduction of solar energy generation cost. Their characteristics are ideal for solar hybrid plants with steam turbines or for solar-only applications at sites with few cloud appearances.

A Annex: Moving boundary model formulations

The following paragraphs explain the modeling of the base model formulation of the MBM. It refers to a layout with two injections of which one (injector A) is in the evaporation section and the other (injector B) is in the superheating section (see Figure A.1). Only the main equations are provided here, the remaining ones can be derived from the articles of Ray [203].

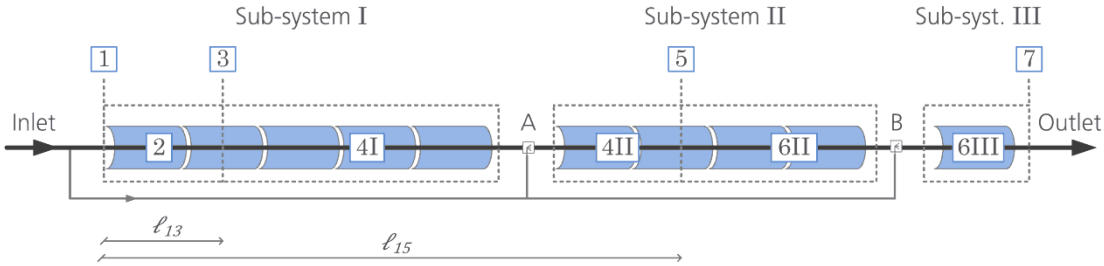

Figure A.1: Overview of sub-systems and states for base model configuration.

The moving boundary between preheating and evaporation section is:

$$\frac{dl_{13}}{dt} = \frac{\left(\dot{m}_1 - \dot{m}_3 - \frac{1}{\rho_2}\frac{\partial\rho_2}{\partial u_2}\Big|_{p2}\left(\dot{m}_1(h_1-u_2) - \dot{m}_3(h_3-u_2) + \dot{q}_2' l_{13}\right)\right)}{A\left(\rho_2 - \rho_3 + \frac{\rho_3}{\rho_2}\frac{\partial\rho_2}{\partial u_2}\Big|_{p2}(h_3-u_2)\right)} \tag{A.1}$$

The specific inner energy u_2 of volume 2 is:

$$\frac{du_2}{dt} = \frac{1}{l_{13}\rho_2 A}\left(\dot{m}_1(h_1-u_2) - \dot{m}_3(h_3-u_2) + \dot{q}_2' l_{13} + \rho_3 A(h_3-u_2)\frac{dl_{13}}{dt}\right) \tag{A.2}$$

The mean absorber wall temperature of volume 2 is described by:

$$\frac{dT_{w2}}{dt} = \frac{1}{\rho_w A_w c_w}\left(\dot{q}_{sol,2}' - \dot{q}_{loss,2}' - \dot{q}_2'\right) + \frac{1}{l_{13}}(\vartheta_{w3} - \vartheta_{w2})\frac{dl_{13}}{dt} \tag{A.3}$$

Note that $\dot{Q}_2$ and $\dot{q}_{loss,2}'$ both are dependent on the wall temperature. Also note that the original formulation in [204] for the second term would result in $\frac{(\vartheta_{w,4I}-\vartheta_{w2})}{L_{1A}}\frac{dl_{13}}{dt}$. The original formulation suggests a smaller effect by the boundary movement. In a later paper, the current formulation is used.

Analogous, we find the specific inner energy of volume 4I:

$$\frac{du_{4I}}{dt} = \frac{1}{l_{3A}\rho_{4I}A}\Big(\dot{m}_3(h_3 - u_{4I}) - \dot{m}_{I,out}\big(h_{I,out} - u_{4I}\big) + \dot{q}'_{4I}l_{3A} - \rho_3 A(h_3 - u_{4I})\frac{dl_{13}}{dt}\Big) \tag{A.4}$$

and the mean absorber wall temperature of volume 4I:

$$\frac{dT_{w4I}}{dt} = \frac{1}{\rho_w A_w c_w}\big(\dot{q}'_{sol,4I} - \dot{q}'_{loss,4I} - \dot{q}'_{4I}\big) - \frac{1}{l_{3A}}\big(\vartheta_{w,3} - \vartheta_{w,4I}\big)\frac{dl_{13}}{dt} \tag{A.5}$$

Again, $\dot{Q}_{4I}$ and $\dot{q}'_{loss,4\mathrm{I}}$ both depend on the wall temperature. It is also assumed that $\vartheta_{w,3} = \vartheta_{w,4I}$.

Within the sub-system II, the moving boundary between evaporation and superheating section is:

$$\frac{dl_{15}}{dt} = \frac{\dot{m}_{II,in}\big(h_{II,in} - u_{4II}\big) - \dot{m}_5(h_5 - u_{4II}) + \dot{q}'_{4II}l_{A5} - l_{A5}A\rho_{4II}\frac{du_{4II}}{dt}}{\rho_5 A(u_{4II} - h_5)} \tag{A.6}$$

Note that the change in l_{13} is already included in volume 4I and, thus, is not explicitly used in the derivative of l_{15}, as must be done in [204].

The internal energy $u_{4\mathrm{II}}$ is approximated by

$$\frac{du_{4I}}{dt} = \frac{1}{2}(h_{IIin} + h_5) \tag{A.7}$$

The wall temperature in the evaporation section is split into two independent parts or states, respectively. Thus, the mean absorber wall temperature of volume 4II is:

$$\frac{d\vartheta_{w,4II}}{dt} = \frac{1}{\rho_w A_w c_w}\big(\dot{q}'_{sol,4II} - \dot{q}'_{loss,4II} - \dot{q}'_{4II}\big) + \frac{1}{l_{A5}}\big(\vartheta_{w,5} - \vartheta_{w,4II}\big)\frac{dl_{15}}{dt} \tag{A.8}$$

Additional equations for the mass flows are:

Outlet mass flow:

$$\dot{m}_7 = \sqrt{\frac{(p_B - p_7)\rho_{6III}}{K_{f,6III}L_{B7}}} \tag{A.9}$$

Outlet mass flow sub-system II:

$$\dot{m}_{II,out} = \sqrt{\frac{(p_5 - p_B)\rho_{6II}}{K_{f,6II}l_{5B7}}} \tag{A.10}$$

Outlet mass flow sub-system I:

$$\dot{m}_{I,out} = \sqrt{\frac{(p_3 - p_A)\rho_{4I}}{K_{f,4I}l_{3A}}} \tag{A.11}$$

The mass flows at the start and end of evaporation are interpolated:

$$\dot{m}_3 = \frac{\left(\dot{m}_1 + \dot{m}_{I,out}\right)}{2} \tag{A.12}$$

$$\dot{m}_5 = \frac{\left(\dot{m}_{I,in} + \dot{m}_{II,out}\right)}{2} \tag{A.13}$$

The following table summarizes the system states as implemented in the extended moving boundary model. The state $h_{1,\mathrm{x1}}$ is for the second order prefilter of the specific inlet enthalpy. Outlet temperature ϑ_7 and temperature before injection B ($\vartheta_{\mathrm{II,out}}$) are not needed for the simulation, but are 'measured' states for information.

Table A.1: System states of the extended moving boundary model for the base formulation.

No.	*State*	*No.*	*State*
1	l_{13}	15	$\rho_{4\mathrm{II}}$
2	u_2	16	$h_{\mathrm{II,in}}$
3	$u_{4\mathrm{I}}$	17	$\dot{q}'_{\mathrm{sol,4II}}$
4	$\vartheta_{\mathrm{w},2}$	18	$\dot{q}'_{\mathrm{sol,6II}}$
5	$\vartheta_{\mathrm{w,4II}}$	19	$\dot{m}_{\mathrm{II,in}}$
6	h_1	20	$u_{6\mathrm{III}}$
7	$\dot{q}'_{\mathrm{sol},2}$	21	$\vartheta_{\mathrm{w,6III}}$
8	$\dot{q}'_{\mathrm{sol,4I}}$	22	$\dot{m}_{\mathrm{III,in}}$
9	$\dot{m}_1$	23	$h_{\mathrm{III,in}}$
10	l_{15}	24	$\dot{q}'_{\mathrm{sol,6III}}$
11	$u_{6\mathrm{II}}$	25	p_A
12	$\vartheta_{\mathrm{w,4II}}$	26	$h_{1,\mathrm{x1}}$
13	$\vartheta_{\mathrm{w,6II}}$	27	(ϑ_7)
14	ρ_5	28	$(\vartheta_{\mathrm{II,out}})$

B Annex: Analytical LTI model for superheater

LTI models for single-phase flow line focus systems with oil as heat transfer fluid have been derived in [278]. They can analogously be used for other incompressible fluids such as liquid water or molten salts. The special case of line focus steam superheaters has been derived by [57] based on [137, 198] and is published in English in [139]. Both approaches derive basic transfer functions for the outlet temperature of a collector depending on inlet temperature, inlet mass flow and irradiance. The current chapter summarizes both approaches and it is shown where there exist differences. The analysis is limited here to the temperature transfer function, since it is the dominant influence and present in all other transfer functions.

The transfer function from inlet to outlet temperature as stated in [278] is

$$G_\vartheta(s) = \frac{\Delta\vartheta_{out}}{\Delta\vartheta_{in}} = exp\left(-s\tau_{res} - N_F \frac{s\tau_{res} + N_{wa}}{s\tau_{res} + N_{wi} + N_{wa}}\right) = e^{-s\tau_{res}}\, e^{-N_F}\, e^{N_F \frac{N_{wi}}{s\tau_{res}+N_{wi}+N_{wa}}} \tag{B.1}$$

Note that in transfer function notation only deviations from a steady state are considered. The complex argument s denotes the Laplace variable. τ_{res} is the throughput time or the residence time of the fluid in the collector, respectively. It can be calculated from the equation

$$\tau_{res} = \frac{\rho_F A_F L_{coll}}{\dot{m}} \tag{B.2}$$

This includes fluid density ρ_F, inner cross-section A_F, collector length L_{coll}, and mass flow $\dot{m}$. The dimensionless characteristic numbers are

$$N_F = \frac{\alpha_i U_F}{\rho_F c_F A_i}\tau_{res} = \frac{\alpha_i U_F L_{coll}}{\dot{m} c_F}$$

$$N_{wi} = \frac{\alpha_i U_F}{\rho_w c_w A_w}\tau_{res} = \frac{\rho_F c_F A_i}{\rho_w c_w A_w} N_F \tag{B.3}$$

$$N_{wa} = \frac{\alpha_a U_a}{\rho_w c_w A_w}\tau_{res}$$

This includes heat transfer coefficient α, circumference U, and heat capacity c. The index F indicates fluid properties, while w indicates tube wall material properties, “a” is for outer, and “i” is for inner tube values. The dimensionless numbers N indicate relations between the heat transfer and the heat storage ability. They are better known as number of transfer units (NTU) (see [257] for details). With the four characteristic variables from equations (B.2) and (B.3)

the temperature transfer function for any collector with incompressible single-phase flow is characterized.

The factor $\alpha_a U_a$ in N_{wa} considers the heat loss to the environment. Originally this was derived for convective receiver losses at low temperatures [278]. However, with modern receivers at high temperatures, the convective heat loss is misleading. Therefore, we use the linearization of the empirical heat loss correlation (3.16) to replace it:

$$\alpha_i U_a \approx \frac{dq_{loss,L}}{d\vartheta} = c_1 + 4c_4\vartheta_{w,0}^3 \tag{B.4}$$

The unit of this factor is [W/m/K] and $\vartheta_{\mathrm{w,0}}$ is the steady state value of the mean wall temperature of the collector. This approximation is within 1 % of the correct heat loss for a temperature deviation of about ± 20 K and within 5 % for a temperature deviation of about ± 40 K with $\vartheta_{\mathrm{w,0}}$ = 400°C. The sensitivity $\alpha_a U_a$ is 1.65 W/m/K in the case of the DISS facility at 400°C.

The influence of fluid or wall temperature changes on the inner heat transfer is expressed by the sensitivity $\alpha_i U_F$. The inner circumference $U_F = \pi d_i$ is about 0.185 m for the new DISS receivers. Thus, all values for $\alpha_i >$ 1000 W/m²/K would lead to a negligible heat loss influence of less than 1 % for the characteristic number (N_{wi}+N_{wa}). A general correlation can be derived for this estimation introducing the maximum share for neglection s_{neg}:

$$N_{wi}s_{neg} \geq N_{wa} \Leftrightarrow \alpha_i \geq \alpha_{i,min} = \frac{1}{s_{neg}\pi d_i}\left(c_1 + 4c_4\vartheta_{w,0}^3\right) \tag{B.5}$$

For s_{neg} = 1 % the characteristic curve is shown in Figure B.1. Note that this curve is specific for the receiver and independent from the fluid used. For an operating point at the new DISS facility at 400°C, 80 bar and an effective irradiation of 375 W/m², the minimum heat transfer coefficient of 1000 W/m²/K is reached. As lower DNI values are barely relevant, we can neglect N_{wa} for this purpose. However, when higher temperatures are desired at the same irradiation level and at the same facility, the share of N_{wa} would be larger than 1 %.

The main temperature transfer function of Eck (eq. 2.8 in [57]) is equivalent to equation (B.1), if heat loss or N_{wa}, respectively, is neglected.

In the temperature transfer function equation (B.1), there is a transcendent term, which causes numerical and structural problems. It should thus be replaced by a rational function to simplify subsequent controller design. We analyze this term now separately and denote it as G_0:

$$G_0(\mathrm{s}) = \exp\left(-N_F\frac{s\tau_{res} + N_{wa}}{s\tau_{res} + N_{wi} + N_{wa}}\right) = e^{-N_F}\, e^{N_F\frac{N_{wi}}{s\tau_{res}+N_{wi}+N_{wa}}} \tag{B.6}$$

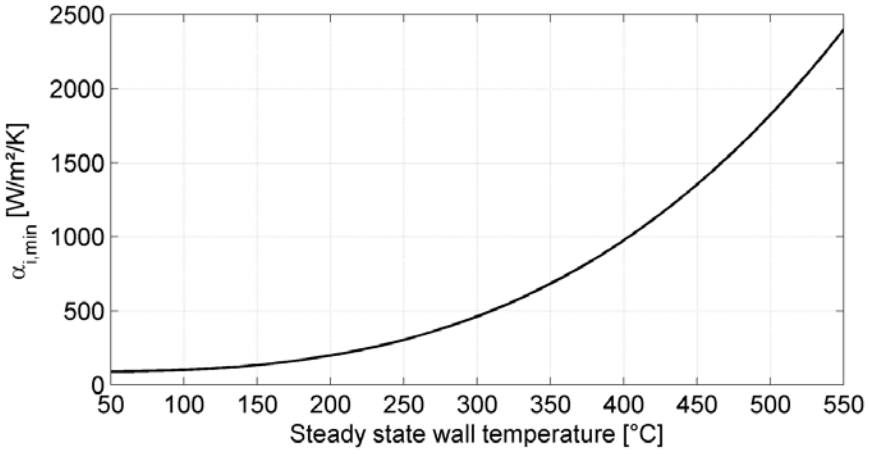

Figure B.1: Minimum inner heat transfer coefficient for new DISS receivers and s_{neg} = 1 %.

One possibility is to use an approximation suggested in [161] as found in [252]. It is used by Eck [57] and then slightly adapted in [139] for Eurotrough collectors. The result of the latter approximation is a serial connection of n_1 first order elements defined by

$$G_0(\mathrm{s}) \approx \tilde{G}_{0,1}(\mathrm{s}) = \frac{1}{(1+s\tau_1)^{n_1}} \tag{B.7}$$

The order and time constant can directly be derived from the characteristic numbers:

$$\begin{aligned} n_1 &= \frac{N_F}{2} - 2, \qquad n_1 \in \mathbb{N} \geq 1 \\ \tau_1 &= \frac{N_F \tau_{res}}{N_{wi} n_1} = \frac{\rho_w c_w A_w}{\rho_F c_F A_i} \frac{\tau_{res}}{n_1} \end{aligned} \tag{B.8}$$

Note that the order n_1 mainly depends on the collector length and process design, while the time constant τ_1 is predominantly changed by the residence time or mass flow, respectively. Thus, the order of the system can well be kept constant for a plant, while the time constant must be adapted to the current operating point. For very large collectors, such as the UltimateTrough [209], this still holds, but should be analyzed depending on the overall configuration individually. For the new DISS facility and outlet conditions of 400°C at 80 bar, we get n_1 = 1 and τ_1 = 39..89 s for a 50 m LS-3 collector, and n_1 = 3 and τ_1 = 27..63 s for a 100 m SL4600+ collector, covering the complete operating range. The heat losses are neglected in this approach, as N_{wa} does not appear anymore in the definitions of n_1 and τ_1. The problem of the definition above is that for long superheating sections the n_1 approximated poles dominate the dynamic behavior, which might result in misleading controller design assumptions. This effect is still acceptable for our purposes, but should also be analyzed individually for other system configurations.

A simpler structure is chosen by Zunft [278], who suggests a PDT_1 element and keeps the constant factor of equation (B.6):

$$G_0(\mathrm{s}) \approx \tilde{G}_{0,2}(\mathrm{s}) = e^{-N_F}\left(1 + \frac{k_2}{1 + s\tau_2}\right) \tag{B.9}$$

Again the time constant and gain can directly be derived from the characteristic numbers. They are calculated by guaranteeing equivalence in steady-state (k_2) and at amplitude of -3 dB (τ_2) [278]:

$$\begin{aligned} k_2 &= \exp\left(\frac{N_F N_{wi}}{N_{wi} + N_{wa}}\right) - 1 \\ \frac{1}{\tau_2} &= \frac{N_{wi} + N_{wa}}{\tau_{res}}\left(\frac{1}{\ln\sqrt{2}}\frac{N_F N_{wi}}{N_{wi} + N_{wa}} - 1\right) \end{aligned} \tag{B.10}$$

Note that by separating the (very small) constant term in equation (B.9) leads to a very high gain k_2. For the new DISS facility at conditions like above, we get k_2 = 51..100 and τ_2 = 32..68 s for a 50 m LS-3 collector, and k_2 = 3140..12'300 and τ_2 = 48..102 s for a 100 m SL4600+ collector for the operating range. Considering $\tilde{G}_{0,2}$ as of [278] completely, we learn that the high gain is compensated by the first constant term and that the resulting transfer function can be further simplified. When neglecting the heat loss, we see that $k_2 \to (e^{N_F} - 1)$ such that

$$G_0(\mathrm{s}) \approx \tilde{G}_{0,2}(\mathrm{s}) \approx \tilde{G}_{0,3}(\mathrm{s}) = \frac{1 + s(\tau_2 e^{-N_F})}{1 + s\tau_2} \tag{B.11}$$

The gain of $\tilde{G}_{0,2}$ is now replaced by one.

The approximation by [278] can also be interpreted as first order element with an additional very fast zero. For large values of N_F, the zero is too fast to be relevant for CSP applications. In consequence, for superheater parabolic troughs with a length greater than 100 m, we can simplify the approximation to a simple first order element:

$$G_0(\mathrm{s}) \approx \tilde{G}_{0,2}(\mathrm{s}) \approx \tilde{G}_{0,4}(\mathrm{s}) = \frac{e^{-N_F \frac{N_{wa}}{N_{wi}+N_{wa}}}}{1 + s\tau_2} \approx \frac{1}{1 + s\tau_2} \tag{B.12}$$

Its gain is one, if we assume heat losses to be negligible. Vice versa, we can use the idea to modify the approach $\tilde{G}_{0,1}$ of Eck [57, 139] by considering heat losses and guaranteeing steady state equivalence:

$$\begin{aligned} G_0(\mathrm{s}) &\approx \tilde{G}_{0,5}(\mathrm{s}) = \frac{k_1}{(1 + s\tau_1)^{n_1}} \\ k_1 &= e^{-N_F \frac{N_{wa}}{N_{wi}+N_{wa}}} \end{aligned} \tag{B.13}$$

Time constant τ_1 and order n_1 are the same as in equation (B.8). This formulation is recommended for the transfer function approximation to be used for G_ϑ in equation (B.1). Because of the significant change in heat capacity in the superheating section, we also have to consider another change in the gain:

$$G_\vartheta(\mathrm{s}) = \frac{\Delta\vartheta_{out}}{\Delta\vartheta_{in}} \approx f_{cp}\frac{c_{p,in}}{c_{p,out}}G_t(\mathrm{s}) = f_{cp}\frac{c_{p,in}}{c_{p,out}}k_1\frac{1}{(1+s\tau_1)^{n_1}}e^{-s\tau_{res}} \tag{B.14}$$

We use definitions of equations (B.8) and (B.13). The factor f_{cp} is 1 in [57] and 0.9 in [139].

With this temperature transfer function, we can also formulate the transfer functions for mass flow and irradiance. The change in irradiation to outlet temperature is [139]:

$$G_{DNI}(\mathrm{s}) = \frac{\Delta\vartheta_{out}}{\Delta G_{eff}} = f_I\frac{c_{p,m}}{c_{p,out}}\frac{w_{ap}\eta_{opt}}{\alpha_{i,m}U_i\tau_{res}}\frac{N_{wi}N_F}{N_{wi}+N_F}\frac{1}{s\left(1+s\frac{\tau_{res}}{N_{wi}+N_F}\right)}(1-G_t(\mathrm{s})) \tag{B.15}$$

And the transfer function from mass flow changes after the injection to outlet temperature is [57]:

$$G_M(\mathrm{s}) = \frac{\Delta\vartheta_{out}}{\Delta\dot{m}_{in}} = -f_M\frac{c_{p,m}}{c_{p,out}}\frac{L_{coll}w_{ap}\eta_{opt}DNI}{c_{p,m}\dot{m}_{in}^2\tau_{res}}\frac{N_{wi}}{N_{wi}+N_F}\frac{1+s\frac{(1-m)\tau_{res}}{N_{wi}}}{s\left(1+s\frac{\tau_{res}}{N_{wi}+N_F}\right)}(1-G_t(\mathrm{s})) \tag{B.16}$$

The factors f_{I} and f_{M} are 0.95 in [139] for a Eurotrough collector. The variable m is the exponent of a Nusselt correlation as derived in [57] to represent the dependency of heat transfer coefficient on mass flow. It can be approximated by 0.8 [57].

Note that the temperature transfer function is present in the mass flow and irradiation transfer function as well. The latter ones both have the same poles. They are characterized by an integrator ($1/s$) and first order delay corresponding to heat transfer characteristics. The mass flow transfer function has an additional zero depending on the change in heat transfer by mass flow. Also mind the negative sign of $G_{\mathrm{M}}(\mathrm{s})$, as a higher mass flow leads to a lower outlet temperature.

The deadtime of $G_{\mathrm{t}}(\mathrm{s})$ is usually approximated by a simple Padé approximation for simplification:

$$e^{-s\tau_{res}} \approx \frac{1-s\frac{\tau_{res}}{2}}{1+s\frac{\tau_{res}}{2}} \tag{B.17}$$

The three transfer functions are fully parameterized based on steady-state energy balances and geometries. They are good approximations for small changes, but care must be taken for strong variations or long simulations.

C Annex: Identified LTI model parameters

The identified linear time-invariant models are explained in chapter 3.4. The following tables list the main parameters. For each model one nominal case is chosen and the minimum and maximum values of all models are given as well. They are all derived for the DISS test facility at nominal conditions of 260°C at the inlet, 400°C and 80 bar at the outlet.

Table C.1: Superheater injection mass flow to outlet temperature, 3 poles and 2 zeros (nominal chosen as -10 %).

DNI $[W/m^2]$		$M_{afterInj}$	k_p	τ_1	δ_1	τ_2	τ_{z1}	δ_{z1}
375	Nom.	0.59	-1011.7	168	0.698	257	71	-0.217
	Min.	0.58	-1032.0	155	0.600	230	71	-0.307
	Max.	0.60	-981.9	169	0.719	278	80	-0.217
450	Nom.	0.72	-844.1	134	0.775	184	58	-0.259
	Min.	0.71	-862.8	126	0.608	179	56	-0.273
	Max.	0.74	-816.7	138	0.784	230	83	0.068
525	Nom.	0.85	-724.0	112	0.794	158	58	0.000
	Min.	0.84	-741.1	107	0.622	156	45	-0.231
	Max.	0.87	-699.1	119	0.794	197	63	0.040
600	Nom.	0.98	-633.6	102	0.878	113	48	-0.013
	Min.	0.97	-649.3	93	0.713	106	38	-0.193
	Max.	1.00	-610.9	129	0.878	156	49	0.074
675	Nom.	1.11	-563.3	91	0.904	98	38	-0.044
	Min.	1.09	-577.7	83	0.739	78	32	-0.053
	Max.	1.14	-542.5	106	0.909	135	41	0.188
750	Nom.	1.24	-507.0	88	0.928	73	32	-0.051
	Min.	1.22	-520.2	76	0.783	65	31	-0.061
	Max.	1.27	-487.9	97	0.936	117	37	0.015
825	Nom.	1.37	-460.9	91	0.915	49	27	-0.043
	Min.	1.35	-473.2	69	0.735	43	24	-0.063
	Max.	1.41	-443.3	94	0.944	120	30	0.269
900	Nom.	1.50	-422.5	87	0.922	36	24	-0.045
	Min.	1.48	-433.9	64	0.805	35	23	-0.061
	Max.	1.54	-406.2	90	0.948	80	26	0.270
975	Nom.	1.64	-390.0	85	0.917	24	22	0.038
	Min.	1.61	-400.6	70	0.842	24	20	-0.057
	Max.	1.67	-374.8	87	0.956	52	23	0.238

Table C.2: Evaporator injection mass flow to temperature before injection, 4 poles/ 1 zero (nominal chosen as -20 %).

DNI $[W/m^2]$		$M_{afterInj}$	k_p	τ_1	δ_1	τ_2	δ_2	τ_{z1}
375	Nom.	0.566	-970.3	69	0.481	137	0.890	6
	Min.	0.566	-970.3	67	0.410	128	0.884	5
	Max.	0.571	-961.1	94	0.514	183	0.900	109
450	Nom.	0.691	-816.7	58	0.452	121	0.885	18
	Min.	0.683	-827.2	51	0.403	108	0.877	7
	Max.	0.708	-792.4	71	0.502	137	0.890	53
525	Nom.	0.815	-704.6	48	0.437	107	0.869	17
	Min.	0.807	-714.1	44	0.412	97	0.868	14
	Max.	0.836	-682.7	68	0.547	138	0.926	97
600	Nom.	0.940	-619.3	43	0.429	99	0.866	25
	Min.	0.930	-627.9	41	0.404	92	0.860	24
	Max.	0.963	-599.3	55	0.527	140	0.911	137
675	Nom.	1.065	-552.5	40	0.416	96	0.855	33
	Min.	1.054	-560.6	38	0.416	87	0.855	33
	Max.	1.092	-533.8	47	0.556	123	0.899	115
750	Nom.	1.190	-498.6	38	0.473	102	0.859	67
	Min.	1.177	-506.0	36	0.436	92	0.859	56
	Max.	1.219	-481.5	41	0.519	119	0.911	112
825	Nom.	1.315	-454.2	35	0.509	97	0.866	72
	Min.	1.301	-461.2	33	0.471	92	0.860	65
	Max.	1.347	-438.3	39	0.630	110	0.929	122
900	Nom.	1.440	-417.1	32	0.494	94	0.861	70
	Min.	1.425	-423.7	30	0.454	92	0.861	67
	Max.	1.476	-402.2	33	0.527	103	0.909	99
975	Nom.	1.565	-385.6	30	0.481	94	0.863	74
	Min.	1.549	-391.8	27	0.426	91	0.863	72
	Max.	1.604	-371.7	31	0.524	107	0.939	124

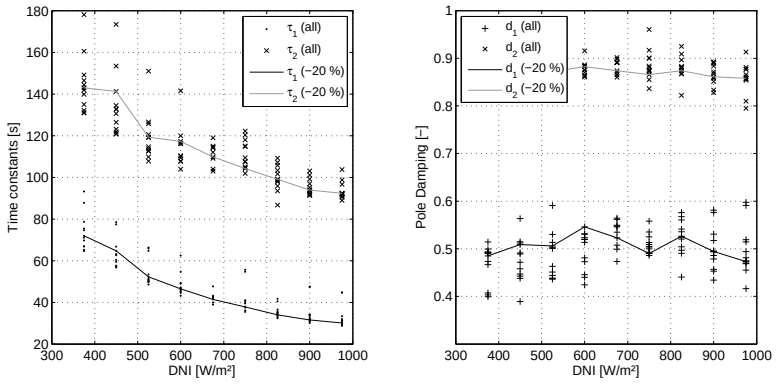

Figure C.1: Pole parameters for evaporation injection to temperature before injection.

Table C.3: Evaporator injection mass flow to outlet temperature, 4 poles/ 3 zeros (nominal chosen as -20 %).

DNI [W/m²]		$M_{afterInj}$	k_p	τ_1	δ_1	τ_2	δ_2	τ_{z1}	δ_{z1}	τ_{z2}
375	Nom.	0.566	-970.3	163	0.53	270	0.91	-374	-0.39	-19
	Min.	0.560	-981.2	147	0.48	241	0.82	-422	-0.40	-24
	Max.	0.580	-944.5	189	0.69	291	0.98	-346	-0.34	-11
450	Nom.	0.691	-816.7	132	0.55	224	0.91	-313	-0.37	-15
	Min.	0.683	-827.2	121	0.50	206	0.81	-348	-0.38	-19
	Max.	0.708	-792.4	136	0.68	245	0.93	-288	-0.35	-5
525	Nom.	0.815	-704.6	111	0.57	190	0.91	-270	-0.36	-12
	Min.	0.807	-714.1	99	0.48	158	0.81	-303	-0.37	-16
	Max.	0.836	-682.7	121	0.67	213	0.97	-250	-0.32	-7
600	Nom.	0.940	-619.3	94	0.59	169	0.90	-243	-0.34	-11
	Min.	0.930	-627.9	72	0.55	133	0.76	-262	-0.35	-13
	Max.	0.963	-599.3	105	0.70	199	0.97	-223	-0.30	-8
675	Nom.	1.065	-552.5	81	0.63	149	0.90	-219	-0.33	-11
	Min.	1.054	-560.6	77	0.60	131	0.87	-274	-0.33	-14
	Max.	1.092	-533.8	97	0.65	152	0.92	-206	-0.26	-8
750	Nom.	1.190	-498.6	73	0.67	131	0.90	-204	-0.31	-13
	Min.	1.177	-506.0	60	0.61	110	0.86	-211	-0.31	-14
	Max.	1.219	-481.5	83	0.73	146	0.92	-188	-0.29	-9
825	Nom.	1.315	-454.2	63	0.70	121	0.89	-193	-0.29	-13
	Min.	1.301	-461.2	57	0.60	115	0.85	-200	-0.29	-14
	Max.	1.347	-438.3	65	0.70	133	0.92	-177	-0.27	-6
900	Nom.	1.440	-417.1	58	0.71	112	0.89	-185	-0.27	-10
	Min.	1.425	-423.7	51	0.58	84	0.72	-261	-0.27	-14
	Max.	1.476	-402.2	84	0.95	124	0.95	-168	-0.20	-4
975	Nom.	1.565	-385.6	53	0.80	101	0.89	-178	-0.25	-10
	Min.	1.549	-391.8	39	0.53	82	0.80	-282	-0.25	-11
	Max.	1.604	-371.7	69	0.88	129	0.89	-167	-0.16	-3

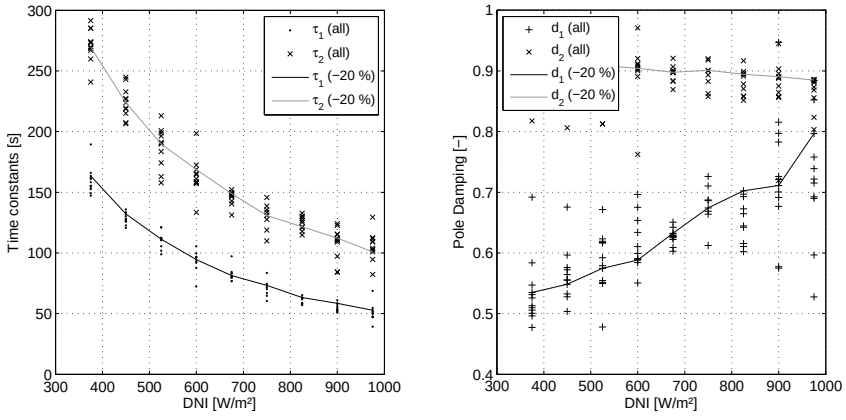

Figure C.2: Pole parameters for evaporation injection to outlet temperature.

Table C.4: Inlet mass flow to temperature before injection, 5 poles/ 2 zeros (nominal chosen as +2 %).

DNI [W/m²]		M_{inlet}	k_p	τ_1	δ_1	τ_2	δ_2	τ_3	τ_{z1}	δ_{z1}
375	Nom.	0.561	-786.6	163	0.25	281	0.62	397	-289	-0.52
	Min.	0.495	-944.2	143	0.24	247	0.62	352	-605	-0.57
	Max.	0.605	-696.5	196	0.31	320	0.65	693	-262	-0.22
450	Nom.	0.684	-649.7	136	0.27	232	0.64	320	-243	-0.49
	Min.	0.604	-786.5	118	0.22	208	0.59	303	-728	-0.54
	Max.	0.738	-573.4	168	0.29	273	0.65	600	-221	-0.17
525	Nom.	0.808	-553.1	116	0.24	200	0.62	280	-240	-0.45
	Min.	0.713	-673.7	102	0.22	179	0.57	218	-532	-0.53
	Max.	0.872	-486.9	139	0.42	235	0.76	528	-195	-0.21
600	Nom.	0.932	-481.2	100	0.24	176	0.63	244	-203	-0.47
	Min.	0.823	-588.8	88	0.23	155	0.55	223	-414	-0.54
	Max.	1.005	-422.8	120	0.30	207	0.66	469	-166	-0.24
675	Nom.	1.055	-425.6	89	0.26	156	0.63	215	-176	-0.48
	Min.	0.931	-522.5	78	0.22	138	0.54	195	-412	-0.53
	Max.	1.138	-373.4	107	0.29	188	0.66	424	-145	-0.21
750	Nom.	1.179	-381.3	83	0.27	142	0.65	190	-166	-0.43
	Min.	1.041	-469.6	72	0.23	126	0.53	175	-267	-0.49
	Max.	1.272	-334.1	106	0.29	181	0.66	396	1030	0.07
825	Nom.	1.303	-345.3	76	0.27	131	0.65	173	-167	-0.41
	Min.	1.150	-426.1	66	0.20	115	0.51	158	-606	-0.48
	Max.	1.406	-302.2	91	0.31	160	0.68	357	-126	-0.12
900	Nom.	1.427	-315.3	69	0.27	121	0.64	160	-140	-0.46
	Min.	1.259	-389.9	62	0.20	108	0.51	147	-510	-0.46
	Max.	1.539	-275.7	86	0.29	151	0.66	333	-124	-0.13
975	Nom.	1.552	-289.9	70	0.33	113	0.70	139	-176	-0.28
	Min.	1.369	-359.2	59	0.19	102	0.50	139	-675	-0.43
	Max.	1.673	-253.2	79	0.33	141	0.70	308	-139	-0.09

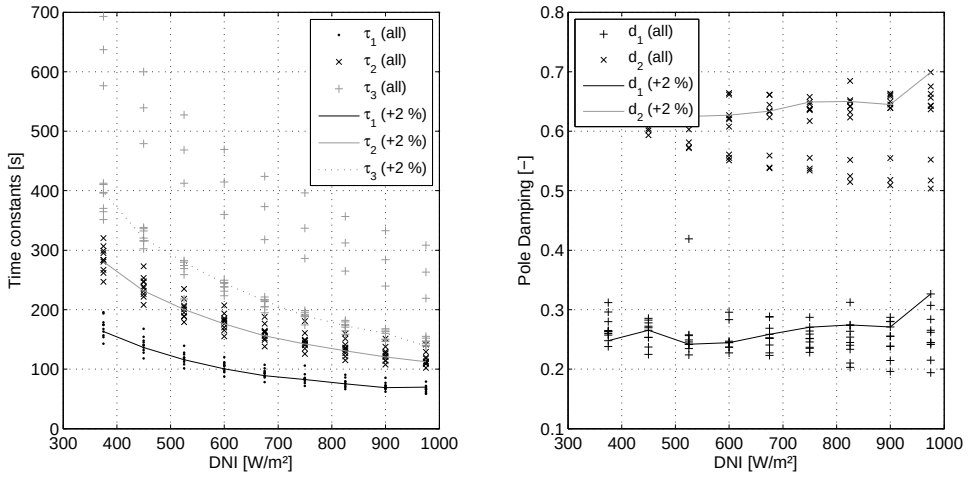

Figure C.3: Pole parameters for inlet mass flow to temperature before injection.

Table C.5: Inlet mass flow to outlet temperature, 5 poles/ 2 zeros (nominal chosen as +2 %).

DNI [W/m²]		M_{inlet}	k_p	τ_1	δ_1	τ_2	δ_2	τ_3	τ_{z1}	δ_{z1}
375	Nom.	0.561	-941.5	237	0.27	399	0.65	563	-327	-0.62
	Min.	0.495	-1052.8	204	0.25	353	0.63	509	-637	-0.67
	Max.	0.605	-861.5	309	0.33	507	0.71	839	-310	-0.28
450	Nom.	0.684	-790.1	195	0.29	328	0.66	454	-263	-0.61
	Min.	0.604	-898.3	169	0.26	291	0.63	416	-608	-0.66
	Max.	0.738	-718.1	258	0.34	405	0.72	695	-252	-0.22
525	Nom.	0.808	-680.5	167	0.29	280	0.66	386	-228	-0.59
	Min.	0.713	-782.9	144	0.26	250	0.63	358	-519	-0.66
	Max.	0.872	-615.5	219	0.33	345	0.70	614	-213	-0.22
600	Nom.	0.932	-597.2	145	0.28	249	0.65	346	-194	-0.60
	Min.	0.823	-693.3	125	0.27	216	0.64	305	-423	-0.66
	Max.	1.005	-538.2	190	0.32	301	0.68	551	-183	-0.23
675	Nom.	1.055	-532.1	129	0.29	221	0.66	306	-170	-0.61
	Min.	0.931	-622.0	111	0.26	194	0.63	279	-406	-0.66
	Max.	1.138	-478.3	168	0.32	269	0.67	502	-158	-0.21
750	Nom.	1.179	-479.8	117	0.30	198	0.67	270	-150	-0.59
	Min.	1.041	-564.0	100	0.27	175	0.63	249	-730	-0.65
	Max.	1.272	-430.3	151	0.33	244	0.67	461	-141	-0.09
825	Nom.	1.303	-436.8	108	0.30	182	0.67	246	-142	-0.57
	Min.	1.150	-515.8	91	0.27	159	0.62	225	-752	-0.64
	Max.	1.406	-391.1	138	0.33	225	0.69	429	-127	-0.08
900	Nom.	1.427	-400.9	98	0.30	167	0.67	227	-125	-0.60
	Min.	1.315	-449.3	84	0.28	146	0.61	205	-162	-0.63
	Max.	1.539	-358.4	113	0.32	190	0.69	350	-116	-0.37
975	Nom.	1.552	-370.4	92	0.34	152	0.70	200	-113	-0.54
	Min.	1.430	-415.9	79	0.28	136	0.60	190	-141	-0.60
	Max.	1.673	-330.8	105	0.34	177	0.70	326	-110	-0.38

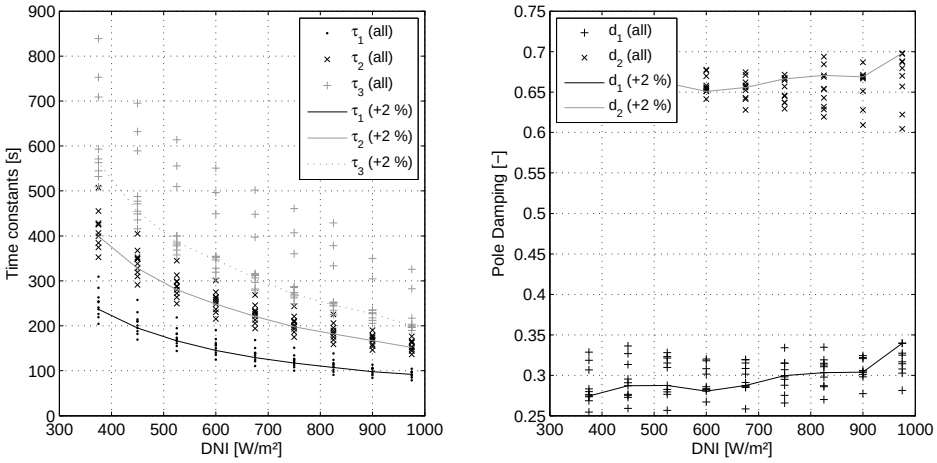

Figure C.4: Pole parameters for inlet mass flow to outlet temperature.

Table C.6: DNI to outlet temperature, 5 poles/ 4 zeros (nominal chosen as -6 %).

DNI *[W/m²]*		M_{out}	k_p	τ_1	δ_1	τ_2	δ_2	τ_3	τ_{z1}	δ_{z1}	τ_{z2}	δ_{z2}
375	Nom.	0.592	1.7	201	0.16	395	0.43	876	-721	-0.20	-617	-0.39
	Min.	0.592	1.6	182	0.15	336	0.42	624	-1200	-0.29	-1331	-0.54
	Max.	0.592	1.7	207	0.19	432	0.50	1186	-498	-0.12	-449	-0.19
450	Nom.	0.723	1.4	177	0.26	314	0.61	484	-515	-0.24	-506	-0.39
	Min.	0.723	1.3	149	0.22	289	0.56	425	-690	-0.29	-1055	-0.53
	Max.	0.723	1.5	183	0.28	333	0.62	679	-414	-0.18	-379	-0.20
525	Nom.	0.854	1.2	154	0.28	268	0.65	383	-447	-0.24	-454	-0.38
	Min.	0.854	1.2	132	0.24	235	0.61	349	-548	-0.29	-900	-0.51
	Max.	0.854	1.3	159	0.29	273	0.65	542	-355	-0.19	-330	-0.20
600	Nom.	0.986	1.1	135	0.29	232	0.67	322	-430	-0.21	-411	-0.36
	Min.	0.986	1.0	116	0.24	206	0.60	301	-526	-0.31	-587	-0.56
	Max.	0.986	1.1	136	0.30	233	0.67	463	-292	-0.18	-295	-0.25
675	Nom.	1.117	1.0	121	0.31	207	0.68	281	-413	-0.19	-382	-0.35
	Min.	1.117	0.9	103	0.25	183	0.61	266	-493	-0.27	-737	-0.48
	Max.	1.117	1.0	121	0.31	214	0.68	431	-293	-0.17	-273	-0.19
750	Nom.	1.248	0.9	108	0.31	187	0.68	252	-364	-0.20	-358	-0.35
	Min.	1.248	0.8	93	0.25	166	0.59	238	-474	-0.25	-656	-0.46
	Max.	1.248	0.9	108	0.31	195	0.68	395	-278	-0.16	-258	-0.20
825	Nom.	1.379	0.8	99	0.32	171	0.69	226	-379	-0.17	-365	-0.31
	Min.	1.379	0.7	85	0.25	151	0.58	216	-460	-0.25	-681	-0.44
	Max.	1.379	0.8	99	0.32	180	0.69	364	-265	-0.15	-246	-0.17
900	Nom.	1.511	0.7	91	0.33	157	0.69	207	-360	-0.17	-348	-0.31
	Min.	1.511	0.7	78	0.26	140	0.57	198	-451	-0.23	-609	-0.42
	Max.	1.511	0.8	91	0.33	166	0.69	338	-258	-0.14	-239	-0.18
975	Nom.	1.642	0.7	83	0.33	145	0.69	192	-333	-0.17	-338	-0.30
	Min.	1.642	0.6	73	0.26	130	0.56	183	-487	-0.22	-592	-0.39
	Max.	1.642	0.7	83	0.35	155	0.70	315	-253	-0.12	-240	-0.18

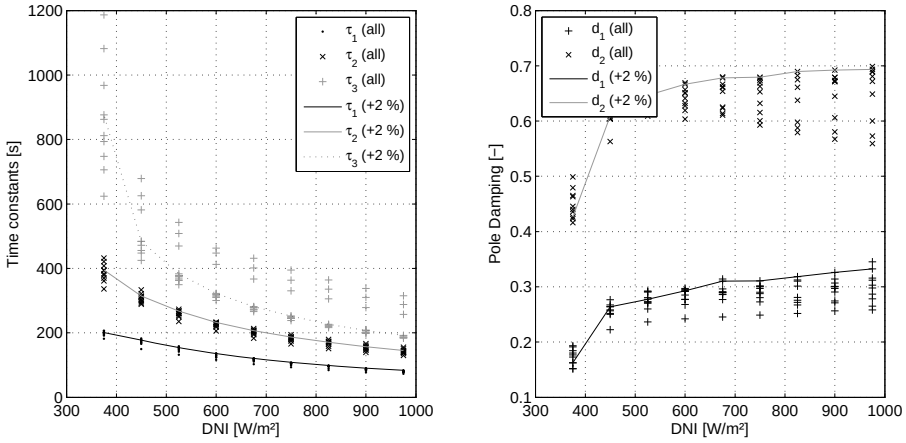

Figure C.5: Pole parameters for DNI to outlet temperature.
(Plot_lti_identeval_dni_Tout_p5z4_PolesTandD_DNI)

Table C.7: DNI to temperature before injection, 5 poles/ 4 zeros (nominal chosen as -4 %).

DNI *[W/m²]*		$M_{befSHInj}$	k_p	τ_1	δ_1	τ_2	δ_2	τ_3	τ_{z1}	δ_{z1}	τ_{z2}	δ_{z2}
375	Nom.	0.570	1.3	144	0.26	249	0.63	356	-286	-0.27	-443	-0.42
	Min.	0.570	1.3	144	0.26	249	0.62	353	-821	-0.32	-702	-0.42
	Max.	0.570	1.4	171	0.35	279	0.65	630	148	0.59	14	0.00
450	Nom.	0.696	1.1	120	0.25	209	0.62	296	-248	-0.25	-409	-0.39
	Min.	0.696	1.1	120	0.25	209	0.60	285	-540	-0.33	-593	-0.40
	Max.	0.696	1.2	138	0.33	232	0.67	537	56	0.68	9	0.00
525	Nom.	0.821	0.9	101	0.26	177	0.63	248	-198	-0.27	-378	-0.37
	Min.	0.821	0.9	101	0.26	177	0.57	248	-755	-0.29	-458	-0.37
	Max.	0.821	1.0	118	0.30	208	0.66	476	51	0.50	10	0.00
600	Nom.	0.947	0.8	88	0.27	155	0.64	213	-178	-0.24	-348	-0.36
	Min.	0.947	0.8	88	0.27	155	0.56	211	-438	-0.29	-383	-0.36
	Max.	0.947	0.9	98	0.33	172	0.69	346	1090	0.03	11	0.00
675	Nom.	1.073	0.7	79	0.28	140	0.65	190	-191	-0.19	-339	-0.34
	Min.	1.073	0.7	79	0.28	140	0.56	179	-510	-0.28	-359	-0.35
	Max.	1.073	0.8	96	0.37	181	0.70	405	-191	-0.07	5	0.00
750	Nom.	1.198	0.6	71	0.26	126	0.63	174	-180	-0.20	-331	-0.32
	Min.	1.198	0.6	71	0.26	126	0.54	169	-4126	-0.27	-369	-0.34
	Max.	1.198	0.7	90	0.33	176	0.68	395	480	0.53	-11	0.00
825	Nom.	1.324	0.6	64	0.28	114	0.65	154	-182	-0.17	-319	-0.31
	Min.	1.324	0.6	64	0.21	114	0.52	154	-3663	-0.23	-361	-0.34
	Max.	1.324	0.6	84	0.32	168	0.68	384	355	0.08	-10	0.00
900	Nom.	1.450	0.5	60	0.30	106	0.67	140	-351	-0.07	-330	-0.28
	Min.	1.450	0.5	59	0.27	106	0.54	140	-467	-0.23	-384	-0.30
	Max.	1.450	0.6	77	0.33	158	0.68	375	225	0.67	-9	0.00
975	Nom.	1.576	0.5	57	0.28	101	0.65	135	-2009	-0.01	-374	-0.23
	Min.	1.576	0.5	52	0.27	100	0.54	127	-2009	-0.23	-377	-0.28
	Max.	1.576	0.5	73	0.36	150	0.69	385	389	0.39	-9	0.00

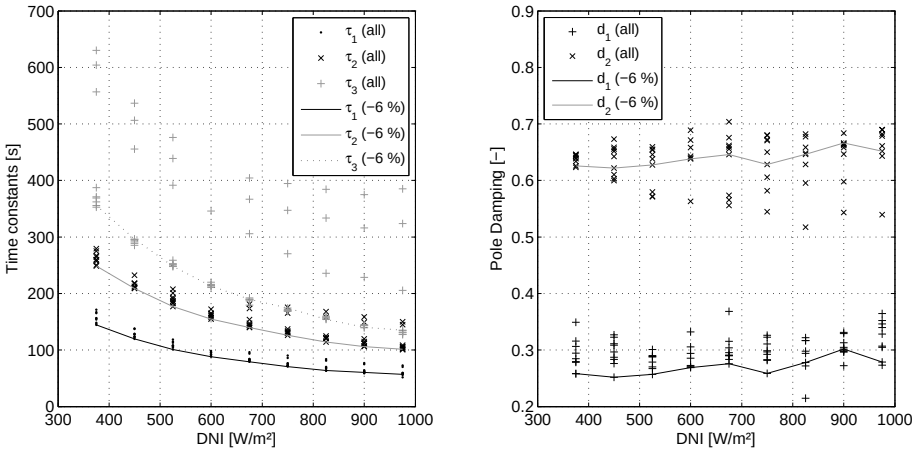

Figure C.6: Pole parameters for DNI to temperature before superheating injection. (Plot_lti_identeval_dni_TbefInj_p5z4_PolesTandD_DNI)

D Annex: Procedure for categorization of DNI classes

The determination of the disturbance or DNI class, respectively, is performed automatically from the data. The accuracy has been validated visually for 60 days of the year 2013 based on 10 s data from PSA. A general applicability cannot be guaranteed and the procedure must be treated as a first start for DNI categorization. The procedure is implemented and shown here in Matlab® code. Comments are given after the % symbol. First, the different values of the criteria variables are determined for each hour. Second, a procedure from visual inspection is performed, which step by step checks for classes. This does not completely cover all cases. Therefore, the third rigorous step categorizes the remaining cases to cover 100 % of the hours. From the 2013 data, about 90 % of the hours are categorized by the second step, while only about 10 % require the rigorous procedure.

Mind that curly brackets for structs are replaced in the code by the following definition: ## starts the struct index and !! ends a struct.

```
% The variable nh is the number of hours of the considered day.
% Each hour is categorized on its own with index kkk.
% The incidence angle modifier of a EuroTrough collector is used (variable IAM.et)
% The 10 s DNI data is stored in the variable DNI_data.
% The indices indcl##kkk!! and indcscl##kkk!! represent the elements of hour kkk within the variables.
% The filter transfer functions are stored in structs tf (slow filter) and tf2 (fast filter).

% Definition of the variables for discriminating the classes:
cat_meanGeff(kkk,1) = mean(DNI_data(indcl##kkk!!).*IAM.et(indcl##kkk!!)); % in W/m²
cat_meanRelDNI(kkk,1) = mean(rel_DNI(indcscl##kkk!!)); % in -
cat_minRelDNI(kkk,1) = min(rel_DNI(indcscl##kkk!!)); % in -
cat_FiltDiff##kkk,1!! = abs(tf.rel_DNI(indcscl##kkk,1!!)-tf2.rel_DNI(indcscl##kkk,1!!)); % in -, vector
cat_maxFiltDiff(kkk,1) = max(cat_FiltDiff##kkk!!); % -
cat_meanFiltDiff(kkk,1) = mean(cat_FiltDiff##kkk!!); % -
cat_minSlowFilt(kkk,1) = min(tf.rel_DNI(indcscl##kkk,1!!)); % -

 if cat_meanRelDNI(kkk,1) >= 0.99 && cat_maxFiltDiff(kkk,1) <= 0.01
    cat_class(kkk,1) = 1; % 1 = A
    cat_className(kkk,1) = 'A';
 elseif cat_meanRelDNI(kkk,1) >= 0.96 && cat_maxFiltDiff(kkk,1) <= 0.05 ...
    && cat_minRelDNI(kkk,1) >=0.9
    cat_class(kkk,1) = 2; % 2 = B
    cat_className(kkk,1) = 'B';
 elseif cat_meanRelDNI(kkk,1) >= 0.96 && cat_maxFiltDiff(kkk,1) <= 0.1 ...
    && cat_minRelDNI(kkk,1) <=0.75
    cat_class(kkk,1) = 3; % 3 = C
    cat_className(kkk,1) = 'C';
```

```
elseif cat_meanRelDNI(kkk,1) >= 0.91 && cat_maxFiltDiff(kkk,1) <= 0.1 ...
   && cat_meanFiltDiff(kkk,1) < 0.03
   cat_class(kkk,1) = 4; % 4 = D
   cat_className(kkk,1) = 'D';
elseif cat_meanRelDNI(kkk,1) >= 0.85 && cat_maxFiltDiff(kkk,1) <= 0.25 ...
   && cat_meanFiltDiff(kkk,1) < 0.08
   cat_class(kkk,1) = 5; % 5 = E
   cat_className(kkk,1) = 'E';
elseif cat_meanRelDNI(kkk,1) >= 0.85 && cat_maxFiltDiff(kkk,1) <= 0.36 ...
   && cat_meanFiltDiff(kkk,1) < 0.11
   cat_class(kkk,1) = 6; % 6 = F
   cat_className(kkk,1) = 'F';
elseif cat_meanRelDNI(kkk,1) >= 0.5 && cat_maxFiltDiff(kkk,1) <= 0.5 ...
   && cat_meanFiltDiff(kkk,1) < 0.16
   cat_class(kkk,1) = 7; % 7 = G
   cat_className(kkk,1) = 'G';
elseif cat_meanRelDNI(kkk,1) >= 0.85 && cat_maxFiltDiff(kkk,1) > 0.45 ...
   && cat_minRelDNI(kkk,1) < 0.2 && cat_fractLrelDNI(kkk,1) > 3.5
   cat_class(kkk,1) = 8; % 8 = H
   cat_className(kkk,1) = 'H';
elseif cat_meanRelDNI(kkk,1) >= 0.6 && cat_maxFiltDiff(kkk,1) > 0.36 ...
   && cat_minRelDNI(kkk,1) < 0.3 && cat_fractLrelDNI(kkk,1) > 6
   cat_class(kkk,1) = 10; % 10 = K
   cat_className(kkk,1) = 'K';
elseif cat_meanRelDNI(kkk,1) < 0.6 && cat_maxFiltDiff(kkk,1) > 0.45 ...
   && cat_minRelDNI(kkk,1) < 0.2 && cat_meanFiltDiff(kkk,1) > 0.15 % besser FractL
   cat_class(kkk,1) = 9; % 9 = J
   cat_className(kkk,1) = 'J';
elseif cat_meanRelDNI(kkk,1) <= 0.2 && cat_minRelDNI(kkk,1) < 0.1
   cat_class(kkk,1) = 11; % 11 = Z
   cat_className(kkk,1) = 'Z';
else
   cat_class(kkk,1) = 0; % ?
   cat_className(kkk,1) = '?';
end

% Rigorous categorization
if strcmp(cat_className(kkk,1),'?')
   cat_secondtry = cat_secondtry+1;
   if cat_minSlowFilt(kkk,1) > 0.95
      cat_class(kkk,1) = 4;
      cat_className(kkk,1) = 'D';
   elseif cat_minSlowFilt(kkk,1) > 0.75 % E, F, H
      if cat_maxFiltDiff(kkk,1) < 0.2
         cat_class(kkk,1) = 5;
         cat_className(kkk,1) = 'E';
      elseif cat_maxFiltDiff(kkk,1) < 0.4
         cat_class(kkk,1) = 6;
         cat_className(kkk,1) = 'F';
      else
         cat_class(kkk,1) = 8;
         cat_className(kkk,1) = 'H';
      end
   elseif cat_minSlowFilt(kkk,1) > 0.45 % G, H, K
```

```
        if cat_maxFiltDiff(kkk,1) < 0.45
            cat_class(kkk,1) = 7;
            cat_className(kkk,1) = 'G';
        else
            if cat_meanFiltDiff(kkk,1) < 0.15
                cat_class(kkk,1) = 8;
                cat_className(kkk,1) = 'H';
            else
                cat_class(kkk,1) = 10;
                cat_className(kkk,1) = 'K';
            end
        end
    else
        if cat_meanGeff(kkk,1) > Geff_min_op
            cat_class(kkk,1) = 9;
            cat_className(kkk,1) = 'J';
        else
            cat_class(kkk,1) = 11;
            cat_className(kkk,1) = 'Z';
        end
    end
end
```

Figure D.1 shows an exemplary result for January 23, 2013 at PSA.

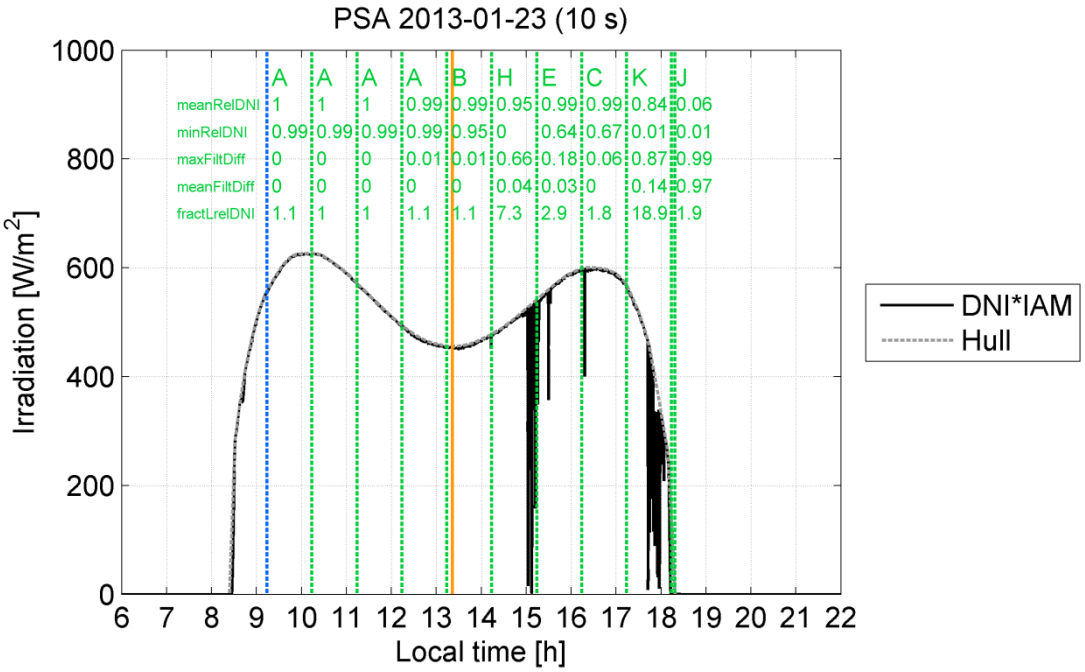

Figure D.1: Exemplary day and categorized hours after start-up with values of selection criteria. (Plot_DNI_PSA_categ_20130123)

References

[1] Adams J., Clark D. R., Louis J. R. & Spanbauer J. P.: *Mathematical Modeling of Once-Through Boiler Dynamics*. Power Apparatus and Systems, IEEE Transactions on, Vol. 84, 2 (1965) p. 146-156

[2] Adamy J.: *Nichtlineare Regelungen*. Springer-Verlag (2009)

[3] Adamy J. & Flemming A.: *Soft variable-structure controls: a survey*. Automatica, Vol. 40, 11 (2004) p. 1821-1844

[4] Alexandrov M. D., Ackerman A. S. & Marshak A.: *Cellular Statistical Models of Broken Cloud Fields. Part II: Comparison with a Dynamical Model and Statistics of Diverse Ensembles*. Journal of the Atmospheric Sciences, Vol. 67, 7 (2010) p. 2152-2170

[5] Alexandrov M. D., Marshak A. & Ackerman A. S.: *Cellular Statistical Models of Broken Cloud Fields. Part I: Theory*. Journal of the Atmospheric Sciences, Vol. 67, 7 (2010) p. 2125-2151

[6] Allgöwer F., Findeisen R. & Nagy Z. K.: *Nonlinear model predictive control: From theory to application*. Journal Chinese Institute of Chemical Engineers, Vol. 35, 3 (2004) p. 299-316

[7] Ami T., Umekawa H., Ozawa M. & Shoji M.: *Traveling void wave in horizontal two-phase flow*. International Journal of Heat and Mass Transfer, Vol. 52, 25–26 (2009) p. 5682-5690

[8] ASME (2011) Boiler and Pressure Vessel Code - Section VIII - Rules for Construction of Pressure Vessels, Division 2.

[9] Aström K. J.: *Ziegler-Nichols Auto-tuners*. CODEN: LUTFD2/TFRT-3167)/01-025 (1982)

[10] Aström K. J. & Bell R. D.: *Drum boiler dynamics*. Automatica, Vol. 36, (2000) p. 363-378

[11] Aström K. J. & Wittenmark B.: *Adaptive Control*. Addison-Wesley Publishing, 2nd edition Aufl. (1995)

[12] Baker O.: *Design of Pipelines for Simultaneous Flow of Oil and Gas*. Oil and Gas J., Vol. 7, (1954) p. 185-195

[13] Barão M., Lemos J. M. & Silva R. N.: *Reduced complexity adaptive nonlinear control of a distributed collector solar field*. Journal of Process Control, Vol. 12, 1 (2002) p. 131-141

[14] Bärmann D., Hein D., Mayinger F., Schad O. & Weiss e.: *Flow oscillations in two-phase flow, their characteristics and effects on burnout*. EURATOM Symposium of two-phase flow dynamics, Eindhoven, the Netherlands (1967)

[15] Barre F. & Bernard M.: *The CATHARE code strategy and assessment*. Nuclear Engineering and Design, Vol. 124, 3 (1990) p. 257-284

[16] Bathias C.: *There is no infinite fatigue life in metallic materials*. Fatigue & Fracture of Engineering Materials & Structures, Vol. 22, 7 (1999) p. 559-565

[17] Bauer T., Laing D., Kröner U. & Tamme R.: *Sodium nitrate for high temperature latent heat storage*. Proceedings of the 11th International Conference on Thermal Energy Storage (EffStock), Stockholm, Sweden (2009)

[18] Belblidia L. A. & Bratianu C.: *Density-wave oscillations*. Annals of Nuclear Energy, Vol. 6, 7–8 (1979) p. 425-444

[19] Benz N., Eck M., Kuckelkorn T. & Uhlig R.: *Development of Receivers for the DSG Process*. Proceedings of the 13th SolarPACES Symposium, (2006)

[20] Berenguel M., Arahal M. R. & Camacho E. F.: *Modelling the free response of a solar plant for predictive control*. Control Engineering Practice, Vol. 6, 10 (1998) p. 1257-1266

[21] Bernardini D. & Bemporad A.: *Scenario-based model predictive control of stochastic constrained linear systems*. Proceedings of the 48th IEEE Conference on Decision and Control, 2009, held jointly with the 2009 28th Chinese Control Conference, Shanghai, China (2009) p. 6333-6338

[22] Bestion D.: *The physical closure laws in the CATHARE code*. Nuclear Engineering and Design, Vol. 124, 3 (1990) p. 229-245

[23] Birnbaum J., Eck M., Fichtner M., Hirsch T., Lehmann D. & Zimmermann G.: *A Direct Steam Generation Solar Power Plant With Integrated Thermal Storage*. Journal of Solar Energy Engineering, Vol. 132, 3 (2010) p. 031014-1 - 031014-5

[24] Birnbaum J., Feldhoff J. F., Fichtner M., Hirsch T., Jöcker M., Pitz-Paal R. & Zimmermann G.: *Steam temperature stability in a direct steam generation solar power plant*. Solar Energy, Vol. 85, 4 (2011) p. 660-668

[25] Birnbaum J., Hirsch T., Eck M., Pitz-Paal R., Fichtner M. & Zimmermann G.: *A Concept for Future Parabolic Trough Based Solar Thermal Power Plants*. Proceedings of the 15th International Conference on the Properties of Water and Steam, Berlin, Germany (2008)

[26] Bongardt J.: *Theoretische Betrachtung der Komponentenermüdung eines solarthermischen Kraftwerkes mit Hilfe transienter Wärmetransportmodelle.* Master Thesis, University Koblenz-Landau / DLR Stuttgart (2014)

[27] Bonilla J., Dormido S. & Cellier F. E.: *Switching Moving Boundary Modeals for Two-phase Flow Evaporators and Condensers*. Communications in Nonlinear Science and Numerical Simulation, Vol. accepted manuscript, 0 (2014)

[28] Boure J. A., Bergles A. E. & Tong L. S.: *Review of two-phase flow instability*. Nuclear Engineering and Design, Vol. 25, 2 (1973) p. 165-192

[29] Brauner G.: *Flexibilisierung des thermischen Erzeugungsparks in Europa - Ein wichtiges Element des Klimaschutzes*. VGB PowerTech, Vol. 2010, 8 (2010) p. 32-35

[30] Bürgel R.: *Handbuch Hochtemperatur-Werkstofftechnik*. Vieweg Verlag, 3rd edition Aufl. (2006)

[31] Burkholder F. & Kutscher C.: *Heat-Loss Testing of Solel's UVAC3 Parabolic Trough Receiver.* National Renewable Energy Laboratory Report, NREL/TP-550-42394 (2008)

[32] Burkholder F. & Kutscher C.: *Heat loss testing of Schott's 2008 PTR70 Parabolic Trough Receiver.* National Renewable Energy Laboratory Report, NREL/TP-550-45633 (2009)

[33] Camacho E. F., Berenguel M. & Rubio F. R.: *Application of a gain scheduling generalized predictive controller to a solar power plant*. Control Engineering Practice, Vol. 2, 2 (1994) p. 227-238

[34] Camacho E. F., Berenguel M. & Rubio F. R.: *Advanced control of solar plants.* Advances in industrial control, Springer (1997)

[35] Camacho E. F., Rubio F. R., Berenguel M. & Valenzuela L.: *A survey on control schemes for distributed solar collector fields. Part I: Modeling and basic control approaches*. Solar Energy, Vol. 81, 10 (2007) p. 1240-1251

[36] Camacho E. F., Rubio F. R., Berenguel M. & Valenzuela L.: *A survey on control schemes for distributed solar collector fields. Part II: Advanced control approaches*. Solar Energy, Vol. 81, 10 (2007) p. 1252-1272

[37] Chen J. C.: *Correlations for boiling heat transfer to saturated fluids in convective flow*. Ind. Engng Chem. Proc. Des. Dev., Vol. 5, (1966) p. 322-329

[38] Cheng W. & Finnie I.: *Stress analysis and fatigue life prediction for a U-bend steam generator tube*. Nuclear Engineering and Design, Vol. 165, 1–2 (1996) p. 101-109

[39] Chisholm D.: *Two-phase flow in bends*. Int. J. Multiphase Flow, Vol. 6, (1980) p. 363-367
[40] Cutler C. R. & Ramaker B. L.: *Dynamic Matrix Control - A computer control algorithm*. Proceedings of the Joint Automatic Control Conference, San Fransicso, CA, USA (1980)
[41] Dersch J., Vogel T., Polklas T. & Tümmers C.: *Solar-only parabolic trough plants with high steam parameters*. Energy Procedia, Vol. 49, Proceedings of the 19th SolarPACES Conference 2013, Las Vegas, NV, USA (2014)
[42] Deutsches Institut für Normung (DIN) (2011) DIN EN 12952-4:2011-10: Water-tube boilers and auxiliary installations - Part 4: In-service boiler life expectancy calculations; German version.
[43] Deutsches Institut für Normung (DIN) (2014) DIN EN 10028-2:2014-12: Flat products made of steels for pressure purposes - Part 2: Non-alloy and alloy steels with specified elevated temperature properties; German version.
[44] Deutsches Institut für Normung (DIN) (2014) DIN EN 10216-2:2014-03: Seamless steel tubes for pressure purposes - Technical delivery conditions - Part 2: Non-alloy and alloy steel tubes with specified elevated temperature properties; German version
[45] Diehl M., Bock H. G., Schlöder J. P., Findeisen R., Nagy Z. & Allgöwer F.: *Real-time optimization and nonlinear model predictive control of processes governed by differential-algebraic equations*. Journal of Process Control, Vol. 12, 4 (2002) p. 577-585
[46] Diehl M., Ferreau H. J. & Haverbeke N.: *Efficient Numerical Methods for Nonlinear MPC and Moving Horizon Estimation.* Nonlinear Model Predictive Control, Springer Berlin/ Heidelberg, Germany (2009)
[47] Diercks D. R., Shack W. J. & Muscara J.: *Overview of steam generator tube degradation and integrity issues*. Nuclear Engineering and Design, Vol. 194, 1 (1999) p. 19-30
[48] Dimenna R. A., Larson J. R., Johnson R. W., Larson T. K., Miller C. S., Streit J. E., Hanson R. G. & Kiser D. M.: *RELAP5/MOD2 models and correlations.* Idaho National Engineering Laboratory Report, NUREG/CR-5194; EGG-2531; ON: TI88016994 (1988)
[49] Ding Y., Kakaç S. & Chen X. J.: *Dynamic instabilities of boiling two-phase flow in a single horizontal channel*. Experimental Thermal and Fluid Science, Vol. 11, 4 (1995) p. 327-342
[50] Dittmar R. & Pfeiffer B.-M.: *Modellbasierte prädiktive Regelung in der industriellen Praxis (Industrial Application of Model Predictive Control)*. at - Automatisierungstechnik, Vol. 54, 12 (2006) p. 590-601
[51] Doležal R.: *Durchlaufkessel : Theorie, Bau, Betrieb und Regelung.* Vulkan-Verlag Essen (1962)
[52] Doležal R.: *Dampferzeugung : Verbrennung, Feuerung, Dampferzeuger.* Hochschultext, Springer, Bericht. Nachdr. Aufl. Berlin (1990)
[53] Doležal R. & Varcop L.: *Process dynamics - Automatic control of steam generation plants.* Elsevier Amsterdam (1970)
[54] Dreyer S., Eichel P., Gnaedig T., Hacker Z., Janker S., Kuckelkorn T., Silmy K., Pernpeintner J. & Lüpfert E.: *Heat loss measurements on parabolic trough Receivers*. Proceedings of the 16th SolarPACES Conference, Perpignon, France (2010) p. 8
[55] Dudley V. E., Kolb G. J., Mahoney A. R., Mancini T. R., Mathews C. W., Sloan M. & Kearney D.: *Test Results - SEGS LS-2 Solar Collector.* SANDIA Report, SAND94-1884 (1994)
[56] Duffie A. J. & Beckman A. W.: *Solar Engineering of Thermal Processes* Wiley-Interscience (1991)
[57] Eck M.: *Die Dynamik der solaren Direktverdampfung und Überhitzung in Parabolrinnenkollektoren.* Fortschritts-Berichte VDI, VDI-Verlag Düsseldorf, Germany (2001)

[58] Eck M.: *Information on coating for ferritic absorber tubes.* Personal Communication (2014)
[59] Eck M. & Eberl M.: *Controller design for injection mode driven direct solar steam generating parabolic trough collectors.* ISES Solar World Congress, Jerusalem, Israel (1999)
[60] Eck M., Eickhoff M., Feldhoff J. F., Fontela P., Gathmann N., Meyer-Grünefeldt M., Hillebrand S. & Schulte-Fischedick J.: *Direct Steam Generation in parabolic troughs at 500°C - First results of the REAL-DISS project.* Proceedings of the 17th SolarPACES Conference, Granada, Spain (2011)
[61] Eck M., Feldhoff J. F., Kretschmann D., Wittmann M. & Schenk H.: *Considering Uncertainties in Research by Probabilistic Modeling.* ASME 2012 6th International Conference on Energy Sustainability, San Diego, CA, USA (2012)
[62] Eck M., Feldhoff J. F. & Uhlig R.: *Thermal Modelling and Simulation of Parabolic Trough Receiver Tubes.* Proceedings of the ASME 2010 4th International Conference on Energy Sustainability, Phoenix, Arizona USA (2010)
[63] Eck M. & Geskes P.: *Experimental investigations on the dynamic fluid behaviour in horizontal absorber tubes with direct solar steam generation.* Journal de Physique IV, (1999)
[64] Eck M. & Hirsch T.: *Dynamics and control of parabolic trough collector loops with direct steam generation.* Solar Energy, Vol. 81, 2 (2007) p. 268-279
[65] Eck M. & Steinmann W.-D.: *Dynamic Behaviour of the Direct Solar Steam Generation in Parabolic Trough Collectors: A Simulation Study.* Proceedings of the 10th SolarPACES Symposium, Sydney (2000)
[66] Eck M. & Steinmann W.-D.: *Modelling and Design of Direct Solar Steam Generating Collector Fields.* Journal of Solar Energy Engineering, Vol. 127, (2005) p. 371-380
[67] Eck M., Steinmann W.-D. & Rheinländer J.: *Maximum temperature difference in horizontal and tilted absorber pipes with direct steam generation.* Energy, Vol. 29, 5-6 (2004) p. 633-659
[68] Eck M. & Zarza E.: *Assessment of Operation Modes for Direct Solar Steam Generation in Parabolic Troughs.* Proceedings of the 11th SolarPACES Symposium, Zurich, Switzerland (2002)
[69] Eck M., Zarza E., Eickhoff M., Rheinländer J. & Valenzuela L.: *Applied research concerning the direct steam generation in parabolic troughs.* Solar Energy, Vol. 74, 4 (2003) p. 341 - 351
[70] Feldhoff J. F.: *Vergleichende Analyse und Bewertung von solarthermischen Kraftwerken mit solarer Direktverdampfung.* Diplomarbeit, RWTH Aachen (2007)
[71] Feldhoff J. F., Benitez D., Eck M. & Riffelmann K.-J.: *Economic Potential of Solar Thermal Power Plants with Direct Steam Generation compared to HTF Plants.* Proceedings of the ASME 2009 3rd International Conference of Energy Sustainability, San Fransisco, CA, USA (2009)
[72] Feldhoff J. F., Benitez D., Eck M. & Riffelmann K.-J.: *Economic Potential of Solar Thermal Power Plants With Direct Steam Generation Compared With HTF Plants.* Journal of Solar Energy Engineering, Vol. 132, 4 (2010) p. 041001-9
[73] Feldhoff J. F. & Eck M.: *Method for generating superheated steam in a solar thermal power plant.* European Patent Office, European patent No. 2454523, PCT/EP2010/057982, (2010)
[74] Feldhoff J. F., Eickhoff M., Karthikeyan R., Krüger J., León Alonso J., Meyer-Grünefeldt M., Müller M. & Valenzuela Gutierrez L.: *Concept comparison and test facility design for the analysis of direct steam generation*

in once-through mode. Proceedings of the 18th SolarPACES Conference, Marrakech, Morocco (2012)

[75] Feldhoff J. F., Eickhoff M., Keller L., Alonso J. L., Meyer-Grünefeldt M., Valenzuela L., Pernpeintner J. & Hirsch T.: *Status and First Results of the DUKE Project – Component Qualification of New Receivers and Collectors*. Energy Procedia, Vol. 49, 2014 (2014) p. 1766-1776

[76] Feldhoff J. F., Eickhoff M., Keller L., León Alonso J., Meyer-Grünefeldt M., Valenzuela Gutierrez L., Pernpeintner J. & Hirsch T.: *Status and first results of the DUKE project – Component qualification of new receivers and collectors*. 19th SolarPACES Conference, Las Vegas, NV, USA (2013)

[77] Feldhoff J. F., Hirsch T. & Pitz-Paal R.: *Modeling of the once-through concept in Direct Steam Generation plants (presentation)*. 9th SOLLAB Doctoral Colloquium, Castle of Hornberg, Germany (2013)

[78] Feldhoff J. F., Hirsch T., Pitz-Paal R. & Valenzuela L.: *Transient models and characteristics of once-through line focus Systems*. 20th SolarPACES Conference, Beijing, China (2014)

[79] Feldhoff J. F., Schmitz K., Benitez D., Laing D., Eck M. & Schnatbaum-Laumann L.: *Final results of the DETOP System Analysis*. Internal Technical DLR Report (2010)

[80] Feldhoff J. F., Schmitz K., Eck M., Schnatbaum-Laumann L., Laing D. & Ortiz-Vives F.: *Comparative System Analysis of Direct Steam Generation and Synthetic Oil Parabolic Trough Power Plants with Integrated Thermal Storage*. Proceedings of the ASME 2011 5th International Conference on Energy Sustainability, Washington, DC, USA (2011)

[81] Feldhoff J. F., Schmitz K., Eck M., Schnatbaum-Laumann L., Laing D., Ortiz-Vives F. & Schulte-Fischedick J.: *Comparative system analysis of direct steam generation and synthetic oil parabolic trough power plants with integrated thermal storage*. Solar Energy, Vol. 86, 1 (2012) p. 520-530

[82] Fernández-García A., Zarza E., Valenzuela L. & Pérez M.: *Parabolic-trough solar collectors and their applications*. Renewable and Sustainable Energy Reviews, Vol. 14, (2010) p. 1695 - 1721

[83] Findeisen R. & Allgöwer F.: *An introduction to nonlinear model predictive control*. 21st Benelux Meeting on Systems and Control, (2002)

[84] Flores A., Saez D., Araya J., Berenguel M. & Cipriano A.: *Fuzzy predictive control of a solar power plant*. Fuzzy Systems, IEEE Transactions on, Vol. 13, 1 (2005) p. 58-68

[85] Flynn D.: *Thermal Power Plant Simulation and Control*. The Institution of Electrical Engineers (2003)

[86] Forschungskuratorium Maschinenbau (FKM) (2002) Rechnerischer Festigkeitsnachweis für Maschinenbauteile aus Stahl, Eisenguss- und Aluminiumwerkstoffen, 4. erweiterte Ausgabe. VDMA-Verlag.

[87] Franke D.: *Ausschöpfen von Stellgrößenbeschränkungen mittels weicher strukturvariabler Regelung / Exhausting bounds on control by means of soft variable structure control*. at - Automatisierungstechnik, Vol. 30, 1-12 (1982) p. 348

[88] Franke D.: *Ein nichtlinearer dynamischer Regler mit adaptiven Eigenschaften (A nonlinear dynamical controller with adaptive properties)*. at - Automatisierungstechnik, Vol. 31, 1-12 (1983) p. 369

[89] Franke R., Krüger K. & Rode M.: *On-line optimization of drum boiler startup*. Proceedings of the 3rd International Modelica Conference, Linköping, Sweden (2003)

[90] Franke R. & Vogelbacher L.: *Nonlinear Model Predictive Control for Cost Optimal Startup of Steam Power Plants (Nichtlineare modellprädiktive Regelung zum kostenoptimalen Anfahren von Dampfkraftwerken)*. at - Automatisierungstechnik, Vol. 54, 12 (2006) p. 630-637

[91] Frasch J. V., Gray A., Zanon M., Ferreau H. J., Sager S., Borrelli F. & Diehl M.: *An Auto-generated Nonlinear MPC Algorithm for Real-Time Obstacle Avoidance of Ground Vehicles*. Proceedings of the 2013 European Control Conference (ECC), Zurich, Switzerland (2013)

[92] Friedel L.: *Improved friction pressure drop correlations for horizontal and vertical two-phase pipe flow*. Proceedings of the European Two-Phase Group Meeting, Ispra, Italy (1979)

[93] García C. E., Prett D. M. & Morari M.: *Model predictive control: Theory and practice—A survey*. Automatica, Vol. 25, 3 (1989) p. 335-348

[94] Geskes P.: *Zweiphasenströmung in Ringkanälen solarer Dampferzeugerrohre*. Fortschritt-Berichte VDI, VDI Verlag Düsseldorf, Germany (1998)

[95] Gnielinski V.: *New equations for heat and mass transfer in turbulent pipe and channel flow*. Int Chem Eng, Vol. 16, (1976) p. 359-368

[96] Goebel O.: *Wärmeübergang in Absorberrohren von Parabolrinnen-Solarkraftwerken*. VDI Fortschrittsberichte, VDI (1998)

[97] Goebel O., Geskes P., Geyer M., Hennecke K. & Herrmann U.: *Direkte Dampferzeugung in Parabolrinnen-Solarkraftwerken*. Forschungsverbund Solarenergie, Vol. Themen 96/97, (1997) p. 110-116

[98] Gros S., Zanon M. & Diehl M.: *Control of Airborne Wind Energy Systems Based on Nonlinear Model Predictive Control and Moving Horizon Estimation*. Proceedings of the 2013 European Control Conference (ECC), Zurich, Switzerland (2013)

[99] Gunger K. E. & Winterton R. H. S.: *A general correlation for flow boiling in tubes and annuli*. Int. J. Heat and Mass Transfer, Vol. 29, 3 (1986) p. 351-358

[100] Haber R., Jörgl H. P. & Pawlik R.: *PID-Regler mit regelfehlerabhängigen Parametern / PID-controllers with error-dependent parameters*. at - Automatisierungstechnik, Vol. 38, 1-12 (1990) p. 266

[101] Hammerstein A.: *Nichtlineare Integralgleichungen nebst Anwendungen*. Acta Mathematica, Vol. 54, 1 (1930) p. 117-176

[102] Hanel L. & Lehner J.: *Enhanced Flexibility for Steam Power Plants Via Model Based Feedforward Control*. Proceedings of the Convergence of Information Technologies and Control Methods with Power Systems, Cluj-Napoca, Romania (2013)

[103] Herrmann U.: *Untersuchungen zur Rohrwandbenetzung bei der Dampferzeugung in horizontalen und geneigten Parabolrinnen-Solarkollektoren - Flagsol Forschungsbericht*. Flagsol GmbH (2004)

[104] Herzog R. & Kägi U.: *Betriebserfahrungen mit einem Zustandsregler mit Beobachter an einer Überhitzer-Temperaturregelung*. Regelungstechnische Praxis, Vol. 26, 8 (1984) p. 351-356

[105] Hirsch T.: *Dynamische Systemsimulation und Auslegung des Abscheidesystems für die solare Direktverdampfung in Parabolrinnenkollektoren*. Fortschritt-Berichte Energietechnik, Reihe 6, No. 535, VDI Verlag Düsseldorf, Germany (2005)

[106] Hirsch T., Eck M., Blanco M., Wagner M. J. & Feldhoff J. F.: *Standardization of CSP performance model projection - latest results from the guiSmo project*. Proceedings of the ASME 2011 5th International Conference on Energy Sustainability, Washington, D.C. (2011)

[107] Hirsch T., Feldhoff J. F., Hennecke K. & Pitz-Paal R.: *Advancements in the Field of Direct Steam Generation in Linear Solar Concentrators—A Review*. Heat Transfer Engineering, Vol. 35, 3 (2013) p. 258-271

[108] Hirsch T., Feldhoff J. F. & Schenk H.: *Start-Up Modeling for Annual CSP Yield Calculations*. Journal of Solar Energy Engineering, Vol. 134, 3 (2012) p. 031004-9

[109] Hirsch T., Martin Chivilet N., Gonzalez Martinez L., Biencinto Murga M., Wilbert S., Schroedter-Homscheidt M., Chenlo F. & Feldhoff J. F.: *DNICast -*

Direct Normal Irradiance Nowcasting methods for optimized operation of concentrating solar technologies - Deliverable 2.1: Technical report on the functional requirements for the nowcasting method. DNICast Deliv. 2.1 (2014)

[110] Ho C. K., Khalsa S. S. & Kolb G. J.: *Methods for probabilistic modeling of concentrating solar power plants*. Solar Energy, Vol. 85, 4 (2011) p. 669-675

[111] Hoagg J. B. & Bernstein D. S.: *Nonminimum-Phase Zeros - Much to do about Nothing*. IEEE Control Systems Magazine, Vol. Classical control revisited, II (2007) p. 45-57

[112] Hoffmann A.: *Numerical analysis of severe slugging in parabolic trough power plants with direct steam generation (presentation)*. 11th SOLLAB Doctoral Colloquium, Melchsee-Frutt, Switzerland (2015)

[113] Hoffmann A., Merk B., Hirsch T. & Pitz-Paal R.: *Simulation of thermal fluid dynamics in parabolic trough receiver tubes with direct steam generation using the computer code ATHLET*. Kerntechnik, Vol. 79, 3 (2014) p. 175-186

[114] International Electrotechnical Commission (IEC) (1991) International Standard IEC 45-1: Steam Turbines - Part 1: Specifications.

[115] International Energy Agency: *World Energy Outlook 2014 - Executive Summary*. Vol. (2014)

[116] Janotte N.: *Requirements for Representative Acceptance Tests for the Prediction of the Annual Yield of Parabolic Trough Solar Fields.* Doctoral Thesis, RWTH Aachen and DLR Cologne (2012)

[117] Janotte N.: *Tracking quality.* Personal Communication (2014)

[118] Jensen J. M.: *Dynamic Modeling of Thermo-Fluid Systems - With focus on evaporators for refrigeration.* Technical University of Denmark (2003)

[119] Jensen J. M. & Tummescheid H.: *Moving Boundary Models for dynamic simulations of two-phase Flows*. Proceedings of the 2nd International Modelica Conference, DLR, Oberpfaffenhofen, Germany (2002) p. 235-244

[120] Johansen T. A., Hunt K. J. & Petersen I.: *Gain-scheduled control of a solar power plant*. Control Engineering Practice, Vol. 8, 9 (2000) p. 1011-1022

[121] Juuso E. K.: *Intelligent Systems Design with Linguistic Equations*. Proceedings of the GMA-Workshop Fuzzy Control, Philadelphia, Pennsylvania, USA (1999)

[122] Juuso E. K.: *Modelling and control of a solar thermal power plant*. Proceedings of the 16th IFAC World Congress, Prague, Czech Republic (2005)

[123] Juuso E. K., Balsa P. & Valenzuela L.: *Multilevel linguistic equation controller applied to a 1 MWt solar power plant*. Proceedings of the American Control Conference, Philadelphia, Pennsylvania, USA (1998) p. 3891-3895 vol.6

[124] Kakaç S., Mayinger F. & Veziroglu T. N.: *Two-Phase Flows & Heat Transfer.* Hemisphere Publ. Corp. Washington, USA (1977)

[125] Kallappa P., Holmes M. S. & Ray A.: *Life-extending control of fossil fuel power plants*. Automatica, Vol. 33, 6 (1997) p. 1101-1118

[126] Kalman R. E.: *A New Approach to Linear Filtering and Prediction Problems*. Transactions of the ASME – Journal of Basic Engineering, Vol. 82 (Series D) (1960) p. 35-45

[127] Kang H.-O., Seo J.-K., Kim Y. W., Yoon J. & Kim K.: *Structural Integrity Confirmation of a Once-through Steam Generator from the Viewpoint of Flow Instability*. Journal of Nuclear Science and Technology, Vol. 44, 1 (2007) p. 64-72

[128] Karg E.: *Zur Bestimmung von Cumulus-Größenverteilungen im Hinblick auf ein Solarturm-Kraftwerk - Aufzeigen möglicher Messmethoden und Auswertung von Landsat-Bildern.* University of Munich, Institute for Meteorology Report (1983)

[129] Kattan N., Thome J. R. & Favrat D.: *Flow Boiling in Horizontal Tubes: Part 1-Development of a Diabatic Two-Phase Flow Pattern Map*. Journal of Heat Transfer - Transactions of the ASME, Vol. 120, 2 (1998) p. 140-147

[130] Kattan N., Thome J. R. & Favrat D.: *Flow Boiling in Horizontal Tubes: Part 2-New Heat Transfer Data for Five Refrigerants*. Journal of Heat Transfer - Transactions of the ASME, Vol. 120, 2 (1998) p. 148-155
[131] Kattan N., Thome J. R. & Favrat D.: *Flow Boiling in Horizontal Tubes: Part 3-Development of a New Heat Transfer Model based on Flow Pattern*. Journal of Heat Transfer - Transactions of the ASME, Vol. 120, 2 (1998) p. 156-165
[132] Khalil H. K.: *Nonlinear Systems*. Prentice Hall (2002)
[133] Khenissi A., Krüger D. R., Hirsch T. & Hennecke K.: *Return of Experience on Transient Behavior at the DSG Solar Thermal Power Plant in Kanchanaburi, Thailand*. Energy Procedia, Vol. 69, Proceedings of the SolarPACES 2014 Conference (2015) p. 1603-1612
[134] Kipp & Zonen: *CHP1 Pyrheliometer Instruction Manual (version 0811)*. (2008)
[135] Kipp & Zonen: *Price List - Solar sensors and meteorological devices*. (2013)
[136] Klefenz G.: *Automatic Control of Steam Power Plants*. Bibliographisches Institut Wissenschaftsverlag (1986)
[137] Klefenz G.: *Die Regelung von Dampfkraftwerken*. Bibliographisches Institut Wissenschaftsverlag, 4th Aufl. Mannheim (1991)
[138] Koch S.: *Modelling and control of a solar-thermal parabolic trough DSG superheater with several parallel rows and central steam separation*. Master Thesis, (2007)
[139] Koch S., Hirsch T. & Eck M.: *Modelling and control of a solar-thermal parabolic trough DSG superheater with several parallel rows and central steam separation*. ASME Conference on Energy Sustainability 2007 (ES2007), Long Beach, CA (USA) (2007)
[140] Kosman G. & Rusin A.: *The influence of the start-ups and cyclic loads of steam turbines conducted according to European standards on the component's life*. Energy, Vol. 26, (2001) p. 1083-1099
[141] Krüger D., Krüger J., Pandian Y., O'Connell B., Feldhoff J. F., Karthikeyan R., Hempel S., Muniasamy K., Hirsch T., Eickhoff M. & Hennecke K.: *Experiences with Direct Steam Generation at the Kanchanaburi Solar Thermal Power Plant*. Proceedings of the 18th SolarPACES Conference, Marrakech, Morocco (2012)
[142] Kruger K., Franke R. & Rode M.: *Optimization of boiler start-up using a nonlinear boiler model and hard constraints*. Energy, Vol. 29, (2004) p. 2239-2251
[143] Laing D., Bahl C., Bauer T., Lehmann D. & Steinmann W.-D.: *Thermal energy storage for direct steam generation*. Solar Energy, Vol. 85, (2011) p. 627-633
[144] Laing D., Bahl C., Fiß M., Hempel M., Meyer-Grünefeldt M., Eickhoff M. & Stückle A.: *Test and evaluation of a thermal energy storage system for direct steam generation*. Proceedings of the 17th SolarPACES Conference, Granada, Spain (2011)
[145] Laing D., Bauer T., Breidenbach N., Hachmann B. & Johnson M.: *Development of high temperature phase-change-material storages*. Applied Energy, Vol. 109, 0 (2013) p. 497-504
[146] Lappalainen J., Blom H. & Juslin K.: *Dynamic process simulation as an engineering tool – A case of analysing a coal plant evaporator*. VGB PowerTech, Vol. 92, 1-2 (2012) p. 62-68
[147] Lecrique M., Tessier M., Rault A. & Testud J. L.: *Multivariable control of a steam generator - Characteristics and results*. Proceedings of the IFAC 7th Triennal World Congress, Helsinki, Finnland (1978) p. 73-80
[148] Ledinegg M.: *Instability of flow during natural and forced circulation*. Die Wärme, Vol. 61, 8 (1938) p. 891-898
[149] Lindsley D.: *Power-plant control and instrumentation - The control of boilers and HRSG systems*. The Institution of Electrical Engineers (2000)

[150] Lippke F.: *Numerische Simulation der Absorberdynamik von Parabolrinnen-Solarkraftwerken mit direkter Dampferzeugung*. Fortschritts-Berichte VDI, VDI-Verlag Düsseldorf, Germany (1994)
[151] Lippke F.: *Simulation of the Part-Load Behavior of a 30 MWe SEGS Plant*. Sandia Report (1995)
[152] Lippke F.: *Direct Steam Generation in Parabolic Trough Solar Power Plants: Numerical Investigation of the Transients and the Control of a Once-Through System*. Journal of Solar Energy Engineering, Vol. 118, 1 (1996) p. 9-14
[153] Lobón D. H.: *Multi-phase flow and heat transfer in solar receivers (presentation)*. 9th SOLLAB Doctoral Colloquium, Castle of Hornberg, Germany (2013)
[154] Lobón D. H., Valenzuela L. & Baglietto E.: *Modeling the dynamics of the multiphase fluid in the parabolic-trough solar steam generating systems*. Energy Conversion and Management, Vol. 78, 0 (2014) p. 393-404
[155] Lucia S. & Engell S.: *Robust Nonlinear Model Predictive Control of a Batch Bioreactor Using Multi-stage Stochastic Programming*. Proceedings of the 2013 European Control Conference (ECC), Zurich, Switzerland (2013)
[156] Lüpfert E.: *PARFOR - Testreport PTR Parabolic Trough Receiver 2005 - Modelling Parameters from Test Results*. DLR Report (2005)
[157] Lüpfert E., Herrmann U., Price H., Zarza E. & Kistner R.: *Towards Standard Performance Analysis for Parabolic Trough Collector Fields*. Proceedings of the 12th International Symposium on Concentrated Solar Power and Chemical Energy Technologies, Oxaca [Mexico) (2004)
[158] MacDonald P. E., Shah V. N., Ward L. W. & Ellison P. G.: *Steam Generator Tube Failures*. Idaho National Engineering Laboratory Report (1996)
[159] Maciejowski J. M.: *Predictive Control with Constraints*. Prentice Hall (2002)
[160] Mandelbrot B.: *How Long Is the Coast of Britain? Statistical Self-Similarity and Fractional Dimension*. Science, Vol. 156, (1967) p. 636-638
[161] Marsik J. & Fortova A.: *Eine neue einfache Methode der Berechnung von Übergangsfunktionen eines Dampferhitzers*. Automatisace, Vol. 6 (1958) p. 188-190
[162] Martin-Sanchez J. M.: *Adaptive predictive control system*. United States Patent, 4197576, (1976)
[163] Materialprüfanstalt Stuttgart (MPA): *Transiente Analyse Solarreceiver*. 902 2980 000 (2014)
[164] Matuszkiewicz A., Flamand J. C. & Bouré J. A.: *The bubble-slug flow pattern transition and instabilities of void fraction waves*. International Journal of Multiphase Flow, Vol. 13, 2 (1987) p. 199-217
[165] Mayne D. Q.: *Model predictive control: Recent developments and future promise*. Automatica, Vol. 50, 12 (2014) p. 2967-2986
[166] Meaburn A. & Hughes F. M.: *Resonance characteristics of distributed solar collector fields*. Solar Energy, Vol. 51, 3 (1993) p. 215-221
[167] Meaburn A. & Hughes F. M.: *A simple predictive controller for use on large scale arrays of parabolic trough collectors*. Solar Energy, Vol. 56, 6 (1996) p. 583-595
[168] Mertins M., Link E., Tscheche M. & Leuckel H.: *Experiences of operation of 30 MW solarthermal power station based on Fresnel collector technology*. Proceedings of the 18th SolarPACES Conference, Marrakech, Morocco (2012)
[169] Miller K. J. & O'donnell W. J.: *The fatigue limit and its elimination*. Fatigue & Fracture of Engineering Materials & Structures, Vol. 22, 7 (1999) p. 545-557
[170] Mills D. R. & Morrison G. L.: *Compact linear fresnel reflector solar thermal power plants*. Solar Energy, Vol. 68, 3 (2000) p. 263-283

[171] Minami K. & Shoham O.: *Transient two-phase flow behavior in pipelines - experiment and modeling*. International Journal of Multiphase Flow, Vol. 20, 4 (1994) p. 739-752
[172] Minzer U., Barnea D. & Taitel Y.: *Evaporation in parallel pipes—splitting characteristics*. International Journal of Multiphase Flow, Vol. 30, 7–8 (2004) p. 763-777
[173] Minzer U., Barnea D. & Taitel Y.: *Flow rate distribution in evaporating parallel pipes—modeling and experimental*. Chemical Engineering Science, Vol. 61, 22 (2006) p. 7249-7259
[174] Moelbak T.: *Robust adaptive control of superheater temperature in a power station*. VGB Kraftwerkstechnik, Vol. 71, 6 (1991) p. 558-561
[175] Morari M. & Zafiriou E.: *Robust Process Control*. Prentice Hall (1989)
[176] Morf H.: *The Stochastic Two-State Cloud Cover Model STSCCM*. Solar Energy, Vol. 85, 5 (2011) p. 985-999
[177] Morf H.: *The Parameterization of Cloud Cover*. Energy Procedia, Vol. 57, 0 (2014) p. 1293-1298
[178] Morille F.: *Modellerstellung für die prädiktive Regelung eines Parabolrinnenkraftwerks mit Direktverdampfung*. Diploma thesis, Karlsruhe Institute of Technolgy and DLR (2013)
[179] Morin G., Kirchberger J., Lemmertz N. & Mertins M.: *Operational results and simulation of a superheating Fresnel collector*. Proceedings of the 18th SolarPACES Conference, Marrakech, Morocco (2012)
[180] Mortensen J. H., Moelbak T., Andersen P. & Pedersen T. S.: *Optimization of boiler control to improve the load-following capability of power-plant units*. Control Engineering Practice, Vol. 6, 12 (1998) p. 1531-1539
[181] Müller-Steinhagen H. & Heck K.: *A simple friction pressure drop correlation for two-phase flow in pipes*. Chem. Eng. Process, Vol. 20, (1986) p. 297-308
[182] Müller M.: *Strömungsphänomene bei der Direktverdampfung in Parabolrinnen-Solarkraftwerken*. VDI-Verlag Düsseldorf, Germany (1995)
[183] Nakamura H. & Akaike H.: *Statistical identification for optimal control of supercritical thermal power plants*. Automatica, Vol. 17, 1 (1981) p. 143-155
[184] Nakamura H., Kukita Y. & Tasaka K.: *Flow Regime Transition to Wavy Dispersed Flow for High-Pressure Steam/ Water Two-Phase Flow in Horizontal Pipe*. Journal of Nuclear Science and Technology, Vol. 32, 7 (1995) p. 641-652
[185] Odeh S. D., Behnia M. & Morrison G. L.: *Hydrodynamic analysis of direct steam generation solar collectors*. Journal of Solar Energy Engineering, Vol. 122, (2000) p. 14-22
[186] Odeh S. D., Morrison G. L. & Behnia M.: *Modelling of parabolic trough direct steam generation solar collectors*. Solar Energy, Vol. 62, 6 (1998) p. 395-406
[187] Oluwande G. & Boucher A. R.: *Implementation of a mutivariable model-based predictive controller for superheater steam temeprature and pressure control on a large coal-fired power plant*. Proceedings of the European Control Conference ECC'99, Karlsruhe, Germany (1999)
[188] Ordys A. W. & Grimble M.: *A multivariable dynamic performance predictive control with application to power generation plants*. Proceedings of the IFAC World Congress, San Francisco, USA (1996)
[189] Patankar S.: *Numerical Heat Transfer and Fluid Flow*. Taylor & Francis (1980)
[190] Paul C., Teichrew O. & Ternedde A.: *Operation experience of the integration of a solar boiler based on Fresnel collector technology into a coal-fired power station*. Proceedings of the 18th SolarPACES Conference, Marrakech, Morocco (2012)
[191] Petukhov B. S. (1970) Heat transfer in turbulent pipe flow with variable physical properties. IN Irvine T. F. & Hartnett J. P. (Eds.) *Advances in Heat Transfer*. New York, Academic Press.

[192] Pickhardt R.: *Anwendung von adaptiven Reglern in einem Solarkraftwerk / Application of Adaptive Controllers to a Solar Power Plant*. at - Automatisierungstechnik, Vol. 48, 10 (2000)
[193] Pickhardt R.: *Nonlinear modelling and adaptive predictive control of a solar power plant*. Control Engineering Practice, Vol. 8, 8 (2000) p. 937-947
[194] Pitz-Paal R., Dersch J. & Milow B.: *Ecostar - European Concentrated Solar Thermal Road-Mapping*. DLR Report, SES6-CT-2003-502578 (2003)
[195] Pointner H., Steinmann W.-D., Eck M. & Bachelier C.: *Separation of Power and Capacity in Latent Heat Energy Storage*. Proceedings of the 20th SolarPACES Conference, Beijing, China (2014)
[196] Poncia G. & Bittanti S.: *Multivariable model predictive control of a thermal power plant with built-in classical regulation*. International Journal of Control, Vol. 74, 11 (2001) p. 1118-1130
[197] Prett D. M., Ramaker B. L. & Cutler C. R.: *Dynamic Matrix Control Method*. Patent U. S., 4349869, (1982)
[198] Profos P.: *Die Regelung von Dampfanlagen*. Springer Berlin (1962)
[199] Raff T., Huber S., Nagy Z. & Allgöwer F.: *Non-linear model predictive control of a four tank system: An experimental stability study*. Proceedings of the IEEE Conference on Control Applications, Munich, Germany (2006) p. 237-242
[200] Ramirez Santigosa L. & Wilbert S.: *METAS - Meteorological station for solar technologies (Presentation)*. Offical inauguration METAS and DUKE on June 6, 2013, Almería, Spain (2013)
[201] Ranjbar K.: *Failure analysis of boiler cold and hot reheater tubes*. Engineering Failure Analysis, Vol. 14, 4 (2007) p. 620-625
[202] Rawlings J. B. & Mayne D. Q.: *Model Predictive Control: Theory and Design* Nob Hill Publishing (2009)
[203] Ray A.: *Dynamic modelling of once-through subcritical steam generator for solar applications*. Applied Mathematical Modelling, Vol. 4, 6 (1980) p. 417-423
[204] Ray A. & Bowman H. F.: *A Nonlinear Dynamic Model of a Once-Through Subcritical Steam Generator*. Journal of Dynamic Systems, Measurement, and Control, Vol. 98, 3 (1976) p. 332-339
[205] Rheinländer J. & Eck M.: *Direct Solar Steam - Preliminary Report on DSG Test Results*. ZSW and DLR Report (2000)
[206] Rheinländer J. & Eck M.: *Numerical Modelling of Pressure Losses - DISS-SC-MI-03*. ZSW Report (2002)
[207] Richalet J., Rault A., Testud J. L. & Papon J.: *Model predictive heuristic control: Applications to industrial processes*. Automatica, Vol. 14, 5 (1978) p. 413-428
[208] Richardson L. F.: *The problem of contiguity: An appendix to Statistic of Deadly Quarrels*. General systems: Yearbook of the Society for the Advancement of General Systems Theory, Vol. 139, 6 (1961) p. 139–187
[209] Riffelmann K., Richert T., Nava P. & Schweitzer A.: *Ultimate Trough® – A Significant Step towards Cost-competitive CSP*. Energy Procedia, Vol. 49, 0 (2014) p. 1831-1839
[210] Rizwan U.: *On density-wave oscillations in two-phase flows*. International Journal of Multiphase Flow, Vol. 20, 4 (1994) p. 721-737
[211] Rosselló Robert A.: *Charakterisierung der thermo-mechanischen Belastungen eines Parabolrinnen-Solarkraftwerks*. Master Thesis, TU Munich and DLR Stuttgart (2015)
[212] Rouhani S. Z. & Axelsson E.: *Calculation of void volume fraction in the subcooled and quality boiling regions*. International Journal of Heat and Mass Transfer, Vol. 13, 2 (1970) p. 383-393

[213] Rubio F. R., Berenguel M. & Camacho E. F.: *Fuzzy logic control of a solar power plant.* Fuzzy Systems, IEEE Transactions on, Vol. 3, 4 (1995) p. 459-468

[214] Ruspini L. C., Marcel C. P. & Clausse A.: *Two-phase flow instabilities: A review.* International Journal of Heat and Mass Transfer, Vol. 71, 0 (2014) p. 521-548

[215] Savateev G.: *Design of non-linear model predictive control for temperature stabilization of a parabolic trough solar-thermal power plant.* Master Thesis, University of Dortmund and DLR Stuttgart (2014)

[216] Schenk H. & Eck M.: *enerMENA: Yield Analysis for Parabolic Trough Solar Thermal Power Plants - A basic Approach.* German Aerospace Center (DLR) Report (2011)

[217] Schenk H. & Hirsch T.: *Simulation von parallelen, unterschiedlich beheizten Verdampfersträngen in einem solarthermischen Kraftwerk* Ebsilon Anwendertagung, Seeheim-Jugendheim (2011)

[218] Schenk H., Hirsch T., Wittmann M., Wilbert S., Keller L. & Prahl C.: *Design and operation of an irradiance measurement network.* SolarPACES Conference, Beijing, China (2014)

[219] Schieritz M., Thumann M. & Vorholz F.: *Oil - The black power (in German).* Die ZEIT, Vol. 47, (2014)

[220] Schildbach G.: *Scenario-Based Optimization for Multi-Stage Stochastic Decision Problems.* Dissertation, ETH Zurich, Switzerland (2014)

[221] Schiricke B.: *Optischer Wirkungsgrad von Parabolrinnenkollektoren: Modellierung und Messung.* Fortschritt-Berichte Energietechnik, Reihe 6, No. 575, VDI Verlag Düsseldorf, Germany (2008)

[222] Schmidt D.: *Steinmüller Taschenbuch Rohrleitungstechnik.* Vulkan Verlag (2005)

[223] Silinga C., Gauché P., Rudman J. & Cebecauer T.: *The South African REIPPP Two-tier CSP Tariff: Implications for a Proposed Hybrid CSP Peaking System.* Energy Procedia, Vol. 69, (2015) p. 1431-1440

[224] Silva R. N., Rato L. M. & Lemos J. M.: *Time scaling internal state predictive control of a solar plant.* Control Engineering Practice, Vol. 11, 12 (2003) p. 1459-1467

[225] Solar Millennium: *The parabolic trough power plants Andasol 1 to 3 - The largest solar power plants in the world - Technology premiere in Europe.* Solar Millennium Report (2009)

[226] Song K.-Y., Gupta M. M. & Homma N.: *Design of an Error-Based Adaptive Controller for a Flexible Robot Arm Using Dynamic Pole Motion Approach.* Journal of Robotics, Vol. 2011, Article ID 726807 (2011) p. 9

[227] Sonnenburg H. G. & Tuomisto H.: *Analysis of a selected two-phase flow phenomenon in VVER reactors with horizontal steam generators.* Nuclear Engineering and Design, Vol. 145, 1–2 (1993) p. 261-269

[228] Steiner D.: *Wärmeübergang beim Strömungsverdampfen von Reinstoffen und von Mischungen.* Habilitation, University of Karlsruhe (1996)

[229] Steinmann W.-D.: *Dynamik solarer Dampferzeuger.* Fortschritts-Berichte VDI, VDI-Verlag Düsseldorf, Germany (2001)

[230] Steinmann W.-D. & Eck M.: *Direct Solar Steam Generation in Parabolic Troughs: Thermal Stress due to Variations in Irradiation.* Proceedings of the 10th SolarPACES Symposium, Sydney (2000)

[231] Stenning A. H. & Veziroglu T. N.: *Density-Wave Oscillations in Boiling Freon-11.* ASME Paper Report (1966)

[232] Strauß K.: *Kraftwerkstechnik - zur Nutzung fossiler, regenerativer und nuklearer Energiequellen.* 4 Aufl. (1998)

[233] Streber H.-P.: *Druckverlustbestimmung in Zwei-Phasen-Strömungen mit hohen Dampfgehalten.* Master Thesis, Universisty of Stuttgart and DLR Stuttgart (2014)

[234] Succo M.: *DSDS - Kostenstudie Solarfeld (Draft).* Tiede- & Niemann Ingenieurgesellschaft mbH Report (2015)
[235] Taitel Y. & Barnea D.: *Transient solution for flow of evaporating fluid in parallel pipes using the drift flux model.* Proceedings of the International conference on multiphase flow (ICMF-2010), Tampa, FL, USA (2010)
[236] Taitel Y. & Barnea D.: *Transient solution for flow of evaporating fluid in parallel pipes using analysis based on flow patterns.* Int. J. Multiphase Flow, Vol. 37, (2011) p. 469-474
[237] Taitel Y. & Dukler A. E.: *A model for predicting flow regime transitions in horizontal and near horizontal gas-liquid flow.* AIChE Journal, Vol. 22, 1 (1976) p. 47-55
[238] Taitel Y., Minzer U. & Barnea D.: *A control procedure for the elimination of mal flow rate distribution in evaporating flow in parallel pipes.* Solar Energy, Vol. 82, 4 (2008) p. 329-335
[239] Taitel Y., Shoham O. & Brill J. P.: *Simplified transient solution and simulation of two-phase flow in pipelines.* Chemical Engineering Science, Vol. 44, 6 (1989) p. 1353-1359
[240] Takitani K. & Sakano K.: *Density Wave Instability in Once-Through Boiling Flow System, (III).* Journal of Nuclear Science and Technology, Vol. 16, 1 (1979) p. 16-29
[241] Taler J., Weglowski B., Gradziel S., Duda P. & Zima W.: *Monitoring of Thermal Stresses in Pressure Components of Large Steam Boilers.* VGB PowerTech, Vol. 82, 1 (2002) p. 73-78
[242] Tanner P., Rasmussen K., Johnson P., Hoermann A. & Cheng W.: *Control of Solar Steam Generators.* Proceedings of the ASME 2011 Power Conference, Denver, CO, USA (2011) p. 309-316
[243] Terdalkar R., Doupis D., Clark M., Joshi A. & Wang C.: *Transient Simulation of High Temperature High Pressure Solar Tower Receiver.* Energy Procedia, Vol. 69, (2015) p. 1451-1460
[244] Thom J. R. S.: *Prediction of pressure drop during forced circulation boiling of water.* Int. J. Heat and Mass Transfer, Vol. 7, (1964) p. 709-724
[245] Thome J. R.: *Wolverine Engineering Data Book III.* Wolverine Tube, Inc. Lausanne, Switzerland (2010)
[246] Thome J. R. & Hajal J. E.: *Two-Phase Flow Pattern Map for Evaporation in Horizontal Tubes: Latest Version.* Heat Transfer Engineering, Vol. 24, 6 (2003) p. 3-10
[247] Tomson T.: *Fast dynamic processes of solar radiation.* Solar Energy, Vol. 84, 2 (2010) p. 318-323
[248] Trebing D.: *Regelkonzepte zur Temperaturstabilisierung eines Parabolrinnenkraftwerks mit Direktverdampfung.* Master Thesis, RWTH Aachen and DLR Stuttgart (2012)
[249] Trieb F.: *Concentrating Solar Power for the Mediterranean Region. German Aerospace Center (DLR) / Institute of Technical Thermodynamics / Section Systems Analysis and Technology Assessment.* MED-CSP Study Report (2005)
[250] Trieb F., Schillings C., O'Sullivan M., Pregger T. & Hoyer-Klick C.: *Global Potential of Concentrating Solar Power.* 15th SolarPACES Symposium, Berlin, Germany (2009)
[251] Uhlig R.: *Dokumentation des ANSYS APDL Makros „AT_3D" zur thermischen und mechanischen Simulation von Absorberrohren für Rinnenkraftwerke.* DLR Stuttgart Report (2010)
[252] Unbehauen H. & Linck E.: *Dynamische Modelle und Simulation von Dampfüberhitzern.* Fortschrittberichte der VDI-Zeitschriften, Reihe 8, VDI-Verlag Düsseldorf (1971)

[253] Valenzuela L.: *Control Automatico de Plantas de Generacion Directa de Vapor con Colectores Solares Cilindro-Parabolicos.* PhD Thesis, University of Almeria/ CIEMAT Madrid (2008)

[254] Valenzuela L., Zarza E., Berenguel M. & Camacho E. F.: *Direct steam generation in solar boilers - Using feedback to maintain conditions under uncontrollable solar radiation.* Control Systems, IEEE, Vol. 24, 2 (2004) p. 15-29

[255] Valenzuela L., Zarza E., Berenguel M. & Camacho E. F.: *Control concepts for direct steam generation in parabolic troughs.* Solar Energy, Vol. 78, 2 (2005) p. 301-311

[256] Valenzuela L., Zarza E., Berenguel M. & Camacho E. F.: *Control scheme for direct steam generation in parabolic troughs under recirculation operation mode.* Solar Energy, Vol. 80, 1 (2006) p. 1-17

[257] VDI: *VDI Heat Atlas.* Springer, 2nd Edition Aufl. Berlin Heidelberg (2010)

[258] VGB PowerTech (2003) VGB-R 512 M: Richtlinie zu Prüfungen betriebsbeanspruchter Läufer und Gehäuse von Dampf- und Gasturbosätzen.

[259] Weglowski B., Taler J. & Duda P.: *Monitoring of Thermal Stresses in Steam Generators.* Proceedings of the 17th International Conference on Structural Mechanics in Reactor Technology (SMiRT 17), Prague, Czech Republic (2003)

[260] Wellers M. H.: *Nichtlineare modellgestützte prädiktive Regelung auf Basis von Wiener- und Hammerstein-Modellen.* Fortschritt-Berichte, Reihe 8, No. 742, VDI Verlag Düsseldorf, Germany (1999)

[261] Wikipedia (2015) Cloud, Cirrus cloud, Cumulus cloud, Cumulonimbus cloud (Articles accessed Jan. 2015).

[262] Wilbert S., Janotte N., Pitz-Paal R., van Wely L. & Geuder N.: *Reduced Uncertainties of Field Pyrheliometers through Improved Sensor Calibration.* Proceedings of the 16th SolarPACES Conference, Perpignon, France (2010)

[263] Winterton R. H. S.: *Where did the Dittus Boelter equation come from?* Int. J. Heat Mass Transfer, Vol. 41, 4-5 (1998) p. 809-810

[264] Wittmann M., Eck M., Pitz-Paal R. & Müller-Steinhagen H.: *Methodology for Optimized Operation Strategies of Solar Thermal Power Plants with Integrated Heat Storage.* Proceedings of the 15th SolarPACES Symposium, Berlin (2009) p. 8

[265] Wittmann M., Feldhoff J. F. & Hirsch T.: *Determination of Correction Factors for Heat Losses at High Temperatures in Parabolic Trough Fields.* Proceedings of the 18th SolarPACES Conference Marrakech, Morocco (2012)

[266] Wojtan L., Ursenbacher T. & Thome J. R.: *Investigation of flow boiling in horizontal tubes: Part I—A new diabatic two-phase flow pattern map.* International Journal of Heat and Mass Transfer, Vol. 48, 14 (2005) p. 2955-2969

[267] Wojtan L., Ursenbacher T. & Thome J. R.: *Investigation of flow boiling in horizontal tubes: Part II—Development of a new heat transfer model for stratified-wavy, dryout and mist flow regimes.* International Journal of Heat and Mass Transfer, Vol. 48, 14 (2005) p. 2970-2985

[268] Yebra L. J., Berenguel M. & Dormido S.: *Extended moving boundary model for two phase flows.* Proceedings of the 16th IFAC World Congress, Prague, Czech Republic (2005)

[269] Zapata J. I.: *Full state feedback control of steam temperature in a once-through direct steam generation receiver powered by a paraboloidal dish.* Proceedings of the ASME 2014 8th International Conference on Energy Sustainability, Boston, MA, USA (2014)

[270] Zapata J. I.: *State estimation of a solar direct steam generation mono-tube cavity receiver using a modified Extended Kalman Filtering scheme.* Solar Energy, Vol. 114, (2015) p. 152-166

[271] Zapata J. I., Pye J. & Lovegrove K.: *A transient model for the heat exchange in a solar thermal once through cavity receiver*. Solar Energy, Vol. 93, 0 (2013) p. 280-293
[272] Zarza E.: *Generación directa de vapor con colectores solares cilindro parabólicos - Proyecto Direct Solar Steam (DISS)*. Colección Documentos Ciemat Madrid (2004)
[273] Zarza E.: *How the name DISS was chosen.* Personal Communication (2014)
[274] Zarza E., Rojas M. E., González L., Caballero J. M. & Rueda F.: *INDITEP: The first pre-commercial DSG solar power plant*. Solar Energy, Vol. 80, 10 (2006) p. 1270-1276
[275] Zarza E., Valenzuela L., León J., Eck M., Hennecke K., Weyers H. D. & Eickhoff M.: *The DISS project: Direct Steam Generation in Parabolic Troughs-Operation and Maintanance Experience and Update on Project Status*. Solar Energy Forum 2001: The Power to Choose, Washington, D.C., USA, April 21-25, 2001, Washington D.C. (2001)
[276] Zarza E., Valenzuela L., León J., Hennecke K., Eck M., Weyers H. D. & Eickhoff M.: *Direct steam generation in parabolic troughs: Final results and conclusions of the DISS project*. Energy, Vol. 29, 5-6 (2004) p. 635-644
[277] Zipf V., Neuhäuser A., Willert D., Gschwander S. & Platzer W.: *Development of a high temperature PCM storage for DSG: First test results with a prototype*. Proceedings of the 18th SolarPACES Conference, Marrakech, Morocco (2012)
[278] Zunft S.: *Dynamik und Regelung von Solarkollektorfeldern zur Prozeßwärme- und Stromerzeugung.* Fortschritt Berichte Energieerzeugung, VDI-Verlag Stuttgart (2003)
[279] Zunft S. & Bissinger N.: *Measurement of steam quality for the control of steam-generating collectors*. Journal De Physique IV, Vol. 9, (1999) p. 501-506
[280] Zürcher O., Favrat D. & Thome J. R.: *Development of a diabatic two-phase flow pattern map for horizontal flow boiling*. International Journal of Heat and Mass Transfer, Vol. 45, 2 (2002) p. 291-301